

# Light Control and Microcavity Lasers Based on Quantum Wires Integrated in Photonic-Crystal Cavities

THÈSE N° 4359 (2009)

PRÉSENTÉE LE 3 AVRIL 2009

À LA FACULTÉ SCIENCES DE BASE  
LABORATOIRE DE PHYSIQUE DES NANOSTRUCTURES  
PROGRAMME DOCTORAL EN PHOTONIQUE

ÉCOLE POLYTECHNIQUE FÉDÉRALE DE LAUSANNE

POUR L'OBTENTION DU GRADE DE DOCTEUR ÈS SCIENCES

PAR

Kirill ATLASOV

acceptée sur proposition du jury:

Prof. O. Martin, président du jury  
Prof. E. Kapon, directeur de thèse  
Prof. D. Deppe, rapporteur  
Prof. Y.-H. Lee, rapporteur  
Prof. V. Savona, rapporteur



ÉCOLE POLYTECHNIQUE  
FÉDÉRALE DE LAUSANNE

Suisse  
2009



# Abstract

Novel light-emitting devices and micro-optical-circuit elements will rely upon understanding and control of light-matter interaction at the nanoscale. Recent advances in nanofabrication and micro-processing make it possible to develop integrable solid-state structures where the optical- and quantum-*confinement* effects determine the density and distribution of the energy states, allowing for mastering the output characteristics. In semiconductor *nanostructures*, such as quantum wires or quantum dots (sometimes referred even to as "artificial atoms") produced by epitaxy, with characteristic dimensions of  $10 \div 20\text{nm}$ , the quantization determines light absorption and emission spectra. Unlike the bulk matter, these important properties depend on the size and shape of the object, which is designed by nanotechnology. In *photonic crystals* and photonic-crystal micro-resonators, on the other hand, due to pronounced bandgap effects acting on light, unprecedented control over reflectivity, transmission and such a fundamental quantum-mechanical property as the density of electromagnetic vacuum-field fluctuations is achieved, the latter defining the rates of *spontaneous emission* of an embedded source. Based on these ideas, a number of passive and active optical and optoelectronic devices is anticipated practically, in particular, semiconductor *microlasers* with extremely low threshold pump-powers and ultimate conversion efficiency.

Within the framework of this thesis we successfully integrated *site-controlled* quantum wires (QWRs) in 2D photonic-crystal (PhC) microcavities, examined the basic spectral and dynamics properties of the system, implemented the QWRs as a testing light source and probed interesting cavity configurations, and finally achieved stimulated emission and lasing.

Starting from the previous studies of the QWR nanostructures, we, first, designed the geometry patterns adapted for implementation in the PhC-cavity system. Crystal growth (by metal-organic vapor-phase epitaxy) of *InGaAs/GaAs* QWRs on such patterns was verified; single and triple vertically stacked identical wires were obtained integrated within a 260-nm thin *GaAs* membrane. The basic properties of such QWRs were checked by photoluminescence spectroscopy. Spectra, power-dependent blueshift and temperature dependence consistent with previous studies were evidenced. Relatively long radiative lifetimes were found (at low – 20K – temperature) in transient spectroscopy, suggesting exciton localization effects and the effective dimensionality in between 0D and 1D.

Identified as the most practically feasible way of exploiting the PhC bandgap effects for achieving high-*Q* truly single-mode resonators, the *membrane* approach in *2D photonic crystals* was then implemented. In our nanofabrication effort we succeeded

in incorporating the QWRs into such PhC cavities with very good site-control. The site control is apparently crucial, as light-matter coupling in an optical cavity and the spontaneous-emission properties are determined by the spatial and spectral matching. Cavity  $Q$ -factors of  $\sim 5000 \div 6000$  were reached. Our technology can be readily extended to schemes involving multiple *site-controlled nanostructures* in single or multiple (e.g. coupled) cavities that are currently of interest for various experiments in quantum physics.

We then examined several interesting cavity configurations including *coupled* and *1D-like* PhC cavities, exploiting QWRs as an embedded local light source. Such cavity geometries are relevant to on-chip photon-transfer lines, single-photon sources, coupled-cavity lasers and quantum-optics experiments. While with 1D-like cavities we were able to track the *0D-1D transition* of the photonic states and observe important implications due to distributed *disorder*, we also found out experimentally and analyzed numerically that in the formation of the coupled states an important feature of *loss splitting* appears having implications on the energy transfer.

On a more fundamental level, we examined PhC-cavity and bandgap effects on the QWR *spontaneous emission*. It was found experimentally that, at low temperature, the QWR spontaneous emission resonantly coupled to the cavity mode can be *enhanced* by factors of  $\sim 2 \div 2.5$ . In addition, the off-resonance part is *inhibited* by a factor of  $\sim 3$ . Such measured factors suggest that the output stems from an ensemble of emitters, which is consistent with a regular QWR inhomogeneous broadening and exciton localization picture. Nevertheless, the enhancement of the spontaneous emission into the cavity mode with respect to any other available modes is then a factor of  $\sim 6$ , which is important for microcavity laser concept based on the *spontaneous-emission control*.

Finally, multi- and *single-mode lasing* is experimentally demonstrated (for the first time). In order to verify the observation of the stimulated emission and lasing, complex analysis of spectral and photon-dynamics characteristics was undertaken and compared to a rate-equation model. Significantly *low threshold* values of  $\lesssim 1\mu W$  (incident power) were achieved, with relatively high *spontaneous-emission coupling* factors of  $\sim 0.3$ .

**Keywords:**

Semiconductors, photonics, nanotechnology, nanoscale, quantum nanostructures, photonic crystals, light-matter interaction, spontaneous emission control, stimulated emission, microcavity laser, optical coupling, frequency splitting, supermodes, energy transfer, 1D system, photonic band, waveguide, quantum wire, quantum dot, epitaxy, MOVPE, micro-processing, nanolithography, ICP reactive ion etching, PhC membranes, GaAs, optical properties, photoluminescence, internal light source, transient spectroscopy.

# Version Abrégée

Les futures générations de sources lumineuses et les composants d'optique intégrée vont reposer sur la compréhension et le contrôle de l'interaction entre la lumière et la matière à l'échelle nanométrique. Les progrès réalisés récemment dans le domaine des nano et micro technologies ont permis de développer des structures intégrables à l'état solide dans lesquelles les *confinements* optique et quantique déterminent la densité et la distribution des états énergétiques permettant la maîtrise des caractéristiques de sortie des composants. Dans le cas des *nanostuctures semiconductrices* telles que les fils ou les boîtes quantiques (ces dernières étant souvent qualifiées de "super-atomes artificiels"), produites par l'épitaxie, et pour lesquelles les dimensions typiques sont de l'ordre de  $10 \div 20\text{nm}$ , la quantification détermine les spectres d'absorption et de l'émission de la lumière. Contrairement au matériau brut, ces propriétés importantes dépendent de leurs *dimensions*, qui peuvent être ajustées grâce aux nanotechnologies. D'un autre côté, les *cristaux photoniques* et les micro résonateurs à base de cristaux photoniques, permettent un contrôle jusqu'à présent inégalé de la réflectivité, de la transmission, ainsi que de la propriété fondamentale de la mécanique quantique qu'est la densité d'états électromagnétiques du vide. Ce dernier définit les taux *d'émission spontanée* d'une source intégrée. Se basant sur ces idées, de nombreux composants actifs ou passifs peuvent être envisagés, et en particulier, des microlasers à semiconducteur avec des seuils extrêmement bas ainsi que l'efficacité de conversion ultimement élevée.

Dans le cadre de cette thèse, nous avons avec succès intégré des fils quantiques (QWRs) dans des microcavités de cristaux photoniques bidimensionnels (PhC). Nous avons examiné les propriétés spectrales basiques et dynamiques, en utilisant les QWRs en tant que source lumineuse de test et ainsi mesuré des configurations de cavité intéressantes, et finalement démontré une émission stimulée et un effet laser.

En partant des études précédentes de QWRs, nous avons, en premier lieu, développé la géométrie de QWRs bien adaptée à une cavité du type de *membrane* de PhC. Sur de tels motifs, on a établi ensuite la croissance (l'épitaxie en phase gazeuse à partir de précurseurs organo-métalliques) des fils à base de *InGaAs/GaAs*. Des fils simples et triples (empilés) ont été donc intégrés au sein d'un mince (260-nm) membrane de PhC. Les propriétés des fils ont été vérifiées par photoluminescence. Les spectres et leurs dépendances (de puissance, de température) *compatibles* avec les études précédentes ont été observés. Puis, en employant la spectroscopie transitoire, on a trouvé des relativement longues durées de vie radiative (à  $T=20\text{K}$ ), ce qui indique des effets de localisation des excitons et donc une dimension actuelle de fils entre 0D et 1D.

La technologie à *membrane* a été identifiée comme étant la plus pratique à mettre en

œuvre pour exploiter des effets des bandes interdites photoniques pour construire des résonateurs mono-modes à *ultimement petits volumes* mais avec des hauts facteurs de qualité. Nos efforts nous ont permis d'incorporer des QWRs dans ces PhCs en contrôlant leurs positionnements. Ce dernier paramètre est très important, compte tenu du fait que le couplage entre la lumière et la matière dépend de l'accord spatial et spectral. Des facteurs de qualité de  $5000 \div 6000$  ont pu être atteints. Notre *technologie* est prête pour être étendue à des configurations pour lesquelles plusieurs nanostructures peuvent être incorporées dans plusieurs cavités couplées.

Nous avons ensuite examiné plusieurs configurations de cavité, dont des cavités à *caractère 1D* et des *cavités couplées*, exploitant des QWRs comme source de lumière. De telles cavités peuvent être intéressantes pour des applications telles que le transfert de photons au sein d'un composant, des sources de photons uniques, des lasers à cavité couplées et des expériences d'optique quantique. Dans le cadre de cette étude des cavités 1D, nous avons pu mettre en évidence la *transition 0D-1D* des états photoniques et en déduire des implications importantes de la distribution du *désordre*. Nous avons de même mis en évidence de manière expérimentale, en appui sur des simulations numériques, que la formation d'états couplés donnait lieu à une *levée de dégénérescence des pertes*, ayant une implication dans le transfert d'énergie.

D'un point de vue plus fondamental, nous avons examiné l'effet de la bande interdite photonique et de la cavité d'un PhC sur l'émission spontanée. Il a été notamment démontré qu'à basse température, le taux *d'émission spontanée* d'un fil quantique en résonance avec une cavité de PhC pouvait être *renforcé* d'un facteur  $\sim 2 \div 2.5$ . De plus, la partie hors résonance est *inhibée* d'un facteur  $\sim 3$ . De telles observations montrent que les caractéristiques de sortie proviennent de la contribution d'un ensemble d'émetteurs, ce qui est en accord avec des effets de localisation d'excitons à basse température. Toutefois, l'augmentation du taux d'émission spontanée dans le mode de cavité par rapport à tout autre mode est de l'ordre de 6, ce qui est important pour les lasers de microcavité basé sur le *contrôle de l'émission spontanée*.

Enfin, des effets *d'émission stimulée* et *laser* multi et mono mode ont été démontrés de manière expérimentale, pour la première fois dans le système de QWR-PhC. Afin de vérifier ces observations, des analyses complexes des spectres de luminescence ainsi que de la dynamique des photons ont été comparées à des modèles basés sur des équations de taux. Des seuils extrêmement bas  $\lesssim 1\mu W$  (de puissance incidente) ont pu être atteints, avec des facteurs de couplage d'émission spontanée relativement élevés ( $\beta \sim 0.3$ ).

### Mots clés:

Semi-conducteurs, photonique, nanotechnologie, échelle nanométrique, nanostructures quantiques, cristaux photoniques, interaction lumière-matière, contrôle de l'émission spontanée, émission stimulée, laser à microcavité, couplage optique, séparation des fréquences, supermodes, transfert d'énergie, système unidimensionnel, bande photonique, guide d'ondes, fils quantique, boîtes quantiques, épitaxie, MOVPE, micro-processing, nanolithographie, plasma à couplage inductif, membrane à PhC, GaAs, propriétés optiques, photoluminescence, source de la lumière interne, spectroscopie transitoire.

# Contents

<b>Abstract</b>	<b>i</b>
<b>Version Abrégée</b>	<b>iii</b>
<b>1 Introduction</b>	<b>1</b>
1.1 Nanotechnology in photonics . . . . .	1
1.2 Semiconductor quantum nanostructures . . . . .	2
1.3 Light-matter interaction . . . . .	5
1.4 Spontaneous-emission control and photonic crystals . . . . .	8
1.5 Applications . . . . .	13
1.6 Thesis goal and outline . . . . .	13
<b>2 Fundamental aspects of quantum wires and photonic-crystal cavities</b>	<b>15</b>
2.1 Optical properties of quantum wires . . . . .	15
2.1.1 Effect of disorder and excitons . . . . .	15
2.1.2 Absorption and gain . . . . .	21
2.1.3 Spontaneous emission . . . . .	25
2.2 Microcavity laser concept . . . . .	27
2.2.1 Spontaneous-emission coupling factor . . . . .	27
2.2.2 Mean photon number and threshold definition . . . . .	28
2.3 Modeling of 2D photonic-crystal microcavities . . . . .	31
2.3.1 2D finite-difference stationary model . . . . .	32
2.3.2 3D FDTD simulations and Padé-Baker approximation . . . . .	37
2.3.3 <i>GaAs</i> refractive index corrections . . . . .	39
2.3.4 Light-cone problem: radiative losses of a 2D photonic-crystal cavity	43
2.4 Chapter summary . . . . .	45
<b>3 Technology and characterization of integrated quantum-wire photonic-crystal structures</b>	<b>47</b>
3.1 Site-controlled quantum wire integrated into a photonic-crystal microcavity	47
3.1.1 Summarized nanofabrication process . . . . .	48
3.1.2 <i>e</i> -beam nanolithography and pattern design . . . . .	48
3.1.3 Metal-organic vapor-phase epitaxy – InGaAs/GaAs V-groove QWR growth . . . . .	51

3.1.4	<i>e</i> -beam writing of PhC with alignment, and proximity-effect corrections . . . . .	56
3.1.5	Plasma etching . . . . .	58
3.1.6	Membrane release and postprocessing (“digital etching”) . . . . .	65
3.2	Characterization and analytical techniques . . . . .	66
3.2.1	Atomic-force microscopy . . . . .	66
3.2.2	Scanning and transmission electron microscopy . . . . .	67
3.2.3	Micro-photoluminescence . . . . .	68
3.2.4	Transient micro-PL spectroscopy . . . . .	71
3.3	Chapter summary . . . . .	72
<b>4</b>	<b>Spontaneous emission of quantum wires in photonic-crystal microcavities</b>	<b>75</b>
4.1	QWR emission spectrum . . . . .	76
4.2	Mode structure of the $L_6$ cavity . . . . .	77
4.2.1	Even and odd modes . . . . .	78
4.2.2	$Q$ enhancement by shifting cavity terminations . . . . .	79
4.3	Coupling of the QWR emission into PhC cavity modes: mode spectroscopy	81
4.3.1	Single QWR in $L_6$ cavity: cavity modes and tuning . . . . .	81
4.3.2	Vertically stacked QWRs in $L_3$ and $L_6$ cavities . . . . .	85
4.4	Emission dynamics and spontaneous emission control . . . . .	88
4.4.1	Emission dynamics of quantum wires in free space . . . . .	88
4.4.2	Quantum-wire emission in photonic-crystal cavities . . . . .	94
4.5	Chapter summary . . . . .	104
<b>5</b>	<b>One-dimensional photonic band formation in <math>L_N</math> photonic-crystal cavities</b>	<b>105</b>
5.1	One-dimensional photonic system . . . . .	106
5.1.1	1D photonic-crystal waveguide . . . . .	106
5.1.2	$L_N$ PhC cavities and the onset of 1D band formation . . . . .	107
5.2	$L_N$ cavity modes in the reciprocal space . . . . .	109
5.2.1	Formalism . . . . .	109
5.2.2	Analysis and results . . . . .	110
5.3	Disorder effects and mode localization . . . . .	113
5.3.1	Partial mode localization . . . . .	113
5.3.2	Discussion: disorder implications . . . . .	116
5.4	Chapter summary . . . . .	116
<b>6</b>	<b>Directly coupled photonic-crystal microcavities</b>	<b>119</b>
6.1	Linear resonant coupling . . . . .	119
6.1.1	Supermode formation, frequency splitting and energy transfer . . . . .	120
6.1.2	Splitting of loss . . . . .	121
6.2	Experimental observation of coupling . . . . .	122

6.2.1	QWR-PhC structure and independent quantum-wire internal light sources . . . . .	122
6.2.2	Mode (de)localization probed by spatially-resolved cavity excitation	123
6.2.3	Loss splitting . . . . .	124
6.2.4	Detuning limits . . . . .	125
6.3	Implications . . . . .	126
6.3.1	Diffractive origin of the loss splitting . . . . .	126
6.3.2	Implications on the energy transfer . . . . .	127
6.3.3	Tailoring the splitting characteristics by intercavity barrier engineering . . . . .	128
6.3.4	Dynamical coupling control using scanning-probe tip . . . . .	129
6.4	Chapter summary . . . . .	132
<b>7</b>	<b>Stimulated emission and lasing in quantum-wire photonic-crystal microcavities</b>	<b>135</b>
7.1	Observable properties of the lasing action . . . . .	136
7.1.1	Background spontaneous emission . . . . .	136
7.1.2	Linewidth narrowing . . . . .	137
7.1.3	Build-up of coherence . . . . .	138
7.2	Multimode quantum-wire photonic-crystal lasers . . . . .	140
7.2.1	Multimode lasing . . . . .	141
7.2.2	Spectral and time-resolved characteristics of a long-cavity QWR-PhC laser . . . . .	144
7.3	Single-mode QWR photonic-crystal lasers . . . . .	146
7.3.1	"Linear" vs lasing output from $L_{3m}$ , $L_6$ QWR-PhC cavities . .	146
7.3.2	QWR-PhC laser onset dynamics . . . . .	148
7.3.3	Details of the spectral features . . . . .	149
7.4	Chapter summary . . . . .	158
<b>8</b>	<b>Conclusions and outlook</b>	<b>159</b>
<b>A</b>	<b>Samples and recipes description</b>	<b>163</b>
A.1	Figure / sample correspondence . . . . .	163
A.2	Some recipes . . . . .	164
	<b>Bibliography</b>	<b>165</b>
	<b>Publications and conferences</b>	<b>188</b>
	<b>Acknowledgments</b>	<b>192</b>
	<b>Curriculum vitae</b>	<b>195</b>



*à mes parents Vera Atlasova et Alexander Atlasov  
et grands-parents Mikhail Potys et Kira Loseva*



# Chapter 1

## Introduction

### 1.1 Nanotechnology in photonics

The main strategy in the field of nanotechnology is to control matter on the scale of one billionth of a meter. Initially, this was pursued in the framework of miniaturization, for the reduction in size makes devices more compact, they consume less power and operate at higher speeds. This has been the major trend followed, above all, in microelectronics. This trend currently proceeds with a technological challenge to shrink the dimensions of devices and systems down to the atomic scales. In parallel, material synthesis starts at the point where the miniaturization aims at, that is, the scale of atoms and molecules. Thus, two main fabrication approaches exist: the so-called *top-down* and *bottom-up*, which are pursued nowadays intensively, either separately or jointly, in the search for new or improved functionalities in electronics and opto-electronics, medical, textile, sustainable energy and other fields. Based on the ability to observe and manipulate matter at nanoscale, new scientific branches (and sub-fields) arise [1]. Among them are e.g. nanoelectronics – comprising molecular electronics, nanocircuitry, nanolithography –, nanomedicine – developing nanosensors, biomarkers, drug-delivery systems on a sub-cell level, nanoneurosurgery, nanotoxicology etc –, nanomaterials – where the science of fullerenes, carbon nanotubes and nanoparticles is advancing – and molecular self-assembly or molecular nanotechnology – raising the perspectives of supramolecular assembly, nanorobotics, self-replicating molecular assemblers of macroscopic matter, DNA-synthesis nanotechnology and programmed self-assembly.

With the new developments in nanoscience and nanotechnology, new concepts build up, of which a good example is *nanophotonics*. As the designed dimensions had reached levels where the matter quantization starts arising, it was rapidly understood that low-dimensional structures [2] can be implemented to dramatically alter the optical properties of active materials employed in the creation and control of light. The electronic structures, such as semiconductor crystal *nanostructures* or metallic plasmonic nanostructures, are then combined with micro-structured *optical media*, respecting the characteristic wavelength of the particle involved (electron and photon), thus concatenating the new nanophotonics concept. The resulting electro-optical and optoelectronic devices (e.g. lasers, modulators, switches, light-emitting diodes, display devices, array

photodetectors, etc.) have revolutionized telecommunications, electronics, display, computer and information technology.

Semiconductor crystals are (traditionally) employed in creation of light, and the *nanostructures*, owing to the quantization effects on charge carriers, add then a possibility to produce light much more efficiently providing the basis for desired spectral optical properties. In addition, quite remarkably, the quantization of photonic states in optical *micro- and nanocavities* that can host the electronic active nanostructures may allow for exerting control on such a fundamental and all-mysterious quantity as vacuum fluctuations. In particular, in the expanding field of so-called *photonic crystals* such a control can be very efficiently implemented in solid state. Combined, these two possibilities open a way for controlling and tailoring the light-matter interaction at the fundamental level, which can be readily employed in development of high-efficiency ultra-low-power-consumption lasers and principally novel non-classical light sources, all suitable for on-chip integrable devices.

## 1.2 Semiconductor quantum nanostructures

The quantum size effects in solid-state matter may arise when the object's dimensions are sufficiently "small". The figure of merit that defines the scale is set by the quantum-mechanical *wave nature* of the particles involved. In the free charge-carrier picture, electrons in metals and semiconductors occupy the allowed energy states following the Fermi-Dirac statistics. The highest occupied quantum state is given by the Fermi energy yielding the Fermi wave vector  $k_F$  that defines the electron motion at this energy. The Fermi wavelength<sup>1</sup> is then given by  $\lambda_F = \frac{2\pi}{k_F}$ , which can be written via the carrier concentration  $N$  (per unit volume in 3D case) as  $\lambda_F = \frac{2\pi}{(3\pi^2 N)^{1/3}}$  [3]. In metals the free electron concentration is of the order of  $10^{22} \text{cm}^{-3}$  leading to  $\lambda_F < 1 \text{nm}$ , whereas for doped semiconductors<sup>2</sup> the much lower concentration (e.g.  $10^{18} \text{cm}^{-3}$ ) results in  $\lambda_F \sim 20 \text{nm}$ . This means that dimensions comparable to the corresponding Fermi wavelengths will result in carrier *quantum confinement*<sup>3</sup>. Such dimensions can be practically attained by current nanotechnology, which has recently resulted in a realization of the *semiconductor quantum nanostructures* called quantum wells (QWs), quantum wires (QWRs) and quantum dots (QDs) representing, respectively, one-, two- and three-dimensional (3D) carrier confinement [2].

<sup>1</sup>It is basically the de Broglie wavelength of an electron at the highest occupied quantum state.

<sup>2</sup>Note that since the donor states are very close to the conduction band, the Fermi energy is meaningful, as being situated within the conduction band, when the donor states are at least partially ionized (e.g. at  $T \gg 0K$ ). The "Fermi energy" of the intrinsic semiconductors lies within the bandgap, where no electrons can exist, and should be referred to as the chemical potential.

<sup>3</sup>Another way of deducing this scale is to consider the carrier de Broglie wavelength  $\lambda_{DB} = \frac{2\pi\hbar}{\sqrt{2m_e E}}$  where  $m_e$  is the electron mass and  $E$  – its energy. In the solid-state crystal the electron motion is subjected to the direction-dependent periodic crystal potential  $V$ , which is an equivalent to an electron moving in free space but with an *effective mass*  $m^*$  that also depends on the direction. The effective mass e.g. for *GaAs* at around the conduction band minimum is  $0.068m_e$ . Therefore the  $\lambda_{DB} \sim 20 \text{nm}$ , which gives a figure of merit for the quantization effects.

Very importantly, all the nanostructures are based on the concept of a *potential well*, which relies on the technological capability of creating *heterostructure* monocrystalline interfaces by the *epitaxial growth* techniques. The potential well is formed when a lower-bandgap material is placed in between higher-bandgap ones (Fig. 1.1). When non-equilibrium carriers are then created (by means of optical pumping or electrical injection) they first “drop” to the states with lower energies which are *within* the material with lower gap. There, the carriers experience the quantum confinement, provided the dimension  $L$  is small enough.

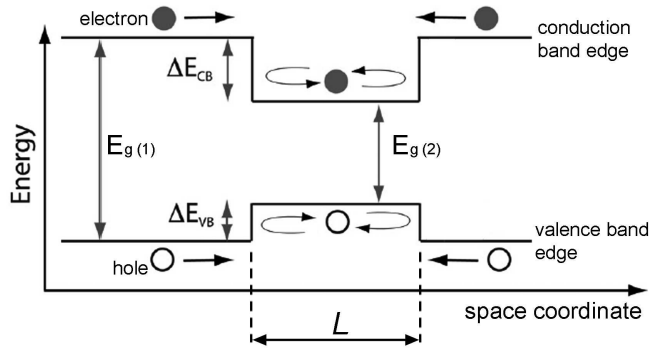


**Figure 1.1:** Illustration of the heterostructure concept. Practically, for example, material (1) can be *AlGaAs* and material (2) – *GaAs*, or *GaAs* and *InGaAs*, respectively.

The carrier wavefunctions and eigenenergies are the solutions of the time-independent Schrödinger equation that in the envelope-function approximation<sup>4</sup> reads:

$$\left[ -\frac{\hbar^2}{2m^*} \nabla^2 + V(x, y, z) \right] \psi(x, y, z) = E\psi(x, y, z) \quad (1.1)$$

where  $\psi(x, y, z)$  is the carrier envelope wave function,  $m^*$  is the carrier effective mass, and  $V(x, y, z)$  is the potential distribution<sup>5</sup>. For the infinitely deep potential wells of a rectangular shape [Fig. 1.2 (a)] 1D, 2D and 3D confinement is given by the low dimensions  $L_z$ ,  $L_z$  and  $L_y$ ,  $L_z$  and  $L_y$  and  $L_x$ , respectively. With respect to the bulk band edge, the energies are given by:

$$E_{n_z} = \frac{\hbar^2 \pi^2 n_z^2}{2m^* L_z^2} + \frac{\hbar^2 (k_y^2 + k_x^2)}{2m^*} \quad 1D \quad (1.2)$$

$$E_{n_z, n_y} = \frac{\hbar^2 \pi^2}{2m^*} \left( \frac{n_z^2}{L_z^2} + \frac{n_y^2}{L_y^2} \right) + \frac{\hbar^2 k_x^2}{2m^*} \quad 2D \quad (1.3)$$

$$E_{n_z, n_y, n_x} = \frac{\hbar^2 \pi^2}{2m^*} \left( \frac{n_z^2}{L_z^2} + \frac{n_y^2}{L_y^2} + \frac{n_x^2}{L_x^2} \right) \quad 3D \quad (1.4)$$

<sup>4</sup>Or, equivalently, the effective-mass approximation. Note also that the equation is written for a single particle. In a general case for solving the crystal band structure all the particles should be treated implying however solving  $\sim 10^{23}$  coupled equations. This is simplified down by use of important assumptions (Born-Oppenheimer, Hartree-Fock and mean-field approximations)

<sup>5</sup>The single-band model, although good for electrons in the conduction band, cannot account for band mixing effects in the valence bands. A multiband model therefore is used for hole states described by the Kohn-Luttinger Hamiltonian-matrix [4, 5]

where  $n_z, n_y, n_x = 1, 2, \dots$  are the level quantum numbers and  $k_{x,y}$  are the wave-vector components along the non-confined directions allowing therefore for free motion there;  $E(k)$  dispersions are known as *energy bands*<sup>6</sup>. The 1D, 2D and 3D confinement results therefore in the discretization of the energy levels bringing about quasi-2D, 1D and 0D electronic systems.

The possible occupancy at these discrete energy levels is then given by the electronic *density of states* (DoS) per unit volume. This quantity is extremely important since, since it enters in all the calculations involving the transitions between the bands, and it has therefore a major impact on the optical properties of the material. Briefly, it can be assessed as follows [8]. It is assumed that since the semiconductor crystal structure is a periodic medium (i.e. composed of adjacent “boxes” of equal size  $\Delta_x \times \Delta_y \times \Delta_z$ ), the periodic boundary conditions apply to the  $\psi$  wave function<sup>7</sup>, which leads to wave vectors of the form  $k_{x,y,z} = l_{x,y,z} \frac{2\pi}{\Delta_{x,y,z}}$ , where  $l_{x,y,z} = \pm 1, 2, \dots$ . We can then calculate the density of states in the  $k$ -space: in the reciprocal volume  $d^3k = dk_x dk_y dk_z$  there are  $\frac{(2\pi)^3}{\Delta_x \Delta_y \Delta_z} = \frac{8\pi^3}{V}$  states (i.e. one per reciprocal volume), provided that the “distance”  $dk_{x,y,z} = \frac{2\pi}{\Delta_{x,y,z}}$ . Then the number of states  $dn$  in the volume  $V$  defines the density of states  $\rho(k)$  via  $d^3n = \rho(k)d^3k$ . And within the volume contained between the two spherical shells of radius  $k$  and  $k + dk$ ,  $dn$  is given by (normalizing per reciprocal unit volume)

$$dn = 2 \cdot \frac{V}{8\pi^3} 4\pi k^2 dk \quad (1.5)$$

where the spin degeneracy was taken into account by the factor 2. The reciprocal volume  $k^2 dk$  can then be obtained from the energy dispersion  $E(k)$  by differentiating. This last procedure applied to the Eq. 1.2 and subsequent integration of the Eq. 1.5 readily yields the DoS for different dimensionality [9]:

$$\rho_{3D} = \frac{(2m^*/\hbar^2)^{3/2}}{2\pi^2} \sqrt{E} \quad (1.6)$$

$$\rho_{2D} = \frac{m^*}{\pi \hbar^2 L_z} \sum_{n_z} \theta(E - E_{n_z}) \quad (1.7)$$

$$\rho_{1D} = \frac{(2m^*)^{1/2}}{\pi \hbar L_z L_y} \sum_{n_z, n_y} (E - E_{n_z, n_y})^{-1/2} \quad (1.8)$$

$$\rho_{0D} = \frac{2}{L_z L_y L_x} \sum_{n_z, n_y, n_x} \delta(E - E_{n_z, n_y, n_x}) \quad (1.9)$$

where  $\theta$  is the Heaviside function. Arising therefore from the discreteness of the allowed energy levels, the DoS of the confined systems, compared to the bulk, exhibits striking

<sup>6</sup>The band dispersion for all possible non-identical crystal directions can be calculated using approximate  $k$ -dependent solutions using the so-called  $k \cdot p$  method [6] or more simplified Kane model [7].

<sup>7</sup>Born-von Karman cyclic boundary conditions, that is, the wave functions should be the same within each “box”, e.g.  $\psi(x + l_x \Delta_x) = \psi(x)$ .

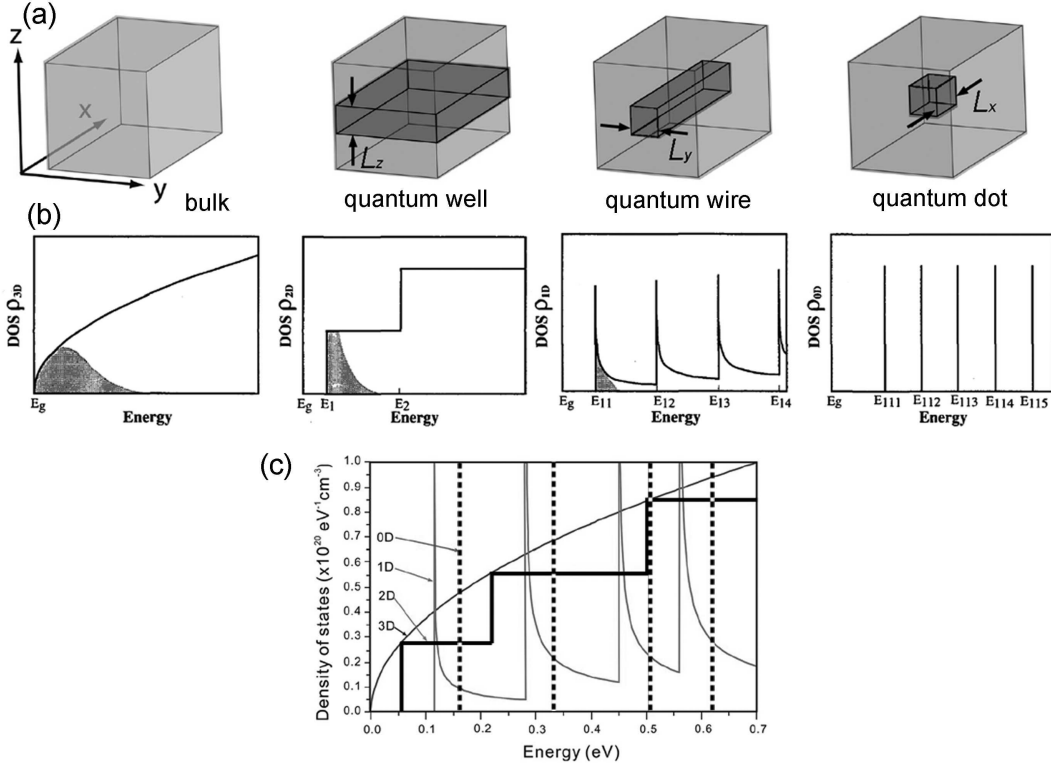


**Figure 1.2:** (a) Schematic illustration of the quantum confined nanostructures. (b) Schematic description of the free-carrier density of states versus dimensionality. The shaded areas indicate the occupied states for equivalent carrier densities [9]. (c) Calculated density of states [10] shown for direct comparison.

non-regularities [Fig. 1.2 (b)], sometimes referred to as *Van Hove singularities* [11], that are most dramatically pronounced in the case of QWRs and QDs [Fig. 1.2 (c)]. Evidently, the major effect of such a DoS modification in low-dimensional semiconductor nanostructures is to confine the carrier energy distribution (at finite temperature) to narrower spectral regions. As a result, in application to lasers, higher optical gain [12] and reduced threshold currents might be achieved [13]<sup>8</sup>.

## 1.3 Light-matter interaction

The energy exchange between light and matter falls into the class of electromagnetic interaction. Therefore, light particles (photons) affect the matter by acting on *charge* carriers (e.g. electrons)<sup>9</sup> and, vice versa, the matter couples to light via charge car-

<sup>8</sup>However, typically, nonuniformities in the nanostructures lead to partial smearing of the DoS singularities limiting, in practice, theoretically predicted characteristics (see Chapter 2).

<sup>9</sup>E.g. *refraction*, as light-matter interaction, can be described through the atomic polarization whereby the incident light induces the electrons to oscillate with respect to the heavy nuclei. The resulting oscillating dipole radiates in tune with the light, and due to the interference the speed of light of the incident wave is reduced [14]. In Maxwell's equations this is introduced by the time-dependent

riers that can release or absorb the energy excess as photons. Three major processes comprise the optical transitions: photon absorption, stimulated emission and spontaneous emission, which is schematized in Fig. 1.3 assuming a simple two-level system. Macroscopically, in the depicted conditions, each transition can take place at a certain

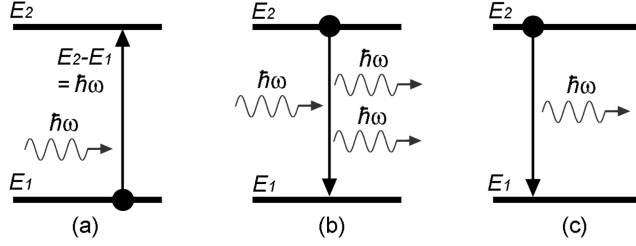


**Figure 1.3:** Schematic illustration of (a) photon absorption, (b) stimulated emission and (c) spontaneous emission.

*transition rate*, defined by a corresponding probability. Fundamentally, these probabilities are given by the *Einstein coefficients*  $B_{12}$ ,  $B_{21}$  and  $A$  [15]:

$$dN_1/dt = -B_{12}N_1 \quad (1.10)$$

$$(dN_2/dt)_{stim} = -B_{21}N_2 \quad (1.11)$$

$$(dN_2/dt)_{spont} = -AN_2 \quad (1.12)$$

where  $N_{1(2)}$  is the *population*<sup>10</sup> of the lower(upper) energy levels, respectively.

When the optical transitions occur between energy bands, as is the case in solid state matter (i.e., polychromatic transitions), in equations 1.10 one has to introduce the *spectral energy distribution*  $\rho_{em}(\nu)$  ( $\nu = \omega/2\pi$ ) that accounts for the transition spread  $\nu + \delta\nu$  (instead of a well-defined frequency as depicted in Fig. 1.3). This spread results from the “spread” of levels 1 and 2, each of which is now given by their population *densities* per unit transition frequency  $\delta N_i = \rho_i(\nu)\delta\nu$  (in  $s \cdot cm^{-3}$ ). With this, the time-dependent population of the energy levels will be defined by the sum of the contributions from all the three processes, which is united in the following *Einstein rate equation* [16]:

$$\frac{dN_1}{dt} = -\frac{dN_2}{dt} = A\delta N_2 + B_{21}\delta N_2 - B_{12}\delta N_1 \quad (1.13)$$

This equation is easily interpreted: the population in the level 1 is reduced due to the absorption ( $-B_{12}\delta N_1$ ) and augmented back because of the spontaneous ( $A \cdot \delta N_2$ ) and stimulated ( $B_{21}\delta N_2$ ) emission. For the level 2 this description is reversed (see minus sign in the equation).

From thermodynamical considerations, examining the rate equation at a steady state (thermodynamic equilibrium), and applying Planck’s law for the spectral energy

charge displacement current.

<sup>10</sup>Number of excited atoms per unit volume at a given energy level.

density  $\rho_{em}(\nu)$ , Einstein obtained the relations<sup>11</sup> between  $A_{21}$ ,  $B_{12}$ ,  $B_{21}$ , namely:

$$B_{21} = B_{12} \quad (1.14)$$

$$B_{12} = \frac{(\lambda/n)^3}{8\pi h\tau_{spont}} = \frac{c_0^3}{8\pi h\nu_0^3 n^3} A \quad (1.15)$$

$$A = \frac{1}{\tau_{spont}} \quad (1.16)$$

where  $\nu_0$  is the frequency,  $n$  is the refractive index of the medium,  $h$  – Planck’s constant and  $\tau_{spont}$  – spontaneous-emission lifetime.

Einstein’s rate-equation method (Eq. 1.13, together with a similar one written for photon population) represents the description basics of the dynamics of light-matter interaction. In particular, taking into account that  $B_{12} = B_{21}$ <sup>12</sup> we observe from Eq. 1.13 that if  $dN_1/dt$ <sup>13</sup> is negative then stimulated emission overwhelms absorption. These are the conditions of *population inversion*, where the medium acts as an amplifier of the passing photon flux, also referred to as medium with a *negative absorption*, or medium with *gain*. This is the basic ingredient for a *laser*. Note that already at this point in our discussion we can observe that the larger density of states of the medium can provide larger gain. The population inversion must be provided by a certain pumping mechanism e.g., via optical absorption (involving however in this case a higher-energy level 3). To obtain lasing, the gain is exploited by means of photon feedback, placing the active medium in an optical cavity.

So far we have discussed stimulated emission and absorption. The phenomenon of *spontaneous emission*, however, cannot be understood using classical description. Insight can be gained from quantum mechanics. The spontaneous emission is not an inherent property of matter but a result of the interaction between the emitter and vacuum. Quantum-mechanically, the vacuum is a “fabric” of space where there exist discrete fields at every point in space and time each characterized by a finite energy (zero-point energy of a harmonic oscillator). Therefore, the vacuum contains a certain density of available electromagnetic states. By interaction of matter with the vacuum, the spontaneously emitted photons may assume these available energies. In a sense, the spontaneous emission is stimulated by the vacuum fluctuations. The spontaneous-emission rate into these states (and the spontaneous-emission lifetime) thus depends on the density of the available energies of the vacuum. Generally, if a transition (from an initial ( $i$ ) to the final ( $f$ ) state) has a constant rate, its probability ( $w_{i \rightarrow f}$ ) can be

<sup>11</sup>These relations can also be obtained within the framework of electromagnetic-field quantization (the importance of which will be discussed here in the context of spontaneous emission). Einstein’s insight was that although the thermodynamics-based derivation is done at equilibrium, the validity of the relations holds also out of equilibrium. This is because the transition probabilities are not fundamentally affected by the presence of other excited atoms in the system.

<sup>12</sup>This is valid only if the levels are not degenerate, otherwise  $B_{12}/B_{21} = g_2/g_1$  where  $g_{1,2}$  is a level’s degeneracy.

<sup>13</sup>Or equivalently,  $N_2 > N_1$ .

expressed by *Fermi's golden rule*<sup>14</sup>:

$$W_{i \rightarrow f} = \frac{2\pi}{\hbar} |M_{if}|^2 \rho_f \quad (1.17)$$

where  $\rho_f$  is the density of final states, and  $|M_{if}| = \int \psi_f^* \hat{V} \psi_i d\nu = \langle f | \hat{V} | i \rangle$  is the coupling term or “matrix element”<sup>15</sup> whereby a potential  $\hat{V}$  operates on the initial state causing the transition. At this point, we shall refer the reader to chapter 2 where we will review the description of spontaneous emission in more detail. Here we would only like to emphasize the importance of the *photon density of states* apparent from the Fermi's golden rule. Indeed, it becomes clear that if it is possible to induce modifications of the photon DoS, then *spontaneous-emission control* can be achieved, which is the basis of fascinating quantum cavity electrodynamics<sup>16</sup> (cavity QED [17, 18]) research branch. Such a DoS modification can be achieved by optical cavities and, notably, due to *photonic bandgap* effects in so-called *photonic crystals* (PhCs).

## 1.4 Spontaneous-emission control and photonic crystals

Whereas the processes of absorption and stimulated emission can be eventually controlled via the matter electronic density of states, the spontaneous emission remains always more mysterious. It is therefore a question of a particular interest of how it can also be harnessed.

As we mentioned in the end of the previous section, the control on the spontaneous-emission process can be exerted via the modification of the vacuum density of states. Originally proposed by Purcell in a conference paper in 1946 [19], the spontaneous-emission rate can be *enhanced* by introducing the emitter into a cavity. The cavity modifies the available vacuum electromagnetic states in such a way that the density of states becomes increased at cavity-mode frequencies following the lorentzian distribution<sup>17</sup> of each mode (Fig. 1.4):

$$\rho_{em}(\omega) = \frac{2}{\pi \Delta\omega_{cav}} \frac{\Delta\omega_{cav}^2}{4(\omega - \omega_{cav})^2 + \Delta\omega_{cav}^2} \quad (1.18)$$

If a two-level emitter then couples to a given cavity mode, it can “see” the increased density of states, and its spontaneous-emission rate, following the Eq. 1.17, will be *enhanced*. In the ideal case<sup>18</sup> the enhancement with respect to the free-space rate is

<sup>14</sup>Derived in the framework of time-dependent *perturbation* theory.

<sup>15</sup>This naming comes from the formulation of quantum mechanics in terms of matrices rather than differential equations.

<sup>16</sup>QED is a relativistic quantum field theory of the electrodynamics, or in technical terms, it is a perturbation theory of the electromagnetic quantum vacuum.

<sup>17</sup>In view of the dissipation present, given by a finite photon lifetime.

<sup>18</sup>A localized oscillating dipole (i) homogeneously broadened such that the spectral width of the transition is less than that of the cavity mode, (ii) there is perfect spectral matching, (iii) the emitter is spatially localized at the cavity-mode field maximum, and (iv) the dipole is parallel to the electric field [20].

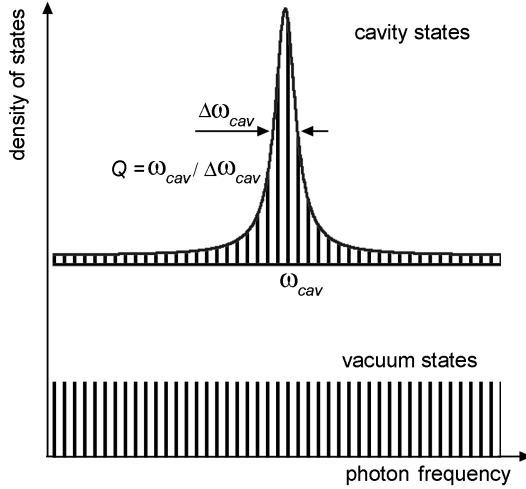


**Figure 1.4:** Illustration to the vacuum states (shown within a short spectral interval) modified by a cavity. The density of states in the cavity is given by quasi-modes (accounting for the finite photon lifetime) “dressed” by the states from the vacuum reservoir.

given by the *Purcell factor* as:

$$F_P = \frac{W_{cav}}{W_{free}} = \frac{\tau_{free}}{\tau_{cav}} = \frac{3Q(\lambda_{cav}/n)^3}{4\pi^2 V_{eff}} \quad (1.19)$$

where  $V_{eff}$  is the cavity effective mode volume<sup>19</sup>. If the emitter is spectrally located off resonance with respect to the cavity mode, its emission rate will evidently be *suppressed*, since the photonic DoS is reduced at these energies.

In order to obtain a significant enhancement effect one has to prepare a cavity with a small mode volume and a high  $Q$ -factor. At optical frequencies, *microcavities* [21] therefore have to be exploited. The major microcavity types employ three main methods of photon confinement, namely, relying on reflection (Fabri-Perot resonance), total internal reflection (whispering-gallery modes) and interference. The latter is particularly interesting bringing about the remarkable field of *photonic bandgap* effects and photonic crystals (PhC) media.

The **PhC medium** is a *periodic* arrangement of, normally, two transparent media that possess different *dielectric constants*. The periodicity is chosen with respect to a given wavelength such that the condition of constructive interference is fulfilled for the wave partially reflected at each interface [Fig. 1.5 (a)]. Hence the forward-propagating wave is attenuated and the back-reflected one – boosted. As a result, the incident wave is strongly reflected back. This reflection efficiency depends on the number of PhC periods and the refractive-index contrast, and can be very close to 100%. Since this relies on interference, the efficient reflection is valid at around a given wavelength forming eventually a *stopband* within this particular spectral region. Another way of getting insight into the photonic *band gap formation* is to consider a one-dimensional periodic medium where a *coupling* of the forward-propagating and backward-propagating waves occur. The dispersion ( $\omega - k$ ) diagram in a medium with a refractive index  $n$  is given by  $\omega(k) = \frac{c_0 k}{n}$  where  $c_0$  is the speed of light in vacuum [Fig. 1.5 (b)]. The dispersion

<sup>19</sup>Which takes into account the actual spatial mode distribution and is defined as  $\int \int \int \frac{n^2(x,y,z) |\vec{E}|^2(x,y,z)}{n^2 |E|_{max}^2} dx dy dz$

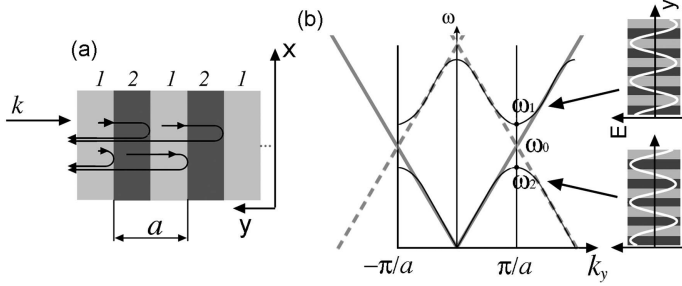


**Figure 1.5:** Illustration to 1D photonic crystal and band-gap formation. (a) Constructive interference. (b) Dispersive characteristics: uniform medium (straight-line bands for  $k_y$  and  $-k_y$  directions) and a periodic one. The gap is formed due to periodicity-driven coupling of the  $k_y$  and  $-k_y$  propagating wave.  $n_1 < n_2$ .

for  $k$  and  $-k$  directions is thus a straight line. Now, if  $n_1 \neq n_2$  the coupling between these bands occurs, namely, due to partial reflections at the interfaces, the counter-propagating waves feed each other. Reflected waves have a  $\pi$  phase shift, and the phase difference of those reflected from similar interfaces is  $\Delta\phi = ka + \pi$ . As implied by the constructive interference, the maximum effect (in one of the directions) is when  $\Delta\phi = 2\pi$ , so  $ka + \pi = m \cdot 2\pi$ ,  $m = 1, 2, 3, \dots$ , from which the maximum coupling occurs at  $k = m \cdot \pi/a$ . The coupling imposes that the frequency  $\omega_0$  has to be corrected by  $\pm\kappa$ , the coupling coefficient<sup>20</sup>, which implies the *frequency splitting* at  $\omega_0$  resulting in band *anticrossing* at this point. The optical fields of the generated modes at  $\omega_1$  and  $\omega_2$  have their electric-field maxima concentrated mostly within the low-index and high-index materials, respectively, defining therefore the lower and upper PhC continuum bands. The period  $a$  is then given by a so-called “ideal-multilayer” condition<sup>21</sup> [24] (or also called Bragg’s condition) and, at normal incidence, basically:

$$a = \frac{\lambda_0}{4n_1} + \frac{\lambda_0}{4n_2} = \frac{\lambda_0}{4} \frac{n_2 + n_1}{n_1 n_2} \quad (1.20)$$

In general, when the layers are not exactly  $\lambda/4n$  optically thick each, but have a certain thickness ratio ( $d_1/d_2$  such that also  $d_1 + d_2 = a$ , i.e. a 1D *fill factor*), we have

$$a = f\lambda_0 \quad (1.21)$$

where  $f$  depends on the index contrast and the fill factor. The described interference effects are the basic principles of operation for distributed Bragg reflectors (DBRs) and distributed-feedback lasers [22, 25]. Iridescent colors in nature [26, 27] are based on this same physics. The effect can be straightforwardly extended to 2D and 3D periodicity.

Due to the periodicity, as it is in semiconductor crystals for charge carriers, the formation of *forbidden zones* or the *band gaps* (see Fig. 1.6<sup>22</sup>) takes place in PhCs for photons. Strictly speaking, within an ideal PhC, a photon with a frequency that

<sup>20</sup>Which can be obtained from coupled-wave equations [22, 23].

<sup>21</sup>Implying simply equal optical-path lengths of layer 1 and 2.

<sup>22</sup>Calculation is done by plane-wave expansion method [28] (by Dr. K. F. Karlsson, now at Linköping University, IFM dept.) for the  $TE$  polarization; index contrast  $n_1 = 1$ ,  $n_2 = 3.19$ ;  $r/a = 0.35$ . The non-identical wave-vector directions are indicated via high-symmetry points in the reciprocal ( $k$ ) space. The easiest way to grasp the idea behind the reciprocal space  $A(\vec{k})$  is to express its relation with the real space  $a(\vec{r})$  via the Fourier transform, e.g.  $A(\vec{k}) = \int_{-\infty}^{\infty} a(\vec{r})e^{2\pi i\vec{k}\vec{r}} d\vec{r}$ .

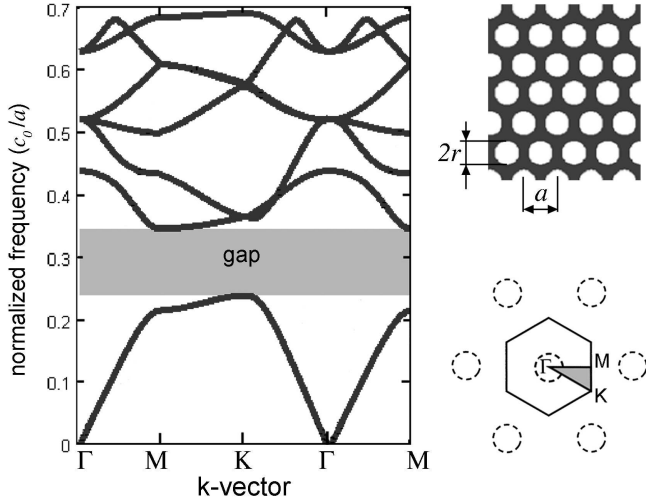


**Figure 1.6:** Band diagram of a 2D photonic crystal. There are no available frequencies for any possible in-plane propagation direction within the gap.

falls within the band gap cannot exist because the density of states vanishes there. Applied to an emitter placed into such a medium, this means that the spontaneous emission should be *inhibited* [29–31]. By creating a defect in the periodic structure one creates *localized* states within the band gap [32]. That is, if photons with frequencies that match those of the localized states are created within the defect, they will be confined to within such *defect cavity modes*. At optical frequencies, the PhC period should be well below one micron (e.g.  $\sim 200 \div 300\text{nm}$  if  $\lambda = 1\mu\text{m}$ <sup>23</sup>.) to get the effect. The periodicity imperfection can be even smaller than the period size, therefore leading to extremely small mode volumes ( $\lesssim (\lambda/n)^3$ ) compared to any other type of optical cavities<sup>24</sup>. The PhC structures can thus provide both the inhibition and enhancement of the spontaneous-emission rate with quite significant Purcell factors.

In the context of the spontaneous emission we shall also introduce the so-called ***weak and strong light-matter coupling regimes*** that can take place in microcavities [33]. This is illustrated in Fig. 1.7. A spontaneous-emission event, when an emitter is in a free space, is inherently an irreversible process. When an emitter is placed in a microcavity resonantly matching a cavity mode, in the weak-coupling regime, the spontaneous-emission decay rate can become much faster, as derived from the Fermi golden rule, resulting in the Purcell effect. The enhancement takes place due to the light-matter coupling<sup>25</sup> (via a locally increased photon DoS). We can assume a certain *coupling strength*  $g$ . If, now, the coupling strength exceeds the mean value of the dissipative<sup>26</sup> decay rates of the emitter and the cavity mode,  $g > \frac{\gamma + \kappa}{2}$ , the system will have two possible eigenstates instead of one ( $\omega_0 \rightarrow \omega_1, \omega_2$ ). Such a frequency splitting, termed

<sup>23</sup>Considering also a "membrane" approach with membrane thickness of  $\sim 200 \div 260\text{nm}$

<sup>24</sup>Although plasmonic structures might provide yet tighter light confinement. They however inherently lack the  $Q$  due to metallic features introducing strong absorption losses.

<sup>25</sup>For example, in a picture of two coupled harmonic oscillators (e.g., two pendula connected by a spring), if one of them is oscillating then the presence of the other one helps dampening these oscillations by means of the coupling, hence the decay is faster.

<sup>26</sup> $\kappa$  is a homogeneous decay rate of the matter polarization and  $\gamma$  is defined by the finite photon lifetime in the cavity as  $\gamma = 1/\tau_{\text{phot}}$ .

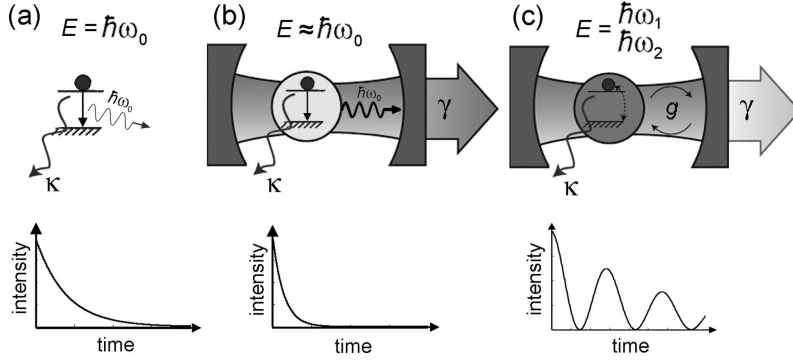


**Figure 1.7:** Light-matter coupling regimes. (a) Emitter in free space. (b,c) Emitter in a microcavity: (b) weak coupling, (c) strong coupling.

as *vacuum Rabi splitting* (VRS) [34]<sup>27</sup>, takes place because the energy is continuously exchanged between matter and light by means of emission and reabsorption. The decay thus becomes reversible, two new states emerge separated by the Rabi frequency  $\Omega_R = 2g$ , and the coupling can no longer be treated as a perturbation.

Irrespectively the coupling regime, the strength  $g$  is given by a transition dipole moment  $d_{if}$ <sup>28</sup> and the mean square electric field of the zero-point fluctuations in the cavity mode<sup>29</sup>  $E_{vac}$  as  $g = d_{if}E_{vac}/\hbar$ . As  $E_{vac}$  is given by  $E_{vac} = \sqrt{\hbar\omega/(2\epsilon_0V_{eff})}/n$  (where  $\epsilon_0$  is the vacuum permittivity, and  $n$  – cavity refractive index), the strong-coupling regime is expected in ultrasmall microcavities. Significantly larger dipole moments can be obtained in quantum-confined solid-state systems (e.g. QDs) compared to atomic ones<sup>30</sup>, hence the VRS regime is interesting for solid-state physics. The splitting can also be increased by  $\sqrt{N_{emt}}$  [36] if an ensemble of  $N_{emt}$  identical emitters is employed making the collective VRS much easier to observe [36,37]. We should however note that emitter ensembles are subject to statistical averaging effects (due to distribution in space and homogeneity), which can hamper these benefits. Secondly, quickly recalling Fig. 1.4, when the homogeneous electronic density of states  $\rho_e(E_{em})$  is broader than that of the modified vacuum states  $\rho_{cav}(E_{em})$  to which it couples, the effect should also average out. This is where the quantum-confined medium becomes increasingly interesting due to peculiar DoS, as was discussed earlier (sec. 1.2). Taking then into account photon and exciton dispersion bands, VRS leads to formation of the so-called *exciton-polaritons* (having e.g. 2D or 1D-like dispersion, and dispersionless in the case of 3D confined structures) that can be regarded as bosonic quasiparticles. This is of particular interest in research on Bose-Einstein condensation and polariton lasers based on spontaneous coherence built-up [38]. Therefore, in summary, both weak and strong light-matter coupling allow for a remarkable control of the spontaneous emission, which can be used in applications to principally novel light sources.

<sup>27</sup>The VRS effect is however not basically different from normal-mode splitting [35] observed e.g. for two classical mechanical oscillators.

<sup>28</sup>More generally, in the framework of the density-matrix formalism, this quantity is  $D_{if}$ , the matrix element of the electric dipole of, e.g. an atom between its initial and final levels.

<sup>29</sup>Arising from the root-mean-square of the vacuum fluctuations or so-called zero-point energy.

<sup>30</sup>Eventually, due to larger  $\lambda_{DB}$ .

## 1.5 Applications

The control of such a fundamental quantity as the zero-point vacuum fluctuations is quite phenomenal. On the other hand, the engineering of the quantum-confined electronic structures allows for designing interesting properties of matter. Bridging the two opens a way of tailoring the intricate mechanisms of light-matter interaction. This provides grounds for the applications in novel *light sources*, particularly interesting *in solid state* as integrable components of complex optoelectronic schemes. One such prominent application is a QD-microcavity system that, based on the Purcell effect and atom-like QD transitions, allows for generation of single indistinguishable<sup>31</sup> photons on demand [39], highly desirable in quantum information science<sup>32</sup> [41] and quantum cryptography [42]. A strong coupling regime allows for coherent energy transfer [43], which is demanded for complex interacting quantum networks represented e.g. by several cavity-QD coupled structure [44] (see also [45]). Single-mode cavities integrated with low-dimensional fully-embedded nanostructures (e.g. QDs, short QWRs or patterned QWs), allowing for the spontaneous-emission control [46], are promising as extremely low-threshold or even “thresholdless” [47, 48] microlasers. Intensively sought for, such structures may yield optoelectronics devices with ultimate energy conversion efficiency [49] and unprecedented speed capabilities [50], which can be employed e.g. in integrated optical interconnects for ultralow-power-consumption electronics. Even light-emitting diodes (LED), based on the efficient spontaneous-emission control can approach characteristics of moderate lasers [51]. The development of such structures is clearly made possible by advances in nanotechnology including accurate “top-down” patterning, crystal growth and predefined “bottom-up” approach of matter self-organization.

## 1.6 Thesis goal and outline

It is the goal of the thesis to study experimentally some of the aspects of light-matter interaction and light control developing novel light sources with advanced output performance characteristics that can be tailored using nanoscale fabrication techniques. To this end, we develop a particular system that employs photonic-crystal microcavities integrated with low-dimensional nanostructures based on *site-controlled* quantum wires. With such a system, our further goal is to examine the possibility to control spontaneous emission and to achieve stimulated emission and low-threshold lasing experimentally. Prior to this thesis work, such QWR-PhC structures have not been demonstrated. However, their applications in nanophotonics can be very promising compared to existing schemes that employ QDs and QWs. Compared to in-plane QWs, a site-controlled QWR-based source provides a smaller active-medium volume and quite good lateral carrier confinement, and, in addition, can yield in-plane polarization anisotropy. Compared to self-ordered QDs, the QWRs, apart from the site control, possess better

---

<sup>31</sup>As the QD spontaneous-emission decay is given by the dephasing due to interaction with the environment (e.g. lattice phonons), the emission rate enhancement produces always an identical decay path leading to the photon indistinguishability.

<sup>32</sup>E.g. in linear-optics quantum computing [40].

spectral purity. And compared to site-controlled QDs, the QWRs provide simpler fabrication technology and a compromise of the active-medium volume (e.g. for obtaining reasonable output powers in microlaser devices).

Our framework includes the following parts:

- ★ establish the technology of integration the QWRs and PhC cavities,
- ★ probe the properties of PhC cavities performing the mode spectroscopy exploiting the QWRs as an integrated internal light source,
- ★ observe the microcavity effect on the QWR spontaneous-emission rates,
- ★ and exercise the possibility of achieving the lasing action in the QWR-PhC integrated system.

The thesis is therefore structured in the following way. Chapter 2 provides several important theoretical and modeling aspects that are required for understanding the properties of realistic QWRs, spontaneous emission, spectral properties of the PhC cavities (by numerical modeling) and the concept of the microcavity laser. In some parts this chapter extends the background introduced in the present preface. Chapter 3 presents the undertaken technological effort that led to realization of site-controlled QWR-PhC structures. In Chapter 4 we will describe experiments on the PhC mode spectroscopy introducing the so-called  $L_N$ <sup>33</sup> PhC cavities and observing the spectral properties of the short ones that are effectively single-mode. In Chapter 5 this will be extended to treat the full  $L_N$  family with the idea of tracking the 1D photonic band formation probed by the cavities of varying length ( $N$ ) and analyzed based on 2D finite-difference computations. The mode spectroscopy is extended then yet further to deal with directly coupled cavities and observe the intriguing complex splitting phenomena in Chapter 6. Next, probing the spontaneous emission is implemented in time-resolved photoluminescence experiments, which are included into Chapter 4. Finally, QWR-PhC microcavity lasers are presented in Chapter 7, examining single- and multi-mode features in the spectral and time domains in order to establish peculiarities of the transition from the spontaneous to the stimulated emission and of the lasing action.

---

<sup>33</sup>A common family where cavities differ by length expressed in terms of a number ( $N$ ) of missing PhC holes in a row.

# Chapter 2

## Fundamental aspects of quantum wires and photonic-crystal cavities

The practical role of quantum wires in the present work is twofold: (i) as an embedded light source for probing PhC cavities and (ii) as a gain medium for lasers. Therefore, it is important to understand their emission spectra, possible gain mechanisms and physics of carrier-photon coupling. As in our special case we use particular 2D PhC optical microcavities, their mode structure needs to be well understood in a quantitative way.

Therefore, in this chapter we will describe several theoretical and modeling aspects important for the present work. These will include the optical properties of quantum wires taking into account disorder and origin of the inhomogeneous broadening, spontaneous emission into free space and emission in microcavity modes, modeling technique of the PhC cavities, microcavity laser concept and description of the stimulated emission, the lasing action, and microcavity laser threshold based on rate equations.

### 2.1 Optical properties of quantum wires

As was introduced in the previous chapter (sec. 1.2), the quantum confinement in low-dimensional nanostructures defines the formation of the density of states (DoS). The density of states determines, in turn, the spectrum of the optical transitions. However, electrons and holes within the semiconductor can interact via Coulomb attraction leading to formation of electron-hole bound states (excitons). This complicates the ideal free-carrier picture presented in the previous chapter (sec. 1.2), and it is particularly important for low-dimensional structures such as QWRs where the excitons can dominate the spectrum. Furthermore, as ideal 1D systems are extremely difficult to fabricate, inevitable disorder that leads to inhomogeneous broadening must be considered. In this section, we will briefly review these aspects.

#### 2.1.1 Effect of disorder and excitons

In practice, the deviation from the ideal quantum confinement takes place due to inevitable fabrication-induced disorder in shape, size and alloy composition, which leads

to inhomogeneous spectral broadening. The broadening acts to suppress the Van Hove singularities in the DoS. This, in the case of QWRs, is illustrated in Fig. 2.1. Indeed, as the broadening reaches the subband separation, the quantum-confinement effect disappears and the structure resembles effectively bulk material.

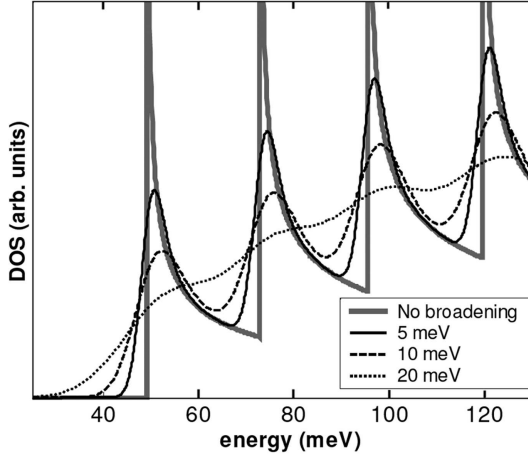


**Figure 2.1:** Calculated 1D density of states (for electrons in a *GaAs* QWR) taking into account a Gaussian broadening, as linewidth of 0, 5, 10 and 20 meV (from [52]).

### 2.1.1.1 Excitonic transitions, exciton localization and inhomogeneous broadening

Further complications –nevertheless leading to a more complete and realistic QWR-medium picture– are imposed by the Coulomb interactions. Introduced initially by Frenkel [53] for ionic crystals, the concept of exciton in semiconductors was developed by Wannier [54] and Mott (see [55] for review) to explain sharp absorption spectral peaks at energies below the conduction band edge. Such features are due to the fact that electrons from the conduction band can interact with holes in the valence band, both being mutually attracted by the Coulomb force<sup>1</sup>. The kinetic characteristics of these new quasiparticles are defined by the two-particle Hamiltonian

$$H_{eh} = \frac{\hat{p}_e^2}{2m_e^*} + \frac{\hat{p}_h^2}{2m_h^*} + V_e(\vec{r}) + V_h(\vec{r}) - \frac{e^2}{4\pi\epsilon|\vec{r}_e - \vec{r}_h|} \quad (2.1)$$

where the Coulomb interaction is recognized in the last term;  $\hat{p} = -i\hbar\nabla$  is the momentum operator and  $m_{c,h}^*$  are the electron and hole effective masses,  $\vec{r}$  – coordinate vector. Introducing the reduced mass  $m_r = \frac{m_e^*m_h^*}{m_e^*+m_h^*}$ , the total mass  $M = m_e^* + m_h^*$ , and decoupling the two-wave particle wavefunction into a relative-motion part  $\psi_{eh}^{rel}$  and the center-of-mass motion part, it is possible [56] to write the Schrödinger equation in the form established for the envelope function for the relative-motion part  $\psi_{eh}^{rel}(\vec{r})$ :

$$\left[ -\frac{\hbar^2}{2m_r^*}\nabla_r^2 + V(\vec{r}) \right] \psi_{eh}^{rel}(\vec{r}) = \left( E - \frac{\hbar^2 K^2}{2M} - E_g \right) \psi_{eh}^{rel}(\vec{r}) \quad (2.2)$$

<sup>1</sup>Note that the exciton concept for 0D QDs is slightly different, since the electrons and holes are bound in QD by the confinement potential. The Coulomb potential then modifies the existing confinement potential adding now either positive or negative contribution.

where  $K$  is the center-of-mass wavenumber (coming from the center-of-mass momentum  $\hat{P} = \hat{p}_e + \hat{p}_h$ ),  $E_g$  – bandgap energy and  $\vec{r}$  – relative coordinate. This equation is actually identical in form to that for a hydrogen atom. The allowed energies are then:

$$E_{n_i, K} = E_g + \frac{\hbar^2 K^2}{2M} - \frac{R^*}{n_i^2}, \quad n_i = 1, 2, \dots \quad (2.3)$$

We see that the exciton energy levels are discrete bands situated *below*  $E_g$ , with a difference which is given by the binding energy (Fig. 2.2). The binding energy is given

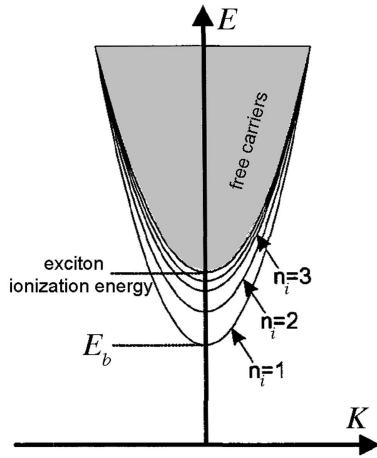


**Figure 2.2:** Schematic illustration of the dispersion of excitonic states in a 1D system.

by  $E_b - \frac{m_r}{m_0} \frac{\epsilon_0^2}{\epsilon^2} R$  ( $R = 13.6\text{eV}$  – Rydberg constant). Such so-called Wannier-Mott excitons (in contrast to Frenkel excitons) have relatively weak electron-hole attraction due to screening by the electrons in the valence band via the dielectric constant, and the typical  $E_b$  values for bulk *GaAs*  $E_b = 4.3\text{eV}$  [57]. However, in the low-dimensional nanostructures the excitons can become also tightly confined, which imposes larger electron-hole wavefunction overlap<sup>2</sup> and, consequently, a significant increase of  $E_b$  [59]. One-dimensional excitons in QWRs can possess  $E_b \gtrsim 20\text{meV}$  [58, 60], which therefore can make them stable almost all the way up to room temperature.

Therefore, in the description of the QWR density of states, one necessarily needs to take the Coulomb interactions into account. At reduced dimensions however the problem becomes quite cumbersome, since it is not possible to introduce relative coordinates in the confined directions. Full numerical computations are normally employed<sup>3</sup>, in particular, for realistic QWR geometries (e.g. V-groove QWRs) [61, 62] or more elegant fractional-dimensional excitonic theory. Interestingly, the latter one, applied to V-groove QWRs [52, 63], relies on  $\alpha$ -dimensional excitonic interband absorption where  $\alpha = 2..1$ , reproducing well the experimental data [63, 64] with less numerical effort. The effect of strong excitonic transitions in 1D media is illustrated in Fig. 2.3 where absorption spectra for V-groove wires for two first subbands are calculated. The effect consists

<sup>2</sup>Which can also be viewed as a decrease in the exciton Bohr radius depending on dimensionality [58].

<sup>3</sup>Based on Hartree-Fock approximation.

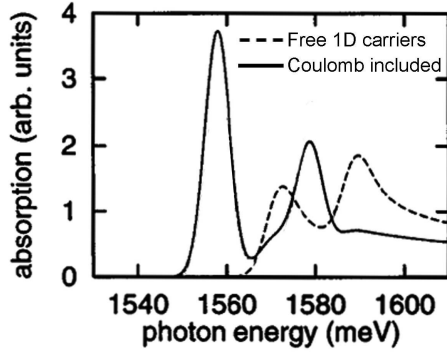


**Figure 2.3:** Comparison between absorption spectra of the V-shape QWR in the free-carrier approximation and including the electron-hole Coulomb correlations, two lowest subbands are taken into account. Gaussian energy broadening of 2 meV assumed (from [61]).

in a dramatic suppression of the 1D free-carrier Van Hove singularities. Instead, however, pronounced excitonic peaks appear. This is consistent with other calculations [65] pointing out that in 1D case (in striking contrast to 3D and 2D [56,66]) the very strong Coulomb interaction leads to Sommerfeld factors [67] lower than unity<sup>4</sup>, which imposes the reduction of the free-carrier absorption (or suppression of Van Hove singularities in DoS) above the band edge<sup>5</sup>.

Now admitting that we have a significant influence imposed by the excitons, we shall consider the inevitable QWR disorder issue referring mainly to the excitons.

### 2.1.1.2 Exciton localization

As we have already mentioned, the fabrication imperfections are inevitable. This eventually leads to broadening of the QWR DoS described by the disorder potential. We shall concentrate on the excitons, as they define the properties of the optical transitions in 1D (at least at low temperature and at low carrier density). The discussion involves to a great extent QWs. Not reducing the generality, it provides the necessary understanding of the disorder issue.

In general, two main effects are expected to contribute to the disorder potential: thickness and alloy fluctuations [69]. In a ternary alloy crystal such as  $Al_xGa_{1-x}As$ ,  $In_xGa_{1-x}As$  some atoms of  $Ga$  are substituted by  $Al$  or  $In$ . During the epitaxial growth, this does not happen in a perfectly systematic way, which creates local perturbations to the crystal periodic potential. Thickness fluctuations arise because transitions from the QWR material to the barrier material are neither abrupt due to segregation effect [70] nor homogeneous at the QWR-barrier heterointerfaces due to monolayer-size fluctuations<sup>6</sup>. These fluctuations occur on the short scale, down to atomic scale, and are referred to as micro-, or better say, nanoroughness [69,71,72] and on longer scales forming extended domains, e.g., monolayer islands [73,74] (see Fig. 2.4 (a)). It has been shown that for sufficiently narrow QWs ( $\sim 5nm$ ) or QWRs a single-monolayer fluctu-

<sup>4</sup>The Sommerfeld factor is defined as the ratio of absorption coefficient of the unbound correlated electron-hole pair to that of the free (above the band edge) electron-hole pair.

<sup>5</sup>By applying DC electric fields of a strength comparable to  $E_b$  the excitons can be ionized, then the 1D DoS is restored [68]

<sup>6</sup>Referring to a cubic crystal lattice, the monolayer (ML) thickness is half the lattice constant (e.g. for  $GaAs$   $1ML = 5.653\text{\AA}/2 \approx 2.83\text{\AA}$ )

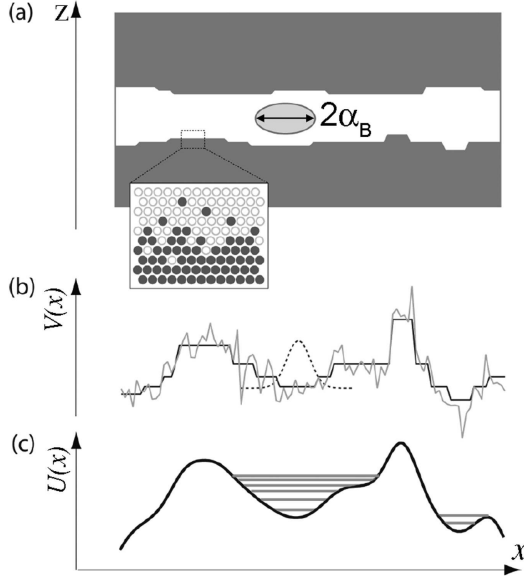


**Figure 2.4:** Illustration of the interface disorder (a) and resulting disorder potential: (b) nanoroughness superimposed on extended domains; (c) averaged potential due to a finite exciton volume [see dotted Gaussian line in (b)]. Energy states are sketched. (adapted from [75]).

ation is sufficient to produce an appreciable effect [76]. When considering the interface fluctuations, it is essential to refer to the disorder scale  $\zeta$  compared to the exciton Bohr radius  $\alpha_B$ .  $\zeta$  normally corresponds to the extension of the domains at the interface. Since, statistically, there can be a variety of the domains not necessarily correlated at different heterointerfaces, for quantitative characterization it is essential to consider correlations between them [77–79], which leads to a more general definition for  $\zeta$  as the characteristic correlation length of the structural potential. For  $\zeta \gg \alpha_B$  the disorder potential is effectively homogeneous, which results in a homogeneous width associated with the excitonic optical transition. Note that the different-size extended domains will lead to different central frequency of each transition in this case. For  $\zeta < \alpha_B$ , the disorder potential tends to average out [see Fig. 2.4 (b, c)] and in the extreme case for very small domains where [71]  $\zeta < \frac{\pi\hbar}{\sqrt{2MV_0}}$  (where  $V_0$  is the local potential), the excitons do not “see” it. Note that the latter case applies to both the alloy segregation effect and the nanoroughness. In total, the actual disorder potential will be imposed by the combination of the nanoroughness and the large-domains fluctuations, which is illustrated in Fig. 2.4 (b, c).

As becomes intuitively clear, this disorder potential induces exciton *localization*. In the theory of localization it is usually considered that the disorder potential affects only the exciton center-of-mass motion<sup>7</sup> and that the overall QW or QWR confinement (due to sufficiently small cross-section) is large enough to decouple the exciton confinement from its motion along the nominally non-confined directions. Then, the exciton localization can be deduced from the center-of-mass motion given by the Schrödinger equation [74, 80]:

$$\left[ -\frac{\hbar^2}{2M}\nabla_{\vec{R}}^2 + U(\vec{R}) \right] \psi_R^{CM}(\vec{R}) = E_{CM} \psi_R^{CM}(\vec{R}) \quad (2.4)$$

<sup>7</sup>Under the assumption that the potential fluctuations are much smaller than  $E_B$ , so that the relative-motion part is not affected. This condition is normally satisfied for realistic nanostructures [74].

where  $\vec{R}$  is the center-of-mass coordinate (which in case of the QWR is only one vector element, i.e.  $x$ , see Fig. 1.2). The effective disorder potential  $U(\vec{R})$  is obtained as a convolution of the lowest-energy bound-exciton wavefunction with the cross-section *averaged* potential fluctuations. Since the wavefunction extension is given by an  $\alpha_B$  large compared to the nanoroughness, the major effect on the exciton localization is due to large-scale thickness fluctuations.

### 2.1.1.3 Inhomogeneous broadening

From the discussion above we can deduce that as the excitons in the QWR can localize within subdomains of different lengths. This will result in a certain spread of energies of the associated transitions. Therefore, an optical transition associated with e.g. a ground state of a relatively long QWR will be inhomogeneously broadened, as being composed of several independent homogeneous sources. This is schematically illustrated in Fig. 2.5

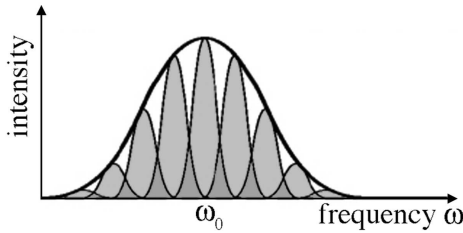


**Figure 2.5:** Illustration to the inhomogeneously broadened spectrum: an ensemble of independent homogeneous emitters effectively “merge” to an envelope broad line (normally, but not necessarily, with Gaussian distribution).

and was observed experimentally using micro-photoluminescence (micro-PL), apertures and SNOM techniques [81–85]. Similar observations were made also in the present work by micro-PL (Fig. 2.6). It is apparent that the QWR emission line at low excitation powers is essentially multi-peaked due to exciton localization<sup>8</sup>. This is a very important point that should be considered for discussion of the QWR emission and gain. In fact, the QWR, at least at low excitation power, may behave like a connected chain of QDs [87].

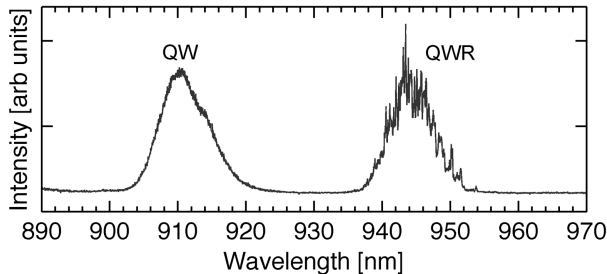


**Figure 2.6:** Measured micro-photoluminescence spectrum of single-layer *InGaAs/GaAs* QWRs (5nm nominal thickness and 15% nominal *In* content, grown by MOVPE on submicron-pitch (260nm) V-groove pattern). Excitation: CW, 514nm, power 0.05μW ( $\simeq 6W/cm^2$ ). T=10K.

<sup>8</sup>We however should note that within the disorder “landscape”, if two particles are localized in neighboring potential pits at the same energy and there is a spatial wavefunction overlap, level repulsion [85,86] can occur leading to energy-level splitting. This correlation is however not easy to infer from regular luminescence spectra, and statistical analysis is needed [85].

### 2.1.1.4 Exciton-exciton interactions

Coulomb correlations become important at high carrier densities, the regime that is potentially interesting for laser applications. In general, in the presence of multiparticle interaction, screening effects may become significant. Above a certain density threshold, e.g.  $N^{-1/3} \simeq \alpha_B$  [88] this can lead to exciton ionization with the creation of electron-hole plasma (e.g. assuming exciton  $\alpha_B \sim 5nm$  [58], the carrier density should be  $\sim 10^{19}cm^{-3}$ , which in 1D would roughly correspond to  $\sim 2 \times 10^6 cm^{-1}$ ). At such high carrier densities bandgap renormalization may take place due to the presence of free carriers. This should result in a spectral red-shift, which has been noticed in 1D systems [89,90]. However the shift is much less pronounced if electron-hole plasma (contrary to just electron plasma) is created [89], which points to persistence of Coulomb correlations in the plasma. It was also shown for 2D [91,92], 0D and localized excitons in 1D systems [93] that exchange interactions between excitons lead to exciton-energy renormalization and, as a result, to a blue-shift. In addition, many-exciton effects (e.g. biexcitons) add up to blue-shift at low temperatures in QDs [94] and disordered QWRs [93]. The exciton-related blueshift has to be however always corrected [92] due to screening, which is why the blue-shift is not overall large. From this discussion it is naturally expected that inhomogeneously broadened ensembles will exhibit an overall blue-shift. Such observations will be important for our discussion involving possible gain mechanisms in QWR-PhC lasers.

## 2.1.2 Absorption and gain

As we have preliminarily seen (sec. 1.3), the stimulated emission and absorption are inherently related, therefore the gain calculations imply, first of all, the evaluation of absorption properties. In fact, in first approximation, gain can be considered as negative absorption. Transition rate probability associated with the absorption can be retrieved from the Fermi golden rule (Eq. 1.17) assuming now transitions from the valence band ( $i$ ) to the conduction band ( $f$ ). Clearly, the density of states is playing key role.

For a given *discrete* two-level system interacting with a photon (of energy  $\hbar\omega$ ) the transition probability simply reads:

$$W_{i \rightarrow f} = \frac{2\pi}{\hbar} |\langle f | H' | i \rangle|^2 \delta(\hbar\omega = E_f - E_i) \quad (2.5)$$

where the energy is conserved via the  $\delta$ -function. The interaction Hamiltonian  $H'$  can be obtained in the semiclassical way. The Hamiltonian of a charged particle (say, electron) in the presence of the electromagnetic field represented by a vector potential  $\vec{A}(\vec{r}, t)$  reads [16]:

$$H = \frac{[\vec{p} - e\vec{A}(\vec{r}, t)]^2}{2m} + V(\vec{r}) + eU(\vec{r}, t) \quad (2.6)$$

where  $V(\vec{r})$  is the potential of a particle (e.g., resulting from the semiconductor) and  $U(\vec{r})$  is the scalar potential due to the electromagnetic wave. By the correspondence principle this Hamiltonian is also that of a quantum system (we omit thus the operator

hat notation). Via the approximation  $(\vec{p} - e\vec{A})^2 \simeq p^2 - 2e\vec{A} \cdot \vec{p}$  (dipole approximation) one can write  $H = H_0 + H'$ , where  $H'$  is considered as a perturbation. The vector potential can be treated within the Coulomb gauge or, alternatively, using Göppert-Mayer gauge, which leads to so-called  $\vec{A} \cdot \vec{p}$  or  $\vec{D} \cdot \vec{E}$  interaction Hamiltonians<sup>9</sup>:

$$H'_{Ap} = -\frac{e}{m}\vec{A}(\vec{r}_0, t)\vec{p} \quad (2.7)$$

$$H'_{DE} = -e\vec{r}\vec{E}(\vec{r}_0, t) \quad (2.8)$$

where  $\vec{r}_0$  is the position of the quantum system (can be taken at origin). In general, the  $H'_{Ap}$  is best applied for transitions involving delocalized states (e.g. absorption between bands) and the  $H'_{DE}$  is best suited for describing transitions between localized states (e.g. defect states, quantum dots). We note that  $-e\vec{r} = \vec{D}$  is actually the dipole operator, which gives us a connection with the coupling strength (see coupling regimes at the end of the sec. 1.4).

The absorption coefficient  $\alpha(\hbar\omega)$ , defined as the photon flux absorbed per unit time and unit volume divided by the incoming flux (i.e. Beer-Lambert's law), is obtained then by summing up over all possible transitions (all conduction/valence bands  $c, v$ , all wave vectors  $k_c, k_v$  and both electron spin states) and taking into account the occupancy of the states  $f_{c,v}$ :

$$\begin{aligned} \alpha(\hbar\omega) &\sim \sum_{c,v} \sum_{\vec{k}_c, \vec{k}_v} |\langle \Upsilon_{c, \vec{k}_c} | H' | \Upsilon_{v, \vec{k}_v} \rangle|^2 \delta(\hbar\omega = E_c(\vec{k}_c) - E_v(\vec{k}_v)) \cdot [f_v\{E_v(\vec{k}_v)\} - f_c\{E_c(\vec{k}_c)\}] \\ &\sim |M|^2 \cdot \rho_{joint}(\hbar\omega) \cdot [f_v - f_c] \end{aligned} \quad (2.9)$$

where the joint density of states  $\rho_{joint}$  comprises the available states in both the conduction and the valence bands and ensures the energy conservation. It basically has the same form as Eq. 1.6-1.9, however, the effective mass is changed to the reduced mass  $m_r$  (introduced in Sec. 2.1.1.1). Thus, the absorption depends strongly on the system's dimensionality. The dipole matrix element  $M$  determines the transitions selection rules. In particular, (i) the absorption strength depends on the overlap between envelope electron-hole wavefunctions, (ii)  $M$  includes  $\delta(\vec{q} = \vec{k}_c - \vec{k}_v)$ , and since the photon momentum  $\vec{q}$  is negligible compared to electron/hole wavevectors<sup>10</sup>, which implies the conservation of momentum  $\vec{k}_c \approx \vec{k}_v$  (vertical transitions), and (iii) as  $-\frac{e}{m}\vec{A} \cdot \vec{p} \sim \vec{e} \cdot \vec{p}$  where  $\vec{e}$  is the light polarization unit vector, the relative orientation between  $\vec{k}_{c,v}$  and  $\vec{e}$  determines the polarization dependence of transitions (which is different for light and heavy holes). The latter is important for QWRs, since due to the lateral confinement (that induces heavy-light hole band mixing at  $\vec{k}_{c,v} = 0$ ) appreciable polarization anisotropy may arise in the  $x - y$  plane [95, 96].

Taking into account the excitonic effects, an example of a QWR absorption coefficient (disregarding the carrier-density effects) for a realistic V-groove (*GaAs*) QWR is

<sup>9</sup>And  $U(\vec{r})$  turns to be zero.

<sup>10</sup> $|\vec{q}| = 2\pi/\lambda$ ,  $|\vec{k}_{c,v}| = 2\pi/a$  where  $a$  is the lattice constant and  $a \ll \lambda$ .

plotted in Fig. 2.7 (calculated by the fractional-dimensional model [63]<sup>11</sup>).

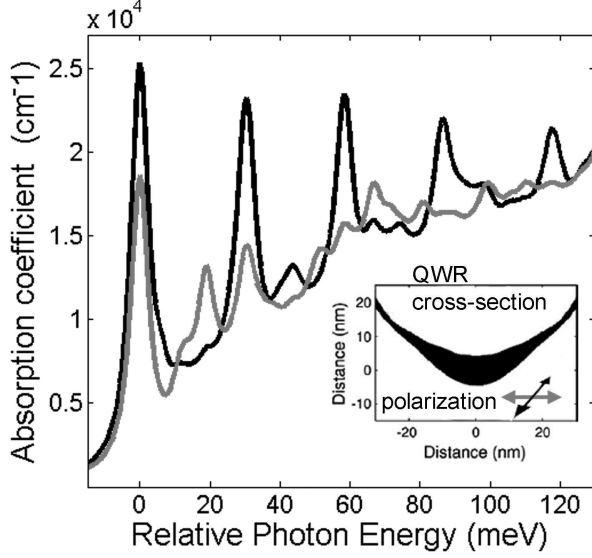


**Figure 2.7:** Calculated absorption spectrum of a V-groove *GaAs/AlGaAs* QWR [63]. Lorentzian broadening of  $6\text{meV}$  is assumed.

In order to calculate the **gain coefficient**, the valence-band and the conduction-band occupancies ( $f_v$ ,  $f_c$ ) have to be considered. Semiconductors are described by the Fermi statistics. At thermodynamic equilibrium the Fermi level is exactly at the middle of the bandgap. When absorption takes place, the occupancies  $f_v$ ,  $f_c$  change, meaning that the Fermi level is shifted, and the system is out of equilibrium. However, within each band the equilibrium is typically established due to the fast interband carrier relaxation. Therefore, one can consider the band occupancies separately, which leads to the notion of the *quasi-Fermi levels*

$$f_{c,v} = \left\{ 1 + \exp \left[ \frac{(E - E_{f_{c,v}})}{k_B T} \right] \right\}^{-1} \quad (2.10)$$

where  $k_B$  is the Boltzmann's constant and  $E_{f_{c,v}}$  are the so-called quasi-Fermi energies. It is clear that, as more and more electrons are promoted to the conduction band,  $E_{f_c}$  shifts more upwards and  $E_{f_v}$  shifts downwards (as the valence band is emptied). Hence, once the difference  $E_{f_c} - E_{f_v}$  exceeds the band-gap energy  $E_g$ , at  $\hbar\omega$  no further photon absorption can happen (*transparency condition*). Then, a bit of further pumping is required in order to establish for a given energy  $\hbar\omega_{21}$

$$E_g < \hbar\omega_{21} < E_{f_c} - E_{f_v}, \quad (2.11)$$

which is the condition<sup>12</sup> for observing gain and when the stimulated-emission rate may exceed the absorption rate. Note that in other words the absorption coefficient becomes *negative*.

<sup>11</sup>Calculation performed by Dr. K. F. Karlsson, now at Linköping University, IFM dept.

<sup>12</sup>Bernard-Duraffourg condition [97].

Calculating the *gain coefficient* in a QWR system is a challenging task, because the free-carrier picture is modified to a large extent developing into a complex interplay between excitonic, many-body effects, free-carrier screening. Quantitative predictions are

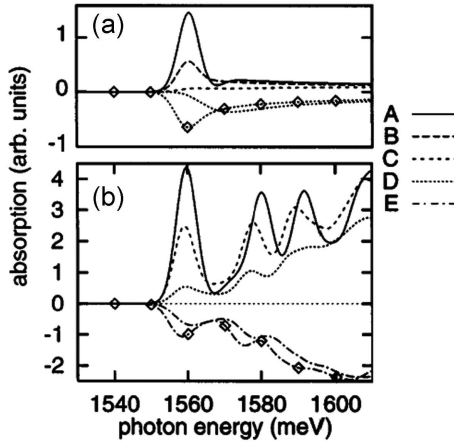


**Figure 2.8:** Nonlinear absorption spectra of a V-shaped QWR at room temperature for carrier densities:  $A = 10^4 \text{ cm}^{-2}$ ,  $B = 5 \times 10^5 \text{ cm}^{-2}$ ,  $C = 10^6 \text{ cm}^{-2}$ ,  $D = 4 \times 10^6 \text{ cm}^{-2}$ ,  $E = 2 \times 10^7 \text{ cm}^{-2}$ . (a) Single-subband case. (b) Twelve-subband model. For comparison, the free-carrier result is shown [in case of D in (a) and E in (b)] as marked with diamonds (note that, for comparison, the free-carrier absorption edge is aligned to that of the exciton). (from [61]).

thus extremely challenging. Within the fractional-dimensional absorption theory that allows nicely for treating an exciton with an arbitrary dimensionality, the gain problem has not been considered. In another approach based on semiconductor Bloch equations (rate equations) the occupancy distribution functions were considered as kinetic variables [61]. The Coulomb potential is included in renormalized fields and subband energies. The result is shown in Fig. 2.8, illustrating well the negative absorption attained at relatively high densities. Since the free-carrier picture stays still modified, the gain can be ascribed to correlated electron-hole plasma. At low temperature however bound

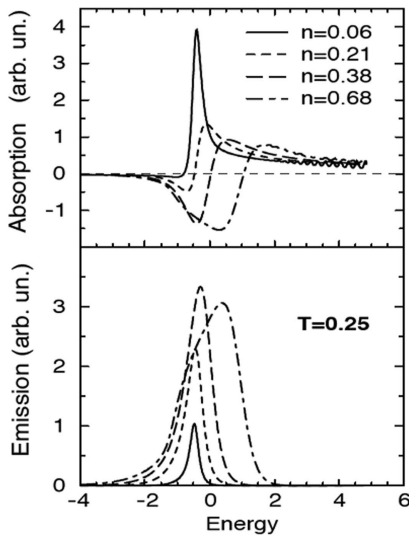


**Figure 2.9:** QWR absorption and emission spectra at various carrier densities. (from [98]).

electron-hole pairs are expected to exist even at high carrier densities due to less efficient screening<sup>13</sup>, which therefore needs to be taken into account. Self-consistent treatment

<sup>13</sup>By assuming “hard” volumes of excitons that free carriers cannot “enter” in the absence of phonons.

of electron-hole correlations in the so-called ladder approximation was proposed in [98]. Due to complexity though, the Coulomb potential was replaced by a simple contact potential. The result is displayed in the Fig. 2.9 showing both the absorption and emission spectra. Sizable gain appears now at relatively low densities ( $\sim 5 \times 10^5 \text{cm}^{-3}$ ,  $n = 0.21$  in Fig. 2.9) suggesting that the gain is provided by excitons rather than free carriers. However it was also suggested that in the gain, correlated electron-hole plasma plays an important role. At high densities the gain peak blue-shifts indicating a change in the carrier nature. Broadening occurs in the emission and eventually blue-shift takes place, which suggests that electron-hole plasma is created at these conditions.

### 2.1.3 Spontaneous emission

The spontaneous emission process implies downward transitions in the absence of the electromagnetic field. In order to take place, it nevertheless necessitates the interaction with available electromagnetic states. Therefore it can only be understood quantum-mechanically as emission due to interaction with electromagnetic vacuum energy states.

#### 2.1.3.1 Emission in free space

If the interaction Hamiltonian doesn't depend on time, the process can be described by the Fermi golden rule (Eq. 1.17). In the dipole approximation (using Eq. 2.8) the frequency-dependent spontaneous-emission rate is therefore written as [33, 99]

$$W_{sp} = \frac{1}{\tau_{sp}} = \frac{2\pi}{\hbar^2} |\langle f | \hat{d} \cdot \hat{E}_{\vec{k},\sigma}^\dagger | i \rangle|^2 \rho_{em}(\omega) \quad (2.12)$$

where  $\hat{E}_{\vec{k},\sigma}^\dagger$  is the electric-field operator of a given mode with  $\vec{k}$ -vector and of  $\sigma = 1, 2$  polarization index.  $\rho_{em}$  is the density of the electromagnetic-field states per unit frequency in a quantization box of volume  $V$  (i.e. a virtual box cavity):

$$\rho_{em} = \omega^2 V / c_0^3 \pi^2 \quad (2.13)$$

Since for a vacuum state the electric-field expectation value  $\langle 0 | \hat{E} | 0 \rangle = 0$  but at the same time the *intensity fluctuations*  $\langle 0 | \hat{E}^2 | 0 \rangle = \hbar\omega/2\epsilon_0 V$ , the electric field effectively arises from the mean square root of the zero-point fluctuations of the vacuum electromagnetic field. The matrix element is given hence by the vacuum energy as

$$|\langle \hat{d} \cdot \hat{E}_{\vec{k},\sigma}^\dagger | \rangle|^2 = d(\omega)^2 \frac{\hbar\omega}{2\epsilon_0 V} \quad (2.14)$$

if the electric field and the dipole moment are parallel<sup>14</sup>.  $d(\omega)$  represents the coupling (the matrix element) between the dipole emitter and the electric field, and generally it is written  $d = \sqrt{\frac{1}{3} |\langle \Psi_l | \vec{d} \cdot \vec{e} | \Psi_u \rangle|}$ , where  $\Psi_{u,l}$  is the wavefunction of the upper/lower

---

<sup>14</sup>Note the dot product

state and the 1/3 factor is the statistical averaging factor for the electric dipole orientation. From Eq. 2.12 we see that the spontaneous-emission rate into the free space is given by<sup>15</sup>

$$W_{sp}^{free} = \frac{1}{\tau_{sp}^{free}} = \frac{2\pi}{\hbar^2} \frac{d(\omega)^2 \hbar \omega \omega^2 V}{2\epsilon_0 V c_0^3 \pi^2} = \frac{|d|^2 \omega^3}{3\pi \hbar \epsilon_0 c^3}. \quad (2.15)$$

### 2.1.3.2 Emission in microcavities

In a general situation where the dipole is homogeneously broadened and the cavity has a certain mode density, the emission is described by the Fermi golden rule (Eq. 2.12) that involves an integral:

$$W_{emi} = \frac{1}{\tau_{sp}} = \frac{2\pi}{\hbar^2} \int_0^\infty |\langle f | \hat{d} \cdot \hat{E}_{\vec{k},\sigma}^\dagger | i \rangle|^2 \rho_{em}(\omega) \mathcal{L}(\omega) d\omega \quad (2.16)$$

The quantized electric-field operator generally has the form  $\hat{E} = E_0(\hat{a} + \hat{a}^\dagger)$  where  $E_0$  is the vacuum energy and  $\hat{a}$ ,  $\hat{a}^\dagger$  are the annihilation and creation operators. In particular, the eigenstates of  $\hat{a}^\dagger$  satisfy  $\hat{a}^\dagger | p \rangle = \sqrt{p+1} | p+1 \rangle$  with  $p$  being the photon number in the mode; i.e.,  $\hat{a}^\dagger$  adds one photon to the mode. Considering for the moment a discrete electric-dipole transition under interaction with quasi-single-mode light, one finds that the matrix element in Eq. 2.12 yields

$$|\langle f | \hat{d} \cdot \hat{E}_{\vec{k},\sigma}^\dagger | i \rangle|^2 = \frac{d^2 \hbar \omega}{2\epsilon_0 V} (p+1) \quad (2.17)$$

This is a very instructive outcome. The emission rate in the presence of a number of photons  $p$  inside the cavity involves two terms. The first one dependent on  $p$  and the second one independent of  $p$ . The term dependent on  $p$  can be associated with the stimulated emission<sup>16</sup>.

Let us now consider the spontaneous emission only, i.e., the case  $p = 0$ . In the single-mode case (in the quasi-mode sense) the cavity density of states  $\rho_{em}^{cav}(\omega)$  is given by a Lorentzian (Eq. 1.18). This has to be compared to the free-space DoS given by Eq. 2.13 (where in the nominator  $n_{opt}^3$  should appear if we consider the refractive index of the cavity medium). Assuming that the emitter broadening  $\mathcal{L}(\omega)$  is much smaller than that of the cavity mode, the comparison<sup>17</sup> [20] of the spontaneous-emission rates gives

$$\frac{W_{sp}^{cav}}{W_{sp}^{free}} = \frac{3Q(\lambda_{cav}/n_{opt})^3}{4\pi^2 V_{eff}} \frac{\Delta\omega_{cav}^2}{4(\omega - \omega_{cav})^2 + \Delta\omega_{cav}^2} \frac{|\vec{E}(\vec{r})|^2}{|\vec{E}_{max}|^2} \frac{\vec{d} \cdot \vec{E}(\vec{r})}{|\vec{d}| \cdot |\vec{E}(\vec{r})|} \quad (2.18)$$

<sup>15</sup>Here only one polarization is considered. Taking into account both polarization directions gives an additional factor of 2 [46].

<sup>16</sup>Actually, as pointed out by Einstein in 1917, due to the coupling of the  $A$  and  $B$  coefficients the emission rate into a single mode with  $p$  photons is proportional to  $A(p+1)$  where the two resulting terms represent the stimulated and the spontaneous emission, respectively.

<sup>17</sup>By "free space" we should understand a given emitter (e.g., embedded within the semiconductor) not in an optical cavity. Therefore, effects like localization volume (that will be introduced in the Chapter 4) cancel out in this ratio.

The very last term (i) describes the orientation matching of  $\vec{d}$  and the electric field. And the term (ii) right before the last one is the value of the electric field at a given position within the cavity with respect to the maximum amplitude. We see that for an ideally matched emitter (e.g., point-like), provided its frequency  $\omega = \omega_{cav}$ , we readily recover the Purcell factor given in Eq. 1.19. This means that the Purcell factor is a figure of merit characterizing the cavity capabilities only.

It is quite important to conclude that if we deal with an ensemble of emitters, then instead of the term (ii) we have to place an integral. This integral should also take into account the term (i) at each point. Thus, in a randomly distributed ensemble of emitters with respect to modal nodes and anti-nodes having a random dipole orientation we can easily get factors  $\sim 0.1^{18}$  of the reduction of  $F_P$ .

If we now take into account a homogeneous broadening of each emitter, larger than the cavity-mode linewidth, yet another multiplying factor should appear in the Eq. 2.18, namely [100]

$$\frac{W_{sp}^{cav}}{W_{sp}^{free}} = \frac{3Q(\lambda_{cav}/n_{opt})^3}{4\pi^2 V_{eff}} \frac{\Delta\omega_{cav}^2}{4(\omega - \omega_{cav})^2 + \Delta\omega_{cav}^2} \frac{|\vec{E}(\vec{r})|^2}{|\vec{E}_{max}|^2} \frac{\vec{d} \cdot \vec{E}(\vec{r})}{|\vec{d}| \cdot |\vec{E}(\vec{r})|} \cdot \frac{\Delta\omega_{cav}}{\Delta\omega_{emitter}} \quad (2.19)$$

## 2.2 Microcavity laser concept

In this section we introduce a general *microcavity* -laser concept, which is based on the spontaneous-emission coupling effect. Proceeding immediately to the semiconductor laser rate equations, we review the issue of the lasing *threshold* and its definition as a *phase transition* from the spontaneous to the stimulated emission quantified by the mode *mean photon number*. We will further briefly discuss limiting factors such as non-radiative recombination and the active-medium volume, which justifies the use of nanostructures such as QDs or QWRs.

### 2.2.1 Spontaneous-emission coupling factor

In microcavity lasers, superior laser output characteristics (in terms of threshold and slope efficiency) can be obtained if the spontaneous emission is efficiently controlled when the number of the cavity modes is greatly reduced. Hence, single-mode cavities are of our interest here. Generally, given by the solution of the Helmholtz equation<sup>19</sup>, the number of possible modes  $N$  depends on the cavity volume  $V$  as  $N_\lambda = \frac{8\pi\nu^3}{3c^3}V = \frac{8\pi}{3\lambda^3}V$ . Therefore if a cavity volume becomes comparable or smaller than the wavelength, at optical frequencies where  $\lambda \sim 1\mu m$  *microcavities* can provide the single-mode regime. Furthermore, since the semiconductor active medium has a finite *gain* bandwidth, the

<sup>18</sup>E.g. consider a single QWR as a chain of QDs fixed at the center of a linear ( $L_N$ , see Chapter 5) PhC cavity. These emitters, provided they emit within the cavity-mode linewidth, "probe" the cavity mode distribution, for which the integral of matching to the field maximum is  $\lesssim 0.25$ . Each emitter in the QWR may have either of the two polarizations with more or less equal probability (see QWR absorption). Thus we have  $0.25 \times 0.5 = 0.125$ .

<sup>19</sup>Here counting the modes for a cavity with perfectly conducting walls [15].

effective number of modes that the medium "sees" can be reduced down to unity, if the cavity size is  $\simeq \lambda^3$ . For example, given  $\lambda = 900\text{nm}$  and  $V = \lambda^3$ , we have per spectral range, say, of 90 nm  $\Delta N_\lambda = \frac{8\pi V \Delta\lambda}{\lambda^4} \simeq 2.5$  modes. That is, with a gain bandwidth of 30 nm, effectively, the cavity is single-mode. If the cavity free spectral range is much larger than the active-medium gain bandwidth, the recombining carriers (or excitons) in the active material may "see" the increased density of the available electromagnetic states of the vacuum given by a single cavity mode, and therefore their spontaneous-emission decay rate ( $1/\tau_{sp}$ ) will be enhanced. At the same time, off-resonance, the decay rate will be inhibited. In that case this is a true cavity quantum-electrodynamics (QED) effect, which is one of the fundamental ideas behind the *microcavity laser* concept [33,101,102].

The spontaneous-emission coupling effect is quantified by a so-called  $\beta$ -factor, which is defined as  $\beta \equiv A_0 / \sum A_i$  [102] by the Einstein  $A$  coefficients of the mode of interest ( $A_0$ ) and of *all* other possible modes. Note, that these other modes include whatever leaky modes as well. This means that  $\beta$  can be increased also just by removing unwanted cavity modes (i.e., without the QED effect). Following the Einstein's concept of the rates in light-matter interaction, the laser output (and performance) is, normally, described by the coupled rate equations [15,102,103] written for the time-dependent free-carrier density  $N(t)$  and the photon population  $p(t)$ , where the  $\beta$ -factor has to be included. For an optically-pumped single-mode laser the equation system can be written in the following way [102]:

$$\frac{dN}{dt} = \frac{L_{in}}{\hbar\omega_{in}V_a} - \frac{N}{\tau_{sp}} - \frac{N}{\tau_{nr}} - \frac{gp}{V_a} \quad (2.20)$$

$$\frac{dp}{dt} = -\frac{\omega_{cav}}{Q}p + gp + \frac{\beta NV_a}{\tau_{sp}} \quad (2.21)$$

In the first equation the free carrier density in the active medium is increased by the pumping rate  $L_{in}/\hbar\omega_{in}$ ; and the carriers are dissipated due to the spontaneous emission into the mode  $-N/\tau_{sp}$ , due to the non-radiative recombination  $-N/\tau_{nr}$ , and due to the stimulated emission because of the gain  $g$  in the active region. Importantly, the  $\tau_{sp}$  here is the spontaneous-emission lifetime of the active material *inside* the microcavity, that is, it can be significantly shorter than that in the "free" space. In the second equation the photon density in the mode grows due to the spontaneous ( $\beta NV_a/\tau_{sp}$ ) and the stimulated ( $gp$ ) emission, and the photons dissipate due to the finite cavity  $Q$ -factor ( $-\omega_{cav}p/Q$ ). Disregarding non-linearities (that lead to important saturation effects at high excitation powers [104]), the semiconductor *optical* gain can be assumed as  $g = g'(N - N_{tr})$ , where the  $N_{tr}$  is the transparency carrier density.

## 2.2.2 Mean photon number and threshold definition

In order to define the laser *threshold* in the most fundamental way, one can consider the balance between the spontaneous and the stimulated emission within the cavity mode (or several modes) versus the pump power. Then, the *equality* of the spontaneous-emission rate and the stimulated-emission rate is a good laser-threshold definition [102], given by the rationale that at this particular pump rate, exactly half of the photons is

added to the mode non-coherently and the other half is added coherently. *Lasing* then occurs, and when the stimulated emission prevails at higher powers a stable regime of the *laser oscillations* is established with a (phase-stable) coherent output and high quantum efficiency.

The rates of the spontaneous and the stimulated emission are fundamentally given by Einstein's  $A$ ,  $B$  coefficients, respectively, and are connected as  $A/B = \rho_\nu$  via the energy density  $\rho_\nu$ . The energy density is given by [15]:

$$\rho_\nu = \rho_{modes} \langle E \rangle \quad (2.22)$$

where  $\rho_{modes}$  is the number of modes per unit volume per unit spectral interval  $\rho_{modes}(\nu) = (1/V)(dN_\lambda/d\nu) = 8\pi\nu^2/c^3$ ; and  $\langle E \rangle (\sim h\nu)$  is the average energy per mode. That is, the energy  $E$  is that in each mode, and the net energy in the system is not necessarily evenly distributed over the available modes. Then, according to Eq. 1.15, the equality  $A = B$  can be fulfilled when  $\rho_{modes} \langle E \rangle = 1$ . That is, the average energy density contained in all the modes equals unity. Since in laser physics it is much more common to deal with the number of photons  $p$  contained in a given cavity mode, given then by  $\langle p \rangle = \langle E \rangle / h\nu$ , the former statement translates into that in order to get equal rates  $A = B$ , the *mean photon number* should be unity<sup>20</sup>. Therefore the lasing threshold is defined by

$$\langle p \rangle_{th} \equiv 1 \quad (2.23)$$

which, of course, simplifies to  $p_{th} \equiv 1$  in the single-mode case.

At steady state ( $d/dt = 0$ ), from the rate equations 2.20, 2.21 it follows that [102] the single-mode output-power laser characteristics is given by the relation:

$$L_{in} = \frac{\hbar\omega_{in}\gamma}{\beta} \left[ \frac{p}{1+p} (1 + \xi) \left( 1 + \beta p + \frac{\tau_{sp}}{\tau_{nr}} \right) - \xi\beta p \right] \quad (2.24)$$

and at threshold ( $p = 1$ ):

$$L_{th} = \frac{\hbar\omega_{in}\gamma}{2\beta} \left[ (1 + \xi) \frac{\tau_{sp}}{\tau_{nr}} + (1 + \beta) + \xi(1 - \beta) \right] \quad (2.25)$$

In these equations  $\gamma = \omega_{cav}/Q = \tau_{ph}^{-1}$  is the photon cavity loss, and  $\xi = \frac{N_{tr}\beta V_a}{\gamma\tau_{sp}}$ . The parameter  $\xi$  is an important parameter interpreted as the photon number in the lasing mode at  $N = N_{tr}$  (medium *transparency*), and it indicates whether the threshold is going to be defined by the material properties (when  $\xi > 1$ ) or the cavity loss (if  $\xi < 1$ ). Importantly, it contains the *active-medium volume*, which has to be “small” in order to benefit from the high spontaneous-emission coupling factor.

Taking for example parameters representing a PhC-QWR laser design, the photon number  $p$  versus the optical pump power (LL curve) is plotted in the Fig. 2.10 for different  $\beta$ -factors. Three main examples are shown:  $\beta = 1$ ,  $\beta = 0.1$ , being the range of values of what one could expect from a microcavity laser, and  $\beta = 0.0001$ , which

<sup>20</sup>We have  $A = B \frac{8\pi\nu^2}{c^3} \langle E \rangle = B\rho_{modes}p h\nu$ . Therefore, per mode, per unit photon energy, the rates  $A = B$  if  $p$  equals unity.

holds for a regular laser. The parameters are  $N_{tr} \simeq 10^{18} \text{cm}^{-3}$ ,  $\tau_{sp} = 300 \text{ps}$  (see section 4.4.2),  $\tau_{nr} \sim 1000\tau_{sp}$  (i.e., negligible),  $\lambda_{in} = 700 \text{nm}$ ,  $\lambda_{cav} = 900 \text{nm}$ ,  $Q = 5000$ ,  $V_a = 5 \times 5 \times 1000 (\text{nm}^3)$ ,<sup>21</sup> and the input power  $L_{in}$  here is corrected for the overall pump-power conversion into carriers supplied to the active region<sup>22</sup>. Clearly, the threshold is reduced by three orders of magnitude down to the  $\sim \mu\text{W}$  regime in the case of high  $\beta$ -factor. Secondly, as  $\beta$  increases, the LL curve becomes smoother in the threshold region, exhibiting a soft turn-on rather than a pronounced kink (Fig. 2.10, inset). Note that for  $\beta = 1$  there is no kink at all. That means that the quantum efficiency of the device is unity, given by  $L_{in} = \hbar\omega_P\gamma p$  both below and above the threshold, which can be viewed as an ultimate conversion efficiency [49].

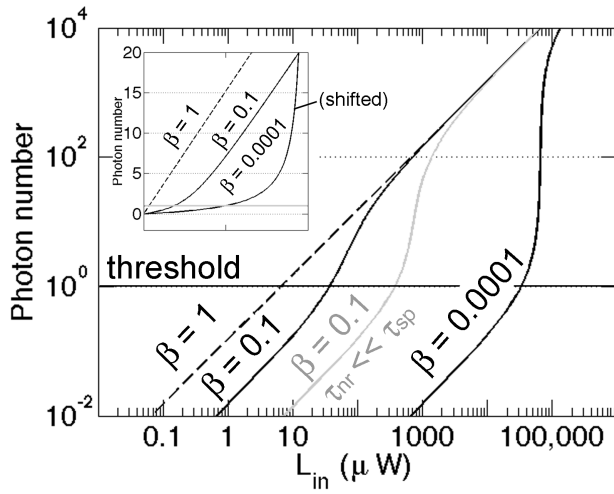


**Figure 2.10:** Photon number in the cavity mode vs optical pump power, according to Eq. 2.24 neglecting the non-radiative recombination (i.e.,  $\tau_{nr} \gg \tau_{sp}$ , although one illustrative example is given for  $\tau_{nr} \ll \tau_{sp}$ ). Parameters: see text. The inset shows curves in a linear scale to illustrate qualitatively the soft turn-on of a high- $\beta$  microcavity laser compared to a regular low- $\beta$  one (note, that the  $\beta = 0.0001$  curve is “shifted”, i.e. plotted in  $\sim \text{mW}$  scale whereas the others - in  $\sim \mu\text{W}$ ).

So far we neglected the *non-radiative recombination*. Assuming now a value of  $\tau_{nr} \simeq \frac{1}{10}\tau_{sp}$ , we immediately get a one-order-of-magnitude penalty to the threshold level (Fig. 2.10); secondly, the LL curves start resembling those of the low- $\beta$  curves. Therefore, the non-radiative recombination is a very important limiting factor, which obviously points out that fully confined active media (like short QWRs or QDs) would be highly useful.

Another important aspect is that we used a “small” active-medium volume. Indeed, if we now take  $V_a = 500 \times 500 \times 1000 \text{nm}^3$  then (in the case of  $\tau_{nr} \simeq 1000\tau_{sp}$ ) the corresponding curve in the Fig. 2.10 (not shown) for  $\beta = 0.95$  virtually coincides with that of the case  $\tau_{nr} \simeq \frac{1}{10}\tau_{sp}$ . Although it does not influence to such a great extent the ideal case where  $\beta = 1$ , the values in the range of  $\beta = 0.99 \div 0.1$  do not result in threshold improvements as compared to much smaller  $V_a$ .

<sup>21</sup>which is an approximate effective  $\text{In}_{0.15}\text{Ga}_{0.85}\text{As}$  QWR size estimated from TEM cross-section images, and ground-state electron probability-density distribution[52].

<sup>22</sup>provided that the carrier relaxation is very fast (sub-ps), this correction factor can be expressed as:  $F = f_{spot}(1 - R)(1 - e^{-\alpha L})f_{active}$ , where  $f_{spot} \sim 0.25$  is the effective overlap between a focussed-beam gaussian spot and the effective area of the cavity,  $R = 0.3$  - reflection for  $\text{GaAs}/\text{air}$  interface,  $\alpha = 10^4 \text{cm}^{-1}$  -  $\text{GaAs}$  absorption coefficient,  $L = 260 \text{nm}$  - thickness within which the carriers are created in the GaAs matrix and then transferred to the active layer,  $f_{active} \sim 0.45$  - fraction of carriers that makes it into the active region (checked by micro-PL measurements as the fraction that recombines in the QWR only).

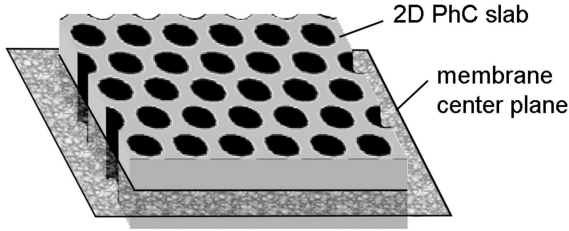


**Figure 2.11:** Schematics of a 2D PhC symmetrical slab.

Summarizing, it is therefore quite clear that having large spontaneous-emission coupling factor and small fully confined active medium brings very favorable conditions to drastically reduce the laser threshold and improve significantly the conversion efficiency already at low pump powers. Additionally, the quantum nature of the active material [13] and excitonic effects [98, 105] may increase the material gain bringing the threshold to yet lower levels.

## 2.3 Modeling of 2D photonic-crystal microcavities

We have already mentioned (sec. 1.4) that photonic-crystals (PhCs) offer unique properties originating from the photonic band-gap effects, which may allow for inhibition and enhancement of the spontaneous emission. Indeed, efficient spontaneous-emission control has been achieved recently using QWs and self-assembled QDs [106] thanks to band-gap effects and 3D photonic confinement. Although 3D PhCs [107, 108] should, in principle, allow for the ultimate 3D photon confinement (including the polarization degree of freedom) via the full band gap, practical solutions employ 2D structures [109]. In 2D PhCs the 3D confinement is achieved via the combination of the *in-plane* band-gap due to periodic dielectric constant with the *out-of-plane* direction governed by the total internal reflection (TIR). Since the confinement strength depends on the index step, the maximum effect can be achieved in the case of semiconductor-air interfaces both for in-plane and out-of-plane cases. This eventually leads to the PhC *membrane* concept widely used for experiments on strongly coupled cavity-QD systems [110–113] and microcavity lasers [114–116].

Due to complexity, such structures cannot be calculated analytically. Therefore, several numerical approaches have been utilized, including plane-wave expansion, tight-binding approach, transfer matrix, finite differences, finite elements and other methods [117, 118]. In our work, modeling based on *finite-differences* numerical method is employed in 2D eigenvalue-problem formulation and, in parallel, full-3D finite-difference time-domain (FDTD) simulation. Such a compromise allows for efficient numerical analysis <sup>23</sup>. In this section we will briefly review the main points of this particular approach.

<sup>23</sup>Relying only on 3D FDTD is impossible, since the simulations are excessively time-consuming (days, weeks). The flexibility can therefore be achieved employing both 2D and 3D models.

### 2.3.1 2D finite-difference stationary model

In the case of a mirror symmetry of the 2D PhC structure along the out-of-plane direction, it is possible to distinguish between TE and TM polarizations. At exactly the membrane center (see Fig. 2.11) this separation is strictly valid. Therefore the problem can be formulated as an eigenvalue problem where the non-infinite slab thickness is taken into account by a proper *effective index*. This is the only important parameter and attention should be paid to its selection. It can be loosely calculated from a three-layer 1D waveguide problem, which can serve as a starting point. It is then however necessary to refine the effective index using a full 3D model, e.g. 3D FDTD simulation where the slab thickness is fixed. After such a refinement, the 2D model provides quite good predictions (and comparison to the experiment) for cavity resonances and the index does not depend on the PhC fill-factor. This has been applied in the present work and will be illustrated in the following subsections.

#### 2.3.1.1 Slab-waveguide modes and the effective index

The three-layer 1D-waveguide (slab-waveguide) problem [see Fig. 2.12 (a)] yields an analytical solution [119]. In this case it is possible to distinguish 2 cases: TE and TM modes as having  $E_z = 0$  or  $H_z = 0$ , respectively. We will concentrate mostly on the TE case (nevertheless the TM modes are also calculated) since, as it follows from the PhC band structure computation for the hexagonal photonic lattice of low-index holes in a high-index bulk, it is hardly possible to open the TM gap with reasonable holes diameters<sup>24</sup>. The waveguide dispersion relation for all the modes reads:

$$\kappa_f h_f - \phi_S - \phi_c = \nu\pi \quad (2.26)$$

where, *in the case of the TE modes*,  $\kappa_f^2 = n_f^2 k_0^2 - \beta_k^2$  ( $k_0 = 2\pi/\lambda_0$  being the wave number,  $\beta_k$  – the propagation constant and  $n_{f,c,s}$  – the refractive indices of the core, cladding and the substrate),  $h_f$  – core thickness and  $\phi$  – the phase shift at the core-cladding boundary. In the case of a symmetrical waveguide  $\phi_c = \phi_s$  and is given by  $\tan \phi_c = \kappa_c/\kappa_f$ , where  $\kappa_c^2 = n_c^2 k_0^2 - \beta_k^2$ . Note that for the guided modes  $\kappa_c$  is imaginary. The propagation constant  $\beta_k = k_0 \cdot n_{eff}$ , and since the optical mode overlaps both with the core and the cladding (as required by the continuity boundary conditions for the Maxwell's equations), the *effective index* satisfies  $n_c < n_{eff} < n_f$ . The first inequality "contains" the cutoff condition at  $n_c = n_{eff}$ . Note that there is no cutoff for the fundamental modes, as imposed by continuity boundary conditions that apply to dielectric waveguides. Thus the dispersion relation serves for finding the effective index for a given mode with a mode index  $\nu$ . For a given wavelength (and *GaAs* refractive index) we can thus readily<sup>25</sup> obtain the dispersion of the effective index versus slab thickness [Fig. 2.12 (b)]. The TM case is also computed (from the TM dispersion equation, respectively). We thus can firstly conclude on how many modes a slab of a given thickness will support, and secondly what the effective index is, for a given mode

<sup>24</sup>The situation is inverted for the case of the lattice of high-index posts within the low-index bulk.

<sup>25</sup>By solving Eq. 2.26 using the bisection method.

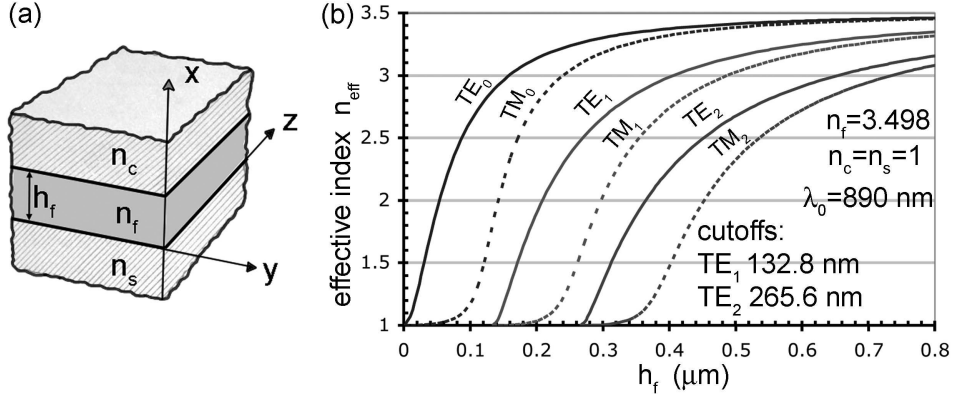


**Figure 2.12:** (a) Schematics of the slab waveguide. (b) Calculated dispersion of the effective index. The particular parameters and cutoff thicknesses ( $\pm 0.1nm$ ) are indicated.  $n_f \approx 3.498$  ( $\pm 0.0025$ ) is the refractive index of *GaAs* at  $890nm$  at  $T = 10K$  inferred from [120].

at a given thickness. This is a preliminarily estimated index in our 2D PhC problem. Note also, concerning the TM modes, that for a given thickness the effective index is much lower for a given TM mode compared to that of a TE mode. Therefore, the mode frequency will be much higher. For the membrane PhC structures that should incorporate V-groove QWRs we opt for a thickness of  $265nm$ . This thickness is selected due to the compromise with the patterning fabrication constraints (see Chapter 3).

Such a  $265nm$  slab supports four modes:  $TE_{0,1}$  and  $TM_{0,1}$ . As we will see from the field distributions, due to parity,  $TE_0$  and  $TM_1$  (even modes with respect to the  $xy$ -plane) are orthogonal to  $TM_0$  and  $TE_1$  (odd modes with respect to the  $xy$ -plane). This is important since 2D-PhC band structure is usually [121] calculated with respect to the parity of the slab modes. It is also worth noting here that due to the large difference in the effective index, the  $TM_1$  mode compared to the  $TE_0$  the former has a much higher frequency. Therefore, within a given PhC band gap the polarization will be well defined.

Let us now consider the guided slab modes. The field distributions will be used later on, in terms of symmetry properties, to construct the wave equation for the 2D PhC problem. Consider propagation along the  $z$ -direction [Fig. 2.12 (a)]. From Maxwell's equations the wave equation **in the TE case** is written for the  $E_y$  field component, and, given  $E_z = 0$ , the *rot* projections yield the following set of non-vanishing field components:  $\{E_y, H_x, H_z\}$  (all dependent only on  $x$ ). Furthermore,  $H_x = -\frac{\beta_k}{\omega\mu}$  ( $\mu = 1$  in the case of non-magnetic material), and  $H_z = \frac{j}{\omega\mu} \frac{\partial E_y}{\partial x}$ . The modes are illustrated in Fig. 2.13 (a). Let us now consider the propagation in the  $y$ -direction. We have then the non-zero field components:  $\{E_z, H_x, H_y\}$ .

In the **in the TM case**<sup>26</sup> for the propagation in the  $z$ -direction ( $H_z = 0$ ) we have the non-vanishing components  $\{H_y, E_x, E_z\}$ . And for the propagation in the  $y$ -direction

<sup>26</sup>The wave equation is written for the  $H_y(x)$  and the other two non-vanishing components follow as  $E_x = \frac{\beta_k}{\omega\epsilon} H_y$  and  $E_z = -\frac{j}{\omega\epsilon} \frac{\partial H_y}{\partial x}$ . Note, the division by the dielectric constant  $\epsilon$  induces the field-distribution jumps of the out-of-plane field component at the interfaces, consistent with boundary conditions.

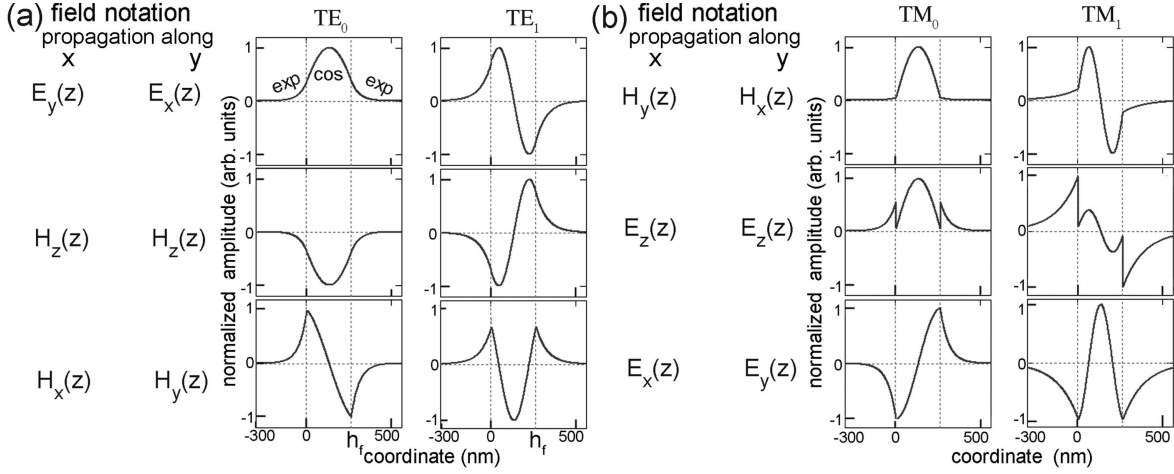


**Figure 2.13:** Slab-waveguide modes. Calculated field distributions of non-vanishing components (a) for the TE-modes, (b) for the TM modes. Slab thickness is indicated ( $h_f$ ). Note, that the field notation is in the 2D-PhC coordinates.

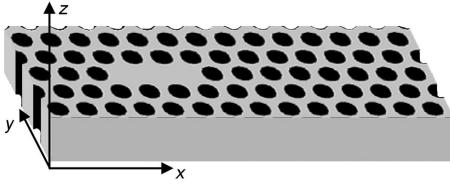


**Figure 2.14:** 2D PhC symmetrical slab (containing a defect cavity), and PhC coordinate system used.

we obtain  $\{H_z, E_x, E_y\}$ . The distributions are shown in the Fig. 2.13 (b).

In the 2D PhC problem, for convenience, we use a different coordinate system, where  $z$  is the out-of-plane direction. Therefore the field indices above have to change accordingly. We then have for the TE case  $\{E_y, H_z, H_x\}$  and  $\{E_x, H_z, H_y\}$ . For the TM case we get  $\{H_y, E_z, E_x\}$  and  $\{H_x, E_z, E_y\}$ .

### 2.3.1.2 Mode symmetry and formulation of the 2D PhC problem

As the 2D PhC slab, schematically shown in the Fig. 2.14, has a mirror symmetry along the  $z$ -direction (see also Fig. 2.11), within its center the modes are given exactly by the field components associated with the slab-waveguide modes. Considering now the modes shown in Fig. 2.13, we can see that within the slab center in the case of the  $TE_0$ -mode  $H_x = H_y = 0$  and in the case of the  $TM_0$ -mode  $E_x = E_y = 0$ . Therefore, we finally obtain the sets of the field components that will govern the PhC modes.  $TE_0$  modes:  $\{E_x, E_y, H_z\}$ ;  $TM_0$  modes:  $\{H_x, H_y, E_z\}$ . The 2D PhC problem is then formulated in terms of a slab of a material with an effective index  $n_{eff}$  and an infinite thickness. At the same time, the in-plane ( $xy$ ) distribution of the dielectric constant can be absolutely arbitrary. Now we construct the wave (or master) equation. Starting from the Maxwell and material equations, assuming a non-magnetic medium in the absence

of static charge,

$$\text{rot}(\vec{E}) = -\frac{\partial \vec{B}}{\partial t} \quad (2.27)$$

$$\text{rot}(\vec{H}) = \frac{\partial \vec{D}}{\partial t} \quad (2.28)$$

$$\vec{B} = \mu_0 \mu \vec{H} \quad (2.29)$$

$$\vec{D} = \epsilon_0 \epsilon \vec{E} \quad (2.30)$$

and making projections to all the coordinates (assuming  $e^{j\omega t}$  time dependence of the fields) we get the following set of equations in the case of the TE modes, provided that  $E_z = H_x = H_y = 0$ :

$$\frac{\partial E_y}{\partial x} - \frac{\partial E_x}{\partial y} = -j\omega \mu_0 H_z \quad (2.31)$$

$$\frac{\partial H_z}{\partial y} = j\omega \epsilon_0 \epsilon E_x \quad (2.32)$$

$$-\frac{\partial H_z}{\partial x} = j\omega \epsilon_0 \epsilon E_y \quad (2.33)$$

From the latter two equations the  $E$ -field components are calculated. Next, introducing these two equations into the first one and assuming that  $c_0 = \frac{1}{\sqrt{\epsilon_0 \mu_0}}$  we get the wave equation for the TE modes:

$$\frac{\partial}{\partial x} \left( \frac{1}{\epsilon} \frac{\partial H_z}{\partial x} \right) + \frac{\partial}{\partial y} \left( \frac{1}{\epsilon} \frac{\partial H_z}{\partial y} \right) + \frac{\omega^2}{c_0^2} H_z = 0 \quad (2.34)$$

Note that, stemming from the initial assumption  $E_z = 0$ , this equation is valid for the  $TE_m$  modes where  $m = 0, 2, 4, \dots$ . This is however enough since normally one is interested in the well-open  $TE_0$  PhC bandgap available, for the hexagonal lattice, at reasonably low frequencies (see section 1.4). The  $TE_1$  gap that might be expected at much higher frequencies (due to low effective index) requires impractically large air-hole sizes. We shall also mention that the hexagonal lattice itself provides a conveniently wide gap, compared, e.g., with a square PhC lattice.

In the case of the  $TM$ -modes, where we have  $H_z = E_x = E_y = 0$  we obtain

$$\frac{\partial H_y}{\partial x} - \frac{\partial H_x}{\partial y} = j\omega \epsilon_0 \epsilon E_z \quad (2.35)$$

$$\frac{\partial E_z}{\partial y} = -j\omega \mu_0 \epsilon H_x \quad (2.36)$$

$$-\frac{\partial E_z}{\partial x} = -j\omega \mu_0 \epsilon H_y \quad (2.37)$$

From the latter two equations we can calculate the  $H_x$  and  $H_y$  components, whereas the wave equation for the  $E_z$  reads

$$\frac{1}{\epsilon} \left( \frac{\partial^2}{\partial x^2} + \frac{\partial^2}{\partial y^2} \right) E_z + \frac{\omega^2}{c_0^2} E_z = 0. \quad (2.38)$$

Again, according to the initial assumption that  $H_z = 0$  and in view of the slab-waveguide mode symmetry, this equation is valid for  $TM_{0,2,4,\dots}$  modes.

In the 2D PhC problem either Eq. 2.34 or Eq. 2.38 is solved using the finite-difference method <sup>27</sup> where the derivatives are discretized at each point as e.g.  $f'_x(x_n, y_n) = \frac{f(x_{n+1}, y_n) - f(x_n, y_n)}{\Delta x}$ . Either Dirichlet (e.g.  $H_z = 0$  for the  $TE$ -modes) or periodic [ $H_z = \exp(jka)$ ] boundary conditions used in the case of confined modes and periodic structures (e.g. PhC waveguides), respectively.

Solving the 2D PhC problem for cavity-mode computations with the Dirichlet boundary conditions poses an issue of the spurious boundary eigenmodes existing within the PhC band gap. Interestingly, it was found that for a periodic structure shown in the Fig. 2.14 (air holes in a semiconductor matrix) cutting the computational domain through the air holes pushes completely out these surface states. Thus, all the cavity modes can be computed in a single run. Secondly, the band gap itself shows up clearly in the frequency domain (“sandwiched” between the PhC upper- and lower-continuum frequencies).

### 2.3.1.3 Out-of-plane confinement: leakage into substrate

In the design of the 2D PhC membrane structures one of the important parameter is the distance between the suspended membrane and the substrate. This is due to the fact that any slab waveguide positioned on top of a substrate will have mode leakage into the substrate due to a finite lower-cladding layer thickness, as imposed, in essence, by the continuity boundary conditions. The leak, and therefore the *losses due to the leak into substrate*, can be significant, producing in addition unwanted interference effects [122–124]. Not going into details of the model, we will only assume the final formula derived in [122] and calculate the losses for the case of air-*GaAs* slab waveguide. Assuming that the leak into the substrate produces only loss  $\alpha_s$  (in  $cm^{-1}$ ) (neglecting, in our case unlikely, interference due to the back-reflection from the substrate bottom), the expression reads

$$\alpha_s \simeq \frac{4q_2 p^2 \cos^2(\kappa_f h_f / 2)}{\beta d_{eff} (p^2 + q_2^2)} e^{-2pd} \quad (2.39)$$

where  $q_2 = \sqrt{k_0^2 n_{substr}^2 - \beta^2}$ ,  $d_{eff}$  is the effective transversal mode size within the waveguide which can be found as  $d_{eff} = \int |u|^2 dz$  ( $u(z)$  - field amplitude) and  $p$  is the characteristic spatial-decay constant of the field in the cladding, i.e.  $p = \sqrt{\beta^2 - n_c^2 k_0^2}$ .

The result of such model applied to  $TE$  modes is shown in the Fig. 2.15. We can conclude that for such a high index contrast as between *GaAs* slab and air cladding the losses due to the leakage into substrate come into play for the  $TE_0$  mode only if  $d < 300nm$ . Note that the losses are higher for the  $TE_1$  mode due to its larger spatial extent and due to much lower effective index.

<sup>27</sup>Implemented on the MATLAB platform.

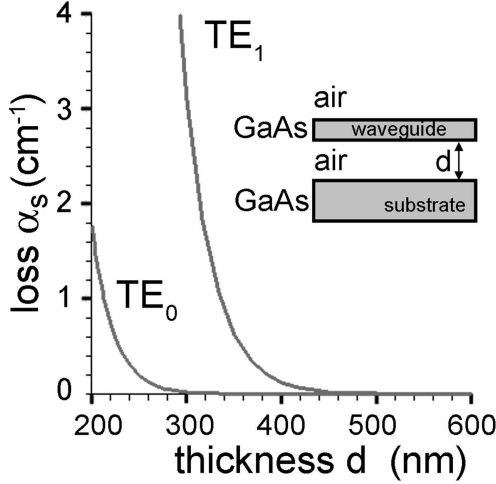


**Figure 2.15:** Loss associated with leakage of the mode along the out-of-plane direction (through the lower cladding of a thickness  $d$ ) into the substrate. At  $d = 500\text{nm}$   $\alpha_s(TE_0) \sim 3 \cdot 10^{-6}\text{cm}^{-1}$  and  $\alpha_s(TE_1) \sim 5.5 \cdot 10^{-3}\text{cm}^{-1}$ .

### 2.3.1.4 Scalability in the PhC problem

Unlike for electrons in solids, there is no fundamental length scale in Maxwell's equations. Therefore if one scales the dielectric-constant distribution by a factor of  $s$  [ $\epsilon'(\vec{r}) = \epsilon(\vec{r}/s) = \epsilon(\vec{r}')$ ] then the Eq. 2.34 is transformed as

$$\frac{\partial}{\partial x'} \left( \frac{1}{\epsilon(\vec{r}/s)} \frac{\partial H_z(\vec{r}/s)}{\partial x'} \right) + \frac{\partial}{\partial y'} \left( \frac{1}{\epsilon(\vec{r}/s)} \frac{\partial H_z(\vec{r}/s)}{\partial y'} \right) + \frac{\omega^2}{c_0^2 s^2} H_z = 0. \quad (2.40)$$

Thus we will have the solutions as  $H'_z = H_z(\vec{r}/s)$  and  $\omega'/s$ , which implies that both the field distribution and the eigenfrequency is only scaled by the factor  $s$ . In all the PhC problems therefore the physics (e.g. properties in terms of band gap) will be maintained irrespectively of  $s$ . For convenience, it is then appropriate to introduce *normalized units* for the quantities such as the distance (in lattice-constant units  $a$ ), frequency  $f = \frac{\omega}{c_0} = \frac{a\omega}{2\pi c_0} = \nu_0 \frac{a}{c_0}$  (so it becomes  $f$  in units of  $c_0/a$ ) and the wave vector  $\vec{k} = \frac{k a}{2\pi}$  (and it becomes  $\vec{k}$  in units of  $2\pi/a$ ).

### 2.3.2 3D FDTD simulations and Padé-Baker approximation

The model presented above proves to be very useful in fast analysis of the confined cavity modes for the  $TE_0$  PhC band gap. However, for maximum accuracy, it is clear that 3D structures need to be computed using a 3D method. For complex structures, iterative 3D FDTD simulations are established as the most efficient, first-principles modeling means. It is however inherently time-consuming and sometimes not so insightful<sup>28</sup> as compared to analytical means. We employed this numerical method in combination with 2D computations for analysis flexibility. As a result, the 3D FDTD allows for the efficient refinement of the effective index with which the 2D model can predict rather accurately single-cavity mode spectra. On the other hand, coupled cavities have to be treated with 3D FDTD only (the 2D model yields much larger coupling strengths, as

<sup>28</sup> "An avalanche of numbers in the desert of ideas".

consistent with the dielectric-constant being extended infinitely along the out-of-plane direction). Cavity radiative losses (and the  $Q$ -factor) can be accurately found only by the real-time field decay, which is obtained in the 3D FDTD. Note that the 2D model, in return, is indispensable for tasks involving the resonant excitation in the 3D simulation using a particular mode pattern. In such tasks the mode pattern is computed in 2D.

The standard Yee algorithm of the FDTD simulations is well established nowadays [125]. Basically, the partial derivatives in the original Maxwell's equations (Eq. 2.27, 2.28) are discretized on a numerical grid. According to Maxwell's equations, the time derivative of, e.g., the  $E$ -field depends on the curl of the  $H$ -field across the space (and vice versa for the  $H$ -field). Therefore in the discretized form, the updated spatial distribution of the  $E$ -field in time depends on the stored distribution and the numerical curl of the  $H$ -field spatial distribution. The  $H$  field is time-stepped analogously. Thus, iterating the updates of the  $E$  and  $H$  fields results in a marching-in-time process. Given an initial condition at  $t = 0$  as a field distribution (source) of one of the six electromagnetic-field vector components, the discretized Maxwell's equations are solved iteratively using a leapfrog time-stepping scheme for performing the field updates. The time-stepping has to satisfy the so-called *stability condition*

$$\Delta t \leq \frac{1}{c_0 \sqrt{(1/\Delta x)^2 + (1/\Delta y)^2 + (1/\Delta z)^2}} \quad (2.41)$$

where  $\Delta x, y, z$  is the finite resolution in the computational domain. It basically implies that the time discretization has to be much smaller compared to the frequency of oscillating electromagnetic field. Assuming generally in normalized units  $c_0 = 1$  and  $\Delta x = \Delta y = \Delta z = 1$ , the stability criterion in 3D space stipulates that  $\Delta t \leq 1/\sqrt{3}$ . In our case the time discretization was thus chosen to be  $\Delta t = 0.5$ . For typical parameters used  $\Delta x, y, z = 0.04a$  the iteration time step then equals  $1it = \Delta t = \frac{0.5}{c_0 \sqrt{(1/\Delta x, y, z)^2}} \approx 1.401 \times 10^{-17} s$ , taking  $a = 210nm$ .

Simulations are normally done using absorbing boundary conditions (e.g., Mur or Liao, or alternatively, so-called perfectly matched layers). Practically, standard Mur boundary conditions (BC) are easiest to implement and are well suited for problems other than scattering<sup>29</sup>. Importantly, symmetry boundary conditions can be also implemented for symmetric structures, which saves greatly the overall computation time.

In order to obtain the frequency resonant spectra, the analysis of the simulated time-evolution of the electromagnetic field is normally performed by the Fourier transform. The discrete Fourier transform (DFT) of a field component  $u(t)$  reads

$$U(N_{it}, \omega) = \sum_{n=0}^{N_{it}} u(n\Delta t) e^{-j\omega n\Delta t} \quad (2.42)$$

where  $N_{it}$  is the number of iterations performed in FDTD with the time step  $\Delta t$ . The resolution in the frequency domain depends on the number of iterations. This is

<sup>29</sup>For the scattering simulations, small-angle reflections may arise causing unwanted interference within the computational domain. Liao boundary conditions [125] are then implemented for such tasks. On the other hand, the Liao boundary conditions are sensitive to parameters, and the simulation has more chances to diverge.

however problematic if relatively sharp resonances are involved. In fact, a spectral width of a given resonance is defined by the time decay of  $u(t)$  and, at the present state of computer development, iterative FDTD simulation for an elaborate 3D-distribution of the dielectric constant can take days and weeks in order to determine the decay rate. One of the methods that can drastically improve the resolution in the frequency domain is based on the *Padé approximation* implemented *using Baker's algorithm* [126, 127]. The Eq. 2.42 can be calculated by introducing the series

$$F(\mathcal{Z}, \omega) = \sum_{n=0}^{\infty} C_n \mathcal{Z}^n \quad (2.43)$$

where  $C_n = u(n\Delta t)e^{-m\omega\Delta t}$ . It is clear that  $F(1, \omega) = U(\infty, \omega)$ . It is known that the Padé approximation can be used to approximate the series from which it is generated, therefore one can approximate the expansion in Eq. 2.43 by the Padé approximant which is defined (e.g. in terms of the Padé table) as

$$[N, M](\mathcal{Z}) = \frac{\sum_{n=0}^M a_n \mathcal{Z}^n}{\sum_{n=0}^N b_n \mathcal{Z}^n}. \quad (2.44)$$

Assuming  $N$  is an even number, it is then possible to approximate

$$F(1, \omega) \approx [N/2, N/2](1), \quad (2.45)$$

and the polynomials in the nominator and the denominator in Eq. 2.44 at each frequency are calculated based on the Baker's recursive algorithm.

Applied to PhC microcavities studied here, the Padé-Baker method allows to determine accurately (within  $< 0.5\%$ ) both the resonant frequencies and high  $Q$ -factors already at  $N_{it} \simeq 10000 \div 15000$ <sup>30</sup>.

### 2.3.3 GaAs refractive index corrections

The very important parameter in both the 2D and the 3D models is the refractive index of the *GaAs* matrix. Around our target wavelength  $\sim 900nm$  *GaAs* has a pronounced index dispersion [128], which needs to be taken into account in simulations. In particular, this is important when multimode PhC cavities with a relatively broad spectrum are computed and such a task is performed in a single run. Moreover, in the 2D model, the correction of the effective index is required prior to the correction for the *GaAs* index dispersion.

#### 2.3.3.1 Refractive-index correction for 3D FDTD

According to the thorough measurements performed by Marple [120] at several temperatures, the near-infrared index  $n_{GaAs}(\lambda)$  is non-linear, however the temperature dependence is the same at different photon energy. We can thus extrapolate these data to 10K

<sup>30</sup>Which is  $\sim 1$  day of a simulation computer time.

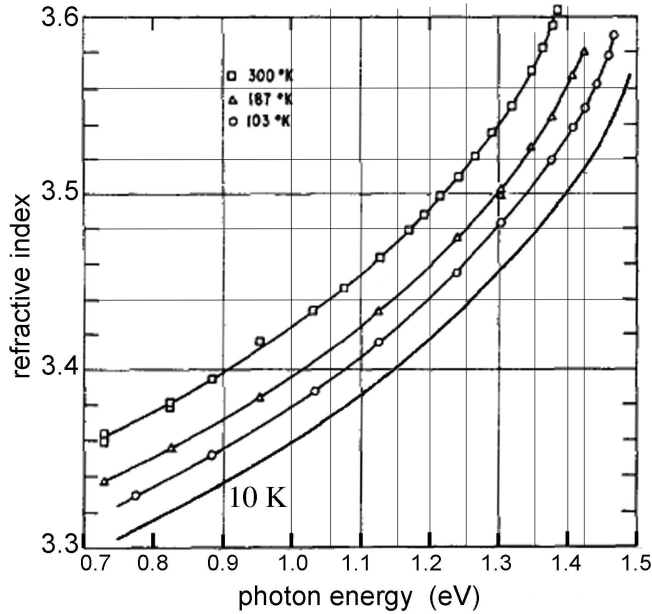


**Figure 2.16:** GaAs refractive index (measured in [120]). The 10K curve is an extrapolation based on the original data.

(see Fig. 2.16). This plot serves for picking up the right index value at a given energy for the 3D FDTD simulation. The simulated spectrum however has to be post-processed since the wavelengths other than the one corresponding to that of the selected index ( $\lambda_{0n}$ ) are not accurate due to the *GaAs* index dispersion. This is done straightforwardly by scaling the wavelength axis around  $\lambda_{0n}$  based on Fig. 2.16. The correction curve for the spectral range of our interest is shown in Fig. 2.17. To implement the correction, at each point on the wavelength axis (of a simulated spectrum using  $n_{GaAs} = 3.518$ )  $\delta\lambda$  has to be added. Note that the use of a different index for a simulation implies that the zero-correction wavelength is changed accordingly (also plotted for reference) and the correction curve will be just vertically shifted.

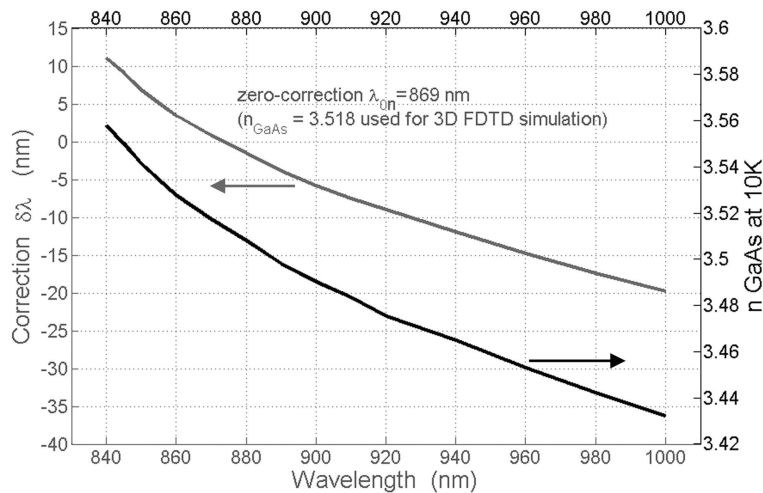


**Figure 2.17:** Correction  $\delta\lambda$  for spectra computed in 3D using the refractive index at  $\lambda_{0n} = 869$  nm. Computation performed at a different  $\lambda_{0n}$  implies a vertical curve shift. Refractive index versus wavelength is also shown for reference.

### 2.3.3.2 Effective-index correction for 2D model

In 3D model the PhC slab is simulated directly. Therefore, the resonant spectrum bears inherently the “knowledge” of the index step in the out-of-plane direction. As a result, the index correction can be done by introducing the *GaAs* index dispersion directly. In the 2D model there is no index step and the structure is described by the effective index  $n_{eff}$ . Therefore, to correct for the dispersive *GaAs* index one needs to calculate  $n_{eff}$  at each wavelength. The most accurate way to implement it is to see how a certain mode of a test PhC structure shifts using the 3D FDTD simulation performed with different *GaAs* indices. This procedure, at the same time, yields the refinement of the first-guess  $n_{eff}$  obtained from the 1D slab-waveguide calculations. Note, that the membrane thickness and PhC lattice constant in this case have to be fixed parameters.

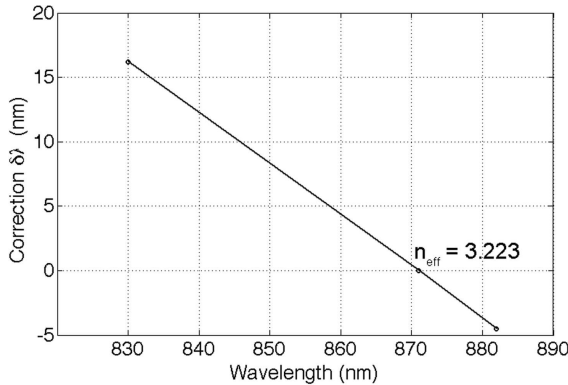


**Figure 2.18:** Correction  $\delta\lambda$  for spectra computed in the 2D model at the indicated  $n_{eff}$ . The effective index is refined using 3D FDTD (see text).

Let us examine the procedure with a relevant example. We take the lowest-order mode ( $M_0$ ) of the  $L_3$  cavity (three missing holes in a row, as shown in Fig. 2.14) as the test mode, and a PhC membrane with a thickness of  $\approx 265nm$  and lattice constant  $a = 210nm$  and the radius of air holes given by  $r/a = 0.32$ . Three 3D FDTD simulations of this structure are then done. First, simulating with  $n_{GaAs}^{10K} = 3.5139$  (valid at  $\lambda_0 = 871nm$ ) results in that the mode is found at  $\lambda_0 = 882.15nm$ . Second, at  $n_{GaAs}^{10K} = 3.58$  (valid at  $\lambda_0 = 830nm$ ) the mode is found at  $898.26nm$ . Third, at  $n_{GaAs}^{10K} = 3.4991$  (valid at  $\lambda_0 = 882nm$ ) the simulation yields the mode at  $878.5nm$ . Now the effective index  $n_{eff}$  entering the 2D model, computing exactly the same in-plane PhC geometry, is iteratively tuned such that the test mode is found at  $882.15nm$ . This establishes the  $n_{eff} \approx 3.223$  at zero-correction wavelength of  $\lambda_{0n} = 871nm$ . The other two points give  $\delta\lambda = +16.2nm$  (at  $830nm$ ) and  $\delta\lambda = -4.5nm$  (at  $882nm$ ). The rest of the range is extrapolated using a linear curve. The correction curve is shown in Fig. 2.18. Note that such a correction does not depend on  $r/a$  because the effective index does not change. Note also that for a given membrane thickness and PhC lattice constant 2D computations on different in-plane geometries can be performed using the same  $n_{eff}$ . The computed spectra then only need to be post-processed using Fig. 2.18. On the other hand, changing the lattice constant  $a$  in the computations implies also the change in the membrane thickness, as the latter is expressed in the units of  $a$ , so the  $n_{eff}$  has to be recomputed accordingly. However, variations of  $a$  within  $\pm 10nm$ , which is what can occur experimentally, are not expected to introduce important inaccuracies,

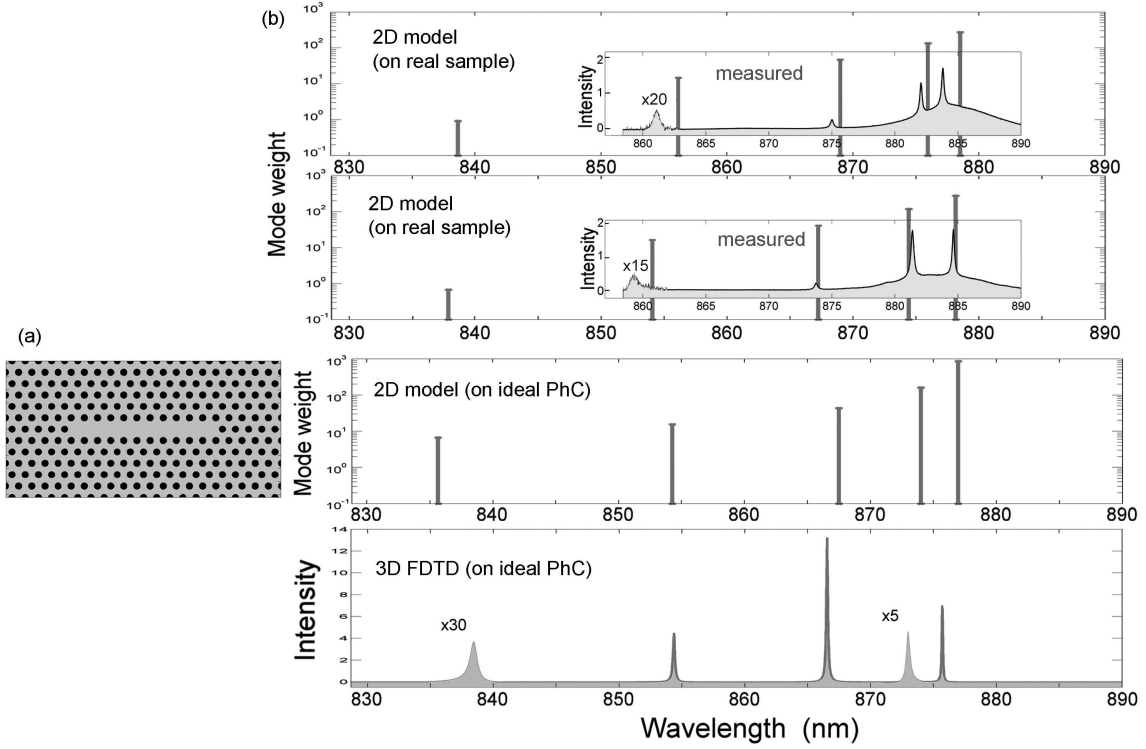


**Figure 2.19:** Comparison of the 2D model to the 3D FDTD and to experimental data. (a) Model structure:  $L_{11}$  PhC cavity,  $r/a = 0.26$ ,  $a = 196\text{nm}$ . (b) Computed spectra. Only odd-symmetry modes (see Sec. 4.2.1) are considered (even-modes spectrum is found at  $\lambda \leq 840\text{nm}$ ). Experimental spectra is photoluminescence from QWRs coupled into PhC modes. Sample geometry:  $r/a \approx 0.26$ ,  $a \approx 197\text{nm}$ . All vertical axes are in arbitrary units. The “mode weight” in the 2D model indicates the inverse out-of-plane loss (see Sec. 2.3.4).

and the 2D analysis can still apply reasonably well.

An example that demonstrates a comparison of the 2D model computation to the 3D simulation where in both models the respective index corrections were made and all compared to experimentally observed resonant spectra of  $L_{11}$  PhC cavities is shown in Fig. 2.19. Note that in the 2D model the same  $n_{eff}$  correction was applied to the whole spectrum uniformly (i.e., to all the modes), while it might be suspected that  $n_{eff}$  changes differently for different modes. We checked using 3D FDTD that for different modes the trends do not vary appreciably with respect to Fig. 2.18. From Fig. 2.19 we can see that the 2D model gives rather good spectrum prediction (compared to experimental data), as verified with the 3D FDTD. We note that, the experimental data had to be offset by  $\approx 6\text{nm}$  in order to match simulations, also to match those made on the imported dielectric-constant distribution from the measured structure (SEM image). This is probably due to inaccuracy in the membrane thickness and the lattice constant<sup>31</sup>.

<sup>31</sup>In the simulations the thickness (in 3D) and  $n_{eff}$  (in 2D) in the normalized units were established using  $a = 210\text{nm}$ . However in the experimental data  $a \approx 200$  had to be used. This eventually can easily account for the  $\sim 5\text{nm}$  offset. Alternatively, in the experimental sample there may be a small

### 2.3.4 Light-cone problem: radiative losses of a 2D photonic-crystal cavity

Whereas small mode volumes are provided by the small size of PhC cavities, it can be questioned whether the losses will not be excessively large such that only marginal  $Q$ -factors are then attained. For example, a Fabry-Perot cavity loss is inversely proportional to the cavity size<sup>32</sup>, so small-volume semiconductor cavities will not have high  $Q$ . However, employing PhCs can compensate for this, since very high mirror reflectivities can be achieved (as e.g. in vertical-cavity surface-emitting lasers). In 2D PhC microcavities this leads to a very efficient in-plane light confinement with an infinite in-plane  $Q_{\parallel}$ -factor for a perfectly periodic structure. The photon leak is then possible only in the out-of-plane direction eventually due to diffraction. Quite remarkably, it turns out that such a diffraction can be efficiently controlled by the in-plane PhC cavity geometry, and thus very high  $Q$ -factors can be attained [129–132] even though the mode volume is very small. In order to estimate the out-of-plane diffractive loss, the so-called *light-cone problem* is solved. In essence, it constitutes the analysis of the in-plane field distribution in the  $\vec{k}_{\parallel}$ -space in order to define the amount of radiative field (with small  $\vec{k}_{\parallel}$ -vectors) with respect to the confined field components (with large  $\vec{k}_{\parallel}$ -vectors).

Consider a slab waveguide shown in Fig. 2.20 (a). It is clear that any propagating field component that does not satisfy the TIR condition will be radiative at the surface. According to the boundary conditions to the Maxwell's equations,  $\vec{k}_{\parallel}$  of a wave with a wave vector  $\vec{k}$  traveling from the core into the cladding *must be conserved* at the interface. The  $\vec{k}_{\parallel}$ -vector satisfies the relation  $k^2 = k_{\parallel}^2 + k_z^2$ , which can be written for  $k_z$  as

$$k_z = \sqrt{k^2 - k_{\parallel}^2} \quad (2.46)$$

We can see that any wave-component with  $k_{\parallel} < k$  will be propagating in the cladding (adding up to the radiative field given by  $e^{ik_z z}$ ) and any field component with  $k_{\parallel} > k$  will be exponentially decaying in the cladding (adding up to the evanescent field given by  $e^{k_z z}$ ) since  $k_z$  becomes purely imaginary. The latter case corresponds to the fully confined field components. The TIR constraint is then given by  $k_z = 0$ , which yields the condition

$$k_{\parallel} = k = \left( \frac{2\pi}{\lambda} n_c \right) \quad (2.47)$$

Let us now examine the problem in the 2D in-plane space [Fig. 2.20 (b)]. Within the material  $\vec{k}_{TIR}$  must be defined such that its in-plane component satisfies Eq. 2.47. Therefore, for a given  $\lambda_0$  we will have different  $|\vec{k}_{TIR}|$ , which in the 3D picture of the  $k$ -space defines the “height” of a cone. The cone is essentially formed by the vector  $\vec{k}_{TIR}$ , and is referred to as the *light cone*. As for membrane structures  $n_c = 1$ , we have  $k_{\parallel TIR} = \frac{2\pi}{\lambda_0}$  within the  $k_{\parallel}$ -plane, and for all the in-plane directions this results in a circle with a radius of  $k_{\parallel TIR} = k_{cone}$ . It becomes clear now that if we do an analysis of the

---

fluctuation of the membrane thickness ( $\sim 8nm$ , due to regrowth on non-planar substrate, measured by AFM), variation in the in-plane  $a$  and variation in  $r/a$  along the out-of-plane direction.

<sup>32</sup>  $\frac{1}{2L} \ln \frac{1}{R_1 R_2}$  where  $L$  is the cavity length and  $R$  – mirror reflectivity.

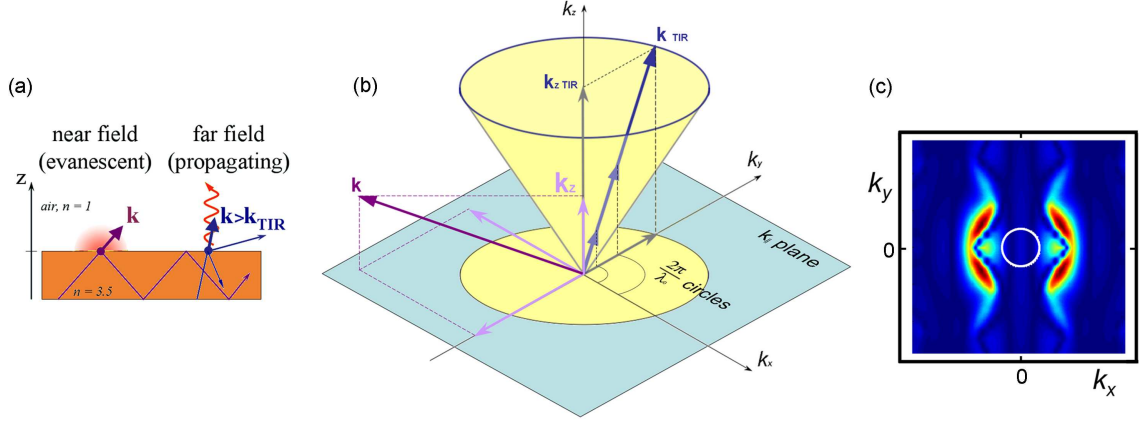


**Figure 2.20:** (a) Sketch of a slab waveguide. (b) Schematics of the light cone in the  $k$ -space. Field components (within the waveguide core) with large  $k_{\parallel}$  (e.g., the pink wave vector) are confined. (c) Example of a computed field distribution ( $E_y$  field component within the slab's central plane) in the  $k_{\parallel}$ -space of an  $L_3$  cavity ( $M_0$  mode; PhC  $r/a = 0.35$ ). Note the field components within the light cone (circled), which leak into the far field.

field-distribution in the  $k_{\parallel}$ -plane we can, by deducing the integral amount of the field components having  $k_{\parallel} \leq k_{\text{cone}}$  compared to that of the components with  $k_{\parallel} > k_{\text{cone}}$ , see how radiative a given mode is. Having then a real-space mode field distribution, the  $k_{\parallel}$  pattern is obtained simply by the Fourier transform (FT). As the radiation is expected to happen from the PhC membrane surface, the field distribution just above the membrane should be used [132] for the light-cone analysis. Such a pattern can be obtained from 3D FDTD simulation. It can however be extremely useful to estimate the relative radiation losses among the modes of a given multimode cavity in the fast 2D model that gives the field distribution within the central sheet of the membrane. Such an experiment, verified with 3D FDTD, shows that it is possible to clearly distinguish between high- $Q$  and low- $Q$  modes, which can be readily applied for determining potentially high- $Q$  modes of a given cavity structure. Since no absolute  $Q$ -value can be deduced from the 2D model, we used a quantity termed “mode weight” which is calculated as (in the case of the  $TE$  modes)

$$\text{Mode Weight} = \frac{1}{\int \int_{k_{\parallel} \leq 2\pi/\lambda_0} dk_{\parallel}^2 |FT(E_x)|^2 + |FT(E_y)|^2 + |FT(H_z)|^2} \times \text{const} \quad (2.48)$$

provided that the fields are normalized<sup>33</sup>. Alternatively (also employed for 3D FDTD)<sup>34</sup>, for comparison of the out-of-plane radiative losses of different structures we calculate the ratio in % of the integrated field intensity within the light cone to that within the whole computed domain. This avoids using unnecessary approximations [132] for computing the radiated power and allows at the same time for the direct comparison.

<sup>33</sup>E.g. in the real space by the 2D “stored energy” as  $\frac{1}{2} \int \int_{XY} \epsilon |E_x|^2 + \epsilon |E_y|^2 + \frac{1}{2} \int \int_{XY} |H_z|^2$ .

<sup>34</sup>And since, whenever 3D FDTD is used for  $Q$ -factor computation, we rely on the Padé-Baker method.

## 2.4 Chapter summary

In this chapter we firstly outlined the main theoretical aspects that have to be familiar with in order to interpret and discuss experimental results on QWR-PhC interaction and coupling, including both the spontaneous and the stimulated emission. Secondly, we introduced the modeling techniques used to understand the properties of the photonic-crystal membrane microcavities implemented in the integrated PhC-QWR system and their design.



# Chapter 3

## Technology and characterization of integrated quantum-wire photonic-crystal structures

Integration of low-dimensional semiconductor nanostructures such as quantum wires (QWRs) and quantum dots (QDs) with high- $Q$  optical microcavities provides the basis for interesting studies of cavity quantum electrodynamics [18] and may lead to various applications in nano-photonic devices. The main challenge for integration of quantum nanostructures and high- $Q$  optical cavities lies in matching the photon energies of the resonator modes to those of the transitions between the quantum confined states, and in accurate positioning of the quantum nanostructures at selected locations within the cavity. At the current stage of development, most work (done mainly on QDs) is pursued using self-assembled nanostructures with no site control and relatively poor control on electronic state energies. Recent progress to overcome this problem includes finding the location of a self-assembled QD on the substrate exploiting strain effects, and positioning the optical microcavity around it [111]. However, a full control on the site and the spectrum of the nanostructures is key to significant advances in the field.

In this chapter, the technology of the incorporation of a site-controlled, V-groove QWR into a two-dimensional photonic-crystal membrane microcavity is presented. The same methods were successfully utilized later on for integrating a single site-controlled QD in similar PhC cavities [133]. In addition, the experimental techniques required for structural and optical characterization of the QWR-PhC system are introduced.

### 3.1 Site-controlled quantum wire integrated into a photonic-crystal microcavity

*InGaAs/GaAs* QWRs are formed by epitaxy in a V-groove pattern defined by electron-beam lithography. The PhC structure is also defined using *e*-beam lithography, making possible accurate, deterministic positioning of the wire with respect to the cavity optical mode pattern. The method allows for the control of both the emission spectrum of the

QWR and its site. In this section we will, first, give a general idea by describing the summarized fabrication process and then introduce details of the technological steps involved which development constituted a major part of the experimental effort in this thesis project.

### 3.1.1 Summarized nanofabrication process

Our integrated QWR-PhC structures are fabricated using a combination of lithography and self-ordered epitaxial growth processes [see Fig. 3.1 (a)]. First, a  $1\mu\text{m}$  sacrificial  $\text{Al}_{0.75}\text{Ga}_{0.25}\text{As}$  layer and a  $200\text{nm}$   $\text{GaAs}$  membrane layer are grown on a (100) exactly oriented ( $\pm 0.02^\circ$ )  $\text{GaAs}$  substrate by metal-organic vapor-phase epitaxy (MOVPE).  $1\mu\text{m}$ -pitch,  $190\text{nm}$  deep V-groove gratings are then etched through a PMMA line-pattern mask. The pattern, with lines oriented along the  $[01\bar{1}]$  direction, is defined by  $e$ -beam lithography. Simultaneously, two groups of alignment marks<sup>1</sup> are written and etched around the gratings. After a standard cleaning procedure, the sample is overgrown by MOVPE with a  $65\text{nm}$   $\text{GaAs}$  layer embedding  $\text{In}_{0.15}\text{Ga}_{0.85}\text{As}$  layers to form the QWRs in the V-grooves [Fig. 3.1(b)]. The growth of the QWR-layers is performed at a relatively low substrate temperature ( $590^\circ\text{C}$ ) in order to obtain narrow QWRs and achieve quick planarization of the V-groove grating [134]. Finally, the PhC cavities are defined on top of the grown QWR wafer such that each of them incorporates a single wire, aligned at the center of the PhC defect [Fig. 3.1(c)]. The PhC pattern is defined by  $e$ -beam lithography in PMMA resist deposited on top of  $\text{SiO}_2$  (30- or 80-nm thick) layer. The pattern is then transferred from the PMMA to  $\text{SiO}_2$  employing  $\text{CF}_4$  or  $\text{CHF}_3/\text{Ar}$  reactive ion etching (RIE). After the transfer and removal of the resist residues in  $\text{O}_2$  plasma, the PhC holes are drilled through the  $\text{GaAs}$  layer by means of either  $\text{Cl}_2/\text{SiCl}_4/\text{Ar}$  RIE or  $\text{BCl}_3/\text{N}_2$  inductively-coupled plasma (ICP) RIE [Fig. 3.1(c)]. The fabrication is completed by selectively removing the sacrificial  $\text{Al}_{0.75}\text{Ga}_{0.25}\text{As}$  layer in  $\text{HF} : \text{H}_2\text{O}$  solution ( $\simeq 4\%$ ), which yields a free-standing  $\text{GaAs}/\text{InGaAs}$  membrane containing the PhC holes and the V-groove QWRs [Fig. 3.1(d)]. In addition, further postprocessing using a citric acid solution was implemented mainly for the purposes of  $\text{GaAs}$ -oxide removal, which enhances the PhC microcavity performance [135].

### 3.1.2 $e$ -beam nanolithography and pattern design

Exploiting the very short wavelength of highly accelerated electrons in free space ( $\lambda \simeq h/mv$ ), the scanning electron microscopy allows for focussing with spot sizes down to  $\sim 1\text{nm}$ . This possibility is readily exploited in  $e$ -beam lithography, where designed dimensions of the pattern elements can go well below  $\mu\text{m}$  sizes [136]. Practically, the ultimate limitations are posed by the electron resist that is normally a polymer. The principle of the  $e$ -beam lithography is that the resist's molecular weight is greatly reduced by the exposure to the electron beam (at a sufficient dose, defined by resist's sensitivity), which is then soluble in a developer. The resolution (and also the pattern roughness) is then limited by the intermolecular forces and molecule gyration size which

<sup>1</sup>Two 4-mark sets aimed at coarse and subsequent fine alignment.

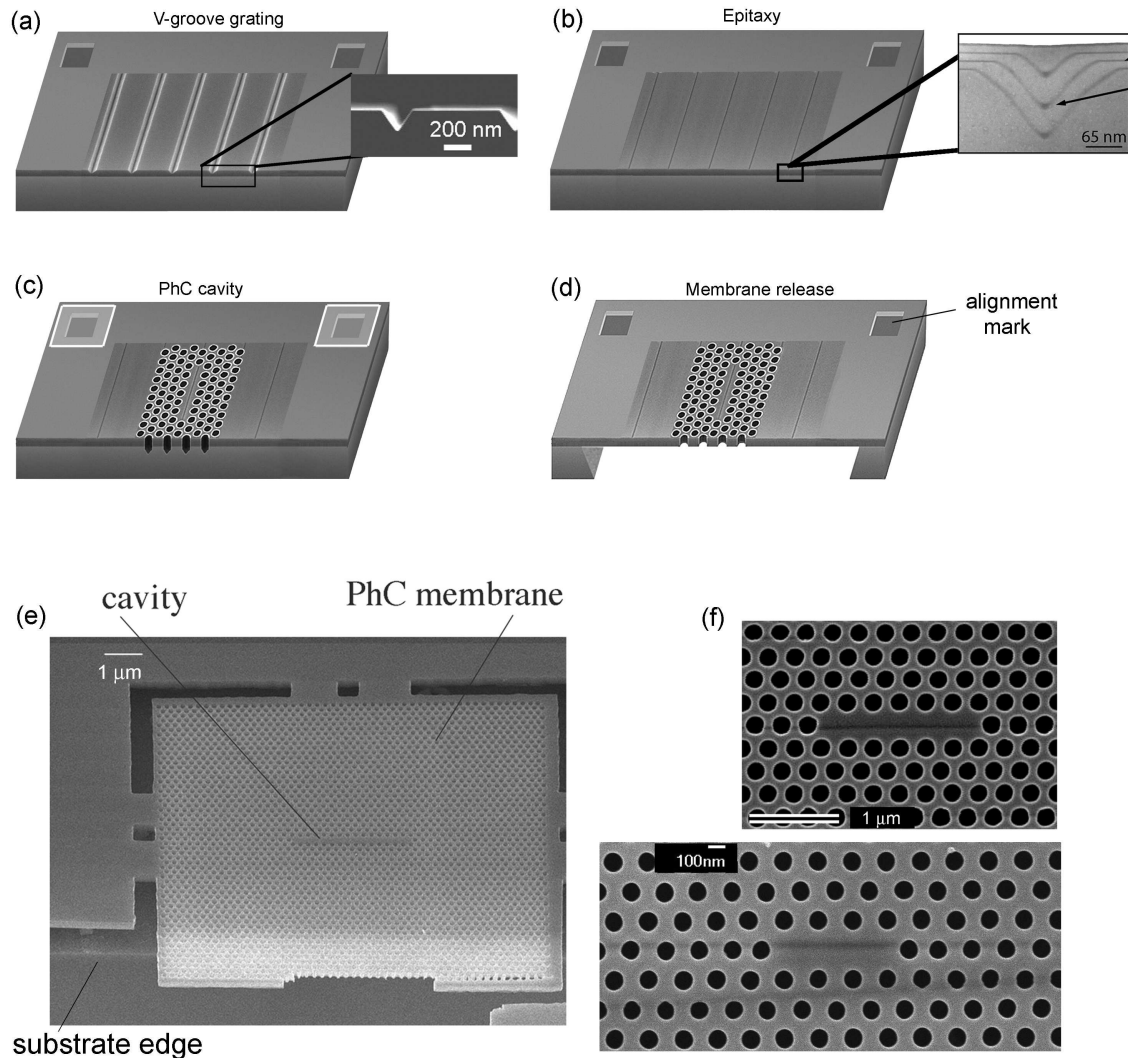


**Figure 3.1:** Technology of site-controlled quantum wires embedded in a photonic-crystal microcavity. Schematics of the fabrication process: (a) V-groove grating is written and etched on the membrane sample, simultaneously, alignment marks are produced; (b) sample is overgrown by MOVPE resulting in the embedded QWRs (see TEM image in the blow-up); (c) grounding on the alignment pattern, PhC structures are positioned at defined locations incorporating a single QWR or a single QWR stack, the holes are drilled by directional plasma etching; (d) the membrane is released by selective wet etching. (e) Oblique SEM view on a released membrane hanging freely over the GaAs substrate. (f) SEM top views of PhC cavities. Note the trace of the residual V-groove that in these cases served to assess the alignment accuracy.

define a probability of detachment of the exposed molecules from the unexposed ones within narrow pattern elements. One of the most common resists is PMMA, and implementing it, features down to  $\sim 5nm$  have been demonstrated [137]. Dimensions down to  $\sim 60 \div 70 nm$  can be reproducibly obtained using commercial PMMA, standard development and conventional SEMs. In this work  $40keV$  JEOL JSM 6400 equipped with the NPGS (v.9) software and writing controller was used. PMMA with a molecular weight of 950000 4% diluted in Anisol was employed for all the writing tasks, spin-coated thicknesses being  $\sim 150nm$  and  $\sim 330nm$  for V-groove and PhC patterns, respectively.

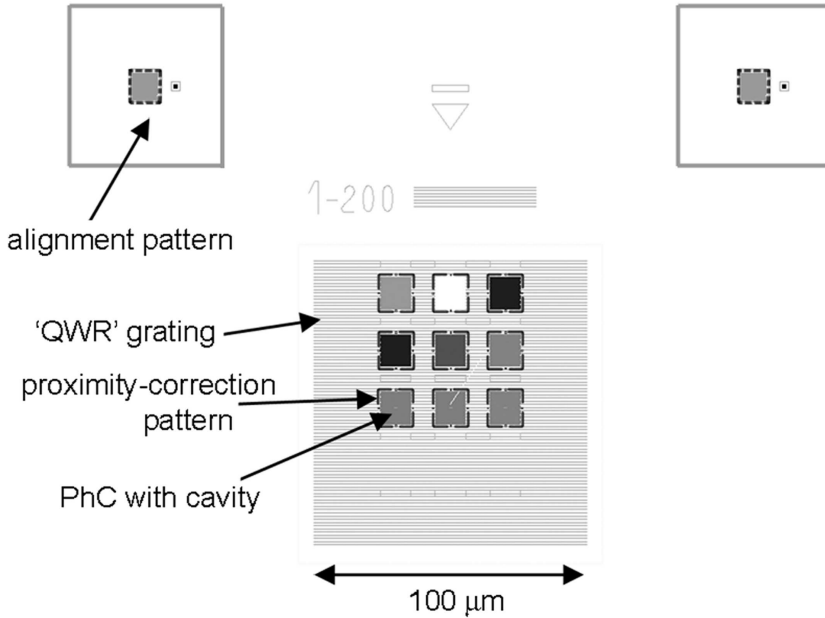


**Figure 3.2:** Design and alignment patterns implemented in the  $e$ -beam lithography step.

Both V-grooves and PhC patterns are written by  $e$ -beam lithography, which allows for performing a high-precision alignment. The general design pattern is shown in Fig. 3.2 (a) and consists of a  $100 \times 100 \mu m^2$  line grating regions with several overlaid PhC patterns each containing a single cavity, plus an alignment pattern aside and proximity-correction structures for the PhCs. The pitch of the grating is  $1 \mu m$ . This is much larger than the lattice constant of the PhC, therefore effectively, the cavity may contain only one QWR. The overall writing field is  $\sim 300 \times 300 \mu m^2$  large and the actually written one is  $\lesssim 100 \times 100 \mu m^2$  in area. The latter is dictated by the astigmatism effect that arises due to the focal-plane curvature when the beam is scanned from one extremity of the field to the opposite side. The grating and the alignment pattern are written first, and the second writing step defines the PhC structures later on, after the MOVPE QWR growth.

### 3.1.2.1 V-groove template

For the line pattern exposure, doses<sup>2</sup> of  $\simeq 3nC/cm$  are sufficient to produce  $\simeq 105nm$  wide lines. These lines are written along the  $[01\bar{1}]$  crystallographic direction, and a subsequent anisotropic etching results in V-groove template with  $\{111\}$ A-oriented sidewalls for the QWR growth. In this work the etching was done directly through the PMMA mask.  $Br : HBr : H_2O$  solution was used, which allows for a good sharpness of the V-grooves<sup>3</sup>. The V-grooves are defined within a  $200nm$  thick  $GaAs$  layer positioned on top of an  $Al_{0.75}Ga_{0.25}As$  layer. The groove depth should therefore be limited to within the  $GaAs$  layer<sup>4</sup>. Etching during  $1 \div 2s$  results in a V-groove depth of  $150 \div 190nm$ , which was used in the experiments reported here (Fig. 3.3). The  $Br$ -based etching in aqueous solution involves mask undercutting, which is useful in rounding off imperfections and which finally defines the V-groove dimensions.

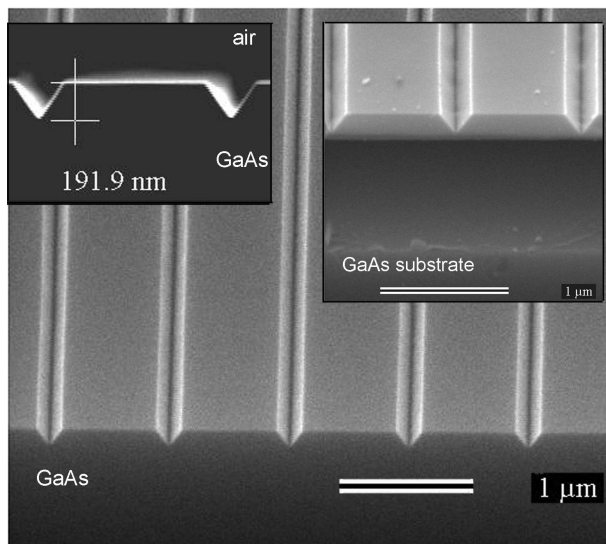


**Figure 3.3:** V-groove templates on membrane  $GaAs/AlGaAs$  samples (main, inset to right – SEM oblique views; inset to left – cross-sectional SEM view). For better illustration, in the inset to the right the  $AlGaAs$  was on purpose selectively etched, so the V-grooves are shown in a free-hanging membrane.

### 3.1.3 Metal-organic vapor-phase epitaxy – InGaAs/GaAs V-groove QWR growth

#### 3.1.3.1 Principles

One of the most efficient ways of quantum-wire fabrication is established using the metal-organic vapor phase epitaxy (MOVPE<sup>5</sup>) on V-grooved non-planar substrates

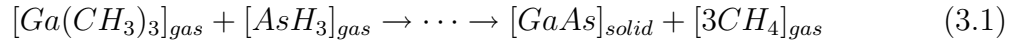
<sup>2</sup>If the scanning grid consists of a single line, the line dose in  $C/cm$  can be defined instead of a standard area dose (in  $C/cm^2$ ), similarly, point doses are defined in  $C$  for single-point exposures.

<sup>3</sup>Secondly, it was adapted from our earlier submicron-pitch V-groove grating design where it allows for preventing a pattern breakdown in case neighbor grooves merge due to a writing defect, which is important in application to DFB-laser gratings.

<sup>4</sup>MOVPE growth is not possible on  $AlGaAs$  substrates due their excessive oxidation.

<sup>5</sup>Sometimes also called MOCVD – metal-organic chemical vapor deposition. We prefer the other name because it refers to the term *epitaxy* – the inherent essence of the ordered *monocrystalline* formation.

[138]. The MOVPE principle is schematized in the Fig. 3.4. Unlike molecular-beam epitaxy where atomic species are directly projected onto the sample surface, in the MOVPE technique the elements are brought to the substrate by organic *precursors*. The substrate is heated ( $\sim 500 \div 800^\circ\text{C}$ ), which allows for the metal-organic species to decompose into a volatile part and an *adatom*. The adatoms on the surface follow the *chemical potential*, which eventually defines where they incorporate into a crystal. Basically, the chemical potential is lower in kinks, dips and monolayer steps because of the higher density of dangling bonds. A qualitative chemical reaction, for example, of a process of formation of GaAs crystal in MOVPE is usually written as:



where the dots stand for a number of complex formation mechanisms [139] that are still not completely understood. As the processes during the growth, namely, precursor

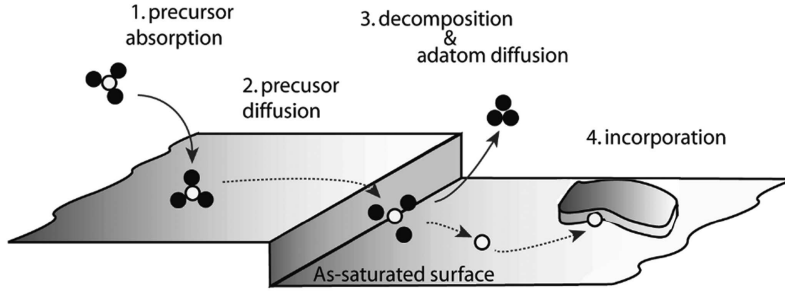


**Figure 3.4:** Illustration of the reaction kinetics and mass transport occurring during MOVPE growth.

decomposition and adatom diffusion are thermally activated, they therefore depend strongly on the *temperature*. The precursors are delivered by a carrier gas, and thus the growth depends largely on the chamber *pressure*. A third important parameter is the relative partial pressure between the precursors bearing the group-V and group-III elements, the so-called *V/III ratio*. It is common to use a large V/III ratio such that the substrate surface is always saturated with *As* providing therefore free bonds to link *Ga* or *In*. Thus, the growth dynamics will mainly depend on the kinetics of the group-III elements. This is very important because it influences the resulting impurity level [140,141]. In the growth involving trimethyl-components  $(\text{CH}_3)_3$  the main residual impurity in the chamber is carbon, and with high V/III ratio, as the number of *As*-vacancies is reduced, the *C* incorporation is less likely.

On *non-planar* substrates the topography of chemical bonds exposed on the surface changes with facet orientation [142], which can lead to higher growth rate in a high-index crystal direction. In the *V-groove* pattern, between the (100) and  $\{111\}$ A facets the growth establishes a new side-wall orientation (e.g.  $\{311\}$ A). The development of this new facet leads to the consumption of the (100) bottom facet, which results in a sharpening of the V-groove. By such a *growth-rate anisotropy*, a *self-limited* profile is established [134,143] (Fig. 3.5). This profile depends on growth conditions. Sharper *GaAs* profiles can be obtained at lower substrate temperatures [134]. This side-wall evolution is accompanied by the effect of *capillarity* that gives the adatoms a preferential diffusion direction towards the bottom of the V-groove. The capillarity acts to

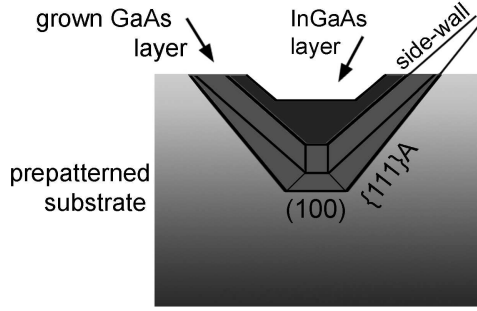


**Figure 3.5:** Simplified schematics of the evolution of the side-wall facet during the MOVPE growth, resulting in self-limited profile. This profile depends on the material composition, hence this can be exploited to form crescent-shape QWRs.

partially compensate the effect of the growth-rate anisotropy. At a steady state, the two effects balance, which finally determines the self-limited profile. The profile depends also on the alloy composition which, in turn, is defined by the group-III adatom diffusion length. At temperatures  $\sim 550^\circ$ , the *In* diffusion length is larger than that of *GaAs* [134]. Therefore for *In*, the self-limited V-groove will have a wider profile at the bottom. Thus a growth of an *InGaAs* content in the *GaAs* template will result in a formation of a thickened *crescent-shape* QWR. Additionally, due to larger diffusion, the *In* will segregate preferentially at the bottom of the V-groove leading to yet increased carrier confinement effect in the QWR. This however is partially compensated by the thermodynamic *entropy of mixing* of the forming alloy [139], which tends to equalize the *In-to-Ga* gradient. Therefore, the QWR morphology is determined by the interplay between the growth-rate anisotropy, capillarity and entropy of mixing [144]. After a formation of an *InGaAs* QWR the deposited material can be changed back to *GaAs*, which will reestablish the self-limited profile of the V-groove template. This opens a way of vertically *stacking identical QWRs*.

### 3.1.3.2 Growth study

In this work the QWR growth was performed on a relatively *shallow* V-grooves in a *sparse* grating ( $1\mu\text{m}$ -pitch). The growth conditions were initially based on previous studies of *InGaAs/GaAs* QWRs [134,145]. We used the growth temperature of  $590^\circ\text{C}$ <sup>6</sup>, V/III ratio of 250, *TMGa*, *TMIn*, *AsH<sub>3</sub>* precursors, *N<sub>2</sub>* carrier gas, chamber pressure as low as  $\sim 20\text{mbar}$ . However, since the geometry (groove depth, grating pitch) in our case is different, we performed growth studies to track the growth evolution and optimize the growth rates. Fig. 3.6 presents results of a growth study performed on a  $250\text{nm}$  deep grating using *Al<sub>0.5</sub>Ga<sub>0.5</sub>As* thin ( $3\text{nm}$ <sup>7</sup>) markers inserted in between  $15\text{nm}$  *GaAs* spacers and  $5\text{nm}$  *GaAs* buffer before the first marker. The study is done using AFM cross-sectional imaging, where the *AlGaAs* markers are clearly seen in a height contrast to due to the much more efficient *AlGaAs* oxidation compared to *GaAs* [146].

<sup>6</sup>In our MOVPE reactor the substrate is placed on a susceptor. The temperature of the susceptor is measured by a thermocouple. The substrate temperature is estimated to be  $\simeq 40^\circ\text{C}$  lower. We refer to that measured by the thermocouple, whereas in literature corrected values are presented.

<sup>7</sup>From now on *nominal* thicknesses are given. That is, when measured on a planar substrate. Note that the thicknesses along the growth direction within the V-groove can be much larger, which depends on growth conditions and instantaneous V-groove geometry during the growth.

From this evolution we can deduce several important parameters for the  $InGaAs$  QWR growth: an appropriate initial buffer-layer thickness determined by the establishment of the self-limited profile, and groove planarization thickness. These two parameters define room for embedding QWRs. Therefore for  $\simeq 160 \div 190nm$  deep V-grooves, the buffer should be at least  $\simeq 15 \div 20nm$ , 3  $\div$  5 QWRs can be stacked and the overall grown thickness is  $\simeq 65nm$  to ensure the planarization.

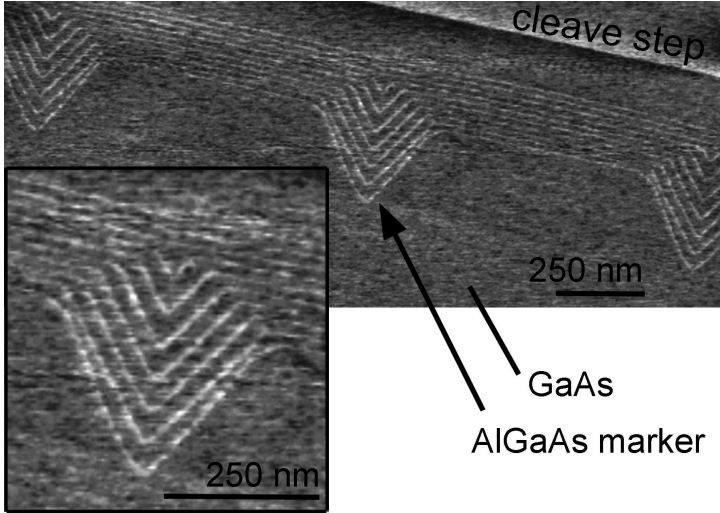


**Figure 3.6:** Growth study of a shallow-groove  $1\mu m$ -pitch profile evolution. AFM image of the cleaved  $(01\bar{1})$  surface. The height of the  $Al_{0.5}Ga_{0.5}As$  markers (bright) is  $\simeq 0.15 \div 0.2nm$ .

### 3.1.3.3 $InGaAs/GaAs$ QWRs and optical properties

$InGaAs/GaAs$  (15%  $In$ -content, nominally) QWRs with nominal thicknesses of  $5nm$  and  $\sim 3nm$  were grown in order to obtain the QWR emission at  $\lambda \simeq 930$  and  $\lambda \simeq 890nm$  respectively. The buffer thickness was  $16nm$  for the triple-QWR samples and  $31nm$  for single QWRs. In the case of triple-QWR samples the inter-wire buffers were  $11nm$ . Fig.

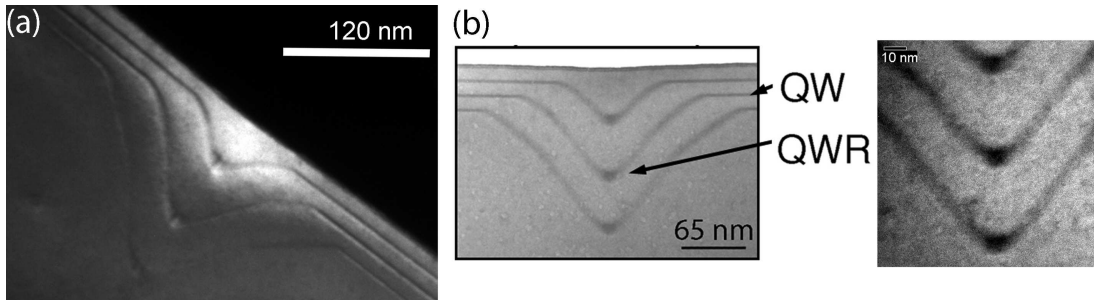


**Figure 3.7:** TEM images of 3 stacked,  $3nm$ -thick  $In_{0.15}Ga_{0.85}As/GaAs$  QWRs grown in a  $190nm$ -deep V-grooves. (a) Dark-field image, (b) Bright-field images. Note the influence of strain on the dark-field contrast in the center of each QWR, suggesting  $\sim 10\%$  higher  $In$  content which acts to enhance the QWR quantum confinement.

3.7 presents transmission-electron microscopy (TEM) (dark- and bright-field) cross-sectional images of  $In_{0.15}Ga_{0.85}As/GaAs$  triple-QWR samples grown on a  $190nm$  deep

grating. We see that since the buffer and the barriers were sufficiently thick, the QWRs are grown within the self-limited *GaAs* profile and that they look identical. Secondly, from the dark-field image we note the influence of *strain*<sup>8</sup> on the dark-field contrast, which indicates larger *In* content at the V-groove bottom within the QWR. The *In* content in the QWR is larger than that of the QW due to *In* segregation towards the bottom of the groove, and the difference can be  $\sim 10\%$  [147]<sup>9</sup>. The effect of strain is important, since it acts to increase the lateral quantum confinement in QWRs [147,148].

The optical quality of the grown QWRs was then checked by means of low-temperature (10K-50K) micro-photoluminescence. Representative normalized spectra of a single- and triple-QWR samples are compared in Fig. 3.8. We first note three important observations related to the single QWRs [Fig. 3.8 (a)]. (i) The full spectrum consists of emission of three parties: *GaAs*, *InGaAs* QWs that grow on planar parts of the V-groove and *InGaAs* QWRs. The QWR emission is recognized at a longer wavelength compared to the QW due to QWR larger thickness. (ii) At high temperature (50K) the QWR

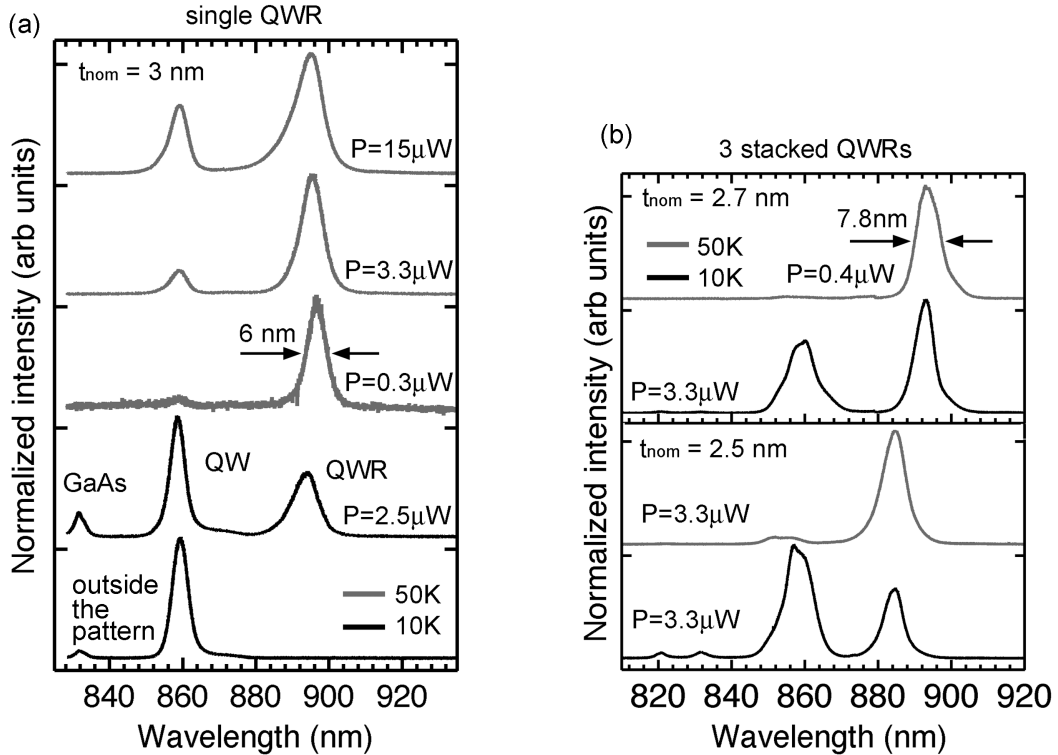


**Figure 3.8:** Micro-PL spectra (10-50K) of (a) single- and (b) triple-QWR  $In_{0.15}Ga_{0.85}As/GaAs$  quantum wires. Nominal QWR thickness ( $t_{nom}$ ) and temperature are indicated. Pump conditions:  $Ar^+$  laser ( $\lambda = 514&488nm$ ), CW, power ( $P$ ) as indicated. Spot size  $\sim 3\mu m$  ( $20\times$  objective lens).

emission dominates due to carrier feeding from the connected QWs [148]. (iii) At high excitation powers band filling effects start occurring, which is manifested by the change

<sup>8</sup>Triaxial strain appears due to a small lattice mismatch between *GaAs* and *InGaAs* alloys.

<sup>9</sup>Estimated by means of electron energy loss spectroscopy (EELS).

in the short-wavelength slope of the QWR emission and build-up of the QW peak (see power dependency in 50K section). Secondly, from the comparison to the triple-QWR structures we note two important things [Fig. 3.8 (b)]. (j) The QWR emission intensity is always larger than that of the QW within the same spectrum, which points to an add-up of the luminescence of the three wires. (jj) There is a single QWR peak in the spectrum, meaning that the spectral matching of the QWRs is good, hence they are practically identical and electronically uncoupled. On average, the full width at half maximum is however slightly larger than that of the single QWR (at 10K:  $\sim 5 \div 6.5nm$  for triple-QWR vs  $\sim 4.5 \div 7nm$  for single QWR; at 50K:  $\sim 7 \div 8nm$  for triple-QWR vs  $\sim 6 \div 7nm$  for single QWR), meaning that, although the matching is reasonably good, it is not perfectly ideal.

### 3.1.4 *e*-beam writing of PhC with alignment, and proximity-effect corrections

After the MOVPE regrowth, the definition of the PhC pattern is performed. The *e*-beam writing is done in the point-exposure mode (i.e., there is only one point exposed for each PhC hole) with doses of the order of  $20 \div 30fC$ , which, depending on the lattice constant, results in circular<sup>10</sup> exposed areas of  $\sim 100 \div 110nm$  in diameter (for  $a = 200 \div 220nm$  respectively). In order to position the PhC cavities around a given QWR, the alignment pattern is employed, and the procedure is done in the following way. Prior to writing the PhC patterns, small-area windows are scanned for the marks

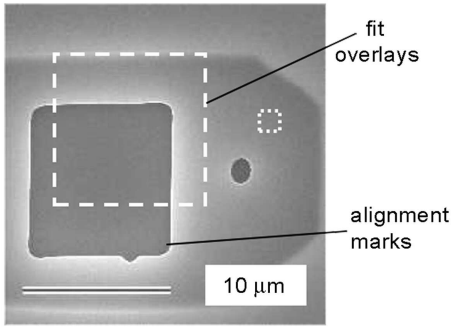


**Figure 3.9:** SEM top-view image showing etched alignment marks in a regrown membrane (note the undercut darker region). Alignment procedure: two sets of alignment marks are exposed, their coordinates are compared to those of the overlays in the design allowing for a coarse and fine correction.

etched into the surface, then compared to the corresponding overlays [Fig. 3.2 (b)], which yields the coordinate transformation matrix and the offset:

$$\begin{bmatrix} x' \\ y' \end{bmatrix} = \begin{bmatrix} A & B \\ C & D \end{bmatrix} \begin{bmatrix} x \\ y \end{bmatrix} + \begin{bmatrix} x_{offset} \\ y_{offset} \end{bmatrix} \quad (3.2)$$

All the coordinates in the PhC pattern are then corrected, and the pattern is written according to the design where several selected QWRs are aligned with the PhC cavities. The alignment accuracy then depends on the etching uniformity (since only the centers of the marks matter if the alignment is done manually). Positioning accuracies of  $\sim 40nm$  were achieved [149].

<sup>10</sup>In order to ensure the roundness, special attention for the SEM coil settling times must be drawn if the beam blander is leaky to avoid parasitic side exposures during relatively long dwells.

### 3.1.4.1 Proximity effects

As the PhC patterns are very dense and the  $e$ -beam acceleration voltage is moderate ( $40\text{keV}$ ), proximity exposure effects can take place on a scale comparable to the pattern size ( $\sim 10\mu\text{m}$ ). The proximity effects arise mainly due to electrons backscattered from within the substrate [150] inadvertently exposing the resist [see Fig. 3.10 (a)]. As a consequence of such an additional exposure, PhC holes in the pattern center can be appreciably larger than those at the periphery, which has been shown [151] to lead to multiple defect states within the PhC bandgap masking the cavity modes.

Two methods were employed to counteract this effect. First, the PhCs were surrounded with a correction pattern adopted from the design in ref. [151]. The dose in the correction pattern is chosen (high enough) such that the proximity exposure effect around this area is comparable to that induced within the PhC pattern center. Therefore the exposure is equalized for all the PhC holes. Secondly, complementary to the correction, smaller diameters for the PhC holes can be written (e.g. with  $r/a \lesssim 0.2$ ), which leads to a much less pronounced proximity effect, since it depends on the exposure time. As the PhC technology involves a  $\text{SiO}_2$  mask and the  $\text{PMMA} \rightarrow \text{SiO}_2$  pattern transfer by the reactive ion etching, the diameters can be further corrected in the  $\text{SiO}_2$  by wet isotropic etching<sup>11</sup>. This etching can additionally act to round slightly the holes in the  $\text{SiO}_2$  mask that can be otherwise rough after the reactive ion etching. Fig. 3.10 (b) gives an illustrative example of a PhC pattern (in the  $\text{SiO}_2$  mask) with the proximity-effect correction.

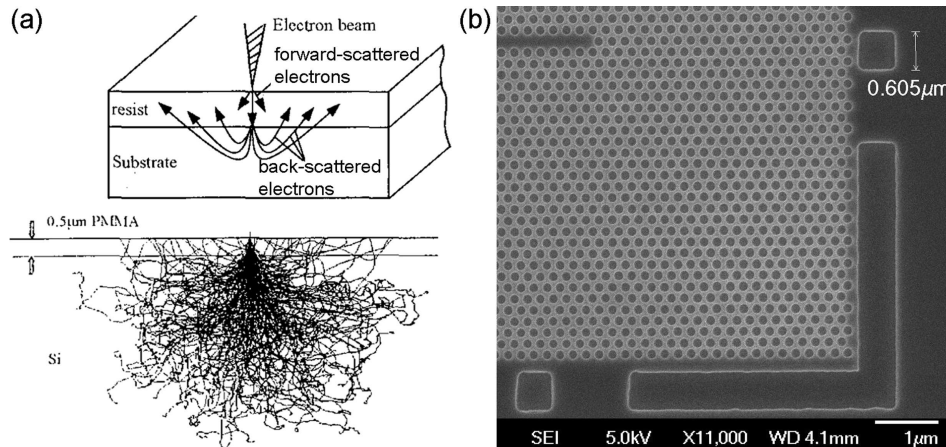


**Figure 3.10:** (a) Proximity effect in electron-beam lithography, lower panel showing electron trajectories simulated by the Monte-Carlo method (from [150]). (b) PhC pattern with the proximity-effect correction illustrating a regularity of hole diameters (in  $\text{SiO}_2$  mask).

<sup>11</sup>E.g. with  $BHF : \text{H}_2\text{O}$ -based solution at known etch rate of  $2\text{nm/s}$ .

### 3.1.5 Plasma etching

In a two-dimensional PhC-cavity, the photon confinement at a particular frequency is assured by the in-plane periodic structure of the dielectric constant perfectly replicated along the out-of-plane direction. Therefore, being of crucial importance, the patterning technique must ensure highly anisotropic material removal with low damage of surfaces and interfaces. In the sphere of semiconductor materials processing, plasma etching has become an established primary tool (compared to direct methods involving e.g. focused ion beam or a pulsed laser) for removal of material allowing for highly reproducible patterns with smooth surface morphologies, anisotropic profiles and high mask/substrate selectivity.

#### 3.1.5.1 Reactive ion etching (RIE)

Standard RIE technology implements radio-frequency (RF) driven discharges in a planar asymmetric<sup>12</sup> configuration known as RF-diodes [152], as shown schematically in Fig. 3.11. The system consists of a vacuum chamber containing two planar electrodes. A high AC voltage applied to the electrode leads to an electrical breakdown in the gas mixture flown through the chamber, which results in plasma formation. The effluent gases bearing the products of the etching reaction are removed by means of a turbomolecular vacuum pump controlled by a butterfly valve to maintain a desired chamber pressure. Typical pressures are not less than  $5 \div 10 mTorr$ , given by the fractional-ionization levels in the plasma (as low as  $10^{-6} \div 10^{-3}$ ) and the discharge stability. The driving AC frequency must be high (typically  $13.56 MHz$ ). This is crucially important for the *plasma self-biasing* near the electrodes, which is the basis of the *ion energy* (sheath voltage<sup>13</sup>). Being light enough to respond to the instantaneous electric field, the mobile cloud of plasma electrons oscillates back and forth within the positively charged bulk, whereas the much heavier ions and radicals cannot follow such frequency. Therefore, averaged over an oscillation period, positively charged sheath regions are created in the close proximity of the electrodes. Due to a time-averaged excess of the positive charge, a strong electric field is created within each sheath *directing* from the plasma to the electrodes. The ions and radicals drifting towards an electrode get therefore accelerated by the sheath field. Note that electron leak from the plasma is prevented by the same fields. Thus, the reactive species are brought to the sample surface where they produce efficient etching by physical bombardment and chemical reactions.

Implemented in our work, the RIE technology served the purposes of the *PMMA* →

<sup>12</sup>One electrode is grounded and the other one is driven.

<sup>13</sup>In the asymmetric configuration with the help of the blocking capacitor, a negative DC bias voltage  $V_{bias} = -(\langle V_A \rangle - \langle V_B \rangle)$  is set up at the driven electrode, which is easily measurable. It is given by the sheath voltages  $V_a$  and  $V_b$  and is related directly to the ion energy if measured properly (considering electrode contamination that insulates the plasma-electrode connection). Accelerating voltages (and thus ion kinetic energies) as high as  $V_{RF}$  can be reached in the asymmetric systems. The source (normally,  $50\Omega$ ) has to be well impedance-matched to plasma discharge (e.g., by a three-element network with a fixed inductor and two tunable shunt capacitors).

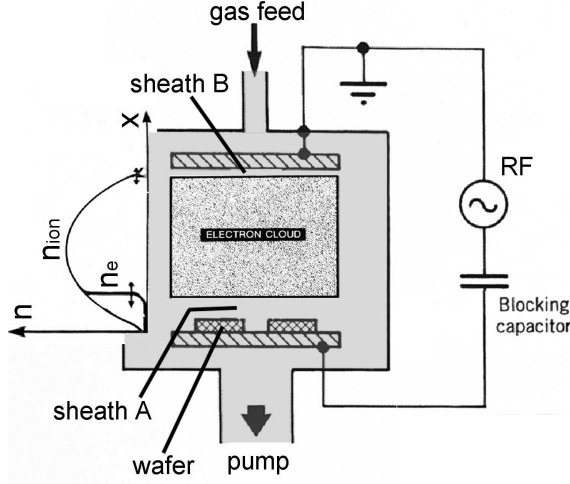


**Figure 3.11:** Principle of the RIE technology. Ion acceleration due to sheath voltage formation via oscillating plasma electron cloud is illustrated in planar asymmetric RF diode.  $n_{ion}$ ,  $n_e$  - ion and electron concentrations, respectively, across the chamber space. (Adapted from [152]).

$SiO_2$  pattern transfer<sup>14</sup> and PhC holes drilling<sup>15</sup> using the fluorine and chlorine gas chemistries respectively, which we will discuss below.

### 3.1.5.2 $SiO_2$ mask

The  $SiO_2$  mask<sup>16</sup> serves as a *rigid* mask for the RIE etching of  $GaAs$ . Since this is the final mask whose features will be reproduced in the real device, the pattern transfer (from  $PMMA$ ) is quite important in the whole PhC technology.

The etching of  $SiO_x$  dielectrics is usually done by means of fluorocarbon- and fluorine-based plasmas such as  $CF_4$ ,  $CHF_3$ ,  $SF_6$  with addition of either  $H_2$ ,  $Ar$  or  $O_2$ .  $F$  atoms and  $CF_x$  radicals, etching chemically the  $SiO_2$ , are known to produce only insignificantly low etch rates. Thus the etching relies mainly on the energetic-ion enhanced processes and sputtering mechanism, which implies high RF powers. Therefore the working recipe must be a compromise between a sufficient etch rate and an acceptable  $SiO_2$ -to- $PMMA$  etching selectivity. This can, in principle, be achieved by working at reasonably low chamber pressures and low RF powers [153]. We established the process in the following way: 7s short post-development  $PMMA$  cleaning with a 50sccm 50W  $O_2$  plasma at 10mTorr, followed immediately (in the process chamber) by the  $CHF_3/Ar$  etching<sup>17</sup>. Smooth profile was obtained (Fig. 3.12) with an acceptable verticality of the PhC holes. The etch rate is relatively slow ( $\simeq 11.6nm/min$ ), which is acceptable in view of, first, a good quality of the residual  $PMMA$  (no cracks or molten parts) and, second, reasonable  $SiO_2/PMMA$  selectivity ( $\simeq 0.37$ ) sufficient for etching through up to 80nm of  $SiO_2$ <sup>18</sup>.

<sup>14</sup>Oxford Instruments, Plasmalab 80.

<sup>15</sup>Oxford Instruments, RIE 90.

<sup>16</sup>Deposited on  $GaAs$  by plasma-enhanced chemical vapor deposition.

<sup>17</sup>At the flow of 25/25sccm, RF power 80W, chamber pressure 10mTorr on a 16°C water-cooled bottom-electrode quartz cover plate; etch time 5'20" (Fig. 3.12).

<sup>18</sup>Such deep masks were used further in the ICP etching of  $GaAs$ , whereas 30nm masks were used in standard RIE.

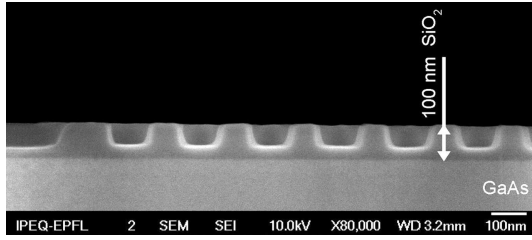


**Figure 3.12:** RIE-etched PhC mask in 100-nm  $\text{SiO}_2$  deposited on  $\text{GaAs}$ . (Cross-sectional SEM image.)

### 3.1.5.3 RIE of $\text{GaAs}/\text{AlGaAs}$

In RIE of III-V semiconductors, *chlorine*-based gas mixtures are well-established [154] standard means that provide fast rates of material removal by *chemical* etch. Though a pure chemical etching is isotropic, by combining it with ion bombardment the anisotropy is achieved. E.g.  $\text{Cl}_2$ ,  $\text{SiCl}_4$ ,  $\text{BCl}_3$ ,  $\text{PCl}_3$  or chlorinated halocarbons may be employed for  $\text{GaAs}/\text{AlGaAs}$  [155]. This is due to their ability to yield highly volatile products of reaction (e.g.  $\text{GaCl}_3$ ), and hence high etch rates. However, admission of pure  $\text{Cl}_2$  to the reactor is not favorable due to its high reactivity (chamber corrosion e.g. via  $\text{HCl}$  due to water residues). Admixtures of  $\text{Ar}$  or  $\text{O}_2$  may serve for dilution of chlorine-based reactive species in the plasma and a certain sidewall passivation, respectively. For PhC

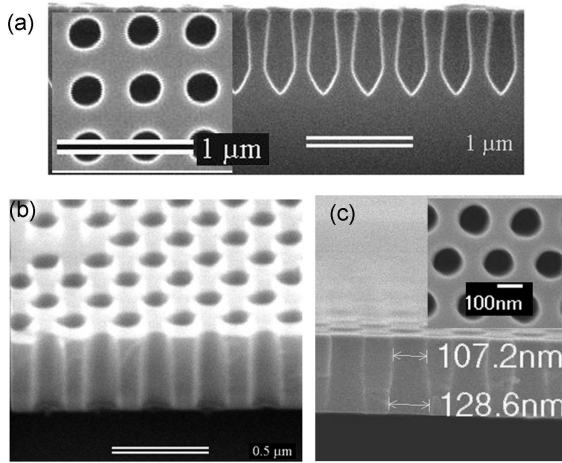


**Figure 3.13:**  $\text{SiCl}_4$ -based RIE of bulk  $\text{GaAs}$  (a) and  $\text{GaAs}/\text{AlGaAs}$  membrane (b,c) samples. The profile quality (mainly, in terms of verticality) is reasonable (b), although large deviations may sometimes occur (due to  $\text{SiO}_2$  mask), seen in membrane cross-section (c), which is difficult to correct using the RIE technique.

sample fabrication, we have adopted the  $\text{SiCl}_4/\text{Cl}_2/\text{Ar}$  recipe<sup>19</sup>.  $\text{GaAs}/\text{SiO}_2$  selectivity is more than 10 (and yet larger for  $\text{AlGaAs}$ ), so relatively thin (30 ÷ 40 nm)  $\text{SiO}_2$  layers could be used. In order to get an acceptable hole verticality, the mask has to have perfectly straight sidewalls of the holes. Typical etch profiles in bulk  $\text{GaAs}$  samples and on (already released) membranes<sup>20</sup> are shown in the Fig. 3.13. Since the RIE technique inherently is not very flexible (e.g., as compared to ICP), this sets quite a stringent parameter window. For example, deviations in  $\text{SiO}_2$  mask fabrication can lead to worse

<sup>19</sup>Partial gas flows 20/3/3 sccm, 10 mTorr chamber pressure, 100 W RF power, measured DC bias  $\sim -250\text{V}$ . Etch time  $\sim 5\text{min}$  [Fig. 3.13 (a,b)], 4 min [Fig. 3.13 (c)].

<sup>20</sup>Note that the  $\text{GaAs}/\text{AlGaAs}$  interface is not a problem, since the etch rates for  $\text{GaAs}$  and  $\text{Al}_y\text{Ga}_{1-y}\text{As}$  are approximately the same because of comparable volatility of the etch products  $\text{GaCl}_x$  and  $\text{AlCl}_x$  (melting points 201°C and 190°C respectively) [156].

hole verticality [see Fig. 3.13 (c)], which quite severely affects the PhC optical response. Correction then is rather difficult and time-consuming to implement. Although some important results (sec. 4.3.1, chap. 6) were achieved using the RIE technology, as soon as the technique became available in our clean-rooms, we proceeded to establishing the *inductively-coupled plasma* RIE process. Using then the  $BCl_3/N_2$  chemistry the verticality problem can be solved owing to  $N_2$ -assisted passivation mechanisms.

### 3.1.5.4 Inductively-coupled plasma (ICP) etching

In high-ion-density dry etching techniques, such as electron cyclotron resonance and the ICP [152] RIE, the plasma ion energy may be significantly lowered without losing in the etch rate. Thus, the physical bombardment of sample and mask surfaces is reduced. As a result, control over selectivity and damage is achieved leading to very smooth surface morphologies.

The main peculiarity of the ICP is the *separate control* over the plasma formation (and its density) and the ion energy, which allows for high process flexibility. The plasma is formed within the ICP source and, independently, a separate RF generator biases the substrate electrode. This RF power then is used only for accelerating the plasma's charged species. The substrate RF powers (and therefore the induced bias) can thus be *an order of magnitude lower* than in a standard RIE RF diode without any loss in plasma stability. At the same time, high etch rates are ensured by the high ion and radical density ( $> 10^{11} cm^{-3}$ ) even at low chamber pressures ( $\sim 1 - 2 mTorr$ ). The low chamber pressures, in addition, allow for efficient etch products evacuation.

The term “inductively-coupled” means that the power is coupled into the plasma by means of electro-magnetic induction (see schematics<sup>21</sup> in Fig. 3.14). AC electric current in the coil creates a strong time-varying magnetic field in the center of the chamber that, in turn, induces a circular electric field concentric to the coil, which results in the high-density plasma formation. At low pressures the plasma from the ICP “head” drifts towards the substrate. To bring anisotropy, a separate RF generator is applied to the substrate, which results in plasma self-biasing and ion acceleration.

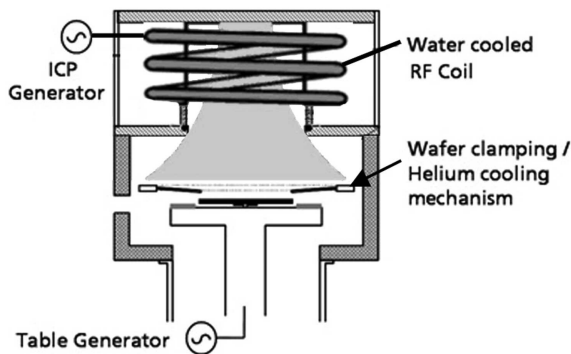


**Figure 3.14:** Schematics of a cylindrical ICP set-up (adapted from [157]).

<sup>21</sup>We used *SENTECH* Instruments GmbH PTSA ICP Plasma Etcher SI 500.

### 3.1.5.5 ICP of $GaAs/AlGaAs$ photonic crystals

$BCl_3$ -based mixtures for dry etching of  $Ga$ -based compound semiconductor materials is an attractive choice under high density plasma conditions [158] providing smooth mask-pattern transfer and anisotropy. In the  $BCl_3$ - or  $Cl_2$ -based chemistries of  $InP$  or  $GaAs$  materials the addition of nitrogen to the gas mixture allows for surface *passivation* [159–161]. No mask undercut takes place because the sidewalls of the etched holes are protected from direct ion bombardment and stay passive to  $Cl$ -based chemical etching, which results in highly anisotropic profiles with good verticality. This is exactly what is required for fabrication of PhC structures.

In the etching of photonic-crystal patterns very small openings are involved (diameter  $\sim 100 \div 150nm$ ), so the etch rates are not expected to be high, and the etching process can differ to a large extent from that of micron-size pattern elements. This may pose some limitations in the choice of the etching parameters. However, using the  $BCl_3/N_2$ -based recipe for our  $GaAs/AlGaAs$  PhCs, we found experimentally that the crucial ICP parameter is the gas-mixture composition, which is explained by the mechanism that involves  $N_2$ -driven surface *passivation*.

First, the ICP etching was tried using  $BCl_3/N_2$  15/5 sccm gas mixture having other parameters reasonably well set<sup>22</sup>. The result is shown in Fig. 3.15. As can be seen,

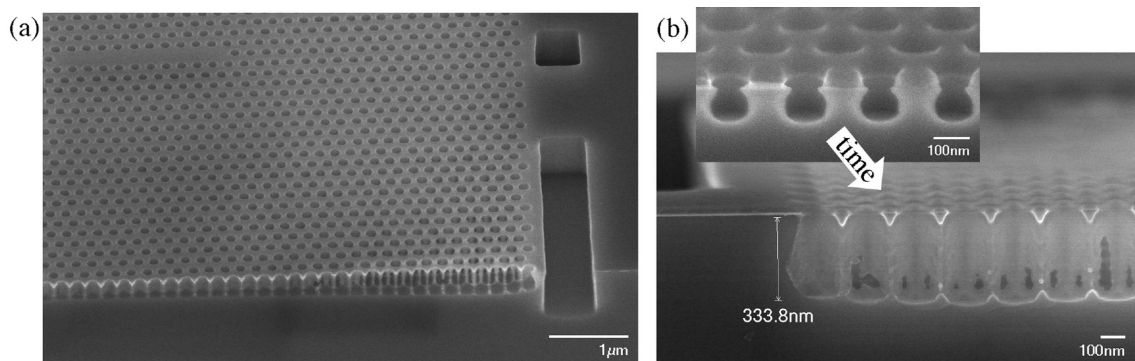


**Figure 3.15:** ICP process at  $BCl_3/N_2$  15/5 sccm without sufficient  $N_2$  passivation (SEM oblique views at different tilts of a cross-sectioned sample). (a) No damage is seen from the top; etch time 100 s. (b) Under the PhC mask the etching is rather isotropic resulting in bubble-like shapes (inset) and merging at sufficiently long etch times (main, 100 s).

the apparent isotropy in material removal results in a severe hole enlargement (bubble shapes) inside the material. Obviously, the PhC holes merge [Fig. 3.15(b)]. Note that at the same time somewhat 5-6 times larger openings ( $\sim 600nm$  wide) look reasonable in terms of side-wall verticality [Fig.3.15(a)]. In this situation, keeping the gas mixture the same, other plasma parameters were tried: lower pressure (0.75 mTorr), 3-fold higher RF substrate bias (60W), higher substrate temperature ( $40^\circ$ ). This however did not improve anyhow the etched profiles.

<sup>22</sup>Chamber pressure 1.5 mTorr, ICP source power 600W, RF power 20 W (giving the DC bias of  $\sim -20V$ ), electrode temperature  $30^\circ C$ .

On the contrary, the increase of  $N_2$  flow in the gas mixture up to 50-70% changed the etching results dramatically. The best hole anisotropy and side-wall verticality were obtained at 70% of  $N_2$  (i.e.  $BCl_3/N_2$  6/14sccm), as presented in Fig. 3.16, though at the expense of the etch rate. The latter doesn't pose a problem since the  $GaAs/SiO_2$  selectivity is high ( $\sim 10$ ), sufficient for managing a properly long etch. From these

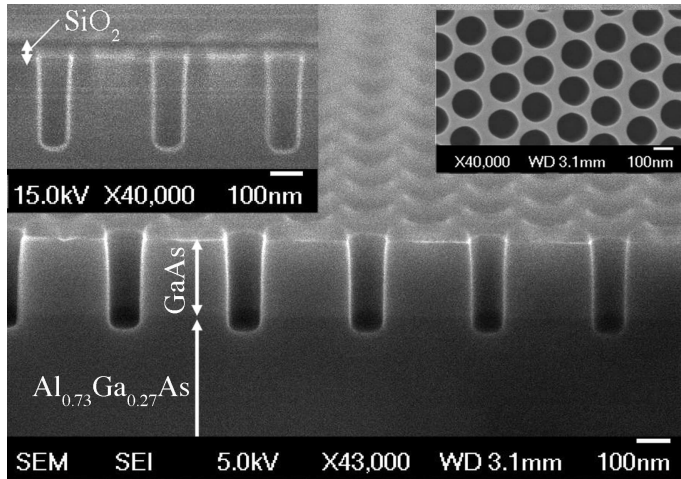


**Figure 3.16:**  $GaAs/AlGaAs$  ICP etching of PhC patterns with good sidewall passivation in the gas mixture  $BCl_3/N_2$  6/14sccm. (main)  $20^\circ$  tilted SEM view, (inset left)  $0^\circ$ -tilt cross-sectional view, (inset right) top view. Residual  $SiO_2$  mask was not removed. The etch time is 260s.

two experiments it becomes clear that in the case of Fig. 3.15 *insufficient side-wall passivation* results in the etching isotropy.

In order to explain the passivation mechanism, it has been suggested that in  $BCl_3/N_2$  etching of  $GaAs$ -based materials an  $N_2$ -driven polymer formation on sidewalls occurs in the presence of photoresist [160, 161]. During the etching, the polymer is essentially formed everywhere on the exposed  $GaAs$  surfaces. Yet on the very bottom of forming holes it is immediately removed via the directional physical bombardement by accelerated heavy  $BCl_3$ -based species. Therefore, whereas the *chemical* etching is efficient on the unveiled bottom, the polymer protects the sidewalls from reactive  $Cl$ -based etchants. However, since we use the  $SiO_2$  mask (cleaned in  $O_2$  plasma prior to the ICP process), no efficient polymer formation is expected. Nevertheless, in the plasma etching that involves nitrogen,  $Ga-N$  and  $As-N$  bonds may form [162]. At high  $N_2$  contents one may expect this to be efficient. The bond strength for  $GaN$  is 27% higher than that of  $GaAs$  [158]. Being not very significant at the bottom, this difference is important for the side-walls, where the impacting ions arrive tangentially to the side-wall surface. The side-walls passivated in such a way<sup>23</sup> stay therefore efficiently protected and the verticality of the profile is achieved.

Note that overpassivation should then result in a certain conicity of the openings. This was indeed confirmed at  $N_2$  contents  $\gtrsim 70\%$ . The overall chart presenting the etch rates and PhC hole profiles depending on the  $N_2$  content is shown in Fig. 3.17.

<sup>23</sup>Actually, in multi-user environment the conditions in the ICP-reactor chamber undergo some changes due to contamination/cleaning. This has been noticed to alter to some extent the trend shown in Fig. 3.17. The alternation is a shift along the  $N_2$  axis. The shift is however not dramatic, e.g.  $70\% \rightarrow 75\%$  ( $BCl_3/N_2$  flows 6/14 sccm to 5/15) if the chamber is very clean.

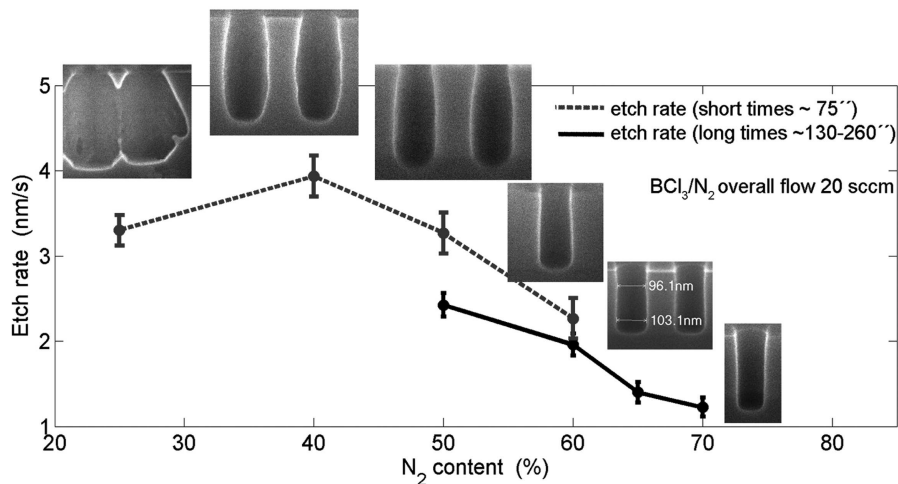


**Figure 3.17:** Etch rates (main) and side-wall verticality (insets, SEM cross-sectional views) for ICP etching of PhC structures in  $BCl_3/N_2$  plasma depending on the  $N_2$  content.  $N_2$ -driven side-wall passivation leads to good verticality, though at the expense of the etching rate. The error bars represent the inaccuracy in hole depth measurement from SEM images.

In Fig. 3.16, it may be noticed that the verticality of the holes changes along the profile. The diameter closer to the surface is larger by 8%. Taking into account the tendency presented in Fig. 3.17<sup>24</sup>, this problem arises due to the *overpassivation* during the initial etching stage. At later times, at a certain depth of the holes, the passivation is balanced and the profile maintains the desired verticality. The etching process of holes with very small diameters is complex and involves feedbacks. For instance, local variation in plasma composition is expected when the holes become deeper due to the change in product removal rate. This is experimentally supported e.g. by the change in the etch rates with increasing depth. Indeed, the measured overall etch rate is higher for shallower holes (see Fig. 3.17, rates measured at 50%  $N_2$  using short and long etch times).

However, these observations suggest that the verticality problem could be ultimately corrected by conducting the process in two steps, which was implemented as follows. First, a relatively short (20s) etching is done with the gas mixture at 50%  $N_2$ . Then, keeping the plasma on, the  $N_2$  content is increased to 70%. The result is shown in Fig. 3.18. We can see that the side-wall verticality in the “entrance” part of the holes gets reasonably well corrected. The profile is continuous because during the two-stage process the stability of the plasma is maintained and no abrupt transitions in the etching dynamics (gas mixture, chamber pressure and DC bias) are monitored [Fig. 3.18 (inset)].

<sup>24</sup>I.e. at lower  $N_2$  concentrations ( $\lesssim 50\%$ ) the initial-stage (closest to surface) hole profile is reversed (“negative” conicity).

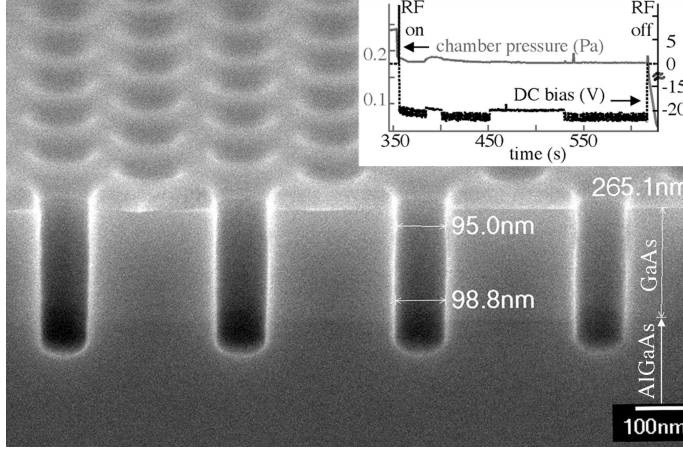


**Figure 3.18:** (Main) cross-sectional SEM view ( $20^\circ$  tilted) of PhC holes profile resulting from the two-stage  $BCl_3/N_2$  ICP etching (20s 50%  $N_2 \rightarrow 240s$  70%  $N_2$ , or by flow 10/10  $\rightarrow$  6/14sccm; chamber pressure 1.4 mTorr (0.185 Pa), ICP source 600W, RF power 20 W (bias  $\sim -20V$ ), electrode temperature  $30^\circ C$ ). Indicated GaAs thickness is corrected for the tilt. Residual  $SiO_2$  mask is still kept on top. (inset) Plasma stability verified by stable pressure and DC bias.

### 3.1.6 Membrane release and postprocessing (“digital etching”)

The final step in the sample fabrication process is the membrane release. In essence, it is simply a wet chemical etching highly selective between  $GaAs$  and  $AlGaAs$ , which acts to undercut the sacrificial  $AlGaAs$  layer ( $\simeq 4\% HF$  solution in water was found to be the best<sup>25</sup>), and is actually widely exploited for the PhC fabrication purposes. However, experimentally, we found that in such processing there exists an important *temperature sensitivity*. Etching in room-temperature ( $\simeq 22^\circ C$ ) solution results in the appearance of multiple membrane *cracks*, and frequently membranes complete break off, which reduces the fabrication yield to  $\lesssim 5 \div 10\%$ . This is usually explained by the water meniscus forces during drying procedure. However we found that if the etching is conducted at slightly elevated temperatures ( $\simeq 30 \div 40^\circ C$ ) absolutely no cracks appear after a standard ambient-temperature water rinse. The result is surprising and cannot be explained by the meniscus reasons. Nevertheless, the fabrication yield is 100% and no cracks are observed (even for excessive, e.g.,  $\sim 60 \times 60 \mu m^2$ , hanging areas).

Postprocessing targeted at improving air-GaAs interfaces in the PhC structures may include cavity-mode tuning and surface passivation strategies, the latter serving mainly for reducing non-radiative recombination. “Digital etching” [135] has been recently proposed as a method to slightly (by  $\simeq 1 \div 2nm$ ) tune (blueshift) a cavity-mode resonance by removing the native  $GaAs$  *oxide*. Importantly, it was simultaneously found that the removal of such an oxide also reduces cavity losses, so the cavity  $Q$  then goes up after first couple of etchings. For this reason we adopted the recipe [135] using a 1mol citric-acid solution<sup>26</sup>. The results consisted in the mode blueshift and improvements in the QWR-PhC device performance all the way up to the observation of lasing, having however important reoxidation implications, which will be discussed in the section 4.3.2.

<sup>25</sup>Buffered  $HF$ ,  $HCl$  were tried, the first found to have bad selectivity and poor etching, and the second resulting in a good undercut but surface contamination and etching of the  $InGaAs$  layer.

<sup>26</sup>I.e. 19.2g of  $C_6H_8O_7$  powder diluted in 100ml of  $H_2O$ ; the etch time is  $\sim 1min$ , self-limited process.

## 3.2 Characterization and analytical techniques

The characterization techniques employed in this thesis work target *structural* and *optical* properties. Correspondingly atomic-force microscopy (AFM), scanning and transmission electron microscopy (SEM, TEM) were used for the former purposes whereas micro-photoluminescence (micro-PL) and time-resolved micro-PL – for the latter ones. In the present section we will very briefly describe their schematics and principles, as well as give relevant data analysis procedures.

### 3.2.1 Atomic-force microscopy

Since the practical realization of the scanning probe microscopy [163], the AFM became a standard tool for measurements of the *surface topography* in solid-state physics, chemistry and bio-chemistry. Implemented in a non-contact (or semi-contact) mode [164] of operation, this technique allows for non-destructive mapping of specimen topography at atomic-scale resolution (see Fig. 3.19). In this technique, a sharp object (probe) placed on a cantilever is brought to the vicinity of the sample surface. The cantilever is driven to oscillate normally to the surface at its resonant frequency (e.g.  $\sim 300kHz$ ). When the sharp probe is nearby the surface, the resonant frequency is shifted which causes the amplitude damping at the measured frequency. This happens mainly due to long-range Van-der-Waals forces ( $\gtrsim 10nm$ ), of the probe-surface interaction [Fig. 3.19 (b)]. This damped amplitude is maintained constant by the feedback system. Therefore, if scanned across the surface, the surface roughness will be reflected in the feedback loop and can be used to reconstruct the topography (topography signal, feedback-error signal). The feedback system is implemented with a laser beam reflected from the cantilever on a *position-sensitive* four-section photodiode. The bending of the cantilever (and the corresponding change in the oscillation amplitude) due to the interaction of the probe (tip) with the surface induces the change in the relative signal on the photodiode parts, which is used to correct for the *set-point* amplitude by approaching/retracting the tip with a piezo.

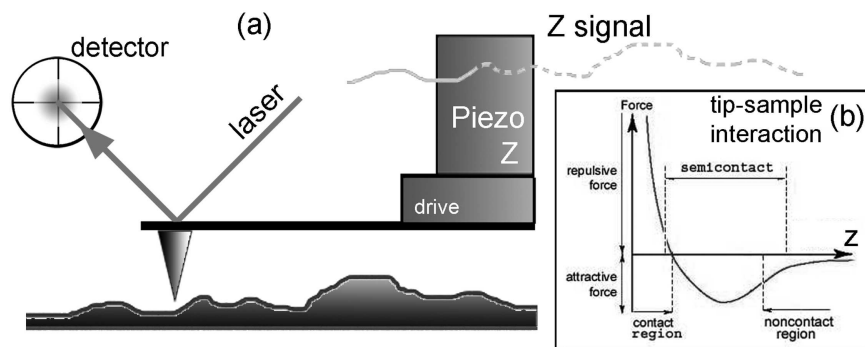


**Figure 3.19:** AFM principles (semi-contact mode). (a) Schematics. (b) Tip-sample interaction force indicating operating regimes.

### 3.2.2 Scanning and transmission electron microscopy

The diffraction limit in imaging optics<sup>27</sup> is essentially dependent on the wavelength of light ( $\lambda_{img}$ ) used for object illumination. Focussing of light is as well diffraction-limited<sup>28</sup>. Therefore, straightforwardly reducing  $\lambda_{img}$  can lead to higher resolution. These ideas are implemented in the electron microscopy. In the SEM technique a tightly focused [165] electron beam scans point-by-point sample's surface. At each point the interaction of a highly-accelerated electrons with matter gives rise to different phenomena (e.g. secondary electron emission, backscattering, Auger processes, X-rays; see Fig. 3.20) useful in inferring material and surface properties. Usually, the secondary elec-

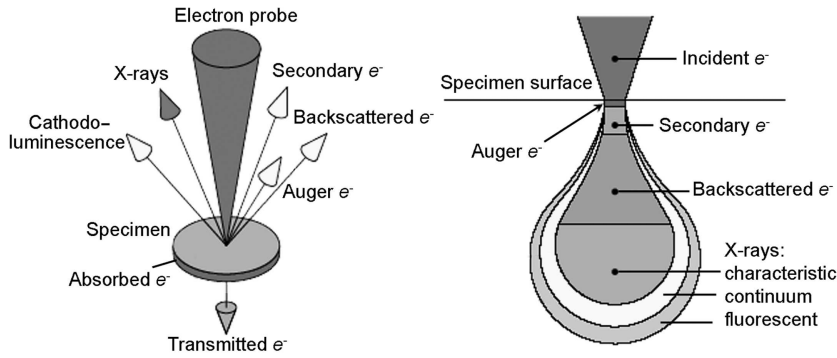


**Figure 3.20:** Variety of signals from beam-specimen interaction in the SEM. Secondary electrons, originating from within only a few  $nm$  below the sample surface, are normally preferred in the surface imaging for the best resolution (adapted from [166]).

trons, struck out by the scanning beam, are used for imaging. The amount of these electrons scattered from a given point towards the detector depends on the spatial orientation of the surface at this particular point with respect to the detector position. Therefore the surface topography is mimicked in the SEM image contrast<sup>29</sup>.

In the TEM technique [167] a highly-accelerated (e.g.  $\sim 200keV$ ) collimated electron beam passes through a thin ( $\sim 50nm$ )<sup>30</sup> specimen (Fig. 3.21). The interaction with matter is reflected in the transmitted beam imaged in the back-focal plane of a magnetic lens on a detector (e.g. CCD camera), where the contrast depends heavily on the sample substance. Therefore, a *chemical contrast* is achieved at the atomic spatial resolution. So-called bright-field and dark-field modes are used as two major methods for image contrast. If the direct transmitted beam is selected, areas where there is no sample are bright; conversely, if the diffracted beam is preferred, these areas are dark. The *InGaAs* layers embedded in the *GaAs* matrix look darker both in bright- and dark-field images. Normally for semiconductor heterostructures like *GaAs/AlGaAs* the dark field is preferred in terms of optimum contrast. If however *InGaAs* layers are present,

<sup>27</sup>Abbe resolution criterion  $\Delta x = 1.22 \frac{\lambda_{img}}{2NA}$

<sup>28</sup>Diameter of the focused spot  $d_0$  is given by  $\lambda_{img}$ , back focal length  $f'$  and the collimated-beam diameter  $d_b$ :  $d_0 = 2.44 \frac{\lambda_{img} f'}{d_b}$

<sup>29</sup>Two SEM models were used for imaging in this thesis: JEOL JSM-6400 and JEOL JSM-6701F with spatial resolution of  $\sim 10nm$  and  $\sim 2nm$  respectively.

<sup>30</sup>Which needs precise mechanical and ion-beam milling techniques for the sample preparation.

the strain contrast may superpose with the chemical contrast. In this work<sup>31</sup> mainly the bright-field images are used, as they show better, strain-free contrast.

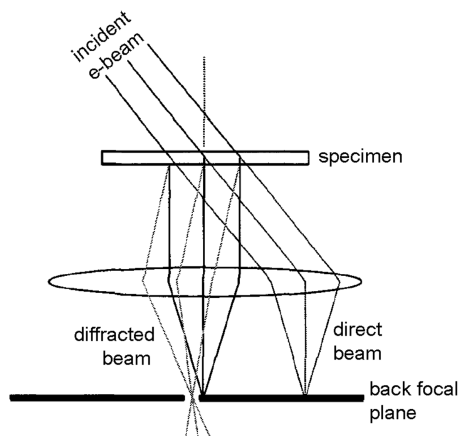


**Figure 3.21:** Principle of transmission electron microscopy. Depending on which signal beam is selected, the system operates in so-called bright or dark field (shown here) mode.

### 3.2.3 Micro-photoluminescence

Photoluminescence (PL) is a non-destructive measurement technique whereby a system is promoted to an excited state via photon absorption, and the PL signal arises after a transition of the excited system to the ground state, where the excess energy is released in the form of a spontaneously emitted photon. Therefore, the properties of the optical transitions are revealed in the spectrum of the intensity versus energy (or wavelength). Since these transitions contain information about material composition, impurities, quantum-confined structures, etc., a large variety of properties can be deduced. This is widely exploited to study direct-bandgap semiconductors due to their high efficiency of radiative recombination. The photoexcitation with a photon of energy

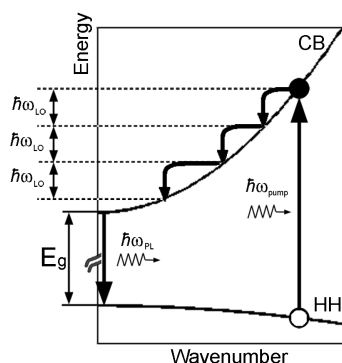


**Figure 3.22:** Illustration of the photoexcitation of an electron, its subsequent phonon-assisted relaxation of the excess energy and radiative recombination yielding PL signal.

larger than the bandgap promotes an electron from the valence band to the conduction band leaving a hole in the former (Fig. 3.22). The non-equilibrium free carriers can first release their excess energy via interaction with the lattice involving optical and acoustic phonons. In polar semiconductors (like GaAs) longitudinal lattice vibrations are mostly

<sup>31</sup>TEM Phillips EM-430, 300 keV, resolution 0.5 nm.

involved due to the Fröhlich interaction [168]; and the carrier relaxation rate ( $\Gamma_{rlx}$ ) via the optical LO phonons is very large (picosecond regime [169]), since the LO-phonon dispersion is nearly constant ( $\hbar\omega_{LO} \approx 37meV$  for GaAs) over the entire Brillouin zone compared to the LA-phonons. Since for the interband transition (recombination) the momentum has to be conserved and optical transitions can only be direct due to a small momentum of a photon, the hole and the electron must have the same momentum during the time defined by the probabilistic radiative rate ( $\Gamma_{rad}$ ). Since  $\Gamma_{rad} \ll \Gamma_{rlx}$ , these conditions are satisfied at the band extrema (for electrons and holes). This is where the optical transition can effectively take place resulting in the PL signal. Depending on the actual band structure and presence of localized states, transitions at different energies may arise, which is especially important in quantum nanostructures. At high carrier densities band filling effects can be present; additionally, carrier-carrier scattering may lead to slower relaxation rates.

The luminescence reflects properties of the excited volume, which is then a statistical distribution leading to inhomogeneous broadening of the spectral features. In order to study single nanostructures, local probe techniques are of much interest [170], e.g. scanning near-field optical microscopy, cathodoluminescence or micro-PL. We used the latter for the control of the excitation volume with  $\sim 2\mu m$  lateral resolution.

### 3.2.3.1 Micro-PL set-up

The set-up schematics<sup>32</sup> is presented in Fig. 3.23. The laser beam is directed to the microscope objective lens which focuses it through the cryostat window on a sample surface. The PL signal is collected by the same objective lens, directed to a lens ( $f' = 40mm$ ) that focusses the collimated beam on the spectrometer's slits. In the spectrometer the light is dispersed horizontally by a grating directly onto an array detector (CCD). Single-grating spectrometers are used (as usually) with the array detector. Every CCD pixel is thus associated with a different wavelength according to the dispersive properties of the grating and elements arrangement within the spectrometer. The full spectrum is thus acquired at once. The sample is placed in a thermal contact with a metallic post in a cold-finger cryostat cooled by the liquid-He flow, which allows for temperature ranges down to  $\simeq 4K$ . This is necessary in order to avoid non-radiative recombination whose rate increases substantially with temperature. Temperature control is implemented based on a Si-diode temperature measurement within the cryostat, a heater and a standard PID-gain feedback system. The excitation is implemented either with a green (514 and 488nm in case of  $Ar^+$  laser, 532nm in case of frequency-doubled Nd:YAG laser) or red (tunable titanium-sapphire (Ti:Sa) laser). In the collection line, a

<sup>32</sup>Two set-ups were employed. *Set-up 1.* Laser: Coherent Innova  $Ar^+$ , Coherent Mira 900-P Ti:Sa; objective lens: Zeiss Epiplan 50 $\times$ , NA=0.5,  $f' = 3.6mm$ ; cryostat: Cryovac Konti; monochromator: Jobin Yvon HR460, grating 1200 grooves/mm, maximum resolution  $\simeq 0.06nm$ ; CCD: Jobin Yvon Spex Spectrum One, 2000  $\times$  800 pixels, Si, cooled in liquid nitrogen.

*Set-up 2.* Laser: frequency-doubled diode-pumped Spectra Physics Millennia Nd:YAG, Spectra Physics Tsunami Ti:Sa; objective lens: Zeiss 50 $\times$ , NA=0.55,  $f' = 3.6mm$ ; cryostat: Janis ST-500; monochromator: Jobin Yvon Triax 550, grating 1200 grooves/mm, maximum resolution  $\simeq 0.06nm$ ; CCD: Jobin Yvon Spex Spectrum One, 2048  $\times$  512 pixels.

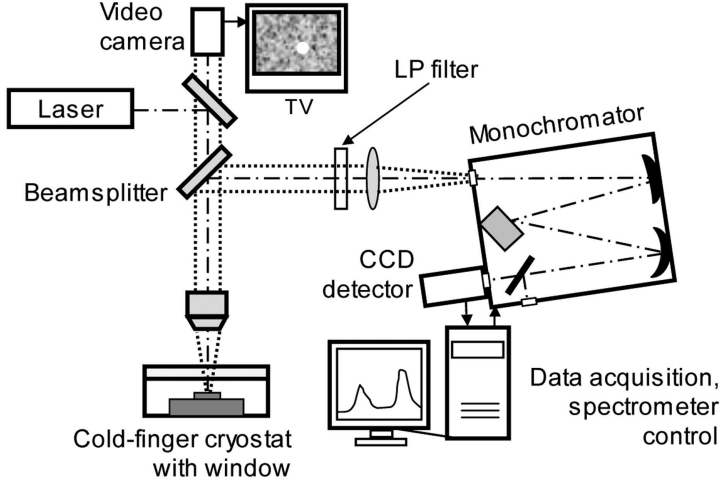


**Figure 3.23:** Schematics of the micro-PL set-up.

long-pass filter cuts the reflected/scattered laser light that, as a stray light, can produce noise in the detected spectrum.

### 3.2.3.2 Spectral analysis

In order to evaluate the properties of the cavity modes present in the PhC-QWR emission, we implemented the following systematic procedure (as shown in Fig. 3.24). The QWR background emission is subtracted from the original spectrum (in a similar way to, for example, ref. [171]), then the fitting of the cavity mode is performed using a lorentzian-function model that in frequency ( $\nu$ ) domain reads:

$$I(\nu) = \frac{2A}{\pi\Delta\nu} \frac{1}{\left[1 + 4\frac{(\nu-\nu_0)^2}{\Delta\nu^2}\right]} \quad (3.3)$$

where  $A$ ,  $\nu_0$ ,  $\Delta\nu$  are the fit coefficients giving the intensity, peak central frequency and the line width respectively. From the fit function converted to the wavelength domain

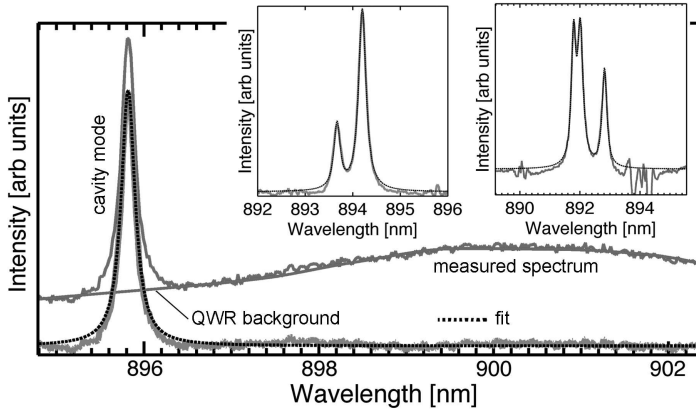


**Figure 3.24:** Example of the QWR-PhC micro-PL spectral analysis (lasing multimode ( $L_{35}$ ) cavity): QWR background is subtracted, then fitting with a lorentzian (or a sum of two, or three, see insets) is done.

$I(\lambda)$  we extract the integrated intensity ( $\int I(\lambda)d\lambda$ ), the peak position and its full width at half maximum (FWHM). For the latter, normalized values  $\lambda_0/\Delta\lambda_0 = \nu_0/\Delta\nu_0$  are

kept, for convenience. The integrated intensity of the background itself can also be evaluated. The integrated intensities are then converted into power units via normalizing by the CCD acquisition time. In multimode cavities, fitting for closely spaced peaks with a sum of two lorentzians or even three was used to extract accurately the mode characteristics<sup>33</sup> (e.g. see sec. 7.2.1). As can be seen from Fig. 3.24, a small discrepancy is found at the foot of the peak, which is due to background subtraction. This error is however systematic. Otherwise the fit accuracy looks good.

### 3.2.4 Transient micro-PL spectroscopy

The PL dynamics can be assessed by exploiting a short-pulse laser excitation implemented with the so-called *time-correlated single-photon counting* technique [172]. The set-up<sup>34</sup> is shown in Fig. 3.25 and operates in the following way. Sample is excited by a pulse from the mode-locked Ti:Sa laser (pulse duration  $\sim 3ps$ , repetition rate  $76MHz$ ) every  $\simeq 13ns$ . Photons emitted by the sample are detected by a micro-channel plate photomultiplier (MCP) connected to a photon counter. The signal from the photon counter is sent to the time-to-analog converter (TAC) and serves as a *start* signal. Every time a photon is detected, a linear-gain amplifier starts building up a voltage

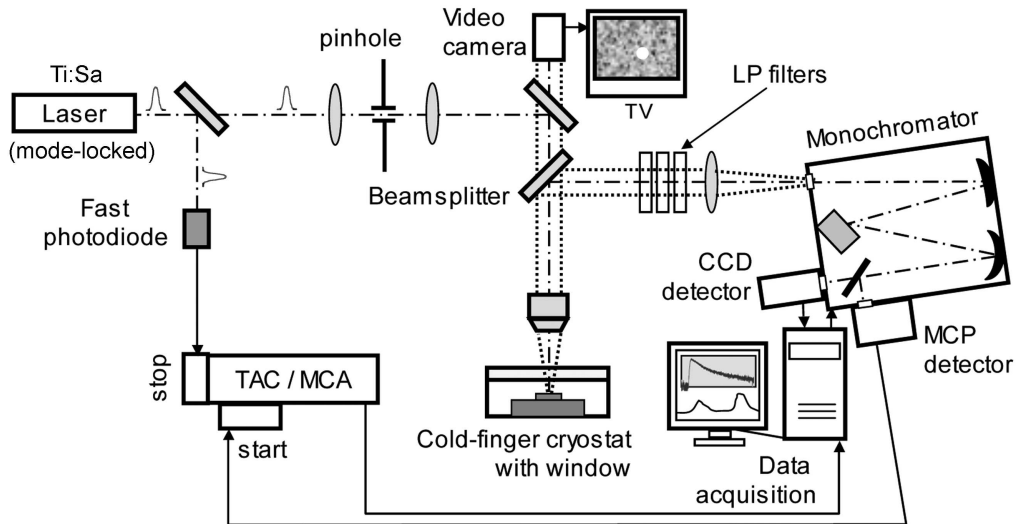


**Figure 3.25:** Schematics of the time-resolved micro-PL set-up. As mode-locking is implemented with narrow slits inducing beam diffraction (hence divergence), spatial filtering (two lenses and a  $50\mu m$ -diameter pinhole) is used in order to obtain a gaussian-like  $\sim 1.5\mu m$  spot (at  $\lambda \simeq 730nm$ ).

until the *stop* signal (next laser pulse) arrives from the fast photodiode. Different start-stop time intervals are then proportional to the different voltages, which is registered

<sup>33</sup>Fitting closely-spaced modes with single lorentzians can easily result in the error of the  $Q$ -factor up to  $\sim 1000$ .

<sup>34</sup>Based on the micro-PL *set-up 2* with Mira laser.

and sorted as a number of events in the multi-channel analyzer (MCA)<sup>35</sup>. By acquiring during some time a *statistical histogram* is built, which, after the time-axis calibration using a delay line, represents a *transient PL*. From this, the carrier-population decay mechanisms can be extracted.

The temporal resolution is given by the instrumental response function (IRF) and in our case it is limited to  $\sim 60ps$  (FWHM of the IRF main peak). The IRF is measured using the laser signal reflected from the sample. On the other hand, for the transient PL, special care is taken to exclude the fast laser signal that can produce artifacts in the histograms. We used several long-pass filters. Measured signal is eventually a convolution of the PL transient with the IRF, therefore in order to extract the characteristic time constants a model function has to be convolved with the IRF in order to obtain the proper fit. An example of a measured PL transient (from a non-lasing  $L_6$ -cavity mode) fitted with a triple-exponential model (one rise and two decay components, see Eq. 4.6) convolved with the IRF is presented in Fig. 3.26. By means of fitting, the accuracy of the inferred time constants can be pushed down to  $\sim 10 \div 20ps$ , provided that the noise level is low.

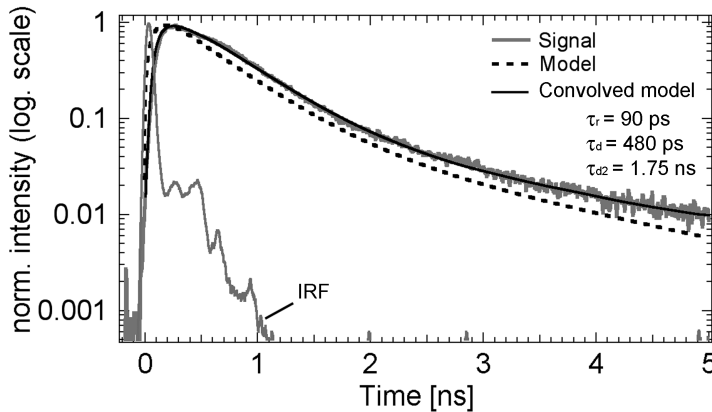


**Figure 3.26:** Example of a transient micro-PL. The histogram is acquired from a non-lasing  $L_6$ -cavity mode. IRF is obtained by measuring the Ti:Sa laser emission. Convolution of the model with the IRF provides a proper fit to the measured data.

### 3.3 Chapter summary

In summary, we have introduced a technology that allows for integrating site-controlled nanostructures like QWRs in PhC microcavities. The ability to fabricate such site controlled photonic systems opens up a way for applications in nano-optoelectronics, especially, novel light *emitters with extremely small active volumes* and coupled quantum nanostructures. In particular, the ability to control both the sites of the QWRs and the position of the optical cavity makes possible the realization of coupled cavities containing individual QDs or QWRs, which is virtually impossible with techniques relying on random nanostructure nucleation.

In parallel, we reviewed the principles of experimental techniques that are involved in the technology, structural and optical characterization of the integrated QWR-PhC

<sup>35</sup>MCP: Hamamatsu C 2773, Peltier-cooled; TAC: Tennelec; MCA: Oxford.

structures. Namely, electron microscopy and *e*-beam lithography, surface patterning, reactive ion etching and inductively-coupled plasma, AFM, micro-photoluminescence and transient spectroscopy were discussed in this context.



## Chapter 4

# Spontaneous emission of quantum wires in photonic-crystal microcavities

Recently a lot of research activity has been devoted to studies of spontaneous emission of quantum-well (QW) and quantum-dot (QD) heterostructures incorporated into optical microcavities [34, 173]. In particular, research into the spontaneous-emission control using tight-confinement photonic-crystal cavities implemented with such active nanostructures gained an increasing interest of the scientific community in photonics [49, 106]. Nanostructures based on quantum wires (QWRs), however, have not received much attention apparently due to difficulties in fabrication and integration into PhC cavities. Popular fabrication methods like cleaved-edge overgrowth of QWRs [174], catalytic nanowire growth [175] or vertical stacking and coupling self-assembled QDs [176] appear to be quite complex. Alternatively, a technology that employs QWR formation within the substrate plane, based on the techniques involving substrate patterning [96, 144, 177] can provide a good basis not only for a dense-array systems [145, 178, 179] but also for the *lateral site control* of one or few nanostructures within a microcavity, in particular PhC cavity, which is crucial for cavity QED-based experiments [111] and can be exploited in devices [102, 180].

QWR arrays incorporated into planar microcavities implementing different dimensionality have been studied in detail in [145]. Based on dense QWR arrays and planar cavities, microcavity lasers – devices expected to have a very high efficiency and low “smooth” threshold due to large spontaneous-emission coupling factor ( $\beta$ -factor, see section 2.2.1) – have also been attempted [178, 181], although showing relatively high thresholds ( $\sim 40mW$ ) and low spontaneous-emission coupling factors ( $\beta \sim 5 \cdot 10^{-4}$ ).

In this chapter we will discuss the *spontaneous-emission* properties of a *single* or *few* (triple uncoupled) QWRs incorporated into PhC microcavities of high finesse (cold-cavity  $Q$  upto  $\sim 5000$ ) and extremely small mode volumes ( $\sim 1(\lambda/n)^3$ ). The latter features are expected to allow for a distinctly single-mode cavity operation required for the microcavity lasers [49, 102] <sup>1</sup>. Furthermore, 2D photonic-bandgap effects are expected

---

<sup>1</sup>See section 2.2.

to significantly affect the spontaneous-emission rates (enhancement and inhibition) due to induced modifications in the density of electromagnetic states within the PhC dielectric environment (see section 4.4). We will start the chapter by implementing the QWRs as an internal light source (ILS) in order to probe and identify the PhC-cavity spectral properties. After that, we will examine the QWR spontaneous-emission rates and modifications brought about by the PhC dielectric environment, keeping in mind that realistic QWRs are inhomogeneously broadened.

## 4.1 QWR emission spectrum

When describing the QWR-PhC technology, we already presented some photoluminescence (PL) properties of single and stacked *InGaAs/GaAs* QWRs fabricated within the framework of the present thesis (see section 3.1.3.3). Here nevertheless we would like to briefly discuss two important features which will give us evidence that these QWRs are consistent with other previously published works ([145, 148]). Namely, temperature and power dependencies of the PL spectra.

A typical temperature dependence of the PL is presented in Fig. 4.1 (a). Here it is measured on QWRs (3 stacked wires) embedded into a non-patterned membrane wafer (i.e. without PhC) using relatively low excitation power. We observe a typical redshift

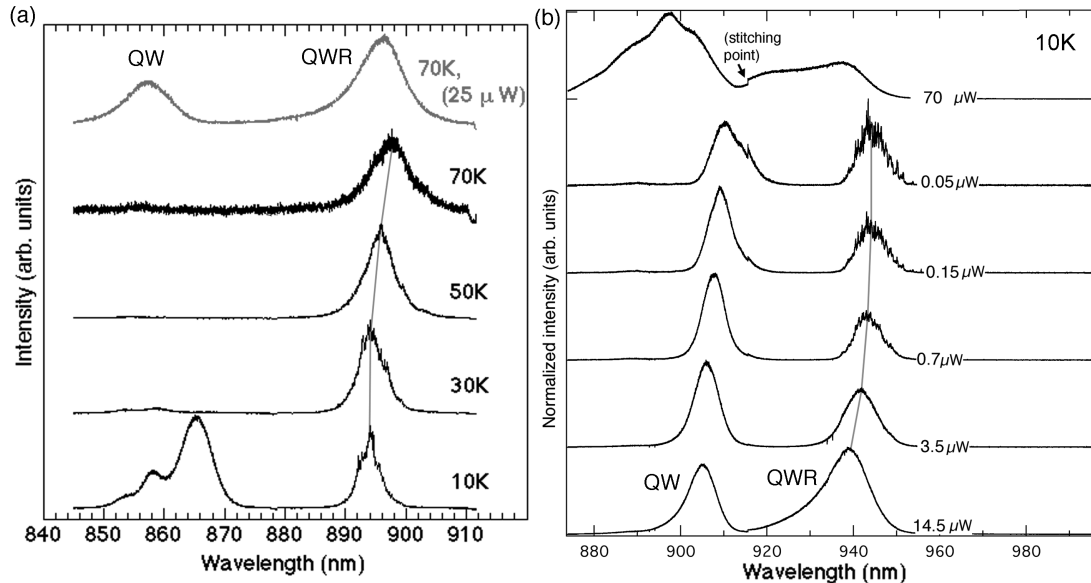


**Figure 4.1:** (a) Temperature dependence of *InGaAs/GaAs* QWR emission (sample: 3 stacked QWRs,  $1\mu\text{m}$  pitch, embedded in a membrane without PhC). Pump conditions: pulsed ( $3\text{ps}$ ,  $78\text{MHz}$ ),  $700\text{nm}$ , average power  $0.5\mu\text{W}$ . (b) Power dependence of *InGaAs/GaAs* QWR emission (sample: single QWR, on a submicron-pitch grating, in *GaAs*). Pump conditions: CW,  $532\text{nm}$ . Connecting lines are guides to the eye.

with temperature, which is expected due to the *GaAs* bandgap shrinking. The shift is pronounced above 30K, and at lower temperatures the effect of exciton localization is

clearly seen in the inhomogeneously broadened QWR emission line. A second important point is that around 50K the side-QW emission is quenched. This is accompanied by an enhancement of the QWR emission, reflecting efficient carrier relaxation (and capture) from QWs to the QWRs, as reported in [148]. At 70K however at the same pump level the QWR signal becomes lower, which is due to non-radiative recombination<sup>2</sup>. At high temperatures (50-70K) the QW can be populated again if higher pump powers are used. Here (at 70K) with a 50-fold pump-power increase the QWs can be populated up to the QWR output level (equal output intensity), which reflects the QWR saturation effect.

We then further examined the power dependency. In Fig. 4.1 (b), an example is shown on *InGaAs/GaAs* single QWRs emitting at slightly longer wavelength (tuned by QWR thickness) and fabricated on a 260nm-pitch gratings. The power-dependence (at 10K) shows a transition from exciton localized states to a smooth curve where localizations are saturated and hence more extended states get populated. This is accompanied by the blueshift of the peak emission intensity. Secondly, the slope of the high-energy QWR tail becomes markedly less steep at high powers reflecting band filling [148]. In the case of a very intense excitation a second QWR subband is probably seen in the spectrum ( $\sim 20nm$ , or  $\sim 35meV$ , blueshifted with respect to the ground subband). The emission blueshift at high carrier densities might be an indication of that electron-hole plasma, however bearing strong Coulomb correlations, is formed (see sections 2.1.1.1, 2.1.2), which can be a likely gain source for QWR lasers [89].

In summary, our observations here are qualitatively consistent with previously reported properties of high quality *InGaAs/GaAs* V-groove QWRs.

## 4.2 Mode structure of the $L_6$ cavity

As an active medium, our basic structure implements QWRs that (ideally) represent a one-dimensional electronic system. Therefore, by general symmetry reasons, the photonic system of choice is also of a 1D type. The  $L_N$  cavities represent N missing holes in a row along a "pitch" direction [see Fig. 4.2 (a)] in a hexagonal PhC lattice. Such a lattice possesses, in general, a relatively broad photonic bandgap, therefore allowing for well-confined cavity states. The  $L_N$  structure is practically convenient, since it allows for both fully confined 0D cavity states if N is reasonably small and for 1D states, where the photon momentum is well defined along the non-confined direction if N is large<sup>3</sup>. Therefore the integrated QWR- $L_N$  - cavity system opens several possibilities of combined dimensionality. The dispersive properties of the  $L_N$  cavities with application to tracking a 1D photonic band formation will be addressed in chapter 5. Here, without loss of generality, we will consider mostly short cavities, like  $L_6$ , the example which will already provide initial insight into the mode structure and anticipated spectral cavity properties.

<sup>2</sup>The QWRs on membrane were measured in between PhC patterned areas with  $\sim 2 \div 3\mu m$  distance to the pattern. Therefore the non-radiative recombination here is likely due to carrier diffusion in QWRs.

<sup>3</sup>See Chapter 5 for a detailed discussion on this matter.

### 4.2.1 Even and odd modes

An  $L_N$  cavity has tightly confined modes with patterns highly intense along the cavity axis, thus ensuring considerable overlap with the coaxially positioned QWR. The spectrum of such a cavity contains modes that originate from three dispersion bands of the so-called W1 waveguide (that is, the  $L_\infty$  “cavity”). This is illustrated in Fig. 4.2. Since the photonic bandgap width is defined by the  $r/a$  ratio and the membrane thickness  $t$ , the highest-frequency band (which is taken into account for calculations in Fig. 4.2) starts being confined for values of  $r/a \gtrsim 0.31$  at  $t \simeq 270\text{nm}$ . The  $Q$ -factor of potentially highest- $Q$  modes of an  $L_N$ -cavity (which stem from regions of flat dispersion) grows al-

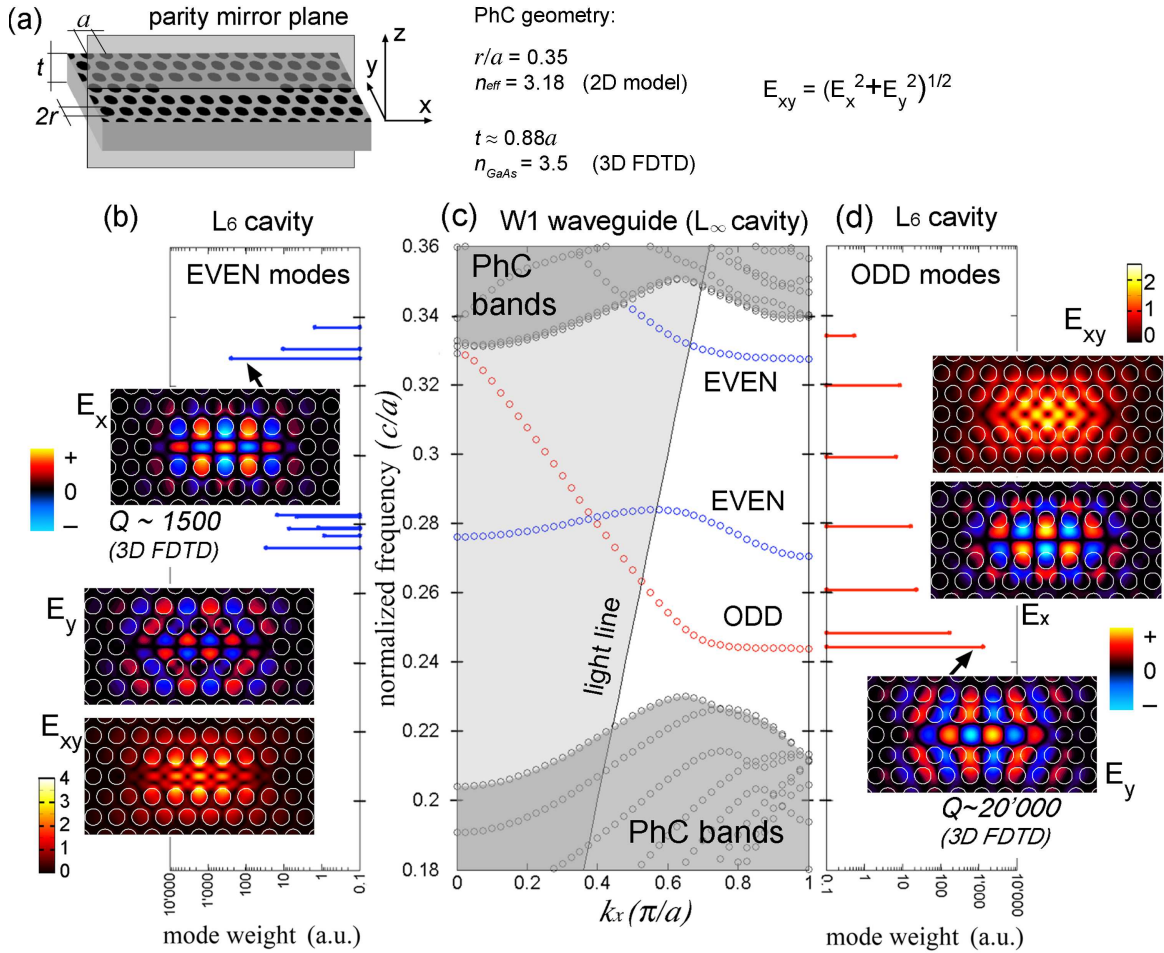


**Figure 4.2:** (a) Sketch of the PhC  $L_6$ -cavity geometry indicating the parity mirror plane. (b, c, d)  $L_6$  cavity modes are compared to the dispersion bands of the W1 waveguide ( $L_\infty$  cavity) calculated using the 2D model with the parameters indicated in (a). The spectra are in normalized units (not corrected for GaAs refractive-index dispersion). Potentially highest- $Q$  modes are pointed out by arrows; their representative mode patterns are shown by the field components, indicating the field polarization within the center of the cavity where a QWR is to be positioned. Corresponding real  $Q$ -factors are computed from the 3D FDTD (for  $\lambda \sim 930\text{nm}$ ).

most linearly with increasing  $N$ . On the other hand, the photonic bands become denser for larger  $N$  (see Chapter 5 for the details of the photonic band formation). Having in prospect applications to microcavity lasers, the  $L_6$  cavity can be a good candidate for achieving sufficiently high  $Q$  while maintaining good mode discrimination (i.e. cavity free spectral range larger than the gain bandwidth). Such a cavity supports both *even* and *odd* modes. The parity definition<sup>4</sup> here is determined with respect to the vertical plane that includes the cavity axis [Fig. 4.2 (a)]. The *odd* modes have optical fields polarized perpendicular to the wire; those with high  $Q$  are found at lower frequencies. The optical near-field pattern ( $E$ -components) of such a mode is shown in the Fig. 4.2(d). The *even* modes, polarized along the wire in the cavity center, have potentially highest  $Q$  at quite high frequencies within the PhC bandgap [Fig. 4.2(c,d)]. As QWRs exhibit characteristic polarization anisotropy due to 2D quantum confinement effects [96, 184] with the optical transitions mainly polarized along or perpendicularly to the QWR axis, matching to a particular cavity mode can be exploited for tailoring the features of the light-wire interaction. However, for anisotropic QWRs, as the discussed V-groove QWRs (i.e. of a crescent-shaped cross-section contrary to circularly-shaped one), efficient coupling to either polarization can occur (because of symmetry breaking [184]). Therefore both *odd* and *even* modes are of interest.

### 4.2.2 $Q$ enhancement by shifting cavity terminations

As seen from the computation of the  $Q$ -factor, the *even* potentially high- $Q$  mode has a relatively low quality factor ( $\sim 1500$ ). This means that the mode has large out-of-plane radiative losses (see section 2.3.4 on the light-cone problem). It has been demonstrated that for 2D PhC cavities small in-plane adjustments of the geometry [129, 130] can significantly affect the out-of-plane losses, therefore allowing for appreciably higher  $Q$ -factors while maintaining mode distributions identical to that of the initial unmodified cavity. In particular,  $\sim 0.15a$  adjustments of the on-axis cavity terminations resulted in dramatic increase of the  $Q$ -factor for the *odd* modes of an  $L_3$  cavity [130, 131]. This result is shown also here in Fig. 4.3 (a) for convenience and will be applied later on in some of our experimental samples.

Developing further this idea, we found that the mode parity (or effective *polarization*) plays an important role in the out-of-plane loss problem. Indeed, the out-of-plane losses of the *odd* modes are mainly governed by the  $E_y$  field component (a factor of  $\sim 10$  larger integral within the light cone compared to that of the  $E_x$  component). On the contrary, the radiation losses of the *even* modes are governed by the  $E_x$  field component. Taking into account this polarization aspect, we propose [185, 186] that for the *even* modes the  $Q$ -factor can be enhanced in a way similar to that for the *odd* modes,

<sup>4</sup>Note that in contrast to a simplified convention [182, 183] we prefer to use the general definition [121] that, by taking into account *all* the field components, is consistent with the vectorial nature of the electromagnetic field. For example, an  $L_6$  mode is *even* with respect to the mirror plane shown in Fig. 4.2(a) if:  $E_x$  – even,  $E_y$  – odd,  $E_z$  – even,  $H_x$  – odd,  $H_y$  – even,  $H_z$  – odd. Conversely, the mode is *odd* if:  $E_x$  – odd,  $E_y$  – even,  $E_z$  – odd,  $H_x$  – even,  $H_y$  – odd,  $H_z$  – even. To draw a conclusion on the parity of a given mode, it is therefore necessary and sufficient to know the parity of  $E_x$ ,  $E_y$  and  $H_z$  components, which can be computed in 2D.

shifting however the *off-axis* cavity terminations [Fig. 4.3 (b)]. Indeed, 3D FDTD simulations predict  $Q$ -factors upto  $2 \div 4 \cdot 10^5$  in the case of the even mode pointed out in

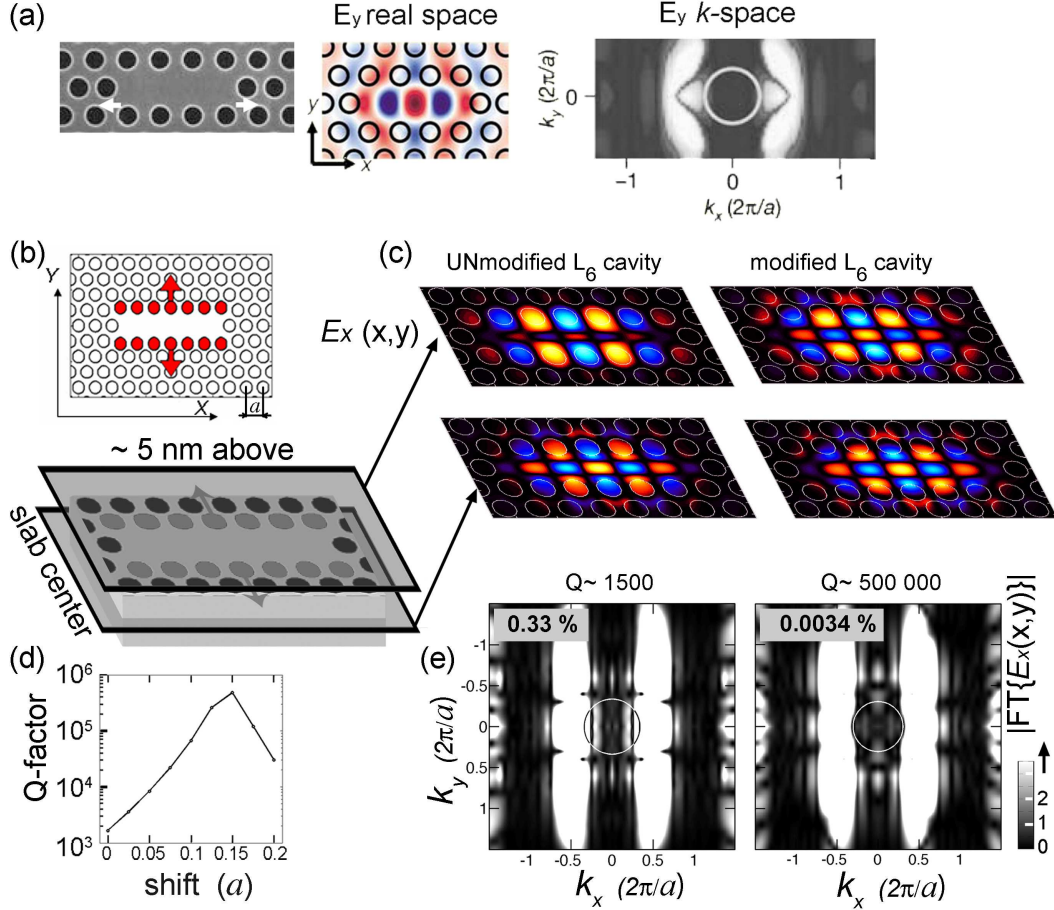


**Figure 4.3:** Cavity  $Q$  enhancement by shifting terminations. (a) For the highest- $Q$  odd mode of the  $L_3$  cavity. Shown: the optimal shift, near-field pattern ( $E_y$  component) in real and  $k$ -space (from [130]). (b-e) 3D FDTD simulations for the highest- $Q$  even mode of the  $L_6$  cavity: (b) schematics of the shift and reference planes, (c) near-field patterns ( $E_x$  component). In the case of the modified cavity the shift is  $0.15a$ . Note the difference in the field distribution above the membrane. (d)  $Q$ -factor versus the shift. (e) 2D Fourier transforms of the  $E_x$  taken within the reference plane above the slab. Note, the colormap range is cut in order to display low-intensity field components in the linear scale for comparison. Insets show the ratio of the intensity integrated within the light cone to that taken over the full domain. The  $Q$ -values are obtained directly from the 3D FDTD using the Padé-Baker approximation.

Fig. 4.2 (b) for the optimal shift of  $\sim 0.15a$  [Fig. 4.3 (d,e); the PhC parameters in the simulations here were  $r/a = 0.35$ ,  $t = 0.65a$ ,  $n_{GaAs} = 3.506$ ]. Such a cavity modification, according to the light-cone analysis, results in a significant reduction of the leaky low- $k_{\parallel}$  field components. On top of it, the redshift of the mode frequency reduces the “area” of the light cone itself, extending therefore the confinement to larger  $k_{\parallel}$ -vectors. The overall effect, illustrated in Fig. 4.3 (c, d), is a 100-fold reduction of the integrated field intensity ( $|E_x|^2$ ) within the light cone (a factor of  $\sim 9$  being attributed to the

frequency redshift). Exploiting this new mode might be of interest for work based on QWRs, where the polarization properties can be important [96].

### 4.3 Coupling of the QWR emission into PhC cavity modes: mode spectroscopy

The preceding section provides a general guideline of the PhC design. On this basis, accurate PhC parameters have to be calculated in order to match a particular emitter's wavelength to the cavity modes. First QWRs implemented in our experiments emitted light at  $\simeq 930nm$ . Provided that the cavity resonances should stem from the  $TE_0$  photonic bandgap and that the slab thickness is fixed at 265 nm due to fabrication reasons, the recommended PhC parameters, in the case of desired matching to the *odd* fundamental mode<sup>5</sup>, are  $a \simeq 210 \div 230nm$ ,  $r/a \sim 0.23 \div 0.27$  for  $a = 210nm$  and  $r/a \sim 0.31 \div 0.34$  for  $a = 220nm$ . In the case of the *even* mode<sup>6</sup>, the recommended parameters are  $a \simeq 290 \div 310nm$  and  $r/a \sim 0.32 \div 0.34$  for  $a = 290nm$  and  $r/a \sim 0.34 \div 0.36$  for  $a = 300nm$ . In the case of the modified  $L_6$  cavity for the even mode, due to the significant frequency redshift, the parameters shift to  $a \simeq 250 \div 260nm$  and  $r/a \sim 0.27 \div 0.29$  for  $a = 250nm$  and  $r/a \sim 0.31 \div 0.33$  for  $a = 260nm$ . Practical designs may cover excessively the  $r/a$  range in order to allow for tuning. This, apart from a coarse tuning possibility (i.e., by varying  $r/a$  in several PhC structures on the same wafer), is an efficient method to verify a consistency in the observation of the PhC-cavity modes, which gives a possibility to unambiguously conclude on the observed cavity spectrum. This method was therefore applied to all the examined structures.

#### 4.3.1 Single QWR in $L_6$ cavity: cavity modes and tuning

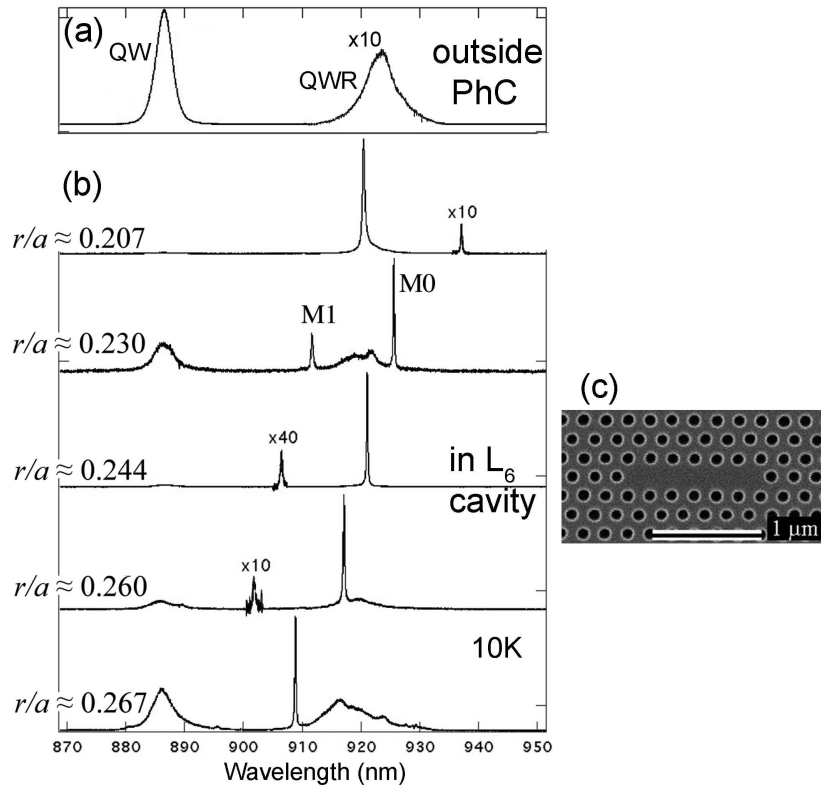
##### 4.3.1.1 *Odd* modes

Figure 4.4 presents low-temperature micro-PL measurements of a single QWR incorporated into the  $L_6$  cavity implementing the  $r/a$  variation. The PhC parameters were such that the *odd* fundamental cavity mode matches the QWR emission around  $\sim 930nm$ ; the PhC geometry was  $a \approx 207nm$  and  $r/a$  tuned within the range of  $\approx 0.2 \div 0.28$ . Compared to the emission spectrum of a “bare” QWR [Fig. 4.4 (a)], the spectra of the wire segments located inside the cavity are significantly different (see Fig. 4.4 (b)). Clearly, the spectrum becomes dominated by the cavity modes. The first higher-order state ( $M_1$ ) and then the fundamental state ( $M_0$ ) are tuned respectively into the resonance with the QWR emission when the  $r/a$  is increased by enlarging the radius of PhC holes (Fig. 4.4 (b), from upper to lower spectrum). The inferred mode blueshift rate deduced from the measured  $r/a$  values and the corresponding spectra is  $\approx 2.3nm_\lambda/nm_r$  given the

<sup>5</sup>Computational parameters. 3D FDTD:  $t = 1.12a$ ,  $n_{GaAs} = 3.5$ . With this, the  $n_{eff}$  in 2D model is tuned (see section 2.3.3.2) to  $n_{eff} = 3.18$ .

<sup>6</sup>Computational parameters. 3D FDTD:  $n_{GaAs} = 3.5$ ,  $t = 0.88a$ . With this, the  $n_{eff}$  in 2D model is tuned to  $n_{eff} = 3.23$ .

average lattice constant of  $\approx 207\text{nm}$ . Note that, as expected, the two modes ( $M_1$  and  $M_0$ ) shift by the same amount. The observed mode structure is fully consistent with expectations [Fig. 4.2 (d)]. The  $M_2$  mode thus should appear at shorter wavelength than the QW emission, and is therefore not seen. Altogether the  $L_6$  cavity with such a PhC geometry ( $r/a \sim 0.26$ ) can confine 4 odd modes. This, compared to Fig. 4.2 (d), is due to a reduced photonic bandgap at  $r/a \sim 0.26$  compared to  $r/a \sim 0.35$ .  $Q$ -factors inferred from the measured linewidths of Fig. 4.4 (b) are  $\simeq 3400 \pm 300$  for the fundamental cavity state ( $M_0$ ) and  $\sim 1800 \pm 200$  for the first higher-order state ( $M_1$ ). No significant dependence on power was observed. In contrast to the resonant QWR-PhC peak, the QW emission is greatly suppressed. This can be interpreted as an efficient coupling of the spontaneous emission from the QWR into a cavity mode, while the QW emission is off-resonance. According to the calculations, the proper range of



**Figure 4.4:** Single QWR in the  $L_6$  cavity coupled to the *odd* lowest-order modes ( $M_0$  and  $M_1$ ); the coupling is verified by the  $r/a$ -tuning. (a) “bare” QWR emission (i.e. outside the PhC patterned region). (b) From upper to lower panels:  $L_6$  cavity states “passing” through the QWR emission when  $r$  is increased (indicated). The  $M_1$ ,  $M_0$  modes, one after another, are tuned into resonance with the QWR. Pump conditions: micro-PL, CW, 514 nm, excitation power  $1\mu\text{W}$ . (c) SEM top-view image of one of the measured structures ( $r/a \approx 0.244$ ).

PhC lattice constants is  $210 \div 230\text{nm}$ . The lattice constants  $\gtrsim 220\text{nm}$ , however, imply very large values of  $r/a$ , which is expected to be detrimental to the cavity  $Q$ -factor due to increased scattering and enhanced sensitivity to disorder. Indeed, such a trend was observed experimentally. For the cavities with  $a = 220 \div 230\text{nm}$   $Q$ -factors not larger

than  $\sim 1600$  were observed for the fundamental  $M_0$  state.

We also examined the case of a  $L_6$  with shifted (coaxially) terminations (as suggested by [130] for the  $L_3$ ). For the optimal shift of  $\sim 0.15a$  the observed  $Q$ -factor of the  $M_0$  state was  $\sim 3500$ , which is identical to the non-modified case presented above. Taking into account the fact that the fabrication-induced disorder in this experiment is not substantial [as seen from the SEM top-view images, e.g. see Fig. 4.4 (c)], this means that the  $Q$ -factors are probably limited by the out-of-plane fabrication disorder due to RIE etching and/or the absorption related to oxidized GaAs/air interfaces [135].

#### 4.3.1.2 Even modes

Having observed the QWR-PhC coupling for the *odd* modes, an experiment aimed at the *even* potentially high- $Q$  modes have then been attempted.  $L_6$  cavities with the geometry parameters of  $a \approx 290 \div 320\text{nm}$  and appropriate  $r/a$  ratios (as suggested for the even modes by computations) have been fabricated and measured. Modes with somewhat low  $Q$ -factors ( $\sim 300$ ) were observed within this region. In the case of the modified  $L_6$  cavity (section 4.2.2), modes with  $Q \sim 1100 \div 1500$  were tracked down. Since the discrepancy with numerical predictions is large, further fabrication effort is needed for QWR coupling with the *even* modes, which could exploit the QWR polarization anisotropy [96] favoring the polarization along the QWR.

#### 4.3.1.3 $TE_1$ -like cavity states

Although an optimal photon confinement in a PhC cavity can be achieved by introducing a defect within a clear bandgap ( $TE_0$ -like in the case of low-index holes inside high-index matrix), symmetry conditions may allow for the presence of confined cavity modes that overlap with continuous bands. Indeed, QWR coupling to  $TE_1$ -like *odd* states have been observed (Fig. 4.5) [149] (with PhC parameters of  $a \sim 280\text{nm}$  and  $r/a \sim 0.28$ ). In fact, the band structure of the studied PhC within the wavelengths of interest is composed of bands that have  $TE_0$ -like,  $TM_1$ -like modes (even slab modes with respect to XY-plane mirror-centered along Z [121]) and  $TE_1$ -like,  $TM_0$ -like modes [odd slab modes; see Fig. 4.5 (b)]. Although the gap is not open for the odd slab modes, there can be regions where only  $TM_0$ -like bands are present. Eventually, the confinement of  $TE_1$ -like PhC cavity modes becomes possible due to only a weak interaction (coupling) between  $TE_1$  and  $TM_0$  bands [149], which however influences achievable  $Q$ -factors (values  $\sim 500 \div 900$  were observed). Nevertheless, an efficient coupling between such low- $Q$  cavity modes and the QWR emission was observed. This was manifested by  $\sim \times 150$  increase of the collected PL intensity<sup>7</sup> almost totally concentrated within the cavity lorentzian line when tuned well into resonance with the QWR emission [Fig. 4.5 (a)].

It is interesting to comment that, in general, for emitters with a broad line the Purcell factor, given by the Eq. 2.19, *is not dependent* on  $Q$  due to the normalizing ratio between

<sup>7</sup>Also luminescence confined to the cavity area was apparent on the CCD video camera even at rather low ( $\sim 1\mu\text{W}$ ) excitation powers.

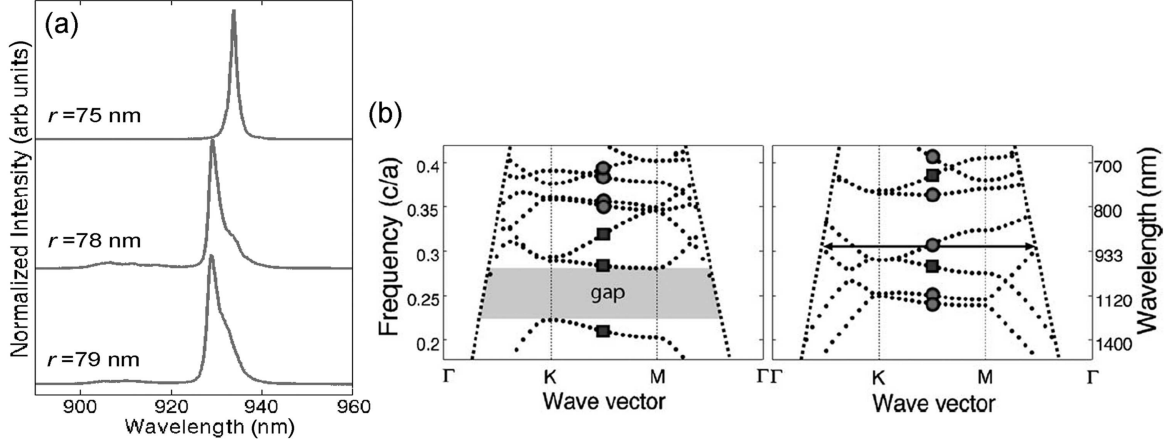


**Figure 4.5:** QWR-emission coupled to low- $Q$   $L_6$ -cavity  $TE_1$  resonance [149]. (a) QWR is tuned by the  $r/a$  ( $a \approx 280\text{nm}$ ). Quite efficient spontaneous-emission outcoupling ( $\times 150$  increase in the collected PL) is observed at QWR-PhC resonance. Conditions: 10K, CW 532 nm,  $\sim 1\mu W$ . (b) Computed (3D FDTD) projected band structure: (left) even slab-waveguide modes (squares,  $TE_0$ -like; circles,  $TM_1$ -like) and (right) odd slab-waveguide modes (squares,  $TE_1$ -like; circles,  $TM_0$ -like). The observed mode is indicated by arrow, its field distribution is similar to that shown in Fig. 4.2 (d).

the cavity-resonance and the emitter spectral widths<sup>8</sup>. The enhancement effect is then defined by the mode volume and the emitter FWHM, if spatial and spectral matching is ideal. Therefore, low- $Q$  cavities can provide an efficient spontaneous-emission output due to short photon lifetime and because a spectrally broad cavity mode may corral emission from a spectrally broad source.

#### 4.3.1.4 Fine tuning by temperature

For practical purposes of cavity-emitter detuning, complementary to the coarse  $r/a$ -tuning method applied above, *in-situ fine-tuning* approaches for spectrally shifting PhC resonances exist and comprise variation of temperature, gas condensation [187] and scanning by a SNOM [188] or AFM [189] tips. Among these possibilities, temperature tuning is the most straightforward to implement. This particular method is also a very useful practical tool for verification of the consistency of modes observations. Namely, first, to distinguish a weakly excited cavity mode from possible localized states of the active medium that are present at low temperature ( $\sim 10K$ ) due to disorder potential. And secondly, to further support conclusions on coupling of a nanostructure emission to the PhC cavity mode by examining the difference in the spectral wavelength shift of the cavity mode with respect to the nanostructure emission [133]. In Fig. 4.6 such a detuning experiment using an  $L_6$   $TE_1$ -like cavity mode and raising the sample temperature from 10K to 90K is presented [149]. It can be seen that the cavity mode red-shifts more slowly than the QWR emission line with increasing temperature, reflecting the larger effect of

<sup>8</sup>Homogeneous line of an emitter in an inhomogeneous ensemble. For disordered QWRs it can be  $\sim 1\text{meV}$

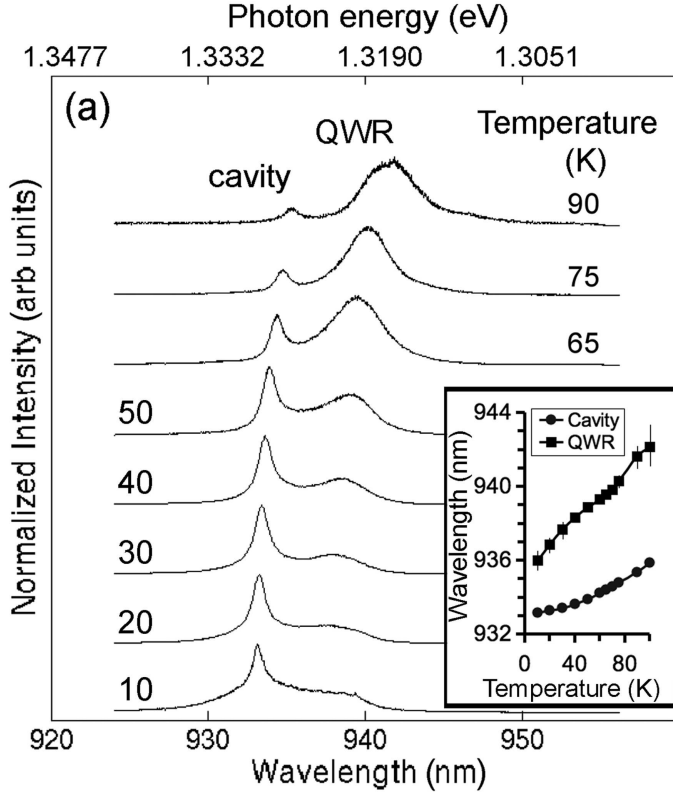


**Figure 4.6:** Fine spectral tuning of a cavity resonance (as an example,  $TE_1$ -like mode of a  $L_6$  cavity is taken). QWR is detuned out of the resonance by raising the sample temperature [149]. Inset: cavity-mode and QWR peak redshift

temperature on shrinking the semiconductor bandgap compared to the induced change of the GaAs refractive index. In this particular experiment, the mode better matches the QWR emission at low temperature and moves out of resonance at higher temperatures.

### 4.3.2 Vertically stacked QWRs in $L_3$ and $L_6$ cavities

Having in mind applications to QWR microcavity lasers (see chapter 7), in order to allow for larger optical gain, we designed *triple*-QWR structures (section 3.1.3.3) incorporated into  $L_N$  PhC cavities. For the microcavity laser small mode volumes and reasonably high  $Q$ -factors would be of particular interest in order to provide large spontaneous-emission coupling factors. Therefore, we considered  $L_6$  and a modified  $L_3$  [coaxially shifted cavity terminations by  $0.15a$  [130], see also Fig. 4.3 (a)]. For measurement convenience<sup>9</sup> the QWR emission wavelength was set at around 890 nm (by adjusting the QWR thickness).

Here we consider only the *odd* cavity modes [e.g. see Fig. 4.2 (d)]. For the 890nm emission wavelength the calculated PhC parameters<sup>10</sup> in this case for the odd PhC modes are  $a \sim 200 \div 210nm$ ,  $r/a \sim 0.24 \div 0.29$  for  $a = 210nm$  and  $r/a \sim 0.3 \div 0.34$  for  $a = 210nm$  taking into account some spectral reserve (to the red) as discussed in section 4.3.1. ICP etching (section 3.1.5.5) and the “digital etching” [135] postprocessing (section 3.1.6) were employed for sample preparation. Apart from the  $Q$ -factors which

<sup>9</sup>Dictated by a reasonable detection efficiency in the time-resolved set-up.

<sup>10</sup>Computational parameters. 3D FDTD:  $t = 1.26a$ ,  $n_{GaAs} = 3.5139$ . With this, the tuned  $n_{eff} = 3.223$  in the 2D model.

were larger, results qualitatively similar to those presented in the Fig. 4.4 were obtained.

#### 4.3.2.1 Mode spectroscopy

Fig. 4.7 (a) displays  $L_6$  spectra for varied  $r/a$  and Fig. 4.7 (b) gives examples of resonances obtained from modified  $L_3$  (dubbed “ $L_3m$ ”) cavities. The measured  $r/a$ -tuning rate is  $\simeq 1.95nm_\lambda/nm_r$ , provided that the average lattice constant is  $a \simeq 198nm$ . Let us now discuss the  $Q$ -factors. Some cavities exhibited a power-dependent non-linear linewidth narrowing, which can be a proper sign for the build-up of stimulated emission [102]. This issue will be further discussed in chapter 7. Here for the measurements of

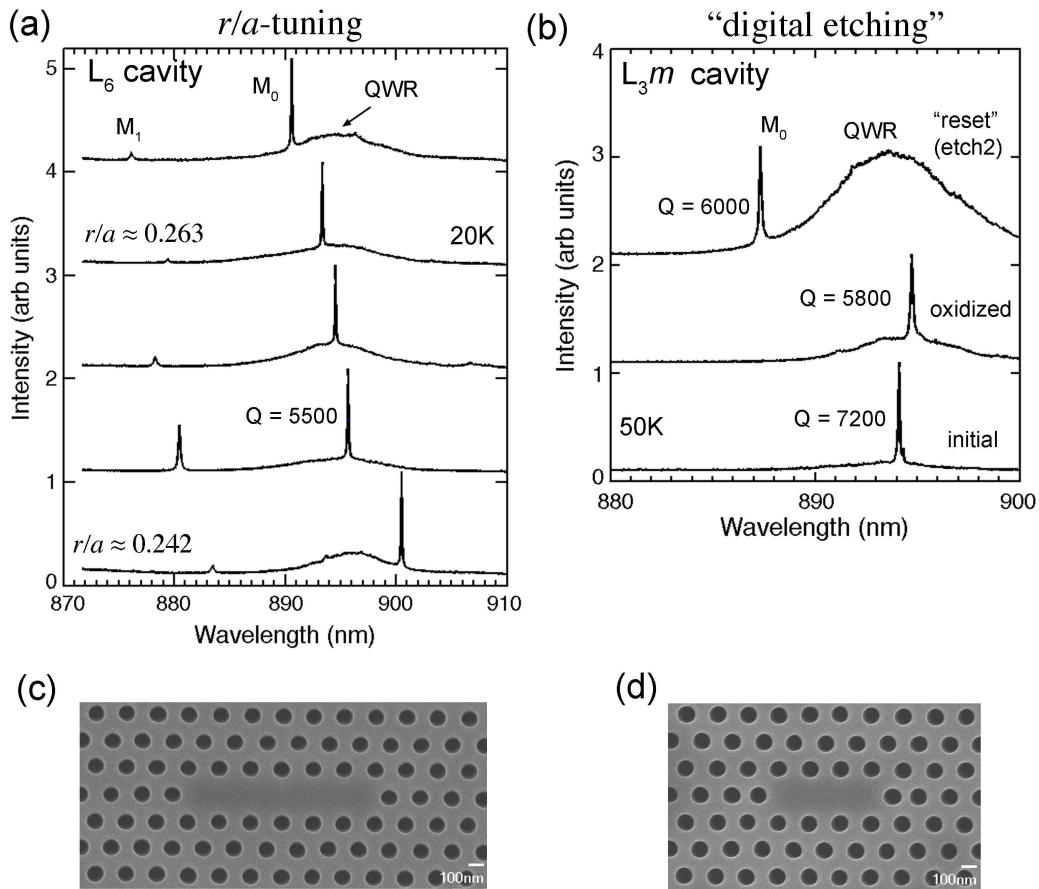


**Figure 4.7:** Spectra of three vertically stacked QWRs in PhC microcavities (at 10K). (a)  $L_6$  cavity. PhC geometry:  $a \simeq 197nm$ ,  $r/a$  is gradually increased from  $\sim 0.24$  (bottom) upto  $\sim 0.27$  (upmost). Pump condition: pulsed ( $\sim 3ps$ ,  $76MHz$ ), 730 nm, average power  $5\mu W$ . (b)  $L_3m$  cavity after “digital etching” (“initial”). PhC geometry:  $a \simeq 197nm$ ,  $r/a \sim 0.25$ . Pump condition: pulsed ( $\sim 3ps$ ,  $78MHz$ ), 700 nm, average power  $1\mu W$  in the “initial” case,  $2\mu W$  in the other two cases. See subsection 4.3.2.2 for discussion. (c) SEM top-view image of the measured  $L_6$  cavity with  $r/a \simeq 0.2424$ . (d) SEM image of the measured  $L_3m$  cavity.

$Q$ -factors we restrict ourselves to either “average” excitation powers (below those asso-

ciated with the onset of the rapid linewidth narrowing) or to cavities that did not show power-dependent non-linearities. Then measured  $Q$ -factors for the  $L_3m$  cavities and for the  $L_6$  cavities were in the range of  $4500 \div 7000$ . Regular (non-modified)  $L_3$  cavities showed  $Q \sim 2700 \pm 300$ . The overall increase of the  $Q$ -factors with respect to values reported in section 4.3.1 is attributed to better sample quality provided by the ICP etching (e.g. see Fig. 3.18), and to the “digital etching” [135] postprocessing. Note that, on average, the “digital etching” does not lead to a detection of significantly enhanced  $Q$ -factors at the average excitation powers ( $\sim 1\mu W$ ). Excluding power-dependent effects (due to coherence) in some devices (see section 7.3.3.3), typical (non-lasing) QWR-PhC  $L_N$ -cavity structures (e.g.  $L_3m$ ,  $L_6$ ,  $L_{11}$ ) show the  $Q$  saturation level at  $\sim 6000$ . This suggests that such  $Q$ -limitation is possibly due to losses related to unpassivated GaAs-air interfaces and regrowth of nonstoichiometric oxide [135]) and not due to the QWR intrinsic absorption (which is power-dependent and saturates much below  $\sim 1\mu W$ ).

#### 4.3.2.2 Implications of tuning by the “digital etching”

In a “digital etching” experiment [135] the natively formed GaAs oxide is selectively removed, which results in PhC modes blueshift and increase of the  $Q$ -factors. Although such a method is useful and extremely easy to implement, it turns out that it has some inconvenient implications, due to the regrowth of the oxide.

Figure 4.7 (b) presents modes of an  $L_3m$  cavity demonstrating at the same time a “digital etching” experiment. Consistent with the original publication [135], after the oxide removal by a first etch (i.e., final step in sample preparation; see the “initial” spectrum), the cavity mode shifts “back” to the red (see “oxidized”). This happens due to the (non-obvious) fact that the natively formed (in air) oxide *grows* not only into the material but also on top of the exposed surfaces of GaAs [146], therefore effectively reducing the  $r/a$  (since the refractive index of the oxide is smaller than that of GaAs). We registered wavelength redshifts of a cavity resonance in the range of  $\sim 1 \div 4.5nm$  on a time scale of one or two weeks. Such a large variation of the observed shifts is probably due to non-uniformities in the formed oxide layer. The mode then can be “reset” by another “digital etching” step. The resetting however produces a significant blue-shift with respect to the initial mode position. Shifts of  $\sim 4.5 \div 6.5nm$  with respect to the initial position were measured after the “resetting”. Such a shift arises from material removal, as the oxide grows not only on the surface but also partially into *GaAs*.

Thus, even though the method is very useful and allows to improve cavity performance (due to the initial  $Q$  enhancement), there arise two important implications. First, the redshift of the mode, along with degradation of the device performance, is inevitable due to the oxide formation, moreover, the oxide forms in an uncontrollable way resulting in a broad range of possible shifts; secondly, resetting is only possible with a significant offset into the shorter wavelengths. The latter circumstance renders the initial frequency matching irretrievable. This also poses a problem for the recycling of the  $Q$ -factor [135]. Indeed, if the mode is reset to a large extent to shorter wavelengths one might expect larger absorption. As seen in Fig. 4.7 (b), even though the  $Q$  recovery was possible, the net effect is not dramatic. In the subsequent experiment on power

dependency the  $Q$ -factor went up to  $\sim 11000$  while in the initial condition it attained the resolution limit of the set-up ( $Q \simeq 14000$ )<sup>11</sup>

## 4.4 Emission dynamics and spontaneous emission control

Since the spontaneous emission is the property of the interaction of matter with the surrounding environment, controlling this interaction opens ways of tailoring the emission characteristics. Implemented in solid state rather than with trapped (e.g. laser-cooled) atoms [190–192], such a possibility can yield applications in efficient light sources [39, 49] that can be integrated into complex photonic circuits [193]. Particularly efficient devices envisaged might employ photonic crystals due to pronounced photonic-bandgap effects [106] that may provide significant alteration of spontaneous-emission rates of embedded active nanostructures.

Here we study the PhC bandgap effects on QWRs in PhC cavities. We limit the main discussion to cavities of small volumes ( $L_6$  and  $L_3m$ , presented in the previous section), since they ensure reasonably large free spectral ranges, which is required for cavity QED effects to be effective [102]. In what follows the PL-emission dynamics is discussed on the basis of the measurements employing the time-correlated photon-counting technique (section 3.2.4) and micro-PL at low (20K) and high (70K) temperatures.

### 4.4.1 Emission dynamics of quantum wires in free space

Since the recombination dynamics in QWR nanostructures is a complex phenomenon [194, 195], this complexity needs to be necessarily taken into account to properly discuss the microcavity and photonic-bandgap (PBG) effects on the wire spontaneous emission. Therefore we start the discussion considering the exciton dynamics properties of the *InGaAs/GaAs* QWRs in free space (“bare” wires), that is, located outside of the PhC-patterned regions.

In non-resonant excitation conditions, the excited charge carriers are created within the *GaAs* matrix and then captured by the QWRs [196] (that have the lowest potential among all other nanostructures) in which they further relax towards available ground states where the recombination takes finally place yielding the PL signal. In general, such a system can be described by a three-level model [7]. The time evolution of the PL signal  $I(t)$  is then set by the fast carrier relaxation from the upper excited state (population) and the much slower radiative decay to the lower level (energy dissipation by spontaneous emission), which is determined by the rise time  $\tau_r$  and the decay time  $\tau_d$ , respectively:

$$I(t) = B_0 + A_0(-e^{-(t-t_0)/\tau_r} + e^{-(t-t_0)/\tau_d}), \quad (4.1)$$

<sup>11</sup>See further discussion in the chapter 7.

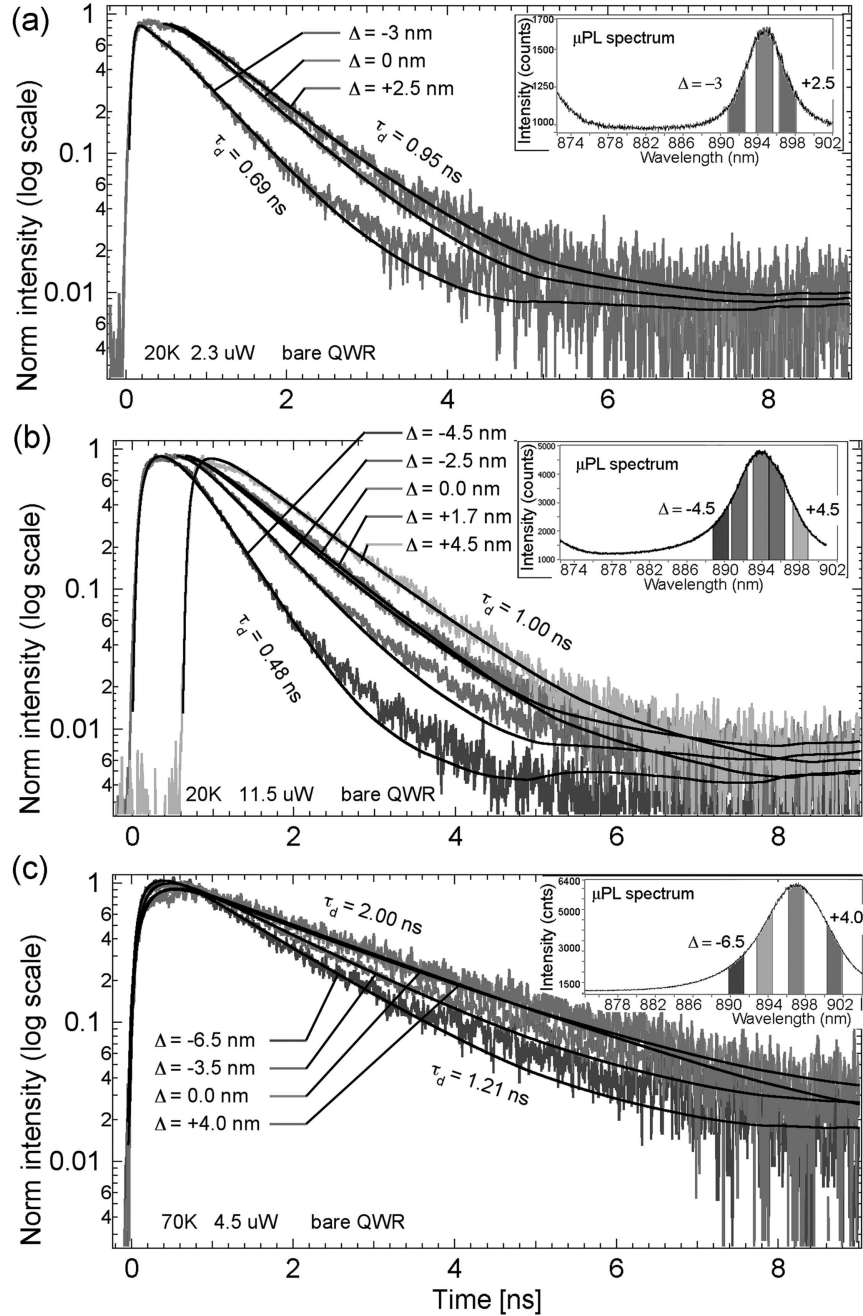


**Figure 4.8:** Spectrally resolved temporal profiles of the micro-PL emission from the *InGaAs/GaAs* QWRs in “free” space measured at different detunings with respect to the corresponding QWR peak. (a) 20K,  $2.3\mu W$ . (b) 20K,  $11.5\mu W$ . The transient at  $\Delta = +4.5nm$  is shifted horizontally for clarity. (c) 70K,  $4.5\mu W$ . Fitting employs single-exponential decay and convolution with the instrumental-response function. Insets present corresponding micro-PL spectra (acquired on the CCD), where spectral “windows” probed in time-resolved measurements are depicted; corresponding detuning  $\Delta$  with respect to peak is indicated.

with  $A_0$ ,  $B_0$  being constants<sup>12</sup>. These relaxation dynamics are defined by microscopic processes (e.g. scattering) and therefore depend on the carrier density and the temperature. Furthermore, it should be strongly influenced by the 1D density of states and Coulomb correlations. Different charge-carrier species may form (e.g. electron-hole plasma, free and localized excitons) and, having different energy-momentum properties, can contribute to the inhomogeneously broadened QWR emission spectrum. Therefore the radiative lifetime is expected to vary across this spectrum, in particular at moderate excitation powers. The high-density regime is nevertheless important, in general, for device applications, and in particular when both spontaneous and stimulated emission are of interest, which is nominally the case for the framework of this thesis. It has been shown however that in the case of QWRs, contrary to QWs, even at very high carrier densities the radiative recombination is dominated by excitons and not by free 1D carriers [197]. In addition, at low temperatures ( $\sim 10 \div 40K$ ), the excitons are strongly localized [194] due to interface roughness [71, 198] within different spatial sites described by a random-fluctuations disorder potential. From this we can eventually expect a mono-exponential spontaneous-emission decay [197] with different time constants if probed locally across the QWR PL spectrum.

#### 4.4.1.1 Bare QWRs at low (20K) temperature

At low temperature ( $\sim 10 \div 20K$ ) the radiative lifetime is expected to decrease towards the high-energy QWR tail. This is because at relatively high excitation powers (electron-hole density  $> 10^5 cm^{-1}$  [195]) the excitonic population can extend from the lower-energy fully localized states to higher-energy more extended ones. The excitonic nature and the exciton confinement due to disorder potential can result in significantly increased lifetimes compared to those of an ideal case [76, 194]. This is verified here by the time-resolved measurements summarized in Fig. 4.8 (a, b) and Fig. 4.9. The data in (a) and (b) represent micro-PL emission transients taken from 890nm triple-QWR<sup>13</sup> structure at 20K at the excitation power of  $\sim 2\mu W$  ( $\sim 130W/cm^2$  or  $\lesssim 10^6 cm^{-1}$ ) in (a), and  $\simeq 5$ -fold increased ( $> 10^6 cm^{-1}$ ) in (b). The different transient curves are acquired each within a narrow spectral window ( $\sim 1.6nm$ ) positioned at a different detuning  $\Delta$  with respect to the QWR peak, as indicated in the insets. The analysis is performed implementing the bi-exponential model of Eq. 4.1 convolved with the instrumental response. Indeed, as expected, the low-energy tail is the “slowest” most likely due to increased localization of excitons as compared to higher energies where the radiative lifetime<sup>14</sup> decreases by  $\sim 50\%$ .

<sup>12</sup>Note that these are *not* the Einstein coefficients.

<sup>13</sup>Note that, as pointed out earlier (section 3.1.2.1), the 3 stacked QWRs are uncoupled and well aligned spectrally, which makes possible the use of such a structure for the present discussion of dynamics, since nominally one expects more or less identical carrier dynamics for each wire in the stack.

<sup>14</sup>We assume that the non-radiative recombination is not efficient at low temperature, hence radiative lifetimes are equal to the measured decay times. We note however that at higher energies in the QWR emission spectrum the decay time constants can also be affected by carrier hopping down to ground states. This can result in faster decay.

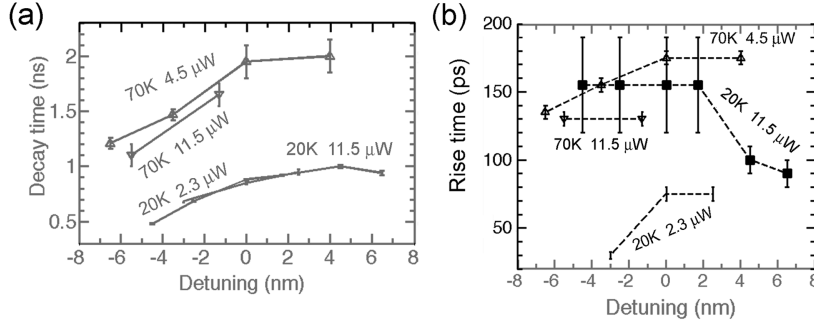


**Figure 4.9:** Overall summary of (a) decay and (b) rise times at different conditions in Fig. 4.8.

This observation is made possible by relatively high carrier densities where higher-energy levels can be efficiently populated. This population is possible due to band filling of the lower-energy states. Comparing the micro-PL spectra in the insets of Fig. 4.8 (a) and (b), one can see that the QWR peak broadens, expanding (its tail) significantly to the high-energy side. The broadening is accompanied by the change in the high-energy slope of the PL peak, namely, the slope becomes much less steep compared to lower powers. This means that the population of higher-energy states indeed happens. At the same time, in the transient PL taken at small detunings this results in observation of a plateau at small delay times, which is explained mainly by the phase-space filling effect [197, 199]. This is further verified in a power dependency at  $\Delta = 0$  (Fig. 4.10). In fact, at high excitation powers the model of Eq. 4.1 fits only if a time translation (up to  $\sim 300 \div 500ps$  for the highest power used) between the rise and the decay is included (see the inset in the upper panel of the Fig. 4.10).

At this point it is worth noting that the emission saturation at  $\Delta = 0$ , observed in the time domain, is already reached at average powers  $\sim 1 \div 2\mu W$  (average density  $\sim 60 \div 120W/cm^2$ ). This value therefore should correspond to a carrier density of  $\sim 10^6 cm^{-1}$  which is just sufficient for the saturation onset of the first QWR subband [61, 197]. Note [Fig. 4.8 (a)] that at the detuning of  $\Delta = -3nm$  for a similar excitation power the saturation is not observed in the transient PL, which supports this estimation. The 5-fold increase in the excitation power [Fig. 4.8 (b)] leads to the emission saturation also at the high-energy QWR tail.

We also would like to note here that the present discussion on the bare QWRs involves two “membrane” kinds of samples. The first is where the QWRs are embedded within the 260-nm *GaAs* membrane grown on top of a thick ( $1\mu m$ )  $Al_{0.7}Ga_{0.3}As$  layer. The latter is a high-energy barrier and is transparent at the excitation wavelength of 730 nm (bandgap  $\simeq 2.058eV$ , or  $\sim 603nm$  [200]). The second one is where this *AlGaAs* (sacrificial) layer is etched away. We checked that these two sample kinds have identical dynamics properties at similar excitation powers, meaning, first, that the actual carrier density is the same in spite of the difference in the interface (*GaAs-AlGaAs* or *GaAs-air*). And secondly, that the slab waveguide does not have an influence. For example, in Fig. 4.10 QWRs situated on the released membrane were used, and the emission saturation features are similar to those of QWRs from a non-released part.

As a second important effect related to high carrier density, the rise time significantly increases with excitation power (Fig. 4.10) indicating that the carrier relaxation

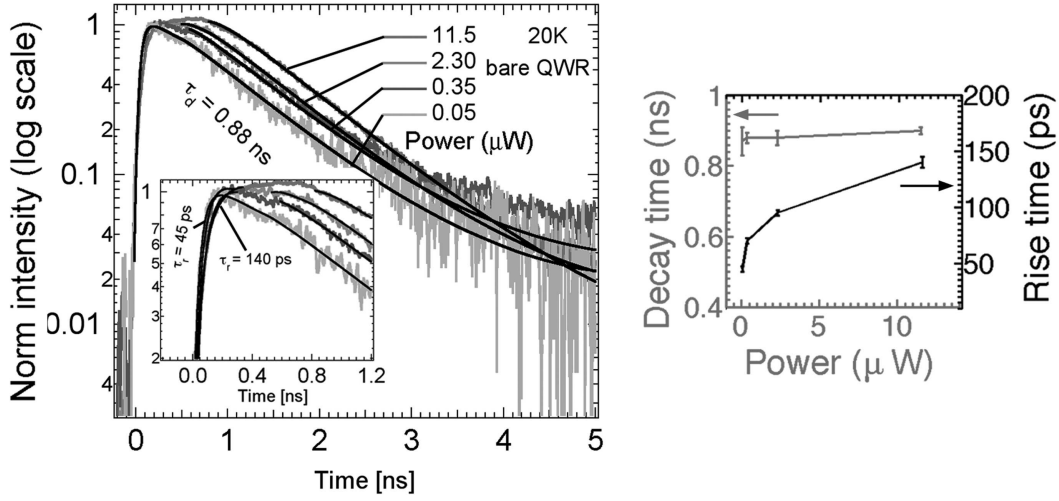


**Figure 4.10:** Power dependence at 20K at  $\Delta = 0.0nm$ . The corresponding decay and rise times are summarized at the right panel.

is slowed down. In addition, at high power similarly large rise time constants are also observed at all the measured negative spectral detunings [see Fig. 4.8 (b) and Fig. 4.9 (b)], which confirms the overall slow relaxation. In the latter case it is difficult to distinguish between the effects of the band filling (observed as a plateau at short delay times) and the slow relaxation (manifested by a large rise time), therefore in the corresponding trend in Fig. 4.9 (b) the error bars are excessively large ( $\pm 35ps$ ). The slow relaxation at low (20K) temperature at high carrier densities may be caused by non-linear phenomena that delay the formation of excitons such as carrier-carrier interactions and the hot-phonon degeneracy accompanying the band filling [201]. Furthermore, since the wires are inhomogeneously broadened due to exciton localization, phonon bottleneck might appear, similar to QDs.

#### 4.4.1.2 Discussion: very long radiative lifetimes

The theoretical result obtained for the spontaneous emission rate in section 2.1.3.1 is valid for an atomic system described by a dipole, either point-like or distributed e.g. isotropically in 3D or 2D [46]. This is interesting since it allows for description of excitons in QWs or QDs [20,202]. In particular, for the *excitons localized* on impurities [203] or due to QW interface roughness. In this respect it is very useful to introduce the so-called *oscillator strength*. It describes the strength of the quantum coupling between two levels (e.g. a transition from  $|i\rangle$  to  $|f\rangle$ ). In terms of the dipole matrix element it can be written as

$$f_0 = \frac{2m_0\omega}{\hbar} |\langle f | \vec{d} \cdot \vec{e} | i \rangle|^2 \quad (4.2)$$

where  $m_0$  is the free electron mass. And for the excitons it is then found that

$$f_{osc} = f_0 \frac{V}{\pi\alpha_B^3} \quad (4.3)$$

where  $V$  is the volume of the crystal. The spontaneous-emission rate is then rewritten as

$$W_{sp} = \frac{1}{\tau} = \frac{n_{opt} e^2 \omega^2}{2\pi \epsilon_0 m_0 c^3} f_{osc} \quad (4.4)$$

where  $n_{opt}$  is the optical refractive index of the medium. The oscillator strength for the excitons depends on the ratio between the volume of the crystal to the exciton volume (determined by  $\alpha_B$ ). For excitons bound at impurities this “volume of the crystal” is then assumed to be that within which the electron and hole wavefunctions effectively overlap, referred to as the so-called “coherence volume” [204]. This volume is covered by the center-of-mass motion, and hence it describes the localization volume. The radiative rate of excitons localized due to the interface roughness<sup>15</sup> in a QWR [205] then scales as

$$\frac{1}{\tau_{bnd}} \sim \frac{V_{loc}}{V_{exciton}} \quad (4.5)$$

Intrinsic QWR lifetimes are expected to be of the order of  $100ps$  [206]. And in our experiments we observed  $\sim 9$ -fold longer times. Assuming then  $V = const \times const \times L_{loc}$  (where the constants are due to 2D confinement) and considering that  $L_{loc} \gtrsim 100 \div 150nm$  doesn't result in an appreciable effect on lifetimes [205] we can then roughly deduce  $L_{loc} \sim 15nm$ . This is approximately twice as smaller than what was estimated for similar (though *GaAs*) wires in [194] where the radiative lifetimes were of the order of  $400ps$ . We shall note that the notion of the “coherence volume” is valid only within the range  $\alpha_B \ll L_{loc} \ll \lambda_0/n_{opt}$  [203], so in our case it is at the limit<sup>16</sup> (as  $\alpha_B \sim 5 \div 10nm$  [58]). In the regime  $L_{loc} \sim \alpha_B$  the radiative rate becomes defined by  $\alpha_B$  and the exciton binding energy, and a QD-like system should be considered.

#### 4.4.1.3 Bare QWRs at high (70K) temperature

At high temperatures above  $\sim 60K$  where the onset of 1D-related carrier diffusion in similar QWRs has been observed experimentally [207], the population kinetics can become complex. More efficient carrier-carrier scattering, exciton-phonon scattering [208] and carrier capture [148] have to be considered. Above 60K a substantial fraction ( $\sim 50\%$ ) of excitons can be ionized [194], however strong Coulomb correlations are expected to be preserved anyway due to the small Sommerfeld factor [61, 65]. Therefore the radiative lifetimes, not governed by purely free carriers, are expected still to be long with a single-exponential decay [197]. Secondly, the overall QWR spontaneous-emission decay time is expected to increase significantly [194] due to population averaging in momentum-space over both optically active and inactive excitons because of the temperature-induced spread in the occupation function [60, 209]. In this work this is also experimentally verified. Fig. 4.8(c) displays micro-PL transients taken at 70K at specific spectral locations across the QWR-emission spectrum (as indicated in the

<sup>15</sup>We should note that for our structures additional source of localization may be due to *In - Ga* alloy fluctuations, which however does not change the description.

<sup>16</sup>Below the limit  $L_{loc} < \alpha_B$  the notion of the coherence volume is obsolete and formulae similar to the atomic case (e.g. point-dipole approach) are suggested [203] for calculation of the radiative rates.

inset). All the transients show rather long decays ( $\tau_d \simeq 1.2 \div 2ns$  depending on  $\Delta$ ). In parallel, we observe that the QWR line broadens and the integrated PL intensity increases compared to the 10K PL signal. This increase of the QWR PL signal (spectrally and temporally integrated intensity) at elevated temperatures (by a factor of  $\sim 4$  here at 70K) happens at the expense of the recombination in the GaAs barrier and the QWs, due to thermally activated carrier channeling from the QWs directly connected to the V-groove QWR similar to what was observed in [148]. Taking this into account, at the excitation power of  $\sim 4.5\mu W$  (average power density  $\sim 250W/cm^2$ ) the carrier density is therefore of the same order as for the Fig. 4.8 (b) because, effectively, almost the whole radiative recombination happens within the QWRs. At such a high density the emission saturation effects should be present. From the fits done using Eq. 4.1 indeed rather long rise time constants ( $\sim 160ps$ ) are deduced [Fig. 4.9 (b)]. Finally, the fact that both the PL spectrally integrated signal and the decay times are increased suggests a *slow non-radiative recombination rate* for such QWRs at 70K.

To summarize this subsection, we have examined the emission dynamics of the *InGaAs/GaAs* QWRs at high carrier densities, the regime potentially interesting for laser device applications. Emission saturation effects were tracked and the relaxation slow-down observed. Characteristic time constants were thus extracted, which will be necessary for examining PhC cavity and bandgap effects for this particular emitter, as well as considering the dynamics properties of QWR-PhC lasers.

#### 4.4.2 Quantum-wire emission in photonic-crystal cavities

To get insight into the effects induced by the PhC cavities on the *spontaneous* emission of the QWR we have to take carefully into account the power dependency of the light emitted into a cavity mode. As will be discussed in detail in chapter 7, both spontaneous and stimulated emission can be present within the mode of interest, which can be observed from the PL transients as, roughly speaking, slow and very fast decay components, respectively [210–212]. Measurements at sufficiently low excitation powers (although high enough to overcome the possible intrinsic QWR absorption) are thus required. For clarity, excluding coherence effects in the present section, we shall concentrate only on PhC-QWR devices that did not feature lasing in power-dependent characteristics. Thus peculiarities of only *spontaneous* emission of QWRs in short PhC microcavities can be discussed here. *Stimulated* emission will be discussed in chapter 7.

In order to properly establish the influence of PhC cavities on the QWR emission, details of QWR carrier dynamics discussed in the previous section have to be taken into account. Namely, the comparison of the decay rates should be done respecting the spectral detuning of the cavity mode relative to the QWR emission peak. Since relaxation effects (e.g. hopping from high-energy down to the low-energy states) may take place, we shall make observations on the Purcell effect only at small spectral detuning with respect to the QWR emission peak. Larger detuning will be then discussed. We concentrate explicitly on the  $L_{3m}$  and  $L_6$  cavities as these small-volume resonators are of particular interest for the single-mode laser devices.

#### 4.4.2.1 Preliminary results on the 930nm single QWR in $L_6$ cavity

First results were obtained on the PhC-QWR sample presented in section 4.3.1.1 which is an  $L_6$  cavity resonantly tuned to match the QWR emission peak [see  $r/a = 0.244$  in Fig. 4.4 (b)]. The result is shown in Fig. 4.11 where a bare-QWR transient micro-PL is compared to that collected with a narrow spectral window ( $\simeq 0.15nm$ ) from the cavity mode. Since the 920nm detection wavelength is at the very limit of our detector sensitivity (quantum efficiency  $< 0.1\%$ ) quite a high excitation power was used (hence there is saturation of the bare QWR), and still the collected signal is somewhat weak. Therefore the quantitative studies on the QWR-PhC spontaneous emission are done

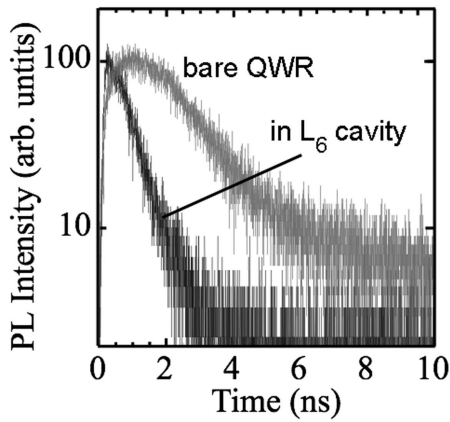


**Figure 4.11:** Transient micro-PL on a single QWR emitting at around  $\sim 930nm$ . Bare QWR is compared to the one collected from the  $L_6$  cavity fundamental mode. Decay times:  $\tau_{bare} \sim 1.2ns$ ,  $\tau_{cav} \sim 0.45ns$ .

with the wires at 890nm (where the quantum efficiency of the detector grows by more than an order of magnitude). And here we would only like to note that (i) in the cavity response we do not see the saturation at short delay times; and (ii), most importantly, the emission rate to the cavity mode is *enhanced* by  $\tau_{bare}/\tau_{cav} \simeq 2 \div 2.5$  (based on exp-decay fits). We will keep it in mind for reference and proceed to more detailed discussion in the next subsections with QWRs emitting at  $\sim 890nm$ .

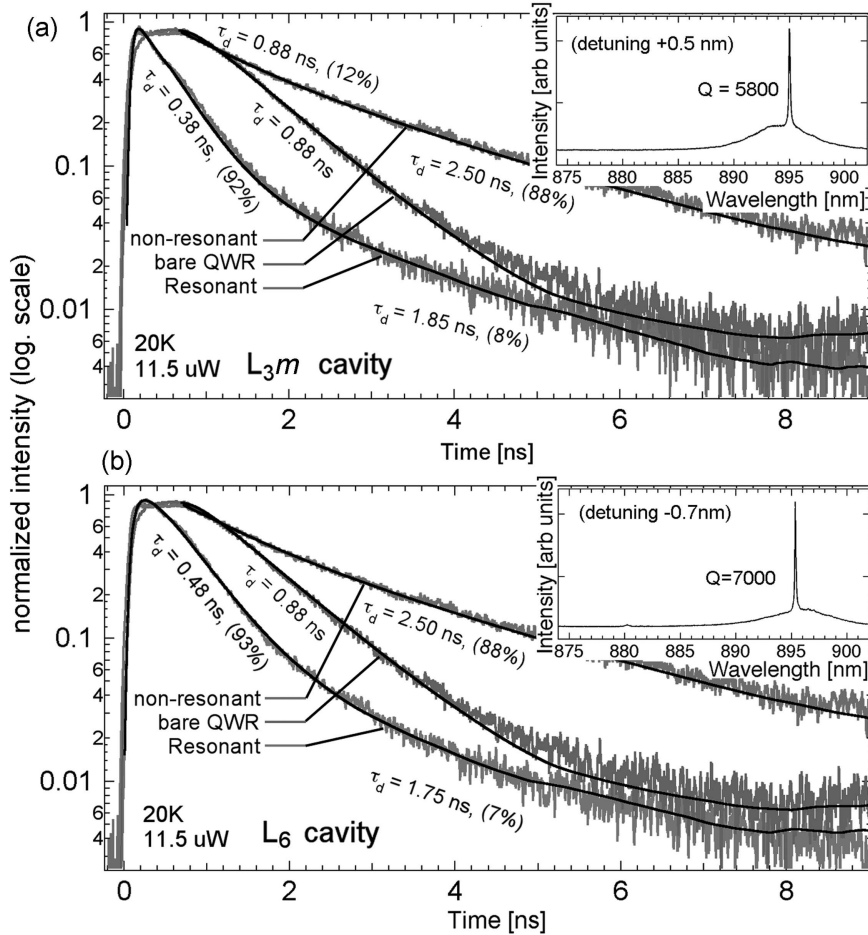
#### 4.4.2.2 $L_3m$ , $L_6$ cavities at low (20K) temperature and the Purcell effect

Figure 4.12 presents measured micro-PL transients of the  $L_3m$  and  $L_6$  cavities tuned into resonance with the QWRs (see the insets). The transients, measured with a narrow spectral window ( $\sim 0.11nm$  with  $70\mu m$  monochromator exit slit width) positioned on the cavity mode, are compared to those taken from the emission peak of a bare QWR and the one located within a different cavity ( $L_3$ ) having largely blueshifted resonance ( $\sim -13nm$ ). In the latter case the detuning is large such that no QWR emission can be coupled to the mode, and at the same time it is ensured (separation  $\sim 40nm$ , see Chapter 5, Fig. 5.1) that the QWR emission cannot couple to low-energy photonic bands outside the PBG. Therefore the QWR emission is located well within the PBG. A first observation made from the analysis of the transients is that the cavity decay cannot be fit with a single exponential. Obviously, two major exponentials are clearly distinguished. This is verified by the fitting procedure that also involves a convolution

with the instrumental response function. Namely, the fitting model is a time-dependent function  $f(t) \otimes \text{IRF}(t)$  where  $f(t)$  is

$$f(t) = B_0 + A_0(-e^{-(t-t_0)/\tau_r} + e^{-(t-t_0)/\tau_d}) + A_1e^{-(t-t_0)/\tau_{d2}} \quad (4.6)$$

We propose that the presence of a double-exponential decay is explained by the fact that within the probed narrow spectral region of the cavity mode not all the QWR emission is coupled into this mode, which has to do with inhomogeneous broadening (see Fig. 2.5). The slower decay rate (time constant  $\tau_{d2} \sim 1.8\text{ns}$ ) is  $\sim 2$  times slower than that of the bare QWR ( $\tau_d \sim 0.88\text{ns}$ ). It is therefore ascribed to the *inhibited* QWR emission within the PBG. The faster component, compared to the bare-QWR emission, evidences an *enhancement* of the emission rate by a factor of  $\simeq 2.33$  and  $\simeq 1.83$  for the  $L_3m$  and  $L_6$  cavities, respectively. The presence of the two decay components is also supported by the micro-PL spectrum [Fig. 4.12 (insets)]. Indeed the cavity mode in each of the two cases is apparently “sitting” on top of the QWR background. According to an estimate



**Figure 4.12:** Transient micro-PL emission from  $In_{0.15}Ga_{0.85}As/GaAs$  QWRs (triple QWRs) in resonance with PhC microcavities (a)  $L_3m$  cavity, and (b)  $L_6$  cavity, compared to both bare QWRs and QWRs out of resonance. The insets show corresponding micro-PL spectra (when in resonance). Experimental conditions: 20K,  $11.5 \mu W$ .

given by the ratio  $A_1/A_0$ , there is less than  $\sim 10\%$  of the QWR emission uncoupled to the cavity mode. The uncoupled emission may stem from the following source. As the inhomogeneous broadening is mainly due to exciton localization, the collected intensity in the spectrum, although within the narrow spectral window ( $\sim 0.15nm$ ), may contain some of the emission from the spectrally off-resonant localized emitters (Fig. 2.5). Since however they are all embedded within the PhC environment, they experience the PBG effect of the emission-rate inhibition.

The enhanced emission rate has to be also compared to that of the QWR spectrally positioned within the PBG but distinctly out of resonance. The corresponding transient in the Fig. 4.12 fits also two exponentials with time constants of  $\simeq 0.88ns$  and  $\sim 2.5ns$  (conservative estimate) suggesting, via the  $A_1/A_0$  ratio, that  $\sim 10\%$  of the emission belongs to the bare QWR. Thus, with respect to the QWR spectrally positioned within the PBG, the enhancement rate produced by the cavity is  $\simeq 6.6$  and  $\simeq 5.2$  for the  $L_3m$  and  $L_6$  cavities respectively. Note that the QWR emission uncoupled to the cavity mode experiences smaller inhibition. This is possibly because the low local density of electromagnetic states within the PBG is still perturbed in this case by the presence of the mode. In the case of the inhibited QWR emission the part “uncoupled” to the PBG can be explained as emission strictly perpendicular to the PhC membrane where the TIR condition is not satisfied.

At this point it is interesting to compare the Purcell effect inferred from the experiment (cavity-induced enhancement of the spontaneous-emission rate by  $F_p \sim 2.33$  and  $F_p \sim 1.83$  for the  $L_3m$  and  $L_6$  cavities, respectively, compared to bare QWRs) to that estimated theoretically. According to Eq. 1.19, given the  $Q$ -factors of  $5000 \div 6000$  and  $6000 \div 7000$  along with mode volumes<sup>17</sup>  $V \sim 0.9$  and  $\sim 1.6(\lambda/n)^3$  for the  $L_3m$  and  $L_6$  cavities respectively, the maximum effect from such cavities is  $F_P \sim 250 \div 500$ . These rather big factors will be significantly reduced due to reasons discussed in section 2.1.3.2. Namely, due to (i) mismatch to the field maximum, (ii) spectral mismatch, (iii) dipole orientation. Importantly, these factors are subject to averaging over the ensemble of distributed localized emitters (localized excitons in QWRs). E.g. some spectrally resonant emitters can be located exactly in the field nodes (see Fig. 4.2 for mode patterns), reducing thus the average measured Purcell effect from the ensemble. Averaging should also include the out-of-plane direction (QWRs shifted vertically with respect to the membrane center in the triple-QWR stack). Altogether  $F_P$  is estimated to be scaled by  $\sim 0.1$ . Secondly, each localized emitter is broadened. Homogeneous broadening (e.g. due to carrier-carrier interaction) can be  $\sim 1meV$ , which, compared to the cavity-resonance linewidth of  $\lesssim 0.15nm$ , gives an additional reduction by  $\sim 0.2$ . Therefore  $F_P$  is expected to reduce down to factors of  $\sim 5$ , which is reasonably close to experimentally observed values. As the distribution of the disorder-induced localized sites is unknown, these estimations can only be qualitative.

The second interesting cavity-related effect observed from the analysis of the Fig. 4.12 concerns the carrier relaxation (that populates QWR states from where<sup>18</sup> then

<sup>17</sup>Calculated from the 3D  $E$ -field profile as  $\int \epsilon |\vec{E}|^2 dx dy dz / \max(\epsilon |\vec{E}|^2)$ .

<sup>18</sup>See also relevant discussion in Sec. 7.3.3.4 and also Fig. 7.15.

the spontaneous emission takes place). As discussed in section 4.4.1, at high enough excitation levels the bare-QWR emission saturates exhibiting a flat plateau at small delay times and a slow relaxation rate (increase of the rise-time constant up to  $\tau_r \simeq 100 \div 150ps$ ). The situation largely changes if the QWRs are placed into a PhC cavity. These changes (Fig. 4.12) touch upon both in-resonance and off-resonance cases. In resonance with the cavity mode, the QWR emission has a short rise time ( $\tau_r \simeq 35ps$ ) and then decays without any delay. Out of resonance, the QWR emission within the PBG clearly shows a rather long ( $\sim 600ps$ ) plateau, however the rise time is similar to that of the resonant condition. At the same excitation power ( $11.5\mu W$ ) the bare QWR is saturated with a similarly long plateau but much longer rise time ( $\tau_r \simeq 150ps$ ). Considering the excitation-beam spot as a Gaussian with a FWHM of  $\sim 1.5\mu m$  and that the PhC  $L_N$  cavity of an effective length of  $\sim 1.5\mu m$  surrounded by air holes has a width of  $\sqrt{3}a$ , the crudely estimated absorbed power on the surface should reduce down to  $\sim 0.2$  of the incident one. On the other hand, the collected integrated PL intensity from the off-resonant cavity is only 10% smaller than that from the bare QWRs on a released-membrane part. However, by comparing the high-energy slopes of these two QWR peaks plotted in log scale [148], we deduce that the carrier density is smaller in the case of the QWRs in the off-resonant cavity. Actually, compared to the corresponding QWR PL peak, the effective carrier density is rather similar to or smaller than that of bare QWRs at  $\sim 2.3\mu W$  (Fig. 4.9). This means that the rise time constant is expected to be low. On the other hand, the length of the saturation plateau in the off-resonant transient is caused by a very slow emptying of the states ( $\tau_d \simeq 2.5ns$ ). Therefore, off-resonance, the QWR emission saturation happens at lower carrier densities compared to bare wires, which is caused by the PBG effect of the *inhibition* of the spontaneous emission.

On the other hand, in-resonance, no saturation effects are observed. This indicates that indeed the emission rate into the cavity mode is *enhanced*, particularly with respect to the off-resonance emission. This is an important point, since, as we have measured, the emission into the cavity mode is much faster compared not only to the off-resonance cavity but also to the emission background spectrally close to the mode, that is, the emission into leaky modes. Significantly favoring the spontaneous emission into the cavity mode with respect to *all* other ones is expected to improve the performance of various light sources, in particular, lasers [102].

#### 4.4.2.3 Cavity-QWR detuning

At large detunings towards shorter wavelengths with respect to the QWR-emission peak, the QWR is expected to have a much faster carrier dynamics [195] [see Fig. 4.8 (a, b)], therefore cavity and PBG effects have, in principle, to be scaled accordingly. Figure 4.13 shows PL transients extracted from a  $L_3m$  cavity with the fundamental mode detuned by  $\simeq -6.5nm$  towards the QWR high-energy tail. As can be seen from the major decay time constant ( $\tau_d = 290ps$ ) the decay of the spontaneous emission into the cavity mode is  $\sim 25\%$  faster compared to the case of zero QWR-cavity mode detuning [Fig. 4.12 (a)]. The inhibited QWR emission measured at the same  $\simeq -6.5nm$  detuning from

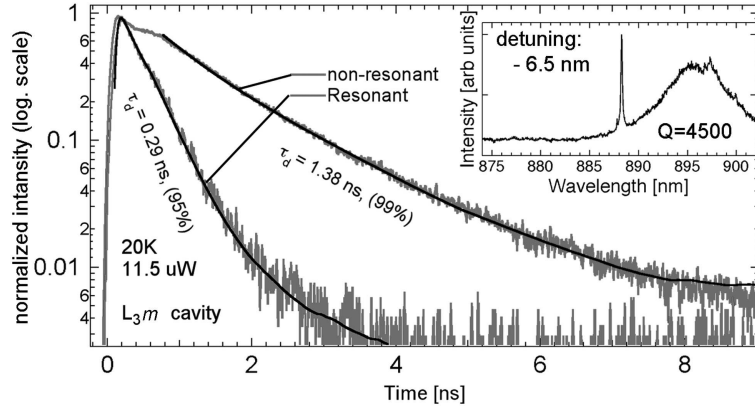


**Figure 4.13:** Transient PL emission from the  $L_3m$  cavity at a large mode-QWR spectral detuning. Also shown is the transient PL signal from QWRs in off-resonance PhC cavity collected at the same detuning. The inset shows corresponding micro-PL spectra (CCD). Experimental conditions: 20K, 11.5  $\mu W$ .

QWRs in the off-resonance PhC cavity ( $L_3$  with mode detuned by  $-13nm$ ) is then given by a decay constant of  $\simeq 1.38ns$  (which is  $\sim 45\%$  shorter time compared to the QWR emission peak from this same cavity). The measured rise times are of the order of  $\simeq 25 \div 30ps$ . The bare QWR taken at  $\simeq -4.5nm$  detuning (the largest detuning measured due to a drop in the PL signal) features a decay time constant of  $\simeq 450ps$  which is expected to decrease further by  $\sim 30\%$  [195] (i.e. down to  $\sim 320ps$ ). Therefore the measured cavity effect becomes somehow much less pronounced ( $\tau_{QWR}/\tau_d \approx 1.1$ ). The weak cavity emission-enhancement effect might be due to carrier hopping from higher-energy to lower-energy states, which suggests that such detuning conditions are not optimal for inferring the Purcell effect. In such conditions, if the cavity effect is small compared to other decay channels in carrier dynamics, a cavity mode may serve just as a carrier-relaxation probe [195] relying on the directionality cavity effect that enhances the PL collection efficiency. On the contrary,  $\Delta = 0nm$  or small positive QWR-cavity spectral detunings would then give correct enhancement factors, which was exploited in the preceding subsection.

#### 4.4.2.4 Power dependence

We further investigated the cavities at different excitation powers. The results are summarized in Fig. 4.14. Starting the discussion with the transients presented in Fig. 4.14 (a) and (b) for the  $L_3m$  and  $L_6$  cavity respectively, we notice that as the excitation power is increased up to relatively high levels ( $\gtrsim 30\mu W$  for  $L_3m$  and  $\gtrsim 20\mu W$  for  $L_6$ ) a certain degradation in the device performance is observed. This is noticed from the build-up of the saturation at small delay times. As seen from the rise exponentials (see zoomed transients in the insets), the emission saturation is governed by a significant increase of the rise time constants (from  $\simeq 30ps$  up to  $\simeq 160ps$  for the  $L_3m$  and up to  $\gtrsim 200ps$  or  $L_6$ ), which indicates a slower relaxation and band filling effect at high carrier densities. In addition, the decay times of the QWR emission coupled to the mode and that “coupled” to the PBG increase and decrease, respectively (see plots in

the second inset), which serves as another indication that the cavity and PBG effects are overwhelmed by slow carrier relaxation. At the same time, since we do not clearly see a formation of the flat plateau at small delay times (as in the case of bare QWRs and QWR emission out of resonance), the carrier relaxation is slowed down mainly by effects in which the phase-space filling, although present, has not the major contributing part. Generally, with increasing excitation power, on the way to lasing, below threshold,

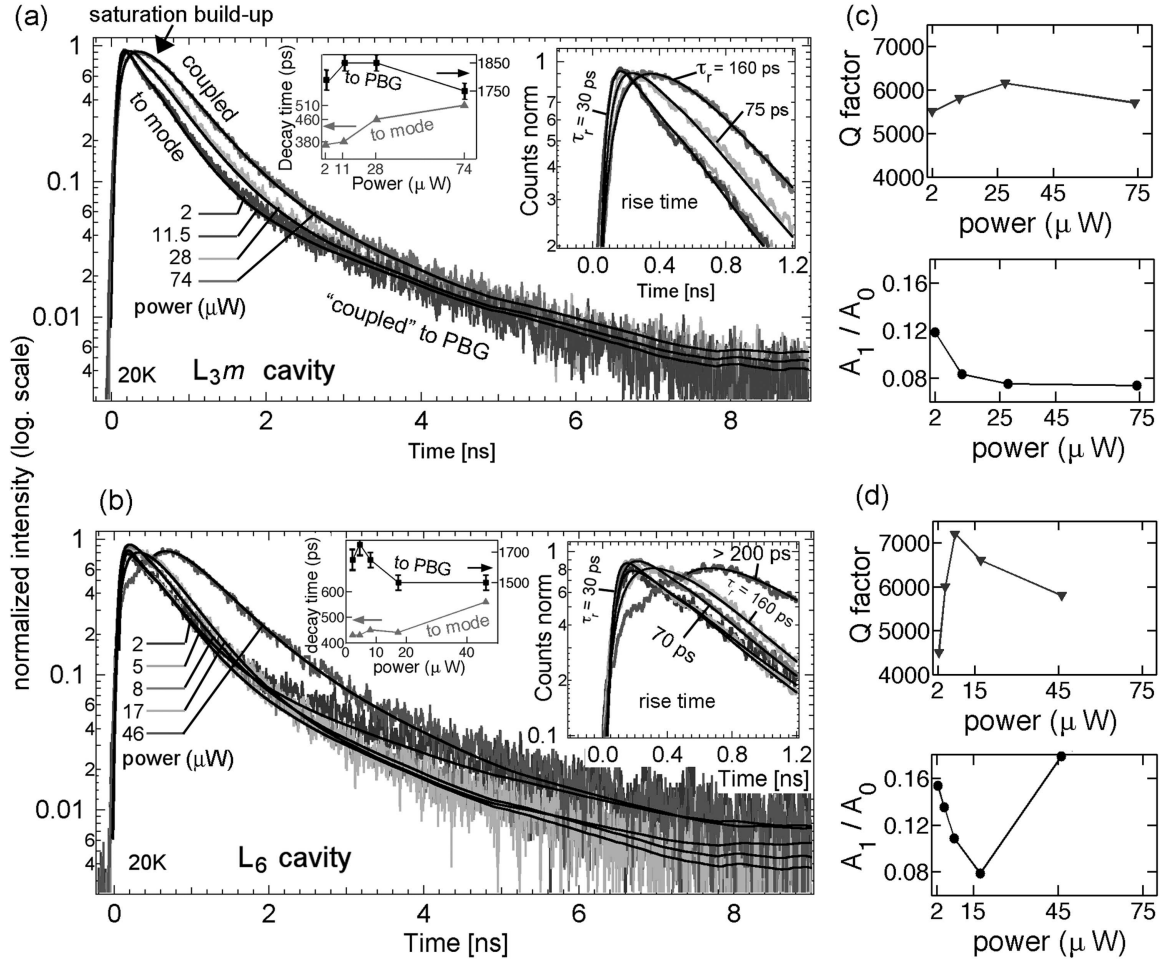


**Figure 4.14:** Power dependence of the transient PL from (non-lasing) (a)  $L_{3m}$  and (b)  $L_6$  cavities presented in the Fig. 4.12. Time constants are summarized in the insets. (c), (d) corresponding  $Q$ -factors extracted from CCD spectra and fraction of the background spontaneous emission (“coupled” to the PBG) estimated from the fits (see Eq. 4.6) for  $L_{3m}$  (c) and  $L_6$  (d) cavity, respectively.

a semiconductor microcavity LED device is expected to exhibit effectively a decrease in the decay times [213] and a non-linear changes in linewidth (narrowing and broadening, then followed by a “fast” decrease above threshold) [102, 214]. Below threshold, one can also expect a decrease of the intensity ratio of the background spontaneous emission with respect to that coupled into the mode. The latter characteristic in the case of non-lasing devices (Fig. 4.14) can be estimated from the transients as a simple ratio

$A_1/A_0$ . In Fig. 4.14 (c) and (d) both  $Q$ -factor and the  $A_1/A_0$  ratio are plotted versus excitation power. We notice that, as the power is increased, the  $Q$ -factors saturate and then decline<sup>19</sup>. At the same time, the  $A_1/A_0$  ratio tends to stabilize or grow, that is, there is no appreciable increase of the emission into the mode, which is also verified in the CCD-acquired micro-PL spectra<sup>20</sup>. Note, that at the same time, the rise times of the transients also grow to a large extent. Therefore it is highly unlikely that these particular PhC-QWR structures can overcome the lasing threshold at yet higher excitation powers due to very slow carrier relaxation.

#### 4.4.2.5 High temperature (70K) characteristics

At high temperatures the recombination in the QWRs can result in more intense PL signal compared to the low-temperature case at similar excitation powers. This is because the energy  $k_B T$  corresponding to 60-70K can exceed both the potential barrier between the QWR and side QWs and the disorder potential. And, effectively, assisted by phonons, a larger number of states can be populated due to the carrier capture from the QWs [148] and the carrier diffusion [207]. Due to these reasons coupling into a cavity mode is expected to be more efficient because of increased optical-mode overlap with the carrier extended states and due to possible scattering of carriers into the mode. (The latter can be caused by formation of a spatial and a spectral hole induced, respectively, by the cavity-mode near-field pattern with pronounced localized antinodes (see Fig. 4.2) and a high- $Q$  resonance into which the spontaneous-emission decay rate is faster compared to that off-resonance.

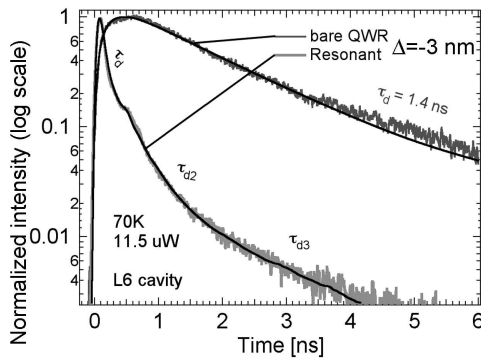


**Figure 4.15:**  $L_6$  cavity at high temperature (70K) compared to the bare-QWR emission at similar spectral detuning  $\Delta$ .

Figure 4.15 presents a micro-PL transient measured from the  $L_6$  cavity previously studied at low temperature in section 4.4.2.2 (and also section 4.4.2.4) compared to a bare QWR at a proper spectral detuning  $\Delta$ . The excitation conditions are similar ( $\simeq 11.5\mu W$ ). Whereas the QWR decay rate is rather slow ( $\tau_d \sim 1.4ns$ ), the major signal emanating from the cavity is very fast. It is however difficult to judge whether

<sup>19</sup>Note that this decline of the measured  $Q$  cannot be ascribed to the effect of linewidth broadening at threshold [214] since the latter for our devices is expected at much lower powers (see chapter 7).

<sup>20</sup>Although the spectra do not change much qualitatively from what is shown in the insets of Fig. 4.12.

the response has to be considered as either non-exponential or containing several exponential decay components. The triple-exponential fit was considered yielding the decay time constants of  $\tau_d \approx 55ps$ ,  $\tau_{d2} \approx 320ps$  and  $\tau_{d3} \approx 1.3ns$  with relative weights of 92, 7 and 1% respectively; the rise time is  $\sim 30ps$ . Whereas the slowest decay component may be ascribed to the emission uncoupled to the mode (as in the case of Fig. 4.12), comparison of the two major decay constants to that of the bare QWR gives an enhancement factor of  $\sim 27$  and  $\sim 4.5$ . According to the previous discussion (sec. 4.4.2.2), the factor of 27 seems to be too big to be assigned to the enhanced spontaneous emission. Similar PL decay was observed for several  $L_3m$  and  $L_6$  cavities with  $\tau_d \sim 50ps$  and  $\tau_{d2} \sim 200 \div 500ps$  (depending on the detuning  $\Delta$ ) although in many cases the fast component was less intense.

Comparing to  $\tau_{d2}$ , the fact that the bare QWR is very slow at this temperature ( $\tau_d \sim 1 \div 2ns$ ) gives an average spontaneous-emission enhancement factor of  $\sim 4.5$ , which is not much higher than the estimated values (section 4.4.2.2). The larger factors, as compared to those obtained at lower temperature, can be probably explained by the hypothesis that whereas in the case of bare QWRs at a high temperature an averaging over the spread excitonic population has to be taken to account for the observed increase in the lifetime [60, 209], the recombination rate into the cavity mode is fixed (at a given wavelength) by the cavity properties that do not depend on the temperature in terms of the excitonic spread. Additionally, fast stimulated emission might be present (accounting for  $\tau_d \sim 50ps$ ) causing also hole burning effects, which can promote (fast) scattering of the high- $k$  carriers into the mode [215]; therefore the effective  $\tau_{d2}$  decreases.

#### 4.4.2.6 Non-radiative recombination (at 70K)

As a second important result, at 70K we did not observe a signature of QWR spontaneous-emission inhibition (Fig. 4.16). The decay rate in this case was measured from several cavities of different lengths ( $L_3$ ,  $L_6$  and  $L_{35}$ ) with resonances shifted to short wavelengths (by  $\sim 4 \div 15nm$ ) with respect to the QWR emission peak; and the signal was acquired from within a relatively narrow spectral window (up to  $\sim 1.9nm$  for the largest QWR-cavity detuning) centered at the QWR emission peak (i.e.  $\Delta = 0nm$ ). The resulting average decay time was found to be  $\langle \tau_d \rangle \simeq 1.12 \pm 0.1ns$ . Several short cavities ( $L_3$ ,  $L_6$ ) exhibited even lower decay time constant of  $\sim 0.8ns$ . These values are nearly twice as smaller as compared to the bare QWR [see Fig. 4.8 (c), Fig. 4.9 (a)], whereas we would expect much slower QWR emission when in off-resonance PhC cavity. In order to explain the experimental observations, we must recall that the radiative lifetime exactly corresponds to the measured decay time only if the *non-radiative* recombination can be neglected, which may not be the case at high temperatures. The radiative lifetime  $\tau_{rad}$  at a given temperature  $T$  can be estimated from the expression for the PL radiative efficiency [194]:

$$\eta(T) = \frac{\tau_d}{\tau_{rad}} = \frac{I_T(\lambda, t)}{I_0(\lambda, t)} \quad (4.7)$$

where  $I$  is the spectrally and temporally integrated intensity. Assuming that at 20K the radiative efficiency is still unity, comparing the micro-PL spectra taken from the

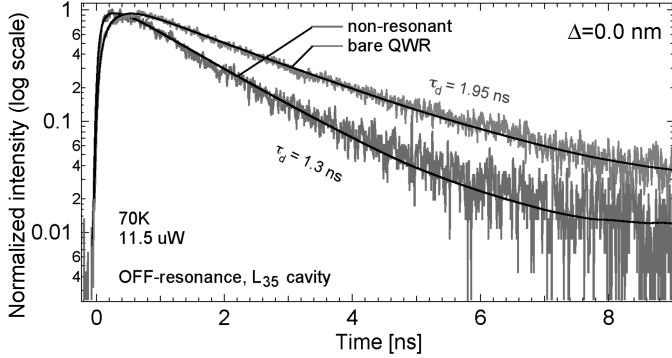


**Figure 4.16:** The “inhibited” spontaneous emission from QWRs incorporated into a long ( $L_{35}$ ) cavity, indicating the presence of non-radiative recombination when compared to the bare QWR. The cavity states are blueshifted by  $\sim 4nm$ , and the transient is taken with a spectral window of  $\sim 2.4nm$  centered at the QWR emission peak (i.e.  $\Delta = 0nm$ ). Bare-QWR micro-PL transient is also at  $\Delta = 0nm$ .

off-resonance cavities at 70K to those at 20K we immediately find that the integrated intensity drops, on average, by a factor of  $\sim 7$ . And by a factor of  $\sim 14$  for the shortest measured decay times. Therefore from Eq. 4.7, the radiative carrier lifetime that characterizes the *inhibited* spontaneous emission is at least  $\tau_{rad} \sim 8ns$ , which gives a Purcell factor of  $\sim 4$ . This value is consistent with that inferred for the resonant cavities. Assuming then at 70K a diffusion coefficient of  $D \sim 5cm^2/s$  [145,207] the diffusion length is  $\sim 2.8\mu m$ , given by  $\sqrt{2D\tau_{rad}}$ . This is much larger than a half of the  $L_3$  or  $L_6$  cavity length and comparable to the  $L_{35}$ -cavity half-length. Since there is a difference in the radiative efficiencies between short ( $\sim 0.7\mu m$  and  $\sim 1.3\mu m$  for the  $L_3$ ,  $L_6$ ) and long ( $\sim 7.1\mu m$  for the  $L_{35}$ ) cavities, for the short ones a major part of the non-radiative recombination must be due to the exciton diffusion, which results in a low radiative efficiency. On the other hand, since for the long cavities, on absolute scale, the decay time is short and the diffusion is less efficient, other non-radiative sources might be involved.

When estimating the radiative efficiency from the PL spectra, we also have to take into account two factors (that may affect the actual carrier density in the QWRs): the loss due to the non-radiative recombination of carriers excited within the *GaAs* matrix or trapped within the QWs on the *GaAs*/air interfaces of the PhC holes; and second, the carrier capture by the QWRs from the side QWs. Including the diffusion-driven non-radiative recombination in the QWRs, the balance between all these processes will define the effective carrier density and the radiative efficiency. The discussion above is correct if the rates of carrier capture  $GaAs \rightarrow QW$ ,  $QW \rightarrow QWR$ ,  $GaAs \rightarrow QWR$  are faster than those non-radiative due to carrier diffusion in *GaAs* and QW followed by recombination on surfaces of the PhC holes, which seems to be a plausible assumption.

Finally, it is useful to estimate the non-radiative lifetime ( $\tau_{nr}$ ) at this (70K) temperature. As the total lifetime of excitons can be written as

$$\frac{1}{\tau_0} = \frac{1}{\tau_{rad}} + \frac{1}{\tau_{nr}}, \quad (4.8)$$

this can be done by comparing the PL decay of QWRs within the off-resonance cavity to the bare QWRs, both at 70K. First, since it was found (sec. 4.4.1.3) that for the bare QWRs at this particular temperature the non-radiative recombination is still not

significant, then the bare-QWR decay constant can be safely assumed as  $\tau_{rad} = 2ns$ . Secondly, taking an average measured value of the decay constant for the off-resonance cavity of  $\tau_0 = 1.1ns$  and assuming that the bare-QWR rate was inhibited by a factor of 4 (i.e.  $\tau_{rad} = 8ns$ ), we get  $\tau_{nr} \simeq 1.25ns$ .

## 4.5 Chapter summary

To summarize the chapter, based on our modeling numerical tools we were able to correctly describe general resonant spectra of short  $L_N$ -type cavities (e.g.  $L_3, L_6$ ) recalling their connection with a corresponding PhC waveguide (W1). This approach will be developed in a greater detail in the next chapter with the application to tracking a 1D photonic band formation and PhC-lattice disorder effects. Here, based on computations, real PhC-cavity samples incorporating single or several vertically stacked QWRs were designed, fabricated and characterized using micro-PL experiments. Rather efficient coupling of the QWR spontaneous emission to the  $L_3, L_6$  cavity modes was observed, and the modes were identified in a consistent way utilizing resonance tuning by the PhC  $r/a$  parameter. Resonance tuning by temperature and by the “digital etching” [135] were also explored, the latter aimed to act against the oxide-related absorption.  $Q$ -factors of up to  $\sim 5000 \div 6000$  were routinely obtained for  $L_3m$  and  $L_6$  cavities (and up to  $\sim 3000$  for the unmodified  $L_3$ ). Pronounced power-dependent  $\lambda/\Delta\lambda$  increase for some of the similar structures was registered (which will be discussed separately in chapter 7). Properties of the spontaneous emission of the  $In_{0.15}Ga_{0.85}As/GaAs$  V-groove QWRs in the PhC cavities were discussed on the basis of time-resolved micro-PL measured at low (20K) and high (70K) temperatures. Cavity-induced spontaneous-emission *enhancement* by factors  $\sim 2 \div 2.5$  was observed, strongly affected by the exciton localization and inhomogeneous broadening of the QWRs (causing averaging effects in the measurement). Complementary, photonic-bandgap induced *inhibition* of the spontaneous-emission rate by a factor of  $\sim 2 \div 3$  (when off-resonance) was experimentally observed at low temperature. At high temperature a strong influence of the non-radiative recombination hindered the observation of this latter effect, although an estimate based on radiative efficiency gives a factor of 4. On the other hand, at high temperature, recombination into a cavity mode seems to be efficient, although further and more detailed studies are required to better verify that. In total, observations made here indicate favorable conditions and a practically feasible perspective of obtaining stimulated emission and low-threshold lasing in such QWR-PhC structures.

## Chapter 5

# One-dimensional photonic band formation in $L_N$ photonic-crystal cavities

Among all possible geometries, cavities of the  $L_N$  type – namely, line defects formed by  $N$  missing holes in a two-dimensional (2D) PhC hexagonal lattice – have established themselves as practically useful 0D and 1D confined photonic structures. These configurations allowed for the observation of strong light-matter coupling [110] and for the realization of quantum-optics experiments [113], single-photon generation [216], photon transfer [193], and PhC bandgap lasers [115]. Recently, long ( $\sim 10 \div 20$  unit cells) 1D-like  $L_N$  cavities have been identified as good candidates for producing extremely high spontaneous-emission enhancement factors, and similar structures, embedding quantum dots, have been proposed for the realization of an ”on chip” single-photon gun [217]. In practice, however, the fabrication of 1D (or even 1D-like) PhC systems is challenged due to their sensitivity to disorder, which induces mode localization and reduces the effective dimensionality.

In the present chapter, we discuss the properties of  $L_N$  cavities of increasing length, showing evidence of a transition from fully confined photonic cavities to a 1D PhC waveguide. These studies were carried out by performing extensive micro-photoluminescence (PL) measurements, as well as by modeling the PhC structures with a 2D finite-difference (FD) method. We also propose that the field distribution of any  $L_N$  cavity mode can be written as a linear combination of the Bloch eigenfunctions of the corresponding  $W$ -type<sup>1</sup> waveguide. Such an analytical approach is insightful for the discussion of 1D photonic band formation. In addition, as in *real* cavities the  $0D \rightarrow 1D$  transition is hindered (although not inhibited) by the presence of disorder, we will examine these important disorder effects experimentally and by numerical analysis.

---

<sup>1</sup>E.g.  $W1$  waveguide is formed just by omitting one row of the PhC holes. Waveguide can be wider (e.g.  $W2$ , two rows) or narrower (e.g.  $W0.6$ , where all the PhC holes are shifted [218]).

## 5.1 One-dimensional photonic system

### 5.1.1 1D photonic-crystal waveguide

In general terms, the frequency eigenstates of a 1D-periodic guiding PhC system are characterized by a well-defined 1D momentum vector,  $k_x$  (where  $x$  is the direction along which the system is periodic). On the other hand, in  $L_N$  cavities, where  $x$  is also a confinement direction, the system accommodates a discrete number of confined modes. By expressing these modes as a linear combination of the 1D Bloch eigenstates of a  $W1$  waveguide, it is possible to verify that in short cavities the high degree of spatial localization results in a  $k_x$ -space spreading over many  $W1$  Bloch functions. This is apparent from the Fourier transform of the real-space mode patterns. As the cavity length is increased, however, the initially broad  $k_x$ -distribution of each mode localizes progressively around specific points of  $k_x$ -space, until the cavity modes become virtually undistinguishable from  $W1$  Bloch functions. When this happens – i.e., when photons are no longer confined along the  $x$  direction – the cavity modes effectively merge into a continuum, giving rise to the 1D band dispersion of a PhC waveguide ( $W1$ ) such as the one sketched in Fig. 5.1 (a).

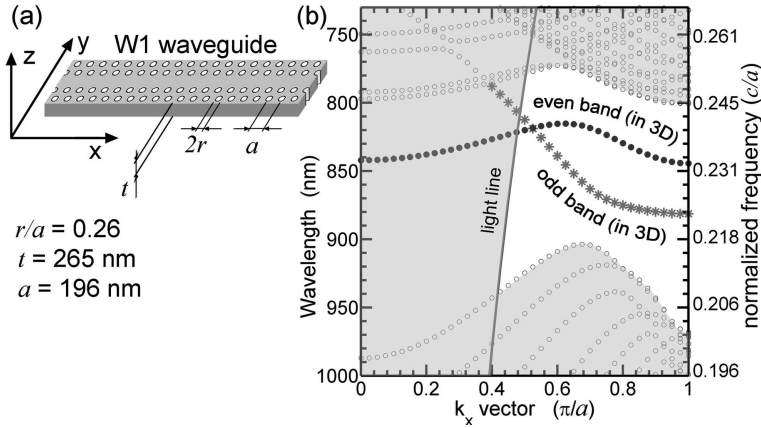


**Figure 5.1:** (a) Sketch of a 2D PhC  $W1$  waveguide. (b) Band diagram calculated for the parameters indicated in (a), with  $n_{eff} = 3.223$  and corrected for the infrared dispersion of  $n_{GaAs}$ . The regions of the PhC continuum and of the radiative (above the light line) leaky modes are shaded in gray. The band parity notation follows the full 3D field distributions. The odd band can be well defined up to a point where it mixes (anticrosses) with the PhC continuum bands (at  $\lambda \sim 780$  nm).

The band structure [Fig. 5.1 (b)] and the Bloch modes of a  $GaAs$ -based PhC  $W1$  – which will constitute the basis for the upcoming analysis – were computed by solving the 2D TE wave equation (see section 2.3.1.2) which can also<sup>2</sup> be written as

$$\vec{\nabla} \times \left[ \vec{\nabla} \times \left( \vec{E}^{nk_x} e^{jk_x x} \right) \right] = \left( \frac{\omega_{nk_x}}{c_0} \right)^2 \epsilon_W \vec{E}^{nk_x} e^{jk_x x} \quad (5.1)$$

<sup>2</sup>In formal calculations here we prefer to use  $\vec{E}$ -field, since written otherwise for the  $\vec{H}$  field the equation is inconvenient having  $1/\epsilon$  term. On the other hand, the wave equation in the 2D FD numerical model is written for the  $H$ -field component ( $H_z$ ) allowing for the scalar formulation.

where  $\epsilon_W$ ,  $\omega_{nk_x}$ ,  $\vec{E}^{nk_x} e^{jk_x x}$  are, respectively, the  $W1$  dielectric constant, eigenfrequency and Bloch function having 1D momentum  $k_x$  and band index  $n$ . The wave equation was solved using the FD method [219], in the effective-index approximation<sup>3</sup> (section 2.3.1) and with periodic boundary conditions. We note (again) that  $n_{eff}$  does not depend on the  $r/a$  and on the in-plane geometry of the PhC cavity, so that the same index value can be used throughout the calculations for both the  $W1$  waveguide and the  $L_N$  cavities. The 2D model is further corrected for the frequency dependence of  $n_{GaAs}$  [120] by a postprocessing procedure (section 2.3.3.2).

The dispersion of the computed  $W1$  waveguide (with parameters indicated in Fig. 5.1) shows two bands confined within the  $TE_0$  PhC bandgap, with parity identified based on the 3D field distributions (see footnote in section 4.2.1).

### 5.1.2 $L_N$ PhC cavities and the onset of 1D band formation

As already mentioned, PhC defect cavities of the  $L_N$  type [see Fig. 5.2 (a)] tend to the  $W1$  waveguide for  $N \rightarrow \infty$ . Intuitively, then, it is reasonable to expect the spectral features of such cavities to bear a resemblance to the  $W1$  dispersion properties at any finite  $N$ . As a preliminary remark, it is indeed interesting to note that the fundamental and the lowest-order  $L_N$  cavity modes<sup>4</sup> share the same parity (odd) with the lowest-frequency  $W1$  band. Computation of the resonant spectra of such cavities [Fig. 5.2 (b)] clearly shows that the density of states grows as  $N$  is increased, with same-order modes (e.g.  $M_0$ ,  $M_1$ ,  $M_2$  etc) shifting towards longer wavelengths. Such a shift is a signature of the reduced photon confinement along the cavity direction ( $x$ ), and it is summarized in Fig. 5.3 (a) for the first 5 lowest-order modes. At some point ( $N \sim 35$  for the fundamental cavity mode) the mode wavelength shift becomes negligibly small. This indicates that photon *confinement along  $x$*  has become insignificant, and it can be taken as a signature of the *onset* of the formation of a 1D photonic band. A similar effect has been recorded for the transition from a semiconductor QD into a QWR [220], whereby electronic states are in question.

The computations described above were compared with the experimental structures, represented by membrane PhC  $L_N$  cavities embedding site-controlled V-groove QWRs acting as the internal light source (ILS) [221]. The samples were fabricated using ICP etching (section 3.1.5.5). A top view of one of these samples is shown in Fig. 5.2 (c). Post-processing by the "digital etching" was also performed (in general, to enhance the cavity  $Q$ -factor). The QWRs were spectrally tuned by the epitaxy, and their PL emission was set to be peaked at 890 nm at low temperature (10K). Spectroscopy experiments on the  $L_N$  cavities were carried out in a micro-PL setup (see section 3.2.3.1, set-up 2), under non-resonant excitation conditions ( $\lambda_{pump} = 700nm$ , pulsed,  $\sim 3ps$ ,  $76MHz$ ). The average excitation power was kept sufficiently low, so that no linewidth narrowing due to stimulated emission (section 7.3.3.3) occurred. Under such conditions, the measured  $Q$ -values for our structures ranged from 3000 ( $L_3$ ,  $M_0$  state) up to  $\sim 7500$  (in  $L_{21}$ ,  $L_{35}$ ).

<sup>3</sup>Here we used  $n_{eff} = 3.223$ , assuming the 3D-based correction (section 2.3.3.2) with  $n_{GaAs} = 3.514$  ( $\lambda = 870nm$ ,  $T = 10K$ ) and membrane thickness of  $t = 265nm$  (at  $a = 210nm$ ).

<sup>4</sup>Out of the whole possible spectrum, see e.g. Fig. 4.2.

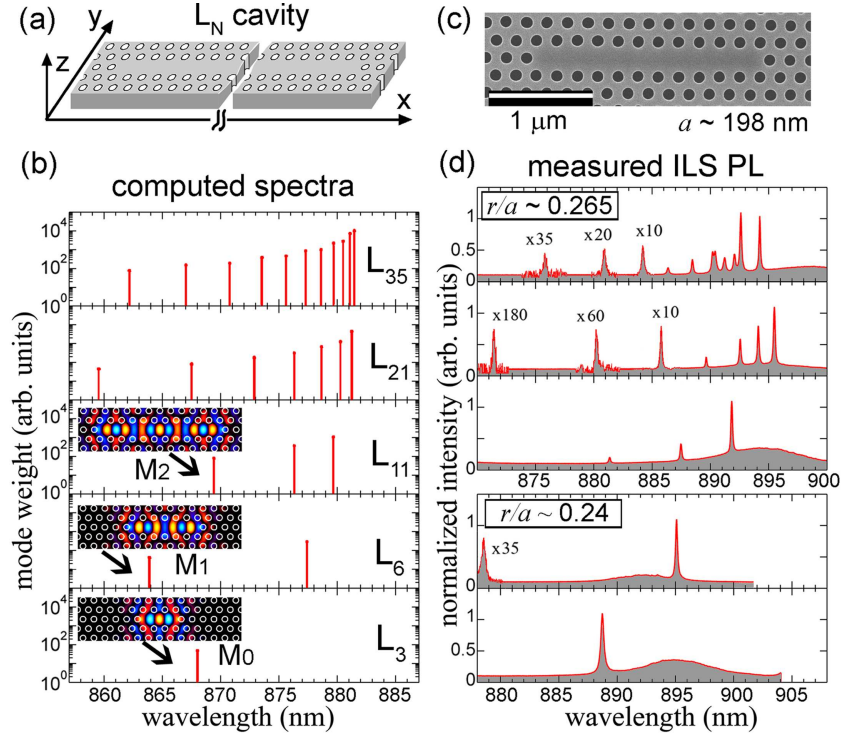


**Figure 5.2:** (a) Sketch of an  $L_N$  cavity. (b) Calculated spectra for the  $L_{3,6,11,21,35}$  cavities based on the same parameters as in Fig. 5.1. The "mode weight" is related to the out-of-plane cavity losses (see Eq. 2.48 in section 2.3.4). The insets show the  $E_y$  field component of some lowest-order mode patterns in corresponding cavities. (c) SEM top-view image of an experimental sample ( $L_{11}$ ); (d) Micro-PL spectra collected from the  $L_{3,6,11,21,35}$  cavities with a QWR embedded as the internal light source (ILS).

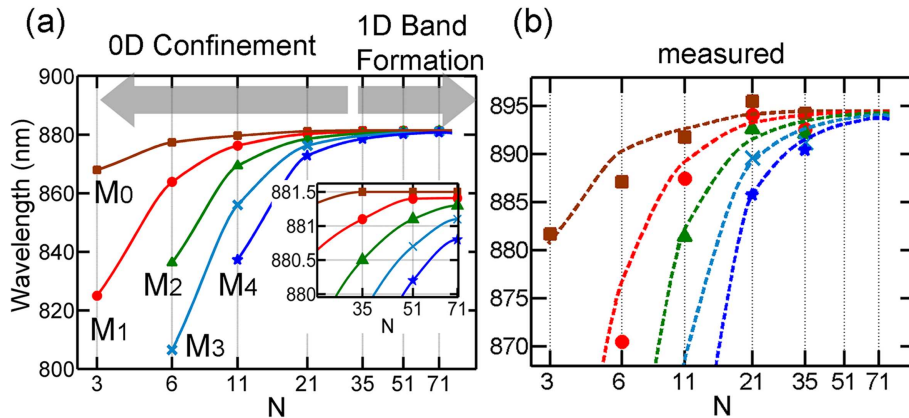


**Figure 5.3:** (a) Summarized plot of the evolution in resonant frequency positions as a function of  $N$  (up to  $N = 71$ ) for the first 5 lowest-order modes (calculated). Continuous lines are guides to the eye. (b) Same as (a), with experimentally obtained values (symbols) superimposed on calculated trends. A  $\sim 13\text{nm}$  uniform offset between experimental and computed resonances was taken into account (see text).

The spectra of the  $L_{3,6,11,21,35}$  cavities are presented in Fig. 5.2 (d). Note that for the  $L_3$  and  $L_6$  cavities we used an  $r/a \approx 0.24$ , while for the  $L_{11,21,35}$  the  $r/a$  was set to  $\approx 0.265$  in order to match the cavity resonances with the QWR emission in each case. The corresponding spectral offset ( $\Delta\lambda \approx 8nm$ ) for  $L_{3,6}$  is taken into account in Fig. 5.2 (d). Note also that the measured spectra are offset from the calculated ones by  $\approx 13nm$  on average. This is mainly due to a difference of  $\sim 2nm$  in the PhC lattice constant (hence  $\Delta\lambda \sim +8nm$ ) and to fluctuations in the hole diameter along the  $z$ -direction ( $\Delta\lambda \sim +5nm$ , due to the slightly reduced diameter measured (in cross-sectional SEM images) at the membrane center). However, due to general PhC scaling laws and because a small shift does not involve a significant spectrum stretching, a direct comparison between the two cases is still accurate. If this offset is taken into account, the experimental data [summarized in Fig. 5.3 (b)] verify quite well the calculated tendencies [Fig. 5.3 (a)].

## 5.2 $L_N$ cavity modes in the reciprocal space

As mentioned in the introduction, important information on the evolution of the  $L_N$  cavities with increasing  $N$  can be obtained by establishing a connection between the  $L_N$ -cavity states and the  $W1$  eigenmodes.

### 5.2.1 Formalism

In principle, the  $\vec{E}$ -field components of the  $m$ -th mode of an  $L_N$  cavity,  $\vec{E}_N^m$ , can be derived by solving the proper wave equation,

$$\vec{\nabla} \times [\vec{\nabla} \times \vec{E}_N^m] = \left(\frac{\omega_N^m}{c_0}\right)^2 \epsilon_N \vec{E}_N^m, \quad (5.2)$$

where  $\omega_N^m$  is the frequency of the  $m$ -th mode and  $\epsilon_N$  is the dielectric constant corresponding to the  $L_N$  cavity. As  $N \rightarrow \infty$ , this structure tends to a PhC  $W1$  waveguide, and Eq. 5.2 transforms into Eq. 5.1. As already noted, the solutions of the latter equation (i.e., the eigenmodes of the PhC  $W1$ ) can be written in terms of Bloch functions of the form  $\vec{E}^{nk_x} e^{jk_x x}$ . If we assume these functions to form a complete basis for those of the  $L_N$  cavity, we can write

$$\vec{E}_N^m = \frac{1}{\sqrt{V}} \sum_{k_x}^{0, \frac{2\pi}{a}} c_{Wk_x}^{m,N} \vec{E}^{Wk_x} e^{jk_x x}. \quad (5.3)$$

Here,  $V$  is the volume of the domain, and we centered our sum on the minimum of the  $W1$  band ( $k_x = \pi/a$ ). In principle, the sum in Eq. 5.3 should extend to all the  $n$  ( $\rightarrow \infty$ ) bands of the waveguide dispersion. For specific modes of the cavity, however, the number of bands to be taken into account can be drastically reduced, by considering the symmetry, the spatial localization and the energy position of the mode with respect to the band diagram of the waveguide. Focussing our attention on the confined cavity

modes that are odd with respect to the  $x = 0$  plane (for  $L_N$  cavities the fundamental mode belongs to this particular class), for example, we can limit the summation in Eq. 5.3 to the odd  $W1$  band shown (in asterisk markers) in Fig. 5.1 (b) (identified by the label  $W$  in Eq. 5.3). It is possible to show [222] that the  $c_{Wk_x}^{m,N}$  coefficients can be obtained as

$$c_{Wk_x}^{m,N} = \sum_G FT \left[ \left( \mathbf{E}_y^{m,N}(x) \right)_{k_x+G} \right] \left( \mathcal{W}_G^{Wk_x} \right)^*, \quad (5.4)$$

where  $\mathbf{E}_y^{m,N}(x)$  is  $\left( E_N^m \right)_y$  integrated over  $y$ . Apart from the Fourier transform of the  $m$ -th cavity mode, Eq. 5.4 includes also  $\mathcal{W}_G^{Wk_x}$  coefficients that depend on the waveguide properties. They are written as [222]

$$\left( \mathcal{W}_G^{Wk_x} \right)^* = \int_{-a/2}^{a/2} dx \int_{-\infty}^{\infty} dy \epsilon_W \left( \vec{E}^{Wk_x} \right)^* e^{jGx}, \quad (5.5)$$

where we reduce to one dimension (by integrating the periodic parts of the Bloch modes over  $y$ ) and take into account that  $\left( \mathcal{W}_G^{Wk_x} \right)^* = \int_{-\infty}^{\infty} \epsilon_W \left( \vec{E}^{Wk_x} \right)^*$  is a function periodic in  $a$  along  $x$  direction (hence, vector  $G$  appears, in units of  $2\pi/a$ ). The  $c_{Wk_x}^{m,N}$  coefficients provide the important *connection* between the cavity modes and the Bloch modes of the corresponding waveguide.

## 5.2.2 Analysis and results

The  $c_{Wk_x}^{m,N}$  coefficients represent the components of  $\vec{E}_N^m$  in the space of PhC  $W1$  modes. In case of a weak dependence of the periodic part of the  $W1$  Bloch modes ( $\vec{E}^{Wk_x}$ ) on  $k_x$ , these coefficients can be evaluated directly by integrating the computed  $\vec{E}_N^m$  over  $y$  and by performing the Fourier transform ( $FT$ ) of the resulting functions of  $x$  (Fig. 5.4 (a); note that due to symmetry reasons,  $\int (E_N^m)_x dy = 0$ , so that only the  $(E_N^m)_y$  component may be considered). Actually, as can be inferred from the direct examination of the computed  $W1$  modes [see Fig. 5.5 (a)] – and also from the corresponding  $\mathcal{W}_G^{Wk_x}$  coefficients [Fig. 5.5 (b)] –, for the PhC structure considered here the condition of a weak dependence of  $\vec{E}^{Wk_x}$  on  $k_x$  is respected throughout the reciprocal space, with the exception of a small region ( $0.65\pi/a < k_x < 0.8\pi/a$ ) where a sharp transition apparently takes place.

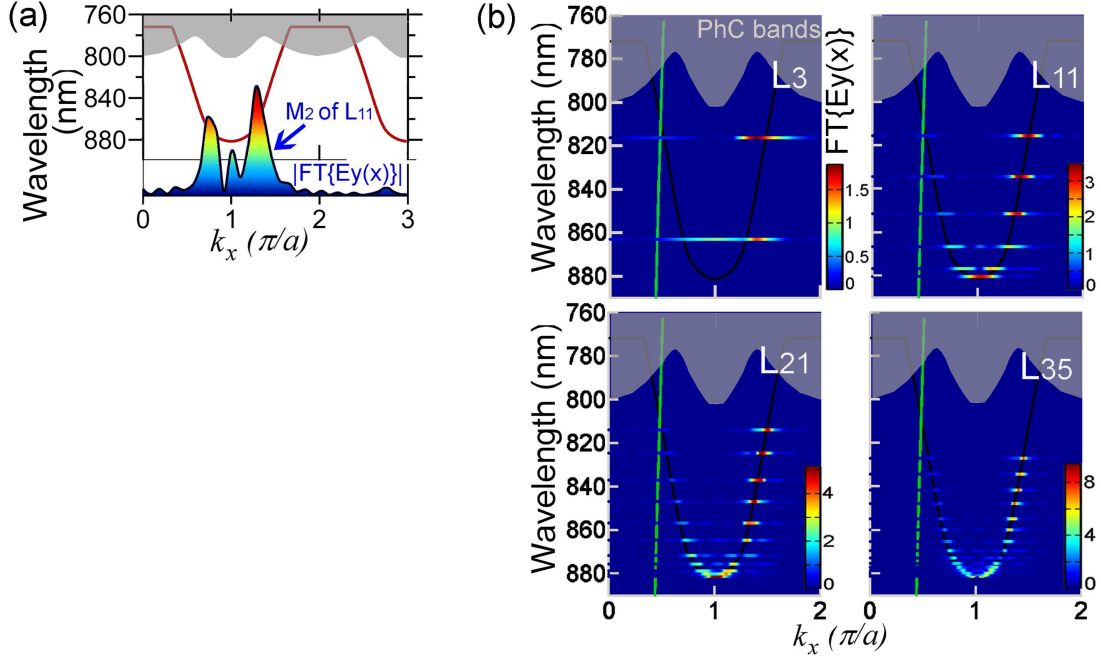


**Figure 5.4:** (a) Periodically extended  $W1$  odd band [see also Fig. 5.1 (b)]. The undefined values are approximated by a constant. The colormap plot is the  $k_x$ -space distribution (Eq. 5.6) of the  $M_2$  mode of the  $L_{11}$  cavity (shown here as an example). (b)  $k_x$ -space distributions calculated from Eq. 5.6 for all the available confined modes for the  $L_3$ ,  $L_{11}$ ,  $L_{21}$  and  $L_{35}$  cavities (for the latter the first 16 modes are shown), positioned at the resonant frequencies; the background black curve depicts the extended band, while the PhC bands are shown as grey-shaded regions. The light line is displayed in green.

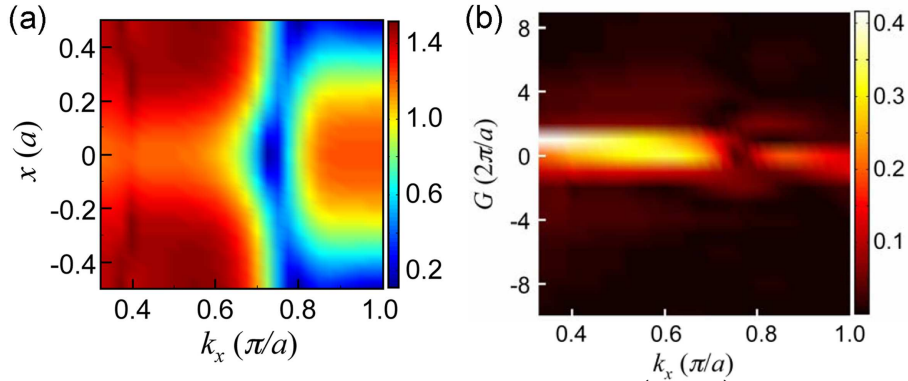


**Figure 5.5:** (a) For each value of  $k_x$ , the dependence of  $\int (\vec{E}^{Wk_x})_y dy$  on  $x$  is plotted as a colormap. The existence of two regions in which  $\vec{E}^{Wk_x}$  is roughly independent on  $k_x$  is clearly evident. (b) For each value of  $k_x$  the corresponding dependence of  $\mathcal{W}_G^{Wk_x}$  on  $G$  is displayed. See text for significance of these quantities.

Intuitively, this can be explained with the existence of *two regimes* in the waveguide dispersion [see Fig. 5.1 (b)]. (i) close to  $k_x = \pi/a$  the anticrossing between the  $W1$  index-guided and the the PBG-guided modes [218] leads to the formation of a band minimum and to a quadratic dependence of  $\omega_{Wk_x}$  on  $k_x$ . In this region ( $0.8\pi/a < k_x \leq 1.0\pi/a$ ), the

periodic part of all the modes is approximately constant with varying  $k_x$  (i.e. identical to the one in the  $W1$  band minimum at  $k_x = \pi/a$ ). (ii) For smaller values of  $k_x$  ( $0.32\pi/a < k_x < 0.65\pi/a$ ), on the other hand, the  $W1$  dispersion is almost linear and governed by the index-guiding mechanism, as in conventional dielectric waveguides. This suggests that the perturbation exerted by the presence of the periodicity in the dielectric constant of the PhC structure may be neglected for modes within this range. Under these conditions,  $\vec{E}^{Wk_x}$  will be equal to a constant plus a small periodic part for all the modes. A third regime can be observed in the range  $0 \leq k_x < 0.32\pi/a$ , where the index-guided waveguide mode anticrosses with the upper PhC bands and cannot be thus defined (hence approximated by a constant<sup>5</sup>). However, the  $c_{Wk_x}^{m,N}$  coefficients associated with the Bloch modes comprised within this range are generally so small that their contribution to the sums in Eq. 5.3 can be disregarded.

According to the above discussion, in Eq. 5.4 we can now assume that  $\mathcal{W}_G^{Wk_x} \approx \text{const}$ , which is indeed valid within the two main dispersion regions (see Fig. 5.5) and, in particular, within our region of interest  $G = [-1, 1]$ . Using then a proper normalization in Eq. 5.4 results in that the  $c_{Wk_x}^{m,N}$  coefficients can be simply approximated by the Fourier transforms of the corresponding cavity modes, i.e.

$$c_{Wk_x}^{m,N} \approx \sum_G FT \left[ \left( \mathbf{E}_y^{m,N}(x) \right)_{k_x+G} \right], \quad (5.6)$$

The summation over  $G$  can be effectively limited to  $G = -1; 0; 1$  (in units of  $2\pi/a$ ), as the Fourier transforms of the modes are concentrated mainly within  $[-2\pi/a, 2\pi/a]$  interval<sup>6</sup> [see 5.4 (a)]. The expression Eq. 5.6 is valid for any  $L_N$  cavity mode with the right symmetry, provided that its projection over the subspace of Bloch  $W1$  modes having  $k_x \in [0.65\pi/a, 0.8\pi/a]$  is sufficiently small. For our PhC structures, this condition is respected by the greatest part of the cavity modes.

The results of the decomposition of the cavity modes in Bloch  $W1$  modes (based on Eq. 5.6) are shown in Fig. 5.4 (b) for different  $L_N$  cavities. First of all, we clearly see that the cavity modes localize around particular  $k_x$ -values, so that with increasing  $N$  their distributions tend to converge to discrete values of the  $W1$  band. The fact that the *one-dimensional momentum vector* of the cavity modes becomes increasingly well-defined as  $N \rightarrow \infty$  is a direct confirmation of the ongoing  $0D \rightarrow 1D$  transition in the character of the cavity modes. In addition, the modes *shift* rapidly in energy down to a certain level. For the ground state ( $M_0$ ), it is the minimum of the dispersion curve. Starting from this point (which occurs at  $N \sim 30$  in the ideal case), any additional shift of  $M_0$  is impossible, and the state practically becomes 1D. From that stage on, the 1D photonic band starts forming (as also presented in Fig. 5.3) and the cavity modes can be viewed as effectively *reconstructing* the  $W1$  dispersion band.

<sup>5</sup>Within  $0 \leq k_x < 0.32\pi/a$  for the PhC structure considered here ( $r/a = 0.26$ ) the  $W1$  modes are no longer confined [see Fig. 5.1 (b)]. The undefined values can however be approximated by a constant [Fig. 5.4 (a)]. We checked that it only results in small corrections for the highest-order cavity modes.

<sup>6</sup>Furthermore, in general terms of the Eq. 5.4, the summation over  $G$  can be limited due to the fact that  $\mathcal{W}_G^{Wk_x}$  coefficients are concentrated mostly within  $[-2\pi/a, 2\pi/a]$  [see 5.5 (b)].

## 5.3 Disorder effects and mode localization

Now let us consider some important implications imposed by the inevitable fabrication-induced disorder in realistic structures.

### 5.3.1 Partial mode localization

Though in general the discussed tendencies are confirmed by the experiments, relatively long cavities ( $N = 21, 35$ ) often show spectral disorder (in the positions of the modes), as observed, for example, for the  $L_{35}$  [Fig. 5.2 (d)]. The extension of our  $k_x$ -space analysis to such real structures is rather interesting, since it can provide valuable information on the effects of structural PhC disorder on the localization – and hence on the effective dimensionality – of the  $L_N$  cavity modes.

To accomplish this goal, the first step is to evaluate the "real" dielectric constant of the PhC structures, by extracting it from top-view SEM images of the actual samples [Fig. 5.6 (a); see also Fig. 5.8]. Then, the modes of the real cavities can be computed with the help of the 2D FD model<sup>7</sup>. For the  $L_{35}$  structure, the FD computation shows clearly that the lowest-order modes localize spatially [Fig. 5.6 (b)] even though the PhC quality seems to be good [Fig. 5.6 (a)]. For these modes, the effective cavity length is hence much smaller than the nominal  $N = 35$ , and the mode energy is increased by the presence of the additional confinement (localization) induced by disorder. The effects of disorder can be also appreciated if Eq. 5.6 is applied to the "real" field distributions, yielding the decomposition of the cavity modes in the space of PhC  $W_1$  eigenfunctions. As shown in Fig. 5.7, the lowest-order modes ( $M_0, M_1, M_2, M_3$ ) suffer from disorder in their spectral positions, which stems from a localization-induced broadening of their distribution in  $k_x$ -space. This broadening – associated with a marked blueshift of the mode energy – is particularly evident for the ground state of the cavity,  $M_0$  (see Fig. 5.7, zoom). For this particular  $L_{35}$  cavity, then, the  $M_0$  state presents evidence of a residual 0D-confinement, which is practically absent in the ideal case. Indeed, a comparison with Fig. 5.4 (b) suggests that the effective cavity length (relative to this mode) is actually similar to that of an  $L_{11}$ . Due to the randomness of the distributed disorder, the spatial localization in a realistic  $L_{35}$  cavity may also be highly asymmetric (with respect to the cavity center), as exhibited, for example, by modes  $M_1, M_2$ , and  $M_3$  in Fig. 5.7.

Experimentally, such mode localization was confirmed by scanning the micro-PL excitation spot (Gaussian distribution,  $\sim 1.5\mu\text{m}$  in its FWHM) along the cavity. Clear mode "competition" was observed (Fig. 5.8). In fact, the efficiency of the excitation of a given mode depends strongly on the *pump position*. Furthermore, this dependence is consistent with the FD-calculated mode patterns [Fig. 5.6 (b)]. Indeed, when the pump is concentrated at left, we observe in the PL spectrum that  $M_2$  and  $M_4$  modes are efficiently excited, since their field distributions are highly localized within the left cavity end. Then with scanning the spot towards the right side we see that in the spectrum, first,  $M_0$  mode appears (whose field is highly concentrated at the cavity center, shifted slightly towards the left end), followed – at around the cavity center – by

<sup>7</sup>Indeed, in our 2D model the in-plane distribution of the dielectric constant can be arbitrary.

the decrease in the intensity of  $M_2$  and  $M_4$  (whose mode patterns become less intense within the cavity central region).

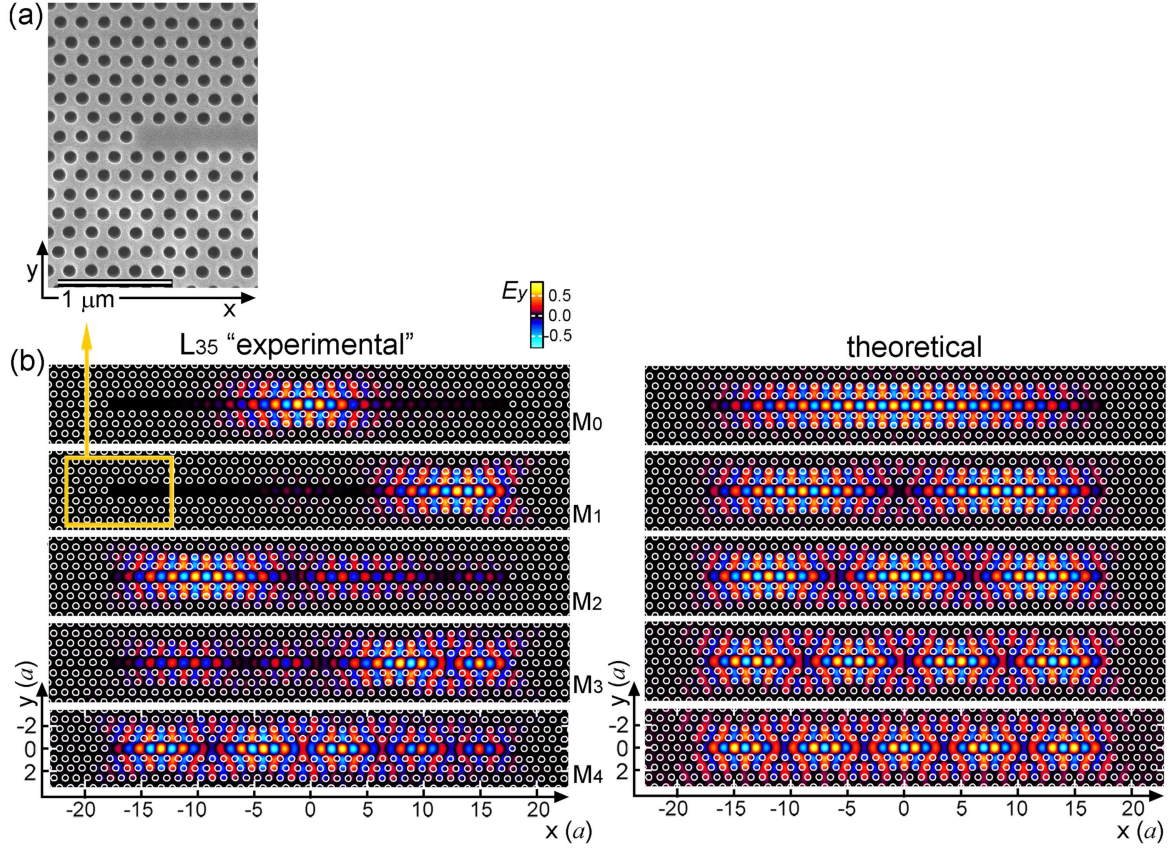


**Figure 5.6:** (a) SEM top-view image (left part) of the measured  $L_{35}$  cavity showing reasonably good sample quality. (b) Mode patterns ( $E_y$  field component) obtained from FD computations performed on the SEM image (first 5 modes are shown). This is compared to the corresponding modes of an ideal structure (right panel).

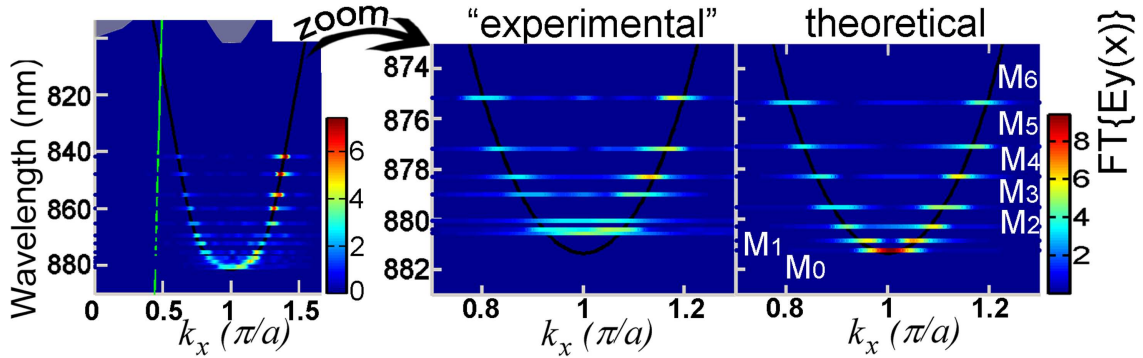


**Figure 5.7:**  $k_x$ -space distributions of the first 14 modes of the measured  $L_{35}$  cavity computed using Eq. 5.6. The zoomed part shows the 7 lowest-order states compared to an ideal structure. (The normalizing constant  $a$  was taken as  $196\text{nm}$  in both cases, for comparison).

Once the excitation spot passes towards the right cavity end,  $M_1$  and  $M_3$  modes appear in the PL spectrum, which is consistent with their patterns being localized mostly closely to the right cavity end. At the very right, these modes indeed gain a lot of intensity in the measured spectrum. On the other hand  $M_0$  doesn't vanish here, which is because its field distribution is still extended (although not very much intense) towards the right cavity end.

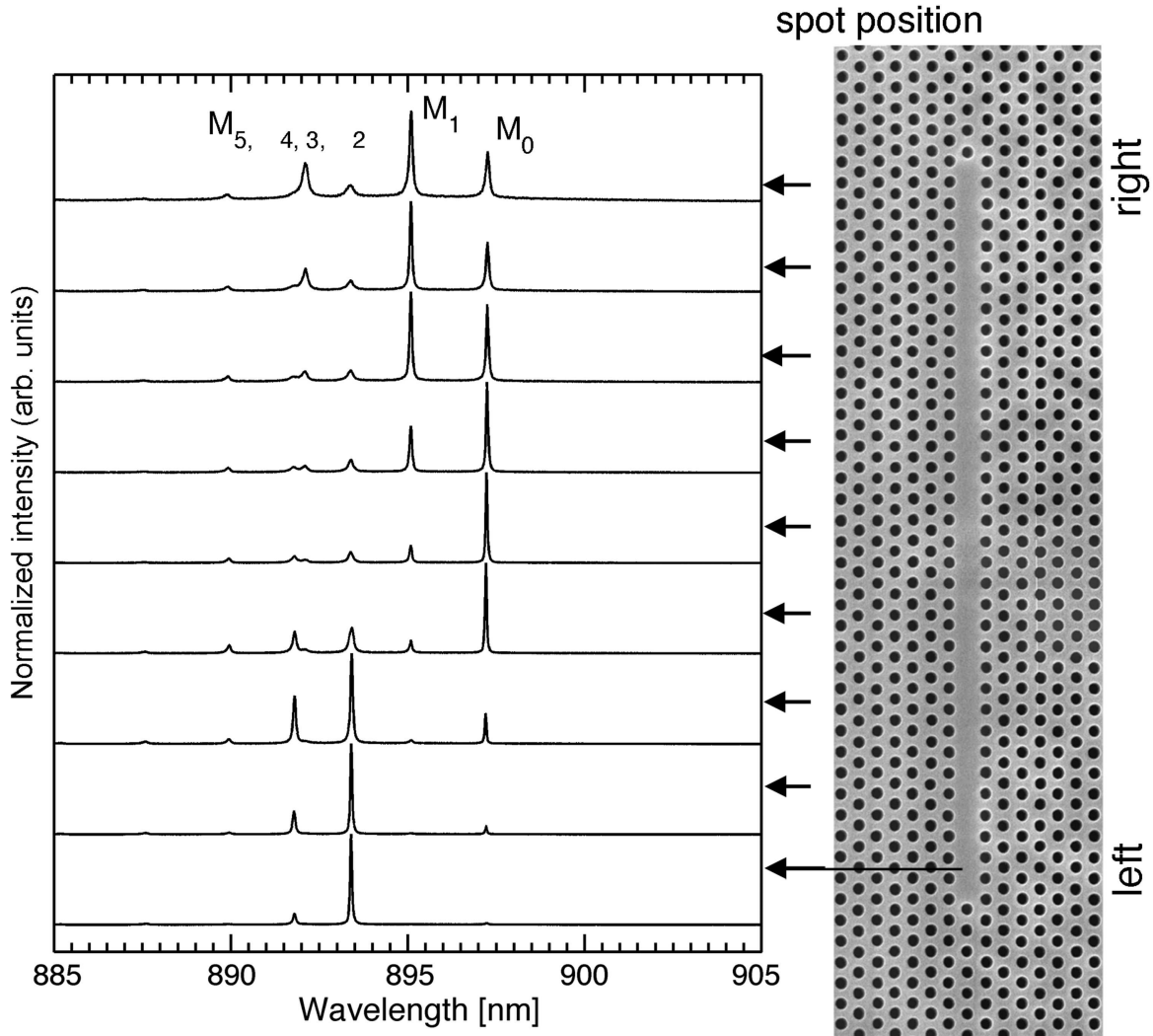


**Figure 5.8:** Partial mode localization evidenced in the micro-PL spectra. The pump spot was scanned along the cavity (sketched at right panel using the SEM top view of the measured sample). At each point, the QWR emission couples better to those cavity modes that have, locally, larger intensity in their field patterns [see Fig. 5.6 (b, left panel)]. Pump conditions: pulsed ( $3ps$ ,  $78MHz$ ),  $700nm$ ,  $12.5\mu W$ .  $T=50K$ .

In this experiment, in order to efficiently excite many cavity modes overlapping with the QWR emission, we used relatively high pump powers ( $12.5\mu W$ , incident average power). Therefore, in the measured spectra the stimulated emission and lasing of some of the modes is not excluded (e.g. one can see that the linewidth of  $M_0$  narrows quite

noticeably once the mode is efficiently excited). However the multimode spectrum is still well preserved, as, due to the inhomogeneous broadening of the QWR, the mode competition [223] (with a complete switching) is not expected to be pronounced and multimode lasing can occur instead (see section 7.2).

### 5.3.2 Discussion: disorder implications

Preliminary statistical studies on SEM images of our structures suggest that the disorder responsible for such mode localization is due to small errors in the positioning of the PhC holes (and not in their size or roundness). It is extremely important, for applications, to understand this effect. For example, in a QD single-photon device based on a long PhC cavity [217] the partial mode localization can drastically reduce the *cavity-QD coupling* efficiency for a given (fixed) position of the QD, hence degrading heavily the performance (e.g. in terms of photon indistinguishability and output efficiency) of such a single-photon source.

Secondly, it is interesting to note that such a disorder affects only the lowest-order modes, while starting from  $M_4$ , the higher-order modes are much less disorder-sensitive. This observation reflects the fact that the high-order cavity modes are mostly composed of  $W1$  Bloch functions situated in the linear part of the waveguide dispersion. As we have already mentioned, these are the index-guided modes, which means that they are inherently insensitive to the periodicity of the dielectric constant. It is then reasonable that small variations in the position of individual holes should leave such modes nearly unaffected.

This property suggests two important conclusions. First, (i) coupling a spatially-controlled emitter (e.g. QD [133,217,224]) to a higher-order cavity mode might represent an efficient strategy to minimize the effects of disorder on the mode localization, thus maximizing the effective cavity length. This might help achieving the extremely high spontaneous emission enhancement factors that were predicted in [217] for long, 1D-like cavities. 1D-polariton studies (where, embedded into the cavity, a QWR electronic system is of interest) might also benefit from the same strategy. Secondly, (ii) in single-photon optical networks where photon transfer from an isolated cavity is done by means of coupling to a terminated waveguide [193] ( $L_N$  cavity), the *photon transfer* through such a waveguide may be hindered due to the partial mode localization. From such a perspective<sup>8</sup>, it might therefore be more favorable to consider coupling to the index-guided modes originating from the linear  $W1$  dispersion part.

## 5.4 Chapter summary

In summary, we studied the evolution of the  $L_N$  PhC cavity system with increasing  $N$ . By writing the cavity modes as a linear combination of the Bloch eigenfunctions of an equivalent PhC waveguide structure ( $W1$  or  $L_\infty$  "cavity"), we were able to track down the  $0D \rightarrow 1D$  transition taking place in these particular structures for  $N \rightarrow \infty$ . This

<sup>8</sup>In addition e.g. to considerations based on the slow light in PhC waveguides [218].

---

analysis allowed for concluding that in the ideal case 1D-like states can form starting from  $N \sim 30 \div 40$ . These 1D states exhibit a well-defined momentum  $k_x$ , and their frequency matches that of a corresponding waveguide mode. In the experiments, however, the distributed PhC disorder leads to partial mode spatial localization. This phenomenon greatly reduces the effective cavity length for the lowest-order (PBG-guided) modes, while leaving the high-order (index-guided) ones nearly unaffected. This has to be taken into account in the design of practical devices, such as single-photon sources and on-chip photon transfer lines.



# Chapter 6

## Directly coupled photonic-crystal microcavities

Coupling of microcavities allows for coherent photon transfer introducing new grounds for development of lasers [50], delay [225], routing [226], and non-linear [227] optical lines, bistability-based ultrafast generators, as well as switchable lasers [228], optical memory [229, 230] and other elements of future integrated photonics circuits. The photon coupling can also form an interaction basis for spatially separated single quantum objects [112, 231], which could be applied in quantum communication and quantum information science. Strongly correlated systems [232, 233] built on coupled exciton-photon polaritons can be created, which could serve to simulate the complexity of basic condensed matter where each “atom” can be addressed individually.

The direct coupling of optical microcavities has been demonstrated in various cavity systems including microdisks [229, 234], distributed Bragg reflector (DBR)-based pillars [235, 236], microspheres [237], microrings [238] as well as in PhC-based few-cavity photonic molecules [239–243] and large-area arrays [50, 225, 227]. Frequency matching has been the main prerequisite in designing such microphotonic devices. However, loss associated with particular cavity confined modes is also an essential parameter, especially in the case of high-Q structures such as PhC defect cavities. Possible differences in the losses of the coupled modes would influence not only the interaction with charge carriers confined in different cavities (altering light-matter interaction e.g. via Purcell effect or influencing coupled-cavity laser performance), but also would affect the efficiency of photon transfer.

### 6.1 Linear resonant coupling

As generally well known, coupling of oscillators results in frequency splitting and supermode formation. As found experimentally in this work, in some circumstances the supermodes may also exhibit *splitting in modal loss*. In what follows we will discuss

both these aspects considering the coupling regime in the absence of nonlinear coupling terms<sup>1</sup>, consistent with the experiment.

### 6.1.1 Supermode formation, frequency splitting and energy transfer

Consider first a generalized system of two coupled oscillators (e.g. confined photons in our case) of free frequencies  $\omega_1$  and  $\omega_2$ , and damping (loss) parameters  $\gamma_1$  and  $\gamma_2$ . In the regime of linear coupling, the complex angular eigen-frequencies (frequencies  $\Omega_{S,A}$  and linewidths  $\Gamma_{S,A}$ ) of the system are given by [245]:

$$\tilde{\Omega}_{S,A} = \Omega_{S,A} + i\Gamma_{S,A} = \frac{1}{2}[\omega_1 + \omega_2 - i(\gamma_1 + \gamma_2)] \pm \frac{1}{2}\sqrt{[\omega_1 - \omega_2 - i(\gamma_1 - \gamma_2)]^2 + 4g^2} \quad (6.1)$$

where  $g$  is the coupling strength and the symmetric ( $S$ )/antisymmetric ( $A$ ) supermodes correspond to the  $+/-$  signs, respectively. In the case of dissimilar cavities (i.e.  $\omega_1 \neq \omega_2$ ), the supermode field distributions become increasingly localized to either one of the coupled parts with decreasing  $g$ . Hence, out of resonance, the energy (photon) cannot be exchanged efficiently between the cavities. On the other hand, if the detuning ( $\omega_1 - \omega_2$ ) is smaller than the coupling strength  $g$ , the supermodes delocalize, and, due to the splitting in frequency, energy transfer can take place. This can be confirmed simply by

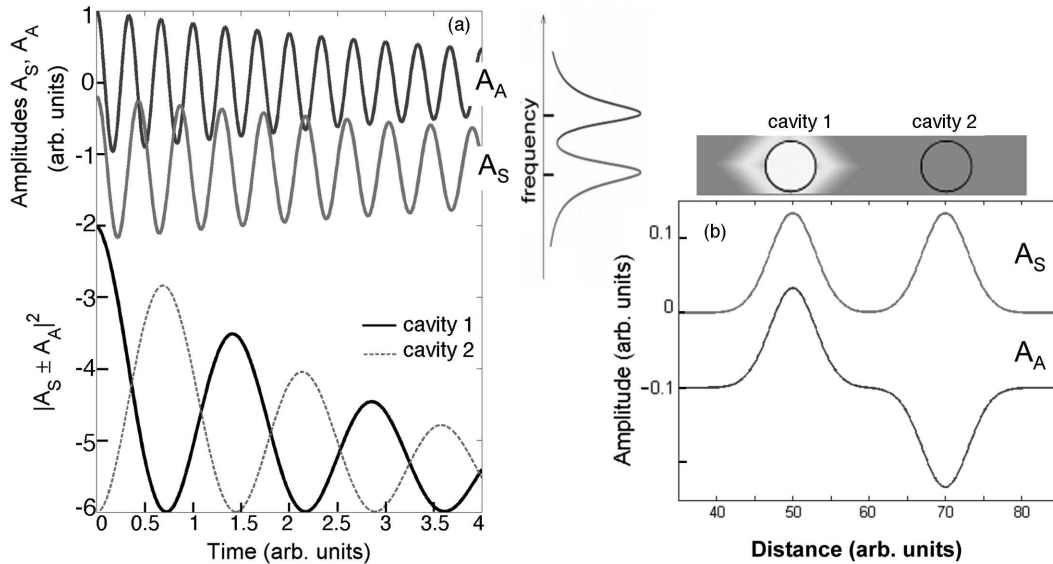


**Figure 6.1:** (a) Time evolution of the field amplitudes of a resonantly coupled system and of the intensity in each of the coupled oscillators in the case of identical supermode losses; (b) field amplitudes of the symmetric and the antisymmetric modes.

considering the time evolution of an optical field initially localized at one of the coupled cavities. The intensity at either cavity then evolves with time as the squared sum of the

<sup>1</sup>Effects arising from non-linear cavity coupling can be found e.g. in [244].

amplitudes and its decay is then given by:

$$|A_S \pm A_A|^2 = A_0^2(\vec{r}) |e^{i\tilde{\Omega}_S t} \pm e^{i\tilde{\Omega}_A t}|^2 \sim e^{-2\Gamma_S t} |e^{i(\Omega_A - \Omega_S)t} e^{-(\Gamma_A - \Gamma_S)t} \pm 1|^2 \quad (6.2)$$

This expression shows that in the case of equal mode losses  $\Gamma_S = \Gamma_A$ , energy can be fully transferred between the cavities due to coherent superposition of the symmetric and the antisymmetric supermodes [illustrated in Fig. 6.1 (b)], limited only by the finite decay time  $2\pi/\Gamma_S$ , which is demonstrated in Fig. 6.1 (a).

### 6.1.2 Splitting of loss

Eq. 6.1 also shows that, apart from splitting in frequencies (that is,  $\Omega_S \neq \Omega_A$ ), the coupled system generally exhibits a splitting in the modal loss with  $\Gamma_S \neq \Gamma_A$ . This happens if the coupling strength is a complex number containing non-vanishing imaginary part  $\Im(g)$ . Then, even if the free frequencies are well tuned ( $\omega_1 \approx \omega_2$ ), the dissimilar supermode losses  $\Gamma_S$  and  $\Gamma_A$  may prevent the energy transfer. Indeed, in the most general case where  $g = \Re(g) \pm \Im(g)$ , loss splitting occurs such that  $\Gamma_S \neq \Gamma_A$  and complete energy transfer is hindered due to the lack of *perfect* destructive interference between the symmetric and antisymmetric coupled modes at phase matching (see Fig. 6.2). Instead, the energy becomes redistributed evenly between the two oscillators.

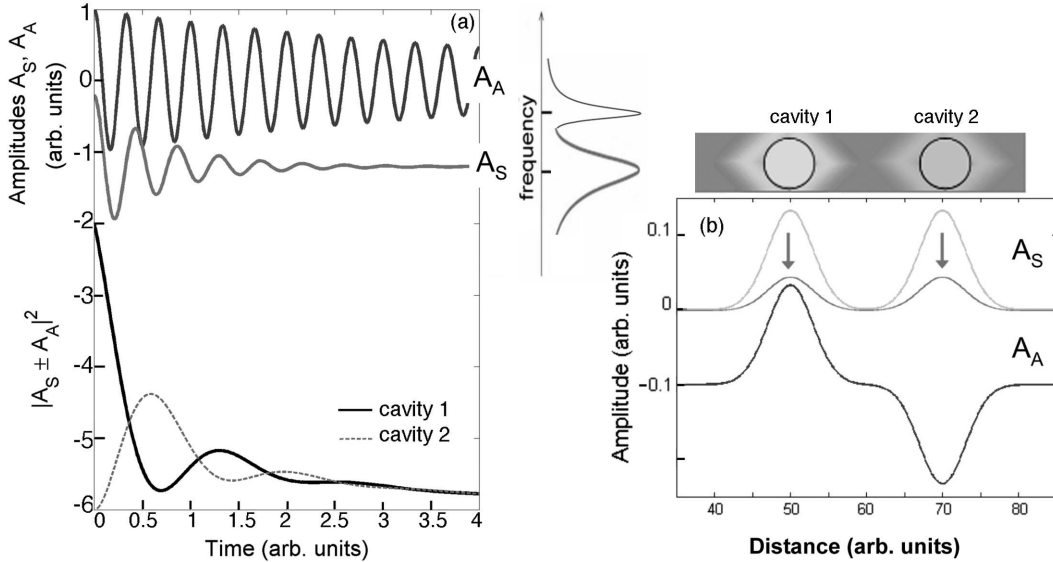


**Figure 6.2:** (a) Time evolution of the field amplitudes of the resonantly coupled system and of the intensity in each of the coupled oscillators in the case where the supermode losses split. The energy is redistributed uniformly between the two oscillators; (b) field amplitudes of the symmetric and the antisymmetric modes at a particular time moment indicating the amplitude decline of the lossy supermode.

## 6.2 Experimental observation of coupling

### 6.2.1 QWR-PhC structure and independent quantum-wire internal light sources

To probe the coupling of two optical microcavities, we used a system consisting of two PhC  $L_3$ -defect cavities each of which contains a monolithically embedded short, site-controlled single QWR (Fig. 6.3 (a)). In the experiments discussed here the  $In_{0.15}Ga_{0.85}As$  QWRs were nominally 5-nm thick, sandwiched between  $\sim 30$ -nm  $GaAs$  barrier layers grown on a  $\sim 155$ nm deep grating. The micro-photoluminescence (micro-PL) spectrum of the "bare"  $InGaAs/GaAs$  QWR heterostructure, located outside the optical cavity, is shown in the Fig. 6.3 (b): the QWR peak is observed at  $\sim 923$ nm, accompanied, as usual, by the QW peak found at  $\sim 886$ nm. The PhC structures were designed accordingly (the PhC pitch  $a \approx 210$ nm and the radius of holes  $r/a \approx 0.255$ ) in order to match the QWR emission to the  $L_3$ -cavity fundamental mode at the frequency within the  $TE_0$  PhC bandgap. The structures incorporate intercavity photonic tunnel barriers consisting of one or more missing holes in a longitudinal configuration [Fig. 6.3 (c,d)]. The PhC holes were defined by the RIE (see section 3.1.5.3). The optical characteri-

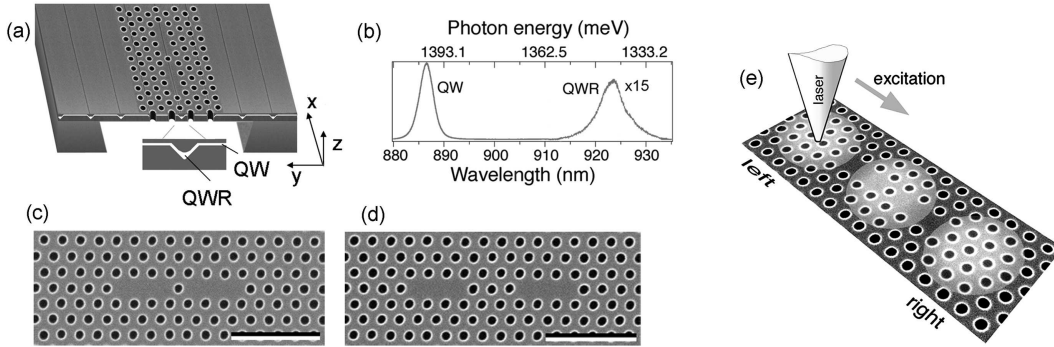


**Figure 6.3:** Experimental arrangement. (a) Schematics of the fabricated structure: free-standing membrane with V-groove QWRs integrated into two coupled PhC  $L_3$  cavities, (b) Low-temperature ( $T=10$ K) micro-PL spectrum of a "bare" QWR located outside the membrane, (c,d) SEM top-views of the measured samples, bars are  $1\mu\text{m}$  long; (e) schematics of the selective pumping configuration.

zation was done by low-temperature (10K) micro-PL. The excitation was performed non-resonantly using a 532-nm frequency-doubled Nd:YAG laser beam focussed by a  $50\times$  objective lens with  $NA = 0.55$  down to  $\sim 1\mu\text{m}$  spot size. Since either of the QWRs can be pumped optically independently, they serve as internal light sources for exciting either one of the cavities. This selective pumping feature [Fig. 6.3 (e)] makes it possible to probe the extent of localization of the cavity modes, as further discussed below, and remove ambiguities in the conclusions on the presence or absence of the cavity coupling in experimental observations. Indeed, if the structure is instead pumped uniformly, the measured spectrum can contain two peaks that may actually originate from the decoupled (detuned) cavities.

## 6.2.2 Mode (de)localization probed by spatially-resolved cavity excitation

Fig. 6.4 (a,d) displays the measured micro-PL spectra for the single- and triple-hole barrier, coupled-cavity structures, each obtained using several locations of the pumping beam. In both cases, two cavity modes can be excited near 910 or 920nm. However, whereas these two modes have the same relative intensity in the case of the single-hole barrier, they exhibit strong dependency on the pumping location for the triple-barrier structure. In particular, for the triple-barrier structure, pumping near the left- or right-cavity yields excitation of predominantly either one of the spectral lines  $M_1$  or  $M_2$  [Fig. 6.4 (d)].

This behavior is explained with the aid of the 3D FDTD simulation of the coupled-

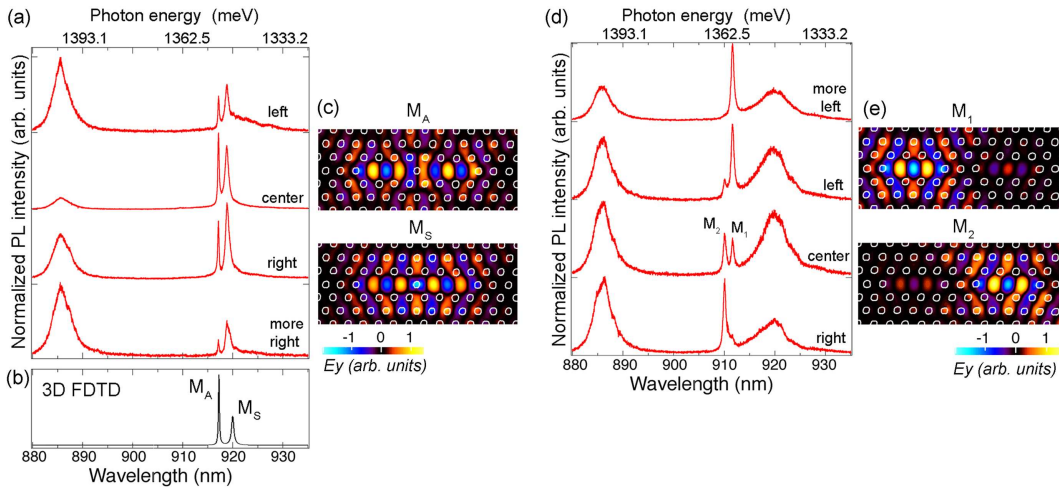


**Figure 6.4:** Evidence for direct coupling of two PhC  $L_3$  microcavities. (a) micro-PL spectrum acquired for different pump locations as shown in Fig. 6.3 (e) for a single-hole barrier structure [Fig. 6.3 (c)]. (b) 3D FDTD simulation of the cavity spectrum using the imported SEM top view of Fig. 6.3 (c). (c) Near-field patterns of the symmetric ( $M_S$ ) and the antisymmetric ( $M_A$ ) supermodes inferred from computed stationary mode distributions ( $E_y$  components) for the single-hole barrier structure. (d) Position-dependent micro-PL spectra for the three-hole barrier structure [Fig. 6.3 (d)]. (e) Near-field patterns for the three-hole structure showing virtually complete localization ( $E_y$  components).

cavity structures. The simulations implement the actual patterns of the PhC structures extracted from SEM images, hence accounting for the fabrication-induced disorder in hole size, shape and position. The simulated spectrum of the single-hole barrier system [Fig. 6.4 (b)] clearly shows a pair of modes, separated by 2.75 nm (6138 GHz), in a good agreement with the observed splitting (1.7 nm, 3803 GHz). The corresponding near-field patterns [Fig. 6.4 (c)], confirm that these modes are indeed the "symmetric" ( $M_S$ ) and the "antisymmetric" ( $M_A$ ) coupled modes of the system. The field distributions (inferred from the 2D model, Sec. 2.3.1) show virtually no localization at either of the coupled cavities, indicating that the coupling in this case is strong enough to overcome the disorder-induced detuning ( $|\omega_1 - \omega_2| \ll 2g$ ). The delocalization is consistent with

the observation in the PL spectra of only small changes in relative intensity of the doublet's peaks at different locations of the pump.

By contrast, the near-field distributions of the two modes confined by the structure with the triple-hole barrier show pronounced localization at either cavity [Fig. 6.4 (e)]. Here, the intercavity coupling is significantly lower than for the single-hole case, and thus the same degree of disorder leads to mode localization. As a result, pumping with the optical beam positioned over either cavity yields excitation of the mode localized at that region.

### 6.2.3 Loss splitting

A distinct feature apparent in the calculated and measured spectra of Fig. 6.4 is that the coupled-cavity modes split not only in resonant wavelength, but also in their losses. For the single-hole barriers, the loss splitting is manifested by measured  $Q$ -factors of 3200 and 1150 for the asymmetric and symmetric supermodes, respectively. On the other hand, the virtually uncoupled  $M_1$  or  $M_2$  modes of the three-hole barrier structures exhibit similar  $Q$ -factors of 1400 and 1520. Since –for the single-hole barrier– the fields of the eigenmodes are completely delocalized [Fig. 6.4 (c)], the coupling term  $g$  in this case is much larger than the detuning. Therefore, the measured splitting can provide a good estimation of  $g$ , yielding  $\Re(g) = 1901\text{GHz}$  and  $\Im(g) = 571\text{GHz}$ . Using these values, the frequency and loss detuning curves can be calculated from Eq. 6.1, which is shown in Fig. 6.5. Note that Eq. 6.1 necessitates the asymmetric splitting in  $Q$ -values, fully consistent with the experiment.

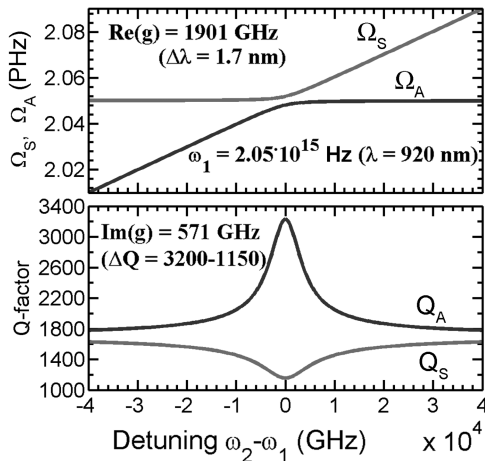


**Figure 6.5:** Calculated complex-frequency splitting vs detuning. The Splitting curves are computed from Eq. 6.1 where the coupling strength  $g$  is estimated from Fig. 6.4 (a)

Note also that the cavity loss parameter approaches  $Q=1700$  for very large detuning, consistent with the measured values for the (virtually uncoupled) modes of the three-hole barrier structure. The fact that the  $Q$ -values in the latter case are lower (1400 and 1520) is explained by the frequency overdamping in the weak-coupling regime [36] implying that each cavity should have  $Q$  lower than that for the unperturbed case. The presence of such very weak coupling in the triple-hole barrier can be noticed in the field distributions [Fig. 6.4 (e)].

### 6.2.4 Detuning limits

In order to further verify the experimental observations, we performed 3D FDTD simulations for intentionally detuned cavities with  $\omega_2 = \omega_1 + \Delta$ . In this case, in order to produce comparable intensities, the modes were excited resonantly by the corresponding field distributions in the central plane of the membrane. These field distributions were obtained from the 2D finite-difference computation. The finite detuning  $\Delta$  was achieved in the simulations by slight modification of the PhC holes surrounding one of the cavities (note the cavity at right position in Fig. 6.6). Technically, the modification is done by assigning a refractive index  $n_{phr}$  to several pixels along the periphery of each hole concerned. Thus, the cavity detuning occurs due to the index difference  $\Delta n = n_{GaAs} - n_{phr}$  or  $\Delta n = n_{phr} - n_{air}$ . Since the computational-domain resolution is 0.04 ( $\sim 8nm$  if  $a = 210nm$ ), only few pixels are involved, and 0.5-nm cavity detuning is achieved with  $\Delta n \simeq 0.25$ , 1-nm detuning - with  $\Delta n \simeq 0.5$  and 2-nm detuning - with  $\Delta n \simeq 1.0$ .

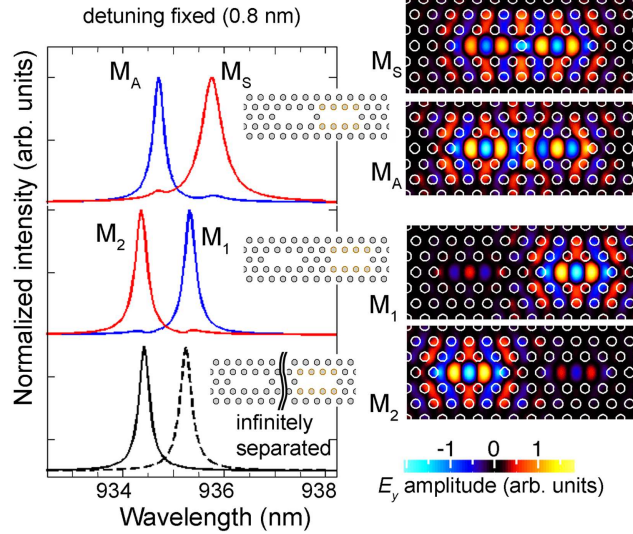


**Figure 6.6:** 3D-FDTD simulated spectral response and  $E_y$  field distributions of the intentionally detuned  $L_3$  cavities (at fixed detuning). Note that the coupling strength is greatly reduced already for a triple-hole barrier, and the mode separation is marginally larger than for an infinite barrier (cavities computed separately). The  $E_y$ -field distributions in the case of the 3-hole barrier show slight mode delocalization, which indicates a very weak, but finite, coupling.

Fig. 6.6 displays the calculated spectra and near-field patterns for  $\Delta \approx 1854GHz$  (0.8 nm); the results reproduce the features observed in the PL spectra and the simulations based on the actual structures, further confirming the interpretation of the coupling behaviour. Note that for a larger cavity detuning of  $\Delta \approx 2nm$ , the simulations yield localized modes even for the single-barrier structure, providing estimation for the maximum detuning tolerated in this PhC geometrical configuration.

## 6.3 Implications

We will identify in this section the mechanisms that give rise to the non-vanishing imaginary part of the coupling coefficient, further discuss implications on the energy transfer based on available experimental data and proceed to looking (by modeling) into how the coupling could be tailored by means of (static) intercavity barrier engineering or using a scanning-probe tip.

### 6.3.1 Diffractive origin of the loss splitting

Insight into the physical mechanisms responsible for the loss splitting can be gained by recalling that the cavity losses of the PhCs discussed here are governed by out-of-plane diffraction. This strongly depends on the PhC geometry and is described by the light cone of the cladding region (see Sec. 2.3.4) [129, 130]. This is different than in the case of other cavity types, e.g., microdisks for which  $Q$  difference of coupled modes ascribed to scattering at imperfections was observed [229]. The relation of the loss splitting to the PhC diffractive losses can be visualized by inspection of the Fourier transform ( $FT$ ) of the near-field pattern within a reference plane located just above the PhC membrane [132]. Fig. 6.7 (a) shows the distributions in the reciprocal ( $k_x, k_y$ ) space computed for ideal (disorder-free) PhC coupled-cavity structures with parameters similar to those used in the experiments. For clarity, the cases of single- and five-hole barriers are compared, the latter being an example of a “long” barrier; a single cavity is also shown, for reference. To aid visualization, Fig. 6.7 (b) illustrates directly the out-of-plane radiation patterns in real space.

Quantitatively, the diffractive losses of each mode were estimated by the ratio of the integrated intensity within the light cone to the integrated intensity within the entire reference-plane:

$$\eta_{\text{diffr}} = \frac{\int_{k_{\parallel} \leq 2\pi/\lambda} |FT(E)|^2 dk_x dk_y}{\int_{k_{\parallel}} |FT(E)|^2 dk_x dk_y} 100\% \quad (6.3)$$

$$|FT(E)|^2 = |FT(E_x)|^2 + |FT(E_y)|^2 + |FT(E_z)|^2 \quad (6.4)$$

(Only the electric component ( $\vec{E}$ ) of the field is considered here, since the time-averaged electromagnetic energy is distributed equally between  $\vec{E}$  and  $\vec{H}$ ). Compared to the corresponding  $Q$ -values of the modes extracted directly from the 3D FDTD temporal response [insets in 6.7 (b)], the results of the light-cone analysis confirm much higher radiation losses for the symmetric mode in the “short”-barrier case. The radiation-loss difference for the “long” barrier is much less pronounced resulting in much smaller loss splitting. Note, that due to formation of the supermode amplitudes, the symmetric mode will always have larger amplitude in the barrier region. However, for sufficiently long barriers, due to tight confinement provided by the PhC, both supermodes do not overlap significantly with the barrier, which equalizes their losses (see 6.7 (b), 5-hole barrier), and the  $Q$ -factors and the radiation patterns then resemble those of an individual  $L_3$  cavity.

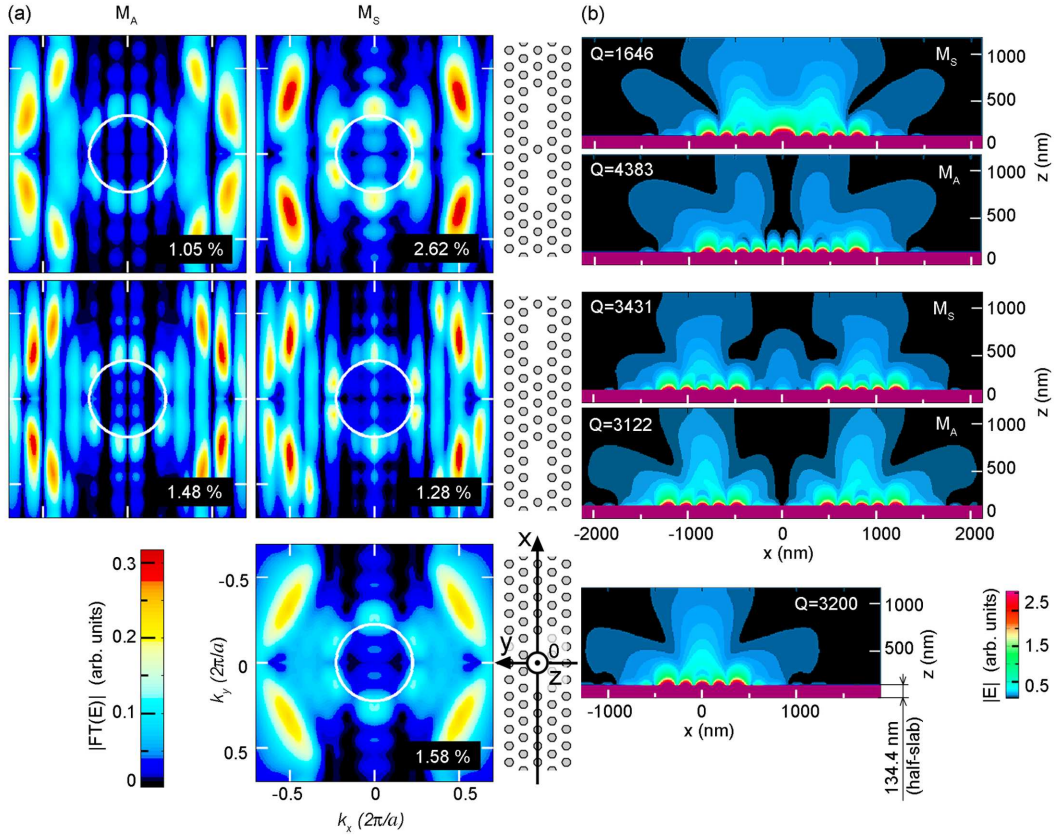


**Figure 6.7:** Diffraction losses of the coupled-cavity system (3D FDTD analysis applied to disorder-free PhC structures). (a)  $E$ -fields of the symmetric ( $M_S$ ) and antisymmetric ( $M_A$ ) modes in the reciprocal  $k$ -space (Fourier transforms at the reference plane above the membrane), for two coupled-cavity structures with different (one-hole, five-hole) barriers schematically illustrated on the right. The corresponding field pattern for the single  $L_3$  cavity is also shown, at the bottom. The leaky field components are situated within the air light cone (encircled area). Calculated from Eq. 6.3, the percentage of the integrated field intensity with  $k$ -vectors located inside the light cone is shown in the insets. (b) Real-space  $E$ -field patterns (absolute value) in the plane perpendicular to the membrane and along the symmetry axis ( $X$ ) of the cavities for the structures of part (a), visualizing the radiation responsible for loss. The  $Q$  factors, shown in the insets, were extracted directly from the 3D FDTD temporal response.

### 6.3.2 Implications on the energy transfer

The splitting of loss [ $Q_A = 3200$ ,  $Q_S = 1150$ , deduced from Fig. 6.4 (a)] results in damping of the energy transfer, as discussed in the beginning of this chapter. The incompleteness of the transfer is recognized by damping of oscillations in the  $|M_A + M_S|^2$  intensity curves with time [Fig. 6.8]. This damping follows in a symmetric way, that is, per transfer cycle, the intensity in the cavity 1 does not decrease all the way down to zero (note in Fig. 6.8 the intensity curve at its first minimum does not reach the time axis) and the intensity in the cavity 2 does not raise accordingly. Consistent with Eq.

6.2, if the overall  $Q$ -values were much higher this would eventually lead to stationary uniform energy redistribution over the two cavities (see also Fig. 6.2).

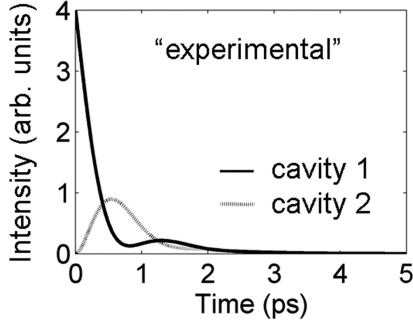


**Figure 6.8:** Calculated from Eq. 6.2, the time evolution of the field intensities in each cavity showing the damped energy transfer in the coupled system. The parameters are inferred from the measured micro-PL for a single-hole barrier [Fig. 6.4 (a)]

### 6.3.3 Tailoring the splitting characteristics by intercavity barrier engineering

Geometrical adjustments of PhC cavity terminations affect dramatically the mode diffraction within the light-cone [130]. Therefore, barrier engineering in between the two coupled cavities – affecting strongly the loss in the coupled system – should be possible. Having direct implications on the photon transfer, the loss splitting and coupling performance can therefore be designed. To this end, we performed numerical modeling based on the disorder-free cavities, first varying discretely the barrier length by adding integer number of holes [Fig. 6.9 (a)], and secondly, changing adiabatically the single-hole barrier [Fig. 6.9 (b)]. In the first case, in addition to the expected rapid decrease of the coupling strength manifested by reduced spectral splitting, we observe a pronounced splitting of losses for short barriers and periodic flipping in the spectral positions of the coupled-system states. The flipping is due to the interference effect between two wave fronts arising from the coupling cavities; depending on the PhC-lattice  $r/a$  constant, the flipping period does not match the “nodes” where  $\Omega_A = \Omega_S$  at an *integer* number of holes in the barrier, which may account for larger splitting in the case of two-hole barrier. If the barrier is removed, the coupled modes degenerate into the fundamental and the first higher-order states of an  $L_7$  cavity. Most importantly, one can notice from the spectra [Fig. 6.9 (a)] that the loss splitting may assume different “sign” (e.g., compare the  $Q$ s of the  $L_7$  cavity and the single-hole structure). Thus, at some intermediate geometry between the two the reversal of the loss splitting sign and equalization of supermode loss is expected. This is indeed confirmed by adiabatically increasing the single-hole barrier [Fig. 6.9 (b)]. The computed trends display two important crossing points:  $\Omega_S = \Omega_A$  and  $\Gamma_S = \Gamma_A$ . Note that mainly the symmetric mode is affected, consistent with arguments presented in section 6.3.1. In particular, at  $\Gamma_S = \Gamma_A$  ( $Q_S = Q_A \approx 5000$ ) one encounters the coupling regime with a fast and *complete back-and-forth transfer* of photons. This is illustrated by the time evolution of the intensity in each of the coupled cavities calculated from Eq. 6.2 [Fig. 6.10 (a)] and simulated by 3D FDTD [Fig. 6.10 (b,c)]. In particular, in the 3D FDTD simulation the energy is injected into the cavity at the right [cavity1, Fig. 6.10 (c)] by exciting the latter with the field distribution corresponding to a linear combination of the symmetric

and the antisymmetric supermodes (obtained from the 2D model) in-phase within the right-cavity region. The intensity then (after some transient period characterized by the presence of a numerical noise) evolves periodically in each of the coupled cavities, switching back and forth between the two ([Fig. 6.10 (b), see also frames of a real-time movie [246] in (c)]. The time of this switching is  $\approx 250fs$ , therefore, the modulation occurs at rates of  $\approx 4THz$ .

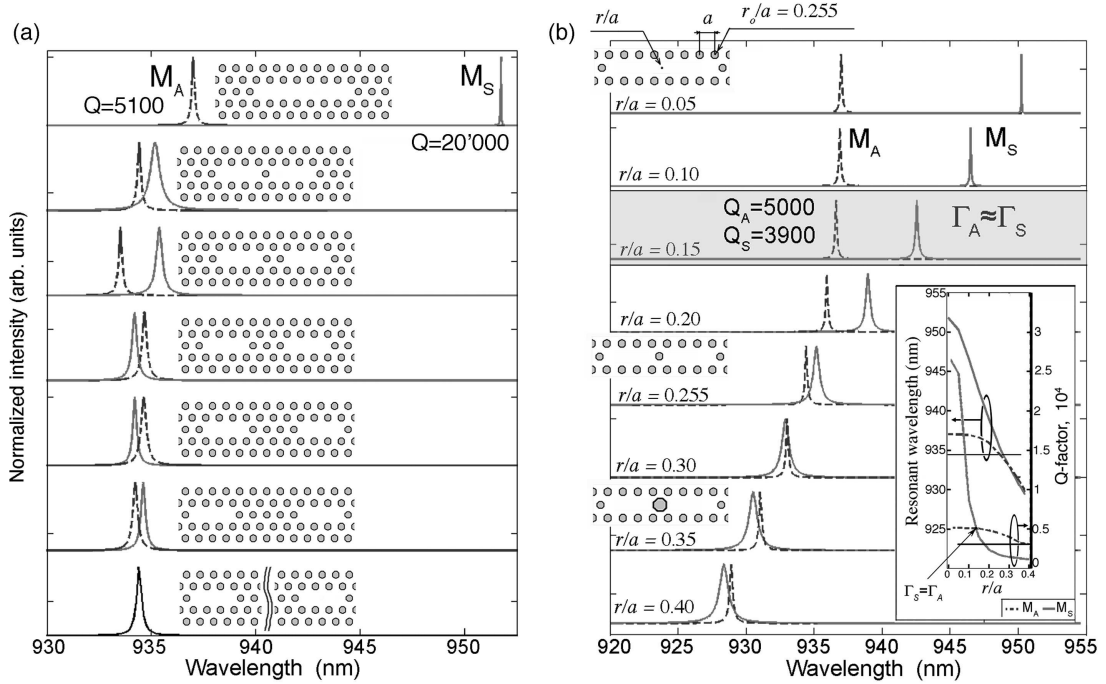


**Figure 6.9:** Design of the coupling by PhC barrier engineering (3D FDTD simulations on disorder-free PhC structures). (a) Spectral response of the two coupled  $L_3$  cavities with increasing barrier length by adding holes. Geometry: the PhC radius of opening  $r_0/a = 0.255$ , the lattice constant  $a = 210nm$ . The field distributions ( $E_y$ ) of the symmetric ( $M_S$ , solid curves) and the antisymmetric ( $M_A$ , dashed) modes are fully delocalized being essentially similar to the ones shown e.g. in the Fig. 6.4 (c). (b) Adiabatic modification of the single-hole barrier by varying the radius of the separating hole from  $r/a = 0$  to  $0.4$  ( $r_0/a = 0.255$  for the rest of the PhC lattice). The trends are also shown in the inset. The crossing point  $\Gamma_S = \Gamma_A$  is highlighted. The horizontal straight lines (inset) indicate the wavelength and the  $Q$ -factor of an unperturbed  $L_3$  cavity.

### 6.3.4 Dynamical coupling control using scanning-probe tip

Direct observation of cavity coupling and the adjustment of the supermode losses may be of interest for the implementation of optical mode control in PhC integrated-optics structures and for quantum cavity electrodynamic experiments, e.g., the achievement of confined polariton coupling [232, 233]. Particularly interesting would be the possibility of dynamic coupling control. This, in principle, could be achieved using external optical beams [247, 248] or scanning probe techniques. In the latter case a local change of

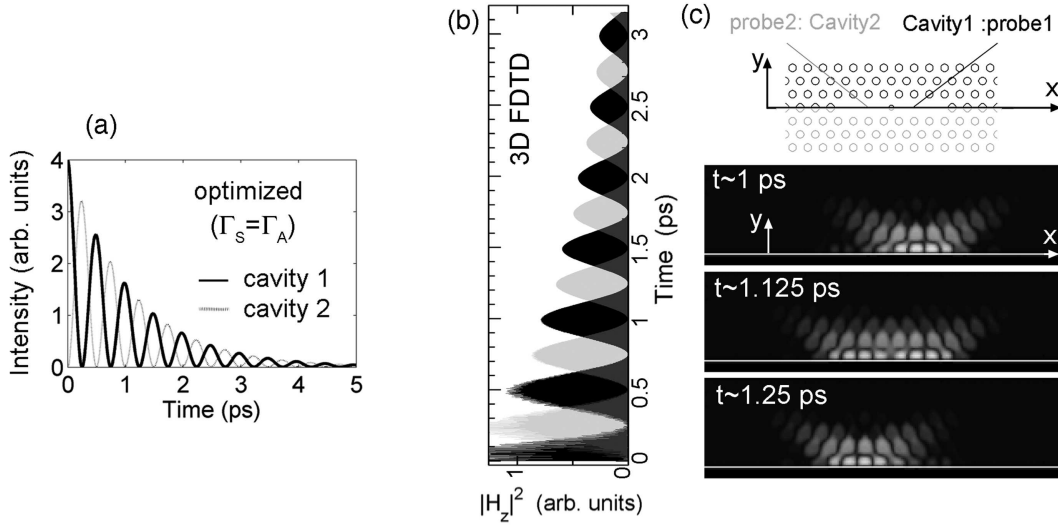


**Figure 6.10:** Energy transfer in an optimized design with no supermode loss splitting. (a) Calculated from Eq. 6.2, the time evolution of the field intensities in each cavity. (b,c) 3D FDTD simulation of the PhC system from 6.9 (b) that shows loss equalization ( $\Gamma_S = \Gamma_A$ ): (b) time evolution of the probed field intensities ( $H_z$  component taken as shown on the sketch in (c) at the membrane center with respect to  $Z$ -axis), (c) near-field distributions in  $\log(1 + |H_z|^2)$  scale, corresponding to different instants in time, as indicated.

the refractive index well within the near field of the coupled system should act as a perturbation that might affect drastically the coupling characteristics. Though scanning with a glass tip ( $n \sim 1.5$ ) of a near-field scanning optical microscope (SNOM) proved not to induce a very significant influence both on the PhC mode's frequency and the  $Q$ -factor [188, 249], two efficient experiments can be envisaged implementing high-index material [250]. The first one is aimed at strongly affecting the coupling barrier, e.g. inserting a semiconductor (with  $n_{tip} \sim n_{PhC}$ ) or metallic tip into a barrier hole to induce or disrupt the efficient coupling. The computed tendencies of the supermodes' complex eigenfrequencies presented in the Fig. 6.9 may then serve as a guide. For example, inserting a semiconductor tip [189] into the single-hole barrier with  $r/a \approx 0.3$  [see Fig. 6.9 (b)] – the situation in which the energy transfer takes an infinite time due to the absence of frequency splitting – should alter the picture such that the  $r/a$  becomes effectively smaller, therefore inducing the splitting in frequency and correcting for the splitting of loss, which turns the efficient energy transfer on. The second possibility is to insert a semiconductor tip into a hole that “belongs” to one of the cavities. This would act to change this particular cavity altogether (e.g. from  $L_3$  to  $L_4$ ). The coupling then is expected to be largely distorted due to a resonance mismatch because of a significant difference in confinement properties between two different  $L_N$  cavities (see chapter 5). Indeed, a numerical experiment confirms such a prediction. Assuming, first, that the rightmost hole of cavity 1 [Fig. 6.11 (a)], is fully filled with Si material ( $n_{Si} = 3.4$ ), the very small difference between the refractive indices of  $GaAs$  ( $n_{GaAs} = 3.51$ ) and Si effectively renders cavity 1 from  $L_3$  to  $L_4$ . Decreased confinement in the  $L_4$  cavity shifts the ground-state frequency to the red (by

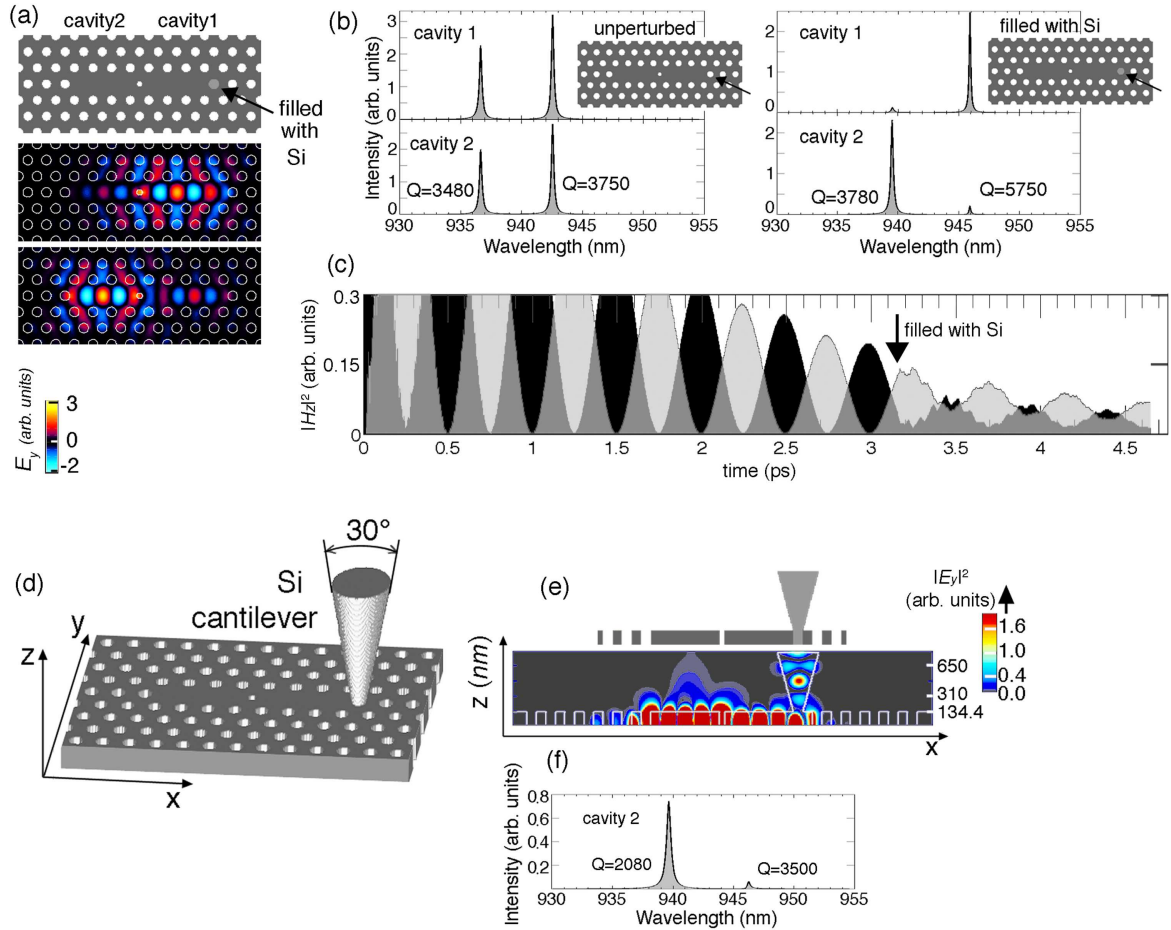


**Figure 6.11:** Energy transfer disturbance by “inserting” a high-index material into a cavity hole: (a-c) assuming that the hole is just filled with Si, (d-f) including the 3D tip geometry. (a) The supermodes exhibit partial localization apparent from the stationary solutions. (b,c) 3D FDTD simulation [continuation of the timeline of Fig 6.10 (b)]. At  $t \approx 3.15ps$  the indicated hole is filled with Si material. (b) Change of the system’s frequency response; note, the amplitude difference, the frequency shift and a change in the  $Q$ -factors. The response is obtained from the probes inserted as depicted in Fig. 6.10 (c). (c) timeline showing the energy transfer: the cavities can still exchange the energy (note the oscillations), however mostly retaining the amount possessed at the moment when cavity 1 was modified ( $t \approx 3.15ps$ ). (d) Sketch of the system with a 3D Si tip; (e) out-of-plane field distribution within the computed domain ( $|E_y|^2$ ) illustrating that energy dissipates via the Si tip; (f) frequency response probed in cavity 2.

$\simeq 3nm$ , see chapter 5, Fig. 5.2), which hinders the formation of the fully delocalized symmetric and the antisymmetric supermodes [see the distributions in Fig. 6.11 (a) and the frequency response in (b)]. Since the underlying interference mechanism of coupling is perturbed, the energy-transfer regime [Fig. 6.11 (c)] is modified accordingly from intensity oscillation towards uniform energy redistribution. At the moment when cavity 1 was modified ( $t \approx 3.15ps$ ) both cavities possessed the energy with larger amount within cavity 2. Since the energy transfer became much less efficient [see transients in Fig. 6.11 (c)], this proportion is then kept. This also means that if cavity 2 accumulated all the energy at the moment of modification (say, at  $t \approx 3.25ps$ ) then, due to the large difference in the amplitudes of the “coupled” modes (Fig. 6.11 (b), right), most of the energy would further stay within cavity 2. The described picture becomes richer if a full 3D structure of a scanning-probe tip is taken into account [Fig. 6.11 (d-f)]. Assuming a reasonable tip geometry (e.g., commercial Olympus silicon cantilever [251]), the Si tip is introduced into the hole that terminates the cavity 1 as shown by the dielectric-constant isosurface in the [Fig. 6.11 (d)]. In addition to the effects discussed above, the tip acts as an energy sink, efficiently outcoupling a part of the energy stored in the system, which can be seen from the field distribution within the domain<sup>2</sup> [Fig. 6.11 (e)]. Such a loss leads to reduced  $Q$ -factors of the modes [Fig. 6.11 (f)], which is consistent with earlier experiments [189]. Since the tip has a high refractive index and perturbs significantly the near-field of the coupled system, the frequencies are slightly shifted further to the red. Thus the energy-transfer regime is qualitatively similar to that seen from the timeline in Fig. 6.11 (c), only the overall decay is faster due to an overall decrease of the  $Q$ -factors in the system. Note, that the effect is slightly exaggerated because, following the time line of Fig. 6.10 (b), we retained the Z-symmetry boundary condition in the simulation used for time-consumption reasons, so in fact, the Si tip is effectively inserted from both sides. A separate simulation employing a non-symmetric structure [exactly as shown in the Fig. 6.11 (d)] suggests that the  $Q$ -factors of the coupled modes be 2900 and 4650 instead of 2080 and 3500 respectively [see Fig. 6.11 (f)].

## 6.4 Chapter summary

In summary, based on the QWR-PhC integrated system, we demonstrated the photonic coupling of two closely spaced PhC membrane defect cavities. The coupled modes split not only in wavelength but also in modal loss, which was observed experimentally. Fully consistent with the theory of coupled oscillators [245], such a loss splitting is given by the imaginary part of the coupling strength. In essence, the loss splitting is explained as arising from the difference in radiative losses of the symmetric and the antisymmetric modes of the system determined by the PhC out-of-plane diffraction. Since these modes beat together to transfer the photons back and forth between the cavities by coherent superposition, such loss difference may prohibit the completeness of the transfer. There-

<sup>2</sup>Acquired during some 70 fs while the energy was more within the cavity 1 (e.g. at time  $t \simeq 4.2ps$ ); the displayed field distribution is similar for both modes, as well as for their amplitude sum.

---

fore, the loss splitting needs to be taken into account in structures which rely on the photon transfer processes, e.g. few QDs laterally coupled via a cavity mode, coupled QD polaritons [233] or transfer of single photons into coupled waveguides [193]. Means for photonic barrier engineering were introduced and shown to be effective in controlling the essential coupling parameters – the complex frequencies of the supermodes. On this basis, proposals for dynamical coupling control by means of scanning-probe-microscopy tips were considered and discussed using 3D FDTD modeling.



# Chapter 7

## Stimulated emission and lasing in quantum-wire photonic-crystal microcavities

The ultimate *conversion* efficiency of a semiconductor laser implies that the generation of a usable photon output does not require passing a threshold [49] (from an inefficient regime at low pump power to highly efficient one at high power). Contrary to regular semiconductor lasers, such a device would have 100% conversion efficiency *at all power levels*<sup>1</sup>. In principle, this ideal case can be realized in a truly single-mode device where all possible emission from the active medium – including both *spontaneous* and *stimulated* emission – is coupled into the only possible cavity mode, which leads to the so-called “thresholdless laser” [47, 49]. The term “thresholdless” here means nothing but the fact that a standard kink in the input-output curve is greatly smoothed (and disappears in an ideal case). In particular, coupling of the spontaneous emission at very low pump powers results in the same device slope efficiency as compared to the high pump powers where the stimulated emission dominates. Although this means the complete absence of a threshold in terms of the classical input-output characteristics, the threshold is still present and it is then fundamentally defined as a *light state transition* from the spontaneous to the stimulated emission. When the spontaneous-emission coupling factor is high, this threshold takes place at very low pump powers. In addition, laser direct-modulation capabilities are expected to improve significantly [214]. From the analysis of the rate equations [102], it becomes clear that PhC microcavities with quantum nanostructures are promising candidates for the realization of such lasers [49], providing truly single-mode cavities and small active-medium volumes<sup>2</sup>.

In the experimental realization of such microcavity laser structures, by definition, there arises an issue of unambiguous verification whether or not a given device actually lases. Indeed, it is no longer possible to firmly conclude the stimulated emission and lasing only by analyzing input-output (light or current) curves. In this chapter we will present quantum-wire PhC-cavity lasers, realized for the first time, and discuss the

---

<sup>1</sup>Provided that the quantum efficiency is unity.

<sup>2</sup>And, in addition, larger material gain due to quantum-confinement and excitonic effects.

basis on which it is possible to conclude the occurrence of stimulated emission and lasing action, verifying that experimentally.

## 7.1 Observable properties of the lasing action

Regular observation of the lasing action in semiconductors includes a pronounced threshold (kink) in the input-output curve and spectral narrowing from a broad spontaneous-emission spectrum superimposed on the multimode closely spaced cavity modes (e.g. Fabri-Perot resonances) to a single or several modes that overcome the threshold. This observation cannot be transferred to microcavity lasers. The input-output curve is smooth, and the cavity single mode, though containing the spontaneous emission, is anyway narrow compared to the background spontaneous emission. Therefore, several characteristics have to be put together in order to establish whether the device lases or behaves like a light-emitting diode (LED)<sup>3</sup>. These characteristics may include the input-output curve, background spontaneous-emission pinning at threshold, mode linewidth narrowing, time-resolved photon dynamics and photon statistics. In particular, the latter two means can provide a *direct* conclusion on the observation of the stimulated emission and lasing.

### 7.1.1 Background spontaneous emission

In some cases of microdevices (e.g. nanopillars, microdisks) that exhibit the lasing action, it is shown that, apart from the build-up of stimulated emission recognized in a non-linear behavior of the input-output curve, the background spontaneous emission at the threshold becomes *clamped* [171, 252]. Such clamping is due to the free-carrier density pinning [253] (i.e. clamping of the quasi-Fermi levels above transparency). However, if the  $\beta$ -factor is increased, the carrier density saturates only *gradually* with the excitation power [103, 253], and the pinning is completely absent in the case of  $\beta = 1$ . Secondly, the observation of the carrier-density pinning can be complicated if the population of the higher-energy states of the active material is present [171]. Third, the *depinning* can also occur due to the carrier diffusion [171] driven by the carrier spatial hole burning effect [171, 211]. Fourth, in effectively multimode microcavities (e.g. sparse spectrum but on a large gain bandwidth), modes reach the threshold at different pump powers [254], so it can be difficult to decide which part of the spontaneous-emission spectrum should be compared to which particular mode in order to conclude on the overall carrier-density pinning. In this respect, inhomogeneously-broadened gain would rather lead to unpinned carrier density. Qualitatively, an idea about the carrier-density evolution in the active medium can be inferred from the mode blueshift [255, 256], which we will discuss more in the experimental sections 7.2.2.1 and 7.3.3.4.

---

<sup>3</sup>Such a LED will though have laser-like properties, i.e. narrow, single-mode emission spectrum. It will, on the other hand, still have poor phase coherence associated with randomness of the spontaneous emission process.

### 7.1.2 Linewidth narrowing

Although the non-linearity in the LL curve can be effectively smoothed out due to high spontaneous-emission coupling factor, the linewidth behavior may at the same time reflect well the build-up of the phase coherence [257] and the onset of lasing. The linewidth behavior can be calculated using either an equivalent circuit model [102, 257, 258] or the intensity- and frequency-noise spectral analysis employing the Langevin formalism [214, 259–261] or the Fokker-Planck method [262].

Importantly, in semiconductor lasers the general trend of the linewidth decrease with power (i.e. the Schawlow-Townes linewidth) is strongly affected by the so-called *linewidth enhancement factor*  $\alpha = \Delta n' / \Delta n''$  [263]. As the linewidth depends on the phase fluctuations of the optical field, the decrease of the spontaneous emission contribution to the mode leads to the linewidth narrowing. However, in addition, due to the intensity fluctuations (associated with random spontaneous emission events), there is a delayed phase change because in order to restore to the steady state the laser field undergoes *relaxation oscillations* during which time ( $\sim 1\text{ns}$ ) there is a *fluctuation in the gain* (imaginary part of the refractive index  $n''$ ) because of the fluctuation of the free carrier density with the field intensity. This will also alter the real part of the refractive index  $n'$  and induce a phase shift and hence the linewidth broadening<sup>4</sup>. Taking that into account, the power-dependent linewidth evolution can be subdivided into three sequential stages [214, 261, 262]: (i) linewidth *narrowing* due to the absorption saturation and the augmentation of the net photon number in the cavity; (ii) linewidth *broadening* due to the coupling between the real and the imaginary parts of the refractive index, and (iii) further “fast” linewidth *narrowing* enabled by the saturation in the intensity fluctuations [261], which evidences the build-up of coherence due to the stimulated emission. In the particular case where the  $\beta$ -factor is large, these transitions are somewhat less abrupt [214] due to high-frequency damping of the relaxation oscillations.

In the *threshold* region the device goes from the spontaneous emission (i) to the high-coherence regime (ii) and (iii). Therefore there is a region where the linewidth does not narrow [266]. This has been observed experimentally [262, 267], and served as a good indication of the threshold, in particular, in high- $\beta$  quantum-dot photonic-crystal lasers [114, 268, 269]<sup>5</sup>.

---

<sup>4</sup>Technically, the  $\alpha$ -factor and the corresponding line broadening by  $1 + \alpha^2$  is given by the Kramers-Kronig relation that tells that the real part of the refractive index is proportional to the derivative of the gain coefficient (that is bound to the imaginary part) [259, 264]. The gain peak in semiconductor materials is power-dependent, blueshifting with power [264, 265]. Therefore  $\alpha$  strongly depends on the spectral position of the lasing mode with respect to the gain curve. Note however that this “position” cannot be well defined in the inhomogeneously broadened medium, i.e. where the emission stems from independent emitters.

<sup>5</sup>We should however note that according to some other reports [215, 270] on microdisk lasers, the linewidth can remain relatively broad above the threshold and its narrowing trend saturates at high powers due to nonequilibrium carrier dynamics (hot carriers) that induce large intensity noise and index fluctuations, and due to a reduction in gain-loss compensation (carrier-density depinning).

### 7.1.3 Build-up of coherence

The discussed above properties extracted from the emission spectra can serve as indirect evidences for stimulated emission and eventually lasing. More direct observations are desirable in order to track down the *light phase transition* from the spontaneous to the stimulated emission taking place at the laser threshold. These include photon dynamics and photon statistics, as further discussed below.

#### 7.1.3.1 Time-resolved photon dynamics

Within this framework, the first method is to measure the *time-resolved* intensity decay (in a pulsed-excitation mode). This allows for probing the device's *photon dynamics* and since the decay rates of the spontaneous and stimulated emission differ to a large extent, the threshold transition is apparent in the transient luminescence [210]. Below the threshold the measured decay time is observed to decrease [213, 271, 272]. At pump powers close to the threshold, this takes place due to a growing contribution of the stimulated emission in the process of augmentation of the cavity photon density [210]. At higher pump powers, the photon *decay* time should drop dramatically, which is a signature of the build-up of coherence due to the *fast stimulated emission*. The transition though is not abrupt, and can be characterized by a gradual appearance of a considerably fast-decaying luminescence component [210, 212, 272] on top of the much slower spontaneous emission. This fast component is attributed to the stimulated emission which dominates the output intensity above the threshold.

Secondly, the *delay time* between the pump pulse and the cavity response *increases* at around the threshold, followed by a steady *decrease* with increasing pump power [210]. The increase below threshold is understood as a photon-density build-up governed by the combined action of the spontaneous and the stimulated emission<sup>6</sup>. The delay-time decrease above the threshold is due to the steady augmentation of the stimulated-emission rate (populating faster the cavity mode with photons), which is generally expected in lasers [273]. This delay-time drop above the threshold [210, 274, 275] can be readily employed as yet another useful *indication of lasing* action.

We illustrate these effects in Fig. 7.1 computing the rate equations (Eq. 2.20, 2.21) in time domain. For this purpose  $L_{in}$  is applied as a Gaussian pulse

$$L_{in}(t) = P \cdot \exp\left(\frac{-4\log(2)(t - t_0)^2}{dt^2}\right); \quad (7.1)$$

of a  $dt = 3ps$  pulse duration with a set delay of  $t_0 = 10ps$ . The rate equations are calculated<sup>7</sup> for different average powers. Fig. 7.1 displays the photon number  $p$  in the cavity mode evolving with time versus the pump power, which is normalized to its threshold value. The threshold value is defined as the power needed to bring the  $p_{max}$  to unity. From Fig. 7.1 we confirm the following. The stimulated-emission rate is  $p$ -dependent.

<sup>6</sup>And also possibly the superluminescence effect.

<sup>7</sup>Other parameters are:  $V_a = 3 \times (5 \times 5 \times 1000)nm^3$ ,  $\tau_{sp} = 300ps$ ,  $\tau_{nr} \simeq 1000\tau_{sp}$ ,  $\lambda_{in} = 700nm$ ,  $\lambda_{cav} = 900nm$ ,  $Q = 5000$ ,  $\beta = 0.3$ ,  $N_{tr} = 10^{18}cm^{-3}$ ; linear gain model is assumed as  $g = g'(N - N_{tr})$  with  $g' = \beta V_a / \tau_{sp}$  [102].

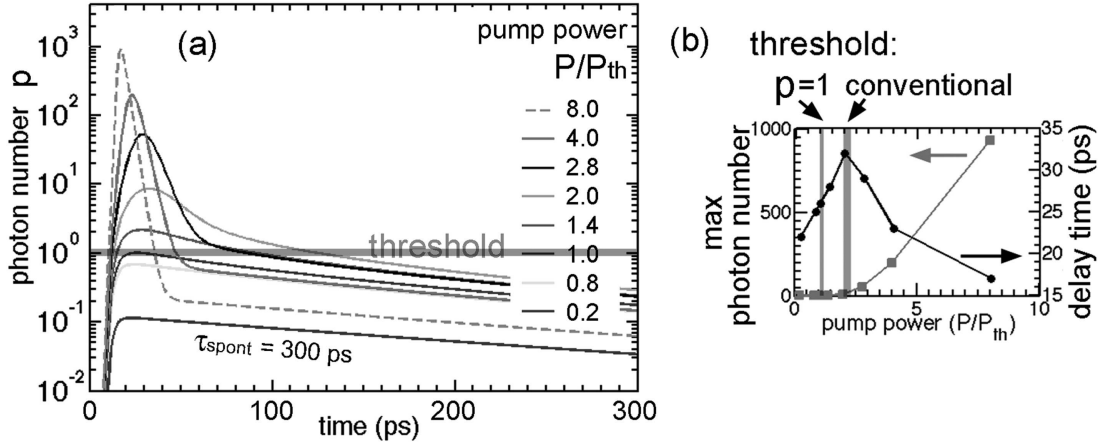


**Figure 7.1:** Calculated photon dynamics for a 3-ps Gaussian-shape pump pulse (set at  $t = 10$  ps delay). (a) Photon number in the cavity mode at different power levels. (b) Input-output curve and the delay time between  $t = 0$  s and the peak of the emitted pulse.

At low pump rates, where  $p > 1$ , the photon density in the mode is augmented by the sum of the stimulated and spontaneous emission, which leads to an increased delay time [210]. During the decay, a faster component appears gradually with increased pump rate due to increasing role of the stimulated emission. At high pump rates, where  $p \gg 1$ , the cavity is fed only by the very fast stimulated emission, hence the delay time decreases, and the decay rate is determined by the cavity  $Q$ . During each pulse, once the carrier density is sufficiently consumed such that  $p \leq 1$ , the decay resumes the spontaneous-emission regime, hence, in total, two decay components are seen.

### 7.1.3.2 Photon statistics

The second method involves the *photon statistics* that characterizes a light source. In the quantum theory of light there exist three distinguishable cases: sub-Poissonian, Poissonian and super-Poissonian intensity-noise distributions, which are associated respectively with so-called antibunched, (random) coherent and bunched light [276]. Whereas the antibunched light is an attribute of single-photon quantum sources [39], the other two cases may be used in characterizing a classical laser device below and above the threshold using Hanbury-Brown and Twiss (HBT) intensity interferometer [114, 277–279]. Both the light flux with a high degree of coherence (e.g. a stable laser) and that partially coherent (chaotic) have intensity fluctuations in time. However for partially-coherent light the intensity fluctuations are much more pronounced and “bunched” at observation times shorter than the coherence time ( $t \lesssim t_c$ ). At the same time laser light has distinctly random intensity noise, which averages its statistics at all times to Poissonian distribution (Fig. 7.2). This is reflected in the second-order correlation function defined as  $g^{(2)}(\tau) = \langle I(t)I(t + \tau) \rangle / \langle I(t) \rangle \langle I(t + \tau) \rangle$  which quantifies the intensity fluctuations and is measured with the HBT technique. Clearly, below threshold there should be a *correlation* (bunching) at  $\tau = 0$ , whereas above the threshold the

source is coherent due to the stimulated emission.

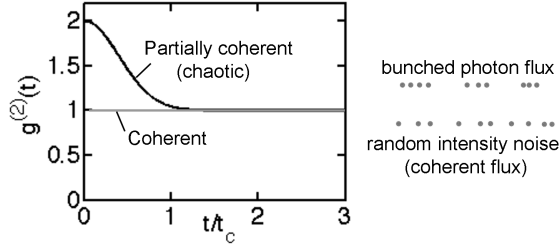


**Figure 7.2:** Illustration of photon statistics for a coherent source and a chaotic source with a coherence time  $t_c$ , (adapted from [276]).

Note however that due to limitations in the time resolution of the measurement instrumentation (normally, given by the APD time jitter), in practice it is not possible to observe the bunching correlation signal coming from very-low-coherence sources. On the other hand, as the source acquires coherence, when the excitation power is increased, the  $g^{(2)}(\tau = 0)$  signal rises and then converges to the Poissonian value  $g^{(2)}(\tau = 0) = 1$ . This transition is detected within the range of  $\sim 0.97 \div 1.02L_{th}$  and for high- $\beta$  lasers is much less apparent ( $g^{(2)}(\tau = 0) \sim 1.1 \div 1.2$  at maximum) [278], which imposes challenges on the measurements if the threshold is unknown.

## 7.2 Multimode quantum-wire photonic-crystal lasers

Before discussing single-mode QWR-PhC structures it is useful to verify experimentally the expected laser behavior discussed in the previous sections on a relatively long cavity, related however (anatomically) closely to the single-mode ones. A laser based on an  $L_{35}$  cavity can be thus quite an appropriate candidate. The  $L_{35}$  PhC cavity is about  $\simeq 7.1\mu m$  long therefore possessing  $\sim 8 \div 10$  modes within the QWR gain bandwidth. The relatively large mode volumes ( $\sim 10(\frac{\lambda}{n})^3$ , although affected by partial mode localization), ensure that the  $\beta$ -factor is expected to be relatively low, so one can envisage a simpler observation of the lasing action compared to the single-mode structures. On the other hand, in addition, it is interesting to examine the multimode-related phenomena in the laser context.

In this section we will first discuss the multimode lasing action experimentally observed from an  $L_{35}$  cavity at low temperature and then, using the temperature tuning to favor the lowest-order mode, we will point out clearly the important spectral and time-resolved characteristics used to conclude the observation of the stimulated emission and lasing.

Measurements were done using micro-PL technique with a Ti:Sa mode-locked laser (Coherent Mira,  $\sim 3ps$  pulse duration,  $76MHz$  repetition rate) operating at  $730nm$ , and the set-up described in the section 3.2.4. The pulsed regime in our experiments, first, allows for excluding sample heating problems and secondly, is just necessary to assess the time-resolved dynamics. All the PhC-QWR experimental structures described in the present chapter contained 3 stacked *InGaAs* (15% of *In*, nominally) QWRs introduced in section 4.3.2.

### 7.2.1 Multimode lasing

Let us start with the observation of the multimode character of the  $L_{35}$  laser. As can be seen from Fig. 7.3 (a), the spectra measured at different pump-power levels do not show a progressive increase in the side-mode suppression ratio, not favoring therefore a particular single mode. It can therefore be an indication of a multimode lasing where some  $\sim 7$  modes are involved. This is not unreasonable, since the modes are relatively densely packed within the spectrum fitting therefore to an *inhomogeneously* broadened single-subband QWR gain. Indeed, from Fig. 7.3 (b), where we plot the input-output curves<sup>8</sup>, modes other than  $M_0$  (i.e.  $M_{1,2,3,4,5}$ ) exhibit threshold-related non-linearity between 5 and  $10\mu W$ . Their intensities however do not finally reach the  $M_0$  level, which

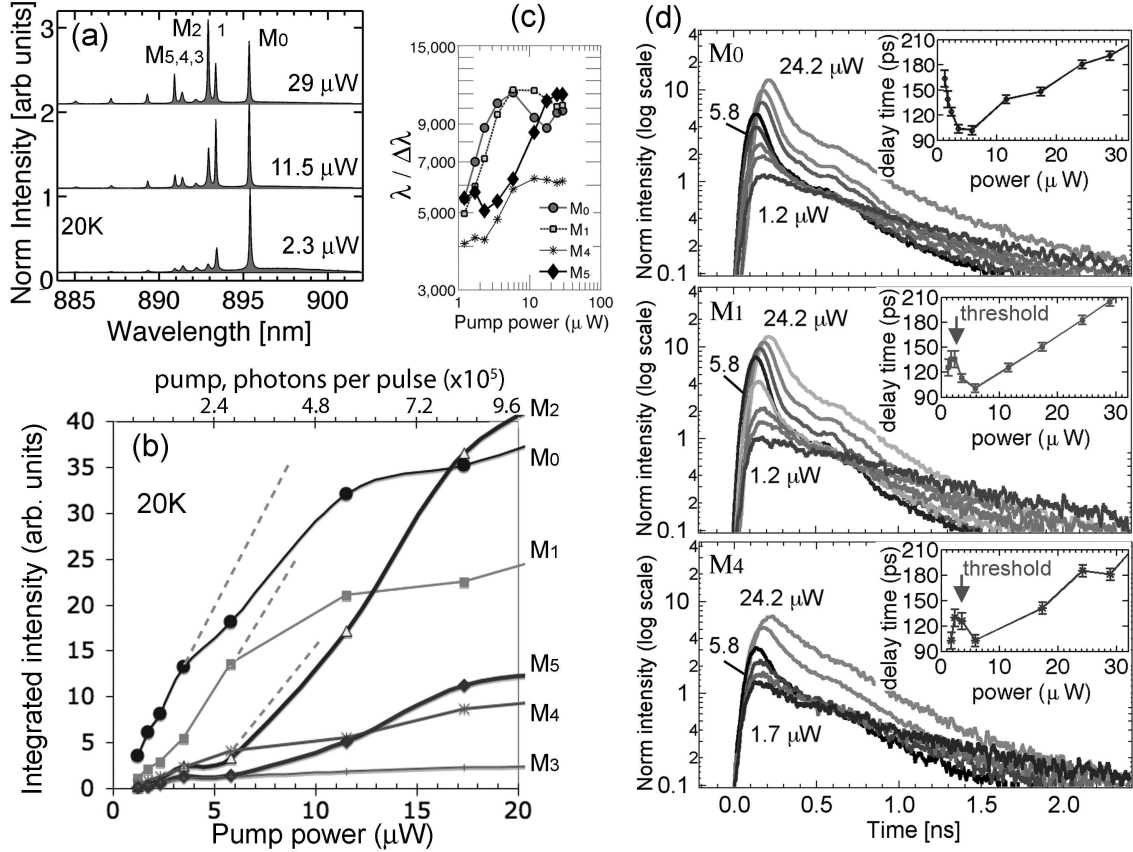


**Figure 7.3:** Observation of the mode competition in  $L_{35}$  PhC laser with  $InGaAs/GaAs$  QWRs. (a) laser spectra at different pump powers. (b) LL curves measured for the first six lowest-order modes; dashed lines indicate possible development if the competition was absent (see text). (c) linewidth trends. (d) Time-resolved signal collected for three modes. The insets show the pump-response time delay. Note that the  $M_0$  mode is apparently just above threshold at the lowest measured power.

<sup>8</sup>The integrated intensity here has a meaning of the output power (integral under the mode peak normalized to CCD acquisition time) and can be compared to the other curves presented in the chapter.

may reflect the gain-curve curvature (i.e. the available gain within this spectral region). Apart from the input-output curves<sup>9</sup> we observe a rather “fast” linewidth narrowing [Fig. 7.3 (c)]<sup>10</sup> and, most importantly, the appearance of the fast emission-decay component in the time-resolved dynamics [Fig. 7.3 (d)] as well as the expected [see Fig. 7.1 (b)] trend of the delay time around the threshold (Fig. 7.3 (d), insets). From this we also see that  $M_0$  is already above threshold within our range of measurements.

Interestingly, as seen from the input-output curves, the intensities of the modes tend to fluctuate depending on the pump power, which points to possible *mode competition*. The mode competition however, in general, is observed in lasers with the *homogeneously* broadened gain peak where the laser tends to oscillate, switching to a mode with higher gain. Different applications (e.g. high-resolution spectroscopy[280], cross gain modulation) require either suppressing or maintaining such an effect.

Let us therefore discuss here multimode lasing in the context of mode competition that may take place in our particular QWR-PhC system. First of all, as can be seen from the spectra [Fig. 7.3 (a)] at different representative power levels, the relative peak intensities of the modes change. This intensity change also takes place for the integrated intensities presented by the light-in light-out (LL) curves [Fig. 7.3 (b)]. Taking into account irregularities in the linewidth-narrowing trends (c) and the time-resolved photon dynamics (d) (and in particular, the *delay time*) may suggest the following possible scenario. Starting from the lowest measured power level ( $\simeq 1.2\mu W$ ) the  $M_0$  is at the point of having just overcome the threshold and it steadily acquires coherence. This is evidenced by the substantial linewidth narrowing, as well as by the build-up of the fast stimulated emission and the drop of the delay time seen in the time domain. The other modes acquire their intensity slowly in a linear way. Between  $\sim 2 \div 3\mu W$  the  $M_1$  mode reaches threshold. This is attested to the delay-time increase and its subsequent drop [see inset for  $M_1$  in (d)]. At this point modes  $M_2$ ,  $M_3$ ,  $M_5$  slightly decline in intensity, as seen from the LL curves. At around  $5\mu W$  there is a transition for the  $M_4$  that manifests itself both in the time domain and in the linewidth trend (transition from the linewidth broadening to the fast narrowing, as expected for semiconductor lasers with a non-zero  $\alpha$ -factor<sup>11</sup>). However, simultaneously, there is a transition for the  $M_2$  and the  $M_5$  modes. The latter two win the competition at this point. This results in a decline of the  $M_4$  mode that might otherwise continue along the corresponding dashed line, saturation of  $M_3$ , and also a decrease in the slope efficiency of both  $M_0$  and  $M_1$  (that could otherwise follow the trends depicted by the dashed lines). Some of the modes try to compete further, which can be deduced from the LL curves and from the delay time trends. In particular, the emission saturation is reflected in the time domain by the increase of the delay time at high excitation powers. Normally (as will also be seen in

<sup>9</sup>The power-dependent characteristics throughout the chapter are expressed in terms of average pump power. Alternatively, one could be interested in the pump-axis represented in units of energy per pulse, or a number of photons per pulse. The latter can be obtained as  $p_{pump} = \frac{\bar{P}}{fh\nu_{pump}}$  where  $\bar{P}$  is the average power,  $f$  – repetition rate,  $h\nu$  – photon energy. This quantity will be assumed for some LL curves in the chapter.

<sup>10</sup>We will later on discuss the narrowing peculiar tendency in section 7.3.3.3.

<sup>11</sup>This question will be further addressed in detail in section 7.3.3.3

single-mode lasers, sec. 7.3.2), such a trend is rather monotonous.

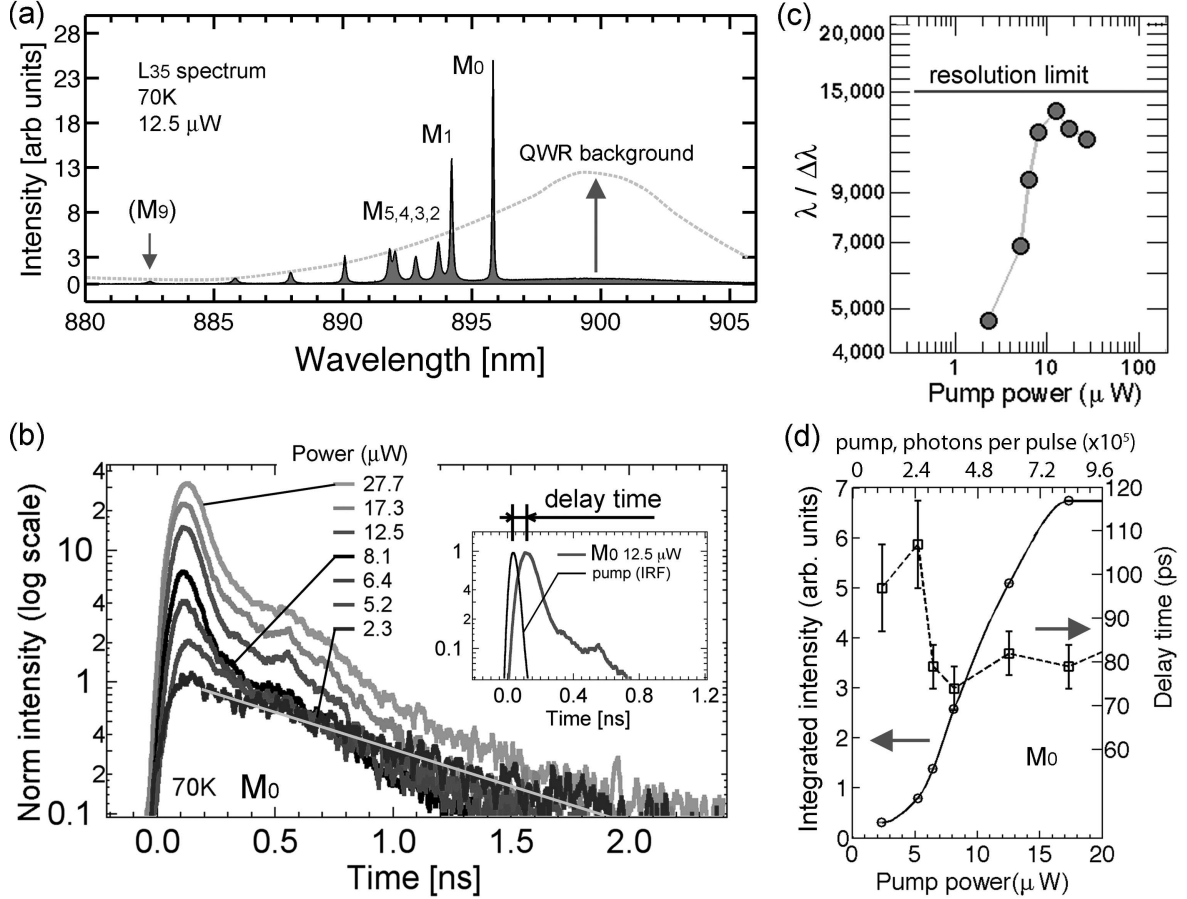


**Figure 7.4:** Spectral and time-resolved properties of the lowest-order mode ( $M_0$ ) of a *InGaAs/GaAs* QWR-PhC laser. (a) Micro-PL spectrum at 70 K. The mode notation and the background QWR spontaneous emission are indicated. (b) power-dependent transient emission collected from the  $M_0$  line; inset shows the delay time between the pump pulse (essentially, Ti:Sa-laser pulse convolved with the instrumental-response function) and the laser response. Note that the bumps at  $\sim 0.4 \div 0.6$  ns are due to the convolution with the IRF. (c) linewidth narrowing. Note that as the peak position does not change significantly, the  $\lambda/\Delta\lambda$  is a good measure which can be compared to the cold-cavity  $Q$ . (d) LL curve and time-delay trend.

Here, on the contrary, variations are observed [see  $M_1$  and  $M_4$  insets in Fig. 7.3 (d)], which can indicate a certain degree of an on-going mode competition. If lasing modes within the effective gain peak can affect their neighbors<sup>12</sup> it means that the (inhomogeneous) broadening in the active medium does not involve totally isolated (localized) emitters. This indicates that at such pump powers the QWR disorder-induced localized states are filled up and the medium is more wire-like (i.e. more homogeneous), which allows for the (partial) mode competition. On the other hand, multimode lasing (without complete switching between the modes) occurs purely due to the inhomogeneous broad-

<sup>12</sup>An effect used in cross gain modulators [223].

ening of the active medium. Note also that the appearance of the higher-order modes at high pump powers reflects saturation of the lower-energy QWR localized states and the gain.

## 7.2.2 Spectral and time-resolved characteristics of a long-cavity QWR-PhC laser

Here we discuss the main characteristics of a given mode of a long-cavity ( $L_{35}$ ) QWR-PhC laser. Since such laser is nominally simpler than short-cavity ones, the trends around the threshold are expected to have more apparent features. This will be useful later on for understanding the properties of the short-cavity QWR-PhC lasing structures. For this purpose, we apply QWR-PhC tuning by temperature (from 20K to 70K), which results in the redshift of the QWR emission, thus the  $M_0$  cavity mode becomes favored with respect to the other ones [see 7.4 (a)]. Now, despite the other modes are present at high pump powers, the  $M_0$  dominates at all power levels (without competing significantly with the other modes) and we can then have a reasonably good clarity of its power-dependent characteristics.

Fig. 7.4 displays a summary of the measured spectral and time-domain characteristics of the  $M_0$  mode of the  $L_{35}$  cavity. Note however that due to partial mode localization, the effective mode volume is reduced (chapter 5), and as we estimated (sec. 5.3), such a mode is rather characteristic of a  $L_{11\div 15}$  PhC cavity.

The time-resolved photoluminescence signal measured at different excitation powers [Fig. 7.4 (b)] exhibits a very remarkable appearance of a *very-fast* (down to  $\sim 50ps$ ) decay component “on top” of a slower one (see a single-exponential base line in the figure). This, as deduced from the spectral analysis, is accompanied by a substantial *linewidth decrease* [Fig. 7.4 (c)]. It thus indicates the *build-up of coherence*, which is due to the increasing role of the *stimulated emission* in the augmentation of the net photon number in the cavity mode. The LL curve shows a non-linear shape with a reasonably visible threshold at around  $\sim 5\mu W$  [Fig. 7.4 (d)]. Finally, the *delay time* between the excitation pulse and the laser response *drops* above this value. Importantly, before the drop there is a certain *increase* of the delay time, as expected from the rate equations. Considering all these characteristics, it is possible to firmly conclude lasing at the  $M_0$  mode in this QWR-PhC long-cavity device.

### 7.2.2.1 Discussion: mode-peak blueshift

Changes in the carrier density can be tracked by the laser wavelength shift. Although scrutinizing such an effect goes beyond the scope of this thesis, we will pay some attention to it, although considering this question in greater detail later on (sec. 7.3.3.4) in the context of single-mode QWR-PhC lasers. And here we would only like to briefly observe the following issues (see Fig. 7.5). First, as a general trend, the mode peak dependency comprises both *red* and *blue* shifts. The blueshift should signify the carrier density increase, and in our case it happens mainly above threshold. In the  $L_{35}$  cavities the magnitude of the blueshift depends on the mode and it generally decreases towards

higher-order modes meaning that the carrier density is lower. This is reasonable, since the QWR intersubband spacing is expected to be large ( $\sim 20\text{meV}$ , between the first heavy-hole and light-hole transitions) compared to the spectral range comprising the first 9  $L_{35}$ -cavity modes ( $\sim 16\text{meV}$ ). That is, another QWR subband is not involved in the gain for these modes. Since the blueshift indicates the augmentation of the carrier density, it in turn signifies that the carrier density is not pinned at a threshold of a given mode, which is also reflected in only *gradual* saturation of the background spontaneous emission observed in the experiment (not shown). This also accounts for why multimode lasing is possible. At pump-power levels of around  $20\mu\text{W}$  the blueshift tends to saturate. At the same power levels we also notice the intensity saturation. As will be discussed a bit further (sec. 7.3.3.4), this may reflect the device saturation due to high carrier density.

Secondly, we note that the mode shift exhibits a maximum, interestingly, the maximum at above the lasing transition, and below threshold we measured a redshift.

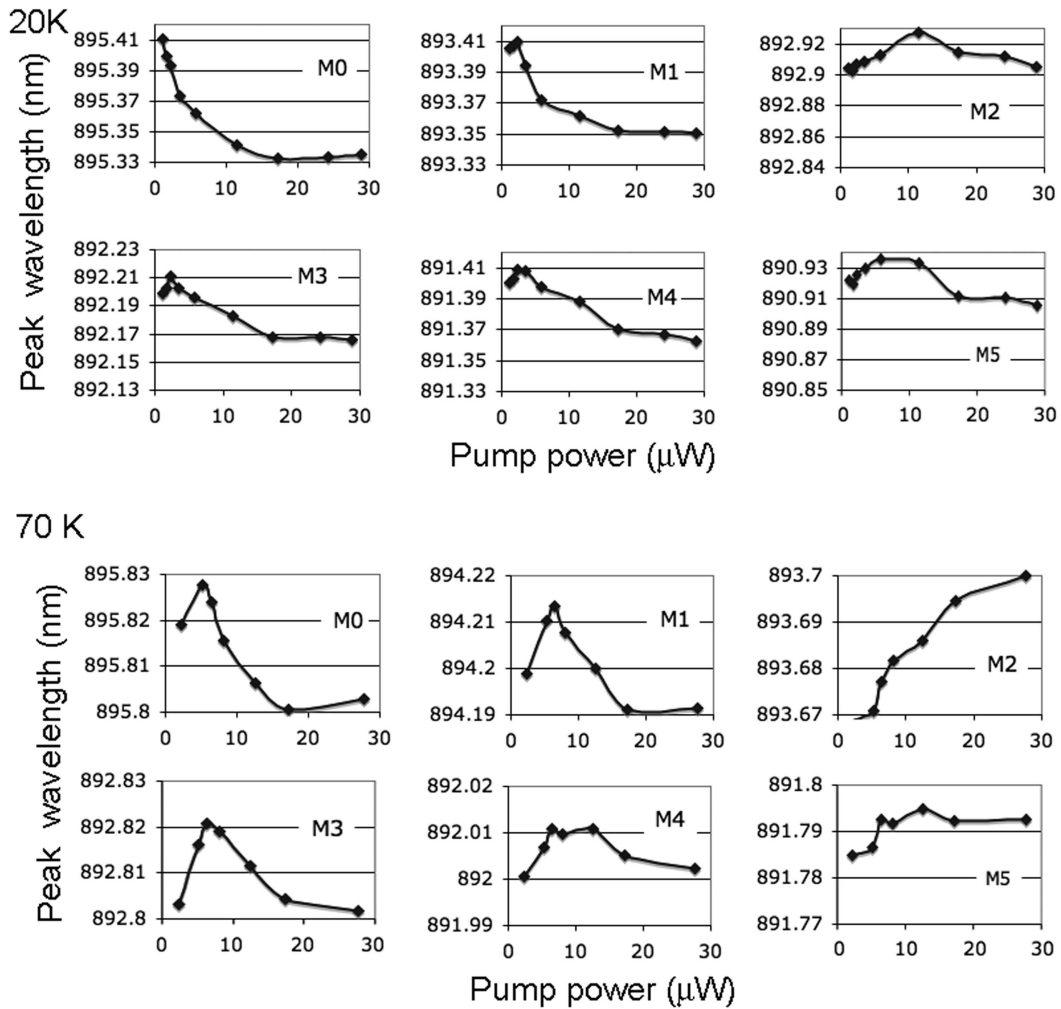


**Figure 7.5:** Mode peak shift observed in the  $L_{35}$  cavity, shown for 6 lowest-order modes at two different temperatures.

### 7.3 Single-mode QWR photonic-crystal lasers

In order to establish the lasing effect for the *single-mode* devices based on  $L_3m$  and  $L_6$  PhC cavities, we analyzed power dependencies of the time-resolved micro-PL signal, LL curves, and linewidth narrowing and then compared them to devices that apparently did not lase. The experimental conditions are essentially the same as in the section 7.2.2.

#### 7.3.1 "Linear" vs lasing output from $L_3m$ , $L_6$ QWR-PhC cavities

Results acquired from  $L_3m$  cavities comparing the behavior of an LED against a laser are presented in Fig. 7.6. The measurements were done at 20K and the "LED" is essentially the structure already presented in the section 4.4.2.4. The most striking difference arises in the time-resolved micro-PL signal. As the excitation power is increased, the LED device [Fig. 7.6(a)] at short delay times exhibits only a clear single-exponential decay with time constants of  $\tau_d \sim 400ps$  (whereas for the bare QWR peak it is  $\tau_d \simeq 880ps$ , see section 4.4.1.1). In contrast, for a non-linear device a very fast component ( $< 50ps$ , deduced here from a double-exponential model convolved with the instrumental response, see Eq. 4.6) is detected "on top" of a slower one ( $\tau_d \sim 350ps$ ) starting from a certain power level. Note that, in principle, when the stimulated emission is present, the double-exponential decay is valid only well above threshold (section 7.1.3.1), and otherwise the decay is a non-linear function dependent on the number of photons in the mode. Nevertheless, here the simple double-exponential decay model is utilized to illustrate the transition. As the estimated Purcell factor (sec. 4.4.2.2) is reduced down to  $\sim 2 \div 3$ , the observed fast decay component cannot stem from the enhanced spontaneous emission. We thus ascribe it to the *stimulated* emission. At a certain excitation level [between 2 and 3  $\mu W$ , see Fig. 7.6(b)] the intensities of the spontaneous-emission and stimulated-emission components within the cavity mode *equalize*, meaning that the mean photon number in the mode is unity and therefore the *lasing threshold* is achieved [102]. These observations in the time domain are supported by a dramatic linewidth decrease (Fig. 7.6 (c), upper panel), whereas the LED device shows only marginal changes, as well as a non-linearity (although rather smooth) in the LL curve (Fig. 7.6 (c), middle panel). A coarse estimation from the LL curve confirms the threshold power of  $\sim 2.5\mu W$ . Both LED and laser devices exhibit gradual emission saturation above  $\sim 15 \div 20\mu W$ , which is likely to be related to carrier relaxation effects in the QWRs, as observed in section 4.4.1.1 (increasing rise times, see Fig. 4.10).

As discussed in section 4.4.2.5, at high temperature, due to effectively reduced QWR disorder effects and the efficient carrier capture from the QWs, the performance of a PhC-QWR light-emitting device can improve. Generally, high-temperature operation, apart from the practical device implementation, can provide faster laser dynamics due to faster carrier relaxation [281]. The optimal operation regime therefore will be defined by a compromise with the non-radiative recombination that, according to the observations made in the subsection 4.4.2.6, was significant for our PhC-QWR structures already at

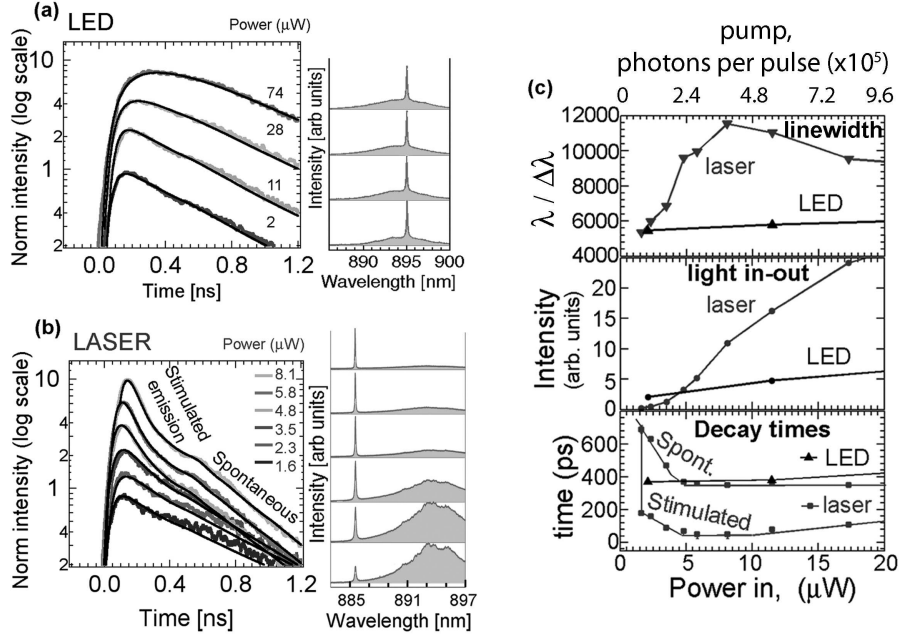


**Figure 7.6:** Time-resolved and spectral characteristics of a "linear" QWR-PhC device compared to those of the PhC-QWR laser at 20K. (a) LED PL transient intensity at different excitation powers, (right) corresponding micro-PL spectra. (b) PL transients at different excitation powers from a lasing device, (right) corresponding micro-PL spectra. The irregularity (bump) appearing in the measured data and in the convolved fit at  $\sim 0.6ns$  delay time is due to the instrumental response. (c) Summary for both (a) and (b) devices: linewidth narrowing, LL curves, and decay times. Lines are guides to the eye. Note that for the lasing structure a distinguishable fast decay component appears only above  $\sim 1 \div 2\mu W$  (indicated by a vertical line).

70K. Therefore the range of 50-70K is interesting in the present work<sup>13</sup>. Fig. 7.7 shows the time-resolved characterization of an  $L_6$ -cavity laser at 70K. The estimated decay times of the fast dominating component are of the order of  $\tau_d \simeq 30 \div 50ps$ , which is around the resolution limit of the measurement set-up. Therefore, as is in the case of Fig. 7.6 (b), the emitted signal is attributed to the *stimulated emission*. The fast decay component dominates the decay at all the measured powers although still evolving at the lowest pump levels, which indicates that the device is *above* the threshold. As in the case of Fig. 7.6, this is further supported by the "fast" linewidth narrowing. The LL curve does not show a transition, which, as already suggested by the PL transients, is due to the fact that the device is above threshold. On the other hand, the output intensity is up to an order of magnitude smaller<sup>14</sup> compared to the case of 20K. This however correlates with the overall decrease of the collected PL signal from the QWR-PhC structures at 70-80K, and is likely due to the non-radiative recombination. Nevertheless,

<sup>13</sup>Further improvements are expected from the surface-passivation sample post-processing, e.g. with  $(NH_4)_2S$  chemistry [282, 283].

<sup>14</sup>Both devices are measured in the same conditions regarding the alignment of the optical set-up.

according to estimations of the non-radiative recombination rate at these temperatures (Sec. 4.4.2.6), the decay-time constant associated with the cavity Purcell effect is still  $\sim 4$  times smaller than that of the non-radiative loss, which eventually allows for lasing.

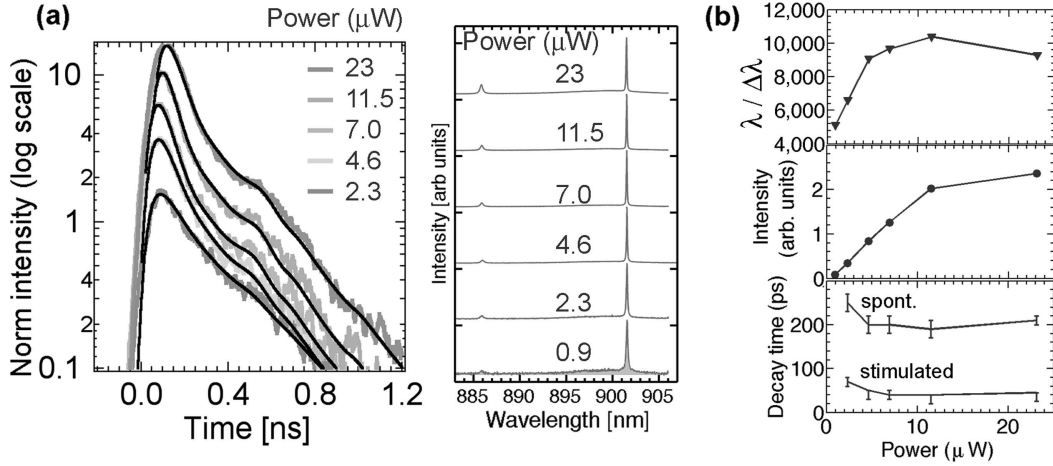


**Figure 7.7:** Time-resolved and spectral characteristics of an  $L_6$ -cavity QWR-PhC laser at 70K. (a) PL transients at different excitation powers, and (right) corresponding micro-PL spectra. (b) Summary on the corresponding spectral and temporal characteristics: linewidth, LL curve, and decay times. Lines are guides to the eye. Note that the device is above threshold for the whole range of measurements.

### 7.3.2 QWR-PhC laser onset dynamics

We shall further discuss the *delay* time between the excitation pulse and the response in the context of threshold and emission saturation (as was also done in section 7.2). In addition, this quantity is important by itself, since it indicates the large-signal modulation capabilities of such devices [284].

As can be inferred from Fig. 7.6 (a) (and also from Fig. 4.14(a,b) of section 4.4.2.4), the delay time in a *non-lasing* device at 20K steadily increases with excitation power due to the increase of the rise time. On the contrary, in a *lasing* structure the delay time starts decreasing at a certain excitation level [Fig. 7.8(a)]. At higher powers, saturation effects take place, which results in a monotonous increase of the rise time constant and hence longer delay times. *Minimum* delay-time values, to which an *optimum* above-threshold operation regime can be assigned, can depend on the excitation conditions and carrier relaxation dynamics. In particular, both the peak delay and the width of the peak in the time domain can strongly depend on the (higher) excitation energy due to (slower) carrier thermalization microscopic processes [275]. In our case the excitation energy is largely detuned from the QWR-PhC resonance ( $\sim 300\text{meV}$ ), therefore if consistent with ref. [275]<sup>15</sup>, the expected (minimum) delay time is  $\sim 50 \div 60\text{ps}$ . At

<sup>15</sup> $In_{0.2}Ga_{0.8}As/GaAs$  quantum-well active medium, 20K,  $\sim 100\text{fs}$  excitation regime.

low temperature (20K) values of  $\sim 80 \div 90ps$  were measured<sup>16</sup> from  $L_3m$  QWR-PhC devices, which is due to slower relaxation dynamics in the QWRs compared to QWs.

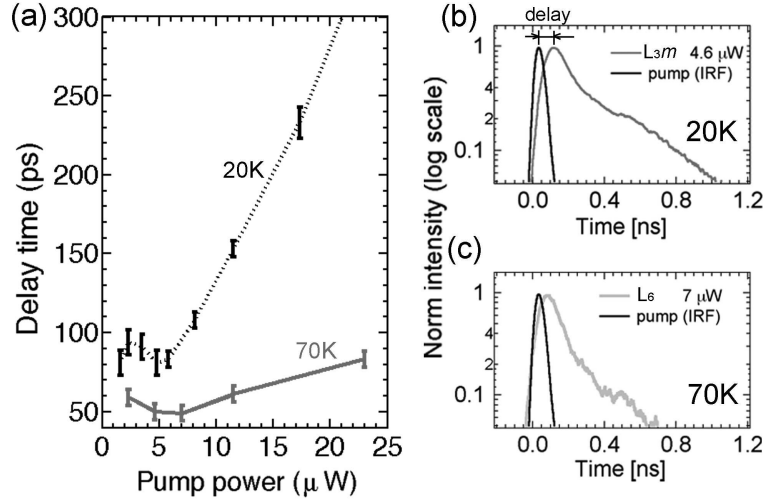


**Figure 7.8:** Delay time between the excitation pulse and the laser response.  $L_3m$  and  $L_6$  cavities. (a) Dependency on the pump power at 20K ( $L_3m$ ), and faster dynamics at 70K ( $L_6$ ). (b,c) PL transients corresponding to the minimum delay time in each case.

The effect of saturation at high excitation power may be due to hot carrier effects [285], which can be particularly important in reduced-dimensionality media such as QWRs and QDs resulting in slow carrier relaxation dynamics. As can be seen from Fig. 7.8 (observed also in section 7.2), the delay time is temperature-dependent resulting in a faster performance at 70K, which points to faster relaxation due to more efficient carrier-phonon interaction<sup>17</sup>. The minimum delay time  $\sim 50ps$  indicates a potential capability of large-signal modulation of  $\sim 20GHz$ . Further improvements are naturally expected at higher temperatures.

### 7.3.3 Details of the spectral features

In this section we will be looking further into details of the spectral characteristics of the QWR-PhC single-mode microcavity lasers. Important peculiarities of the mode *linewidth* narrowing, the peak *shift*, the light-in light-out (LL) curves considering also the QWR *background* spontaneous emission are examined. Since, according to the preceding

<sup>16</sup>In the experiment, since 3 longpass filters (overall thickness  $\sim 8mm$ ) were used in the collection path to eliminate the laser light reflected from the sample, the arrival of the signal is  $\simeq 14ps$  later (assuming the glass refractive index of  $n \approx 1.5$ ) compared to the the time-resolved signal of the excitation pulse that was measured without the filters.

<sup>17</sup>Note that the cavity length affects only little the QWR saturation, and as discussed in section 7.2, the delay-time increase for  $L_{35}$  cavity starts at similar pump powers as for the  $L_3m$ . Therefore the temperature should have the major effect.

discussion, the dynamical properties are expected to be improved at higher temperatures, in the present section experiments were performed at 50K, which was chosen as a compromise temperature regarding the non-radiative recombination (at 70K). The pumping conditions were kept consistent with those of the section 7.3.1, although a different laser was used (Spectra Physics Tsunami Ti:Sa at 700nm, modelocked with pulse duration  $\sim 3ps$  and the repetition rate of 78MHz).

### 7.3.3.1 LL curves

Examining several  $L_3m$  and  $L_6$  cavities, we observed different types of devices that can be categorized into three groups: lasers, LEDs and those in between the first two. Here for clarity and in order to assess the distinction between the *single-mode* LED and

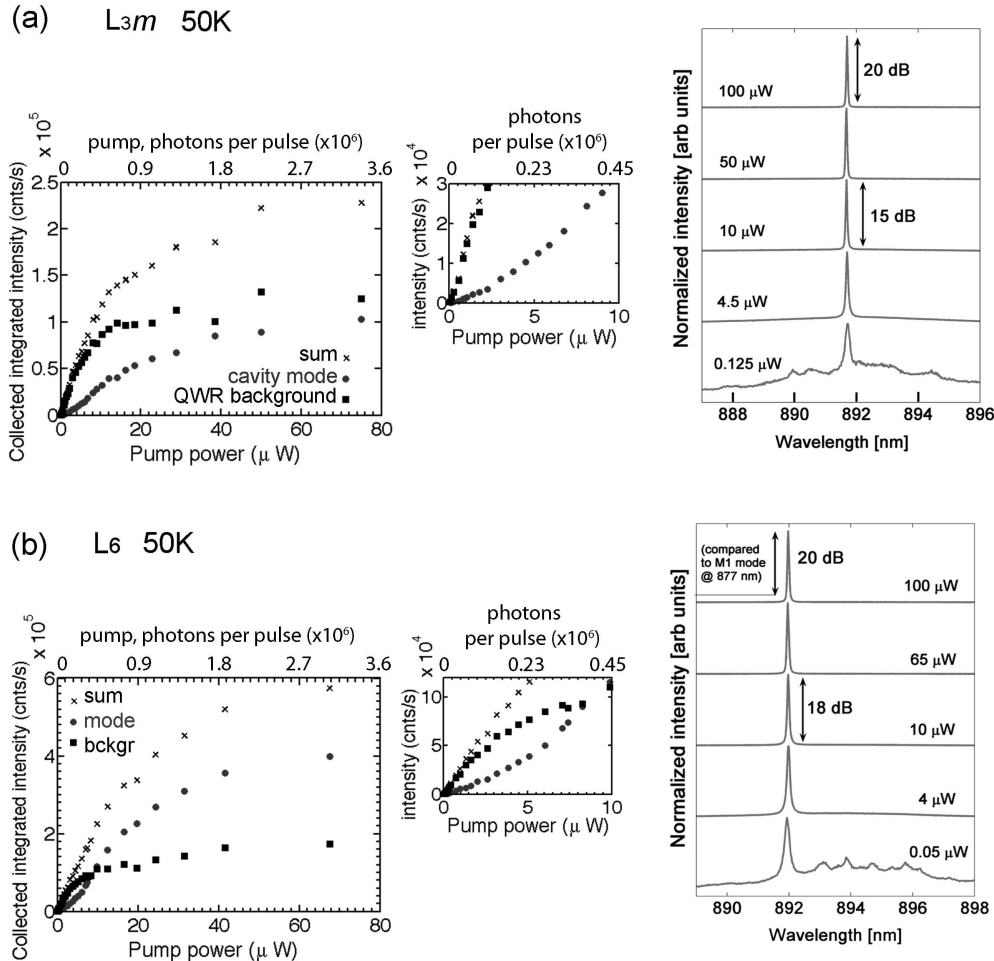


**Figure 7.9:** Output power (in units of CCD counts per second) dependencies for lasing QWR-PhC devices. The analysis includes cavity-mode and QWR background integrated intensities. (a)  $L_3m$  structure, (b)  $L_6$  structure. Corresponding spectra are shown to the right (linear scale).

laser operating regimes we will discuss these two well-defined groups. The evaluation of spectral features (output power, background emission, linewidth, peak position) is based on the procedure described in section 3.2.3.2.

Figure 7.9 displays the collected integrated intensity (in CCD counts per second) for the mode and for the QWR background emission in the case of *lasing* devices. As can be seen from the LL curves, the intensity within the cavity mode grows in a *non-linear* fashion with increasing pump power. Moreover, the *differential efficiency*, given by the derivative  $dL_{out}/dL_{in}$ , *increases* with power. At the same time, the background QWR *spontaneous* emission grows linearly at very low powers, followed by a gradual saturation (slope *decline*). Although the background tends to saturate at  $\sim 20\mu W$ , this point on the cavity-mode LL curve does not correspond at all to the expected lasing threshold ( $\lesssim 1\mu W$ , as will be deduced further, mainly from the linewidth trends, sec. 7.3.3.3). The saturation happens in a rather gradual manner, suggesting that the carrier density is *not pinned* at threshold, which can either be due to the carrier diffusion [171] enabled by the spatial hole burning [211] or it reflects the high- $\beta$  property of a microcavity laser [103, 255, 256], or is simply due to the inhomogeneous broadening (ensemble of independent emitters). Since it is not possible to completely separate these effects, we will have to refrain from making conclusions based on carrier-density pinning argument.

The *differential efficiency* can be a good means to distinguish between the LED and laser regimes. Essentially, it is expected to grow for a laser overcoming the threshold, and to decline for an LED that does not have any threshold. A *non-lasing*  $L_6$  device is presented in Fig. 7.10. In this case, the spectrum looks somewhat similar to a lasing de-

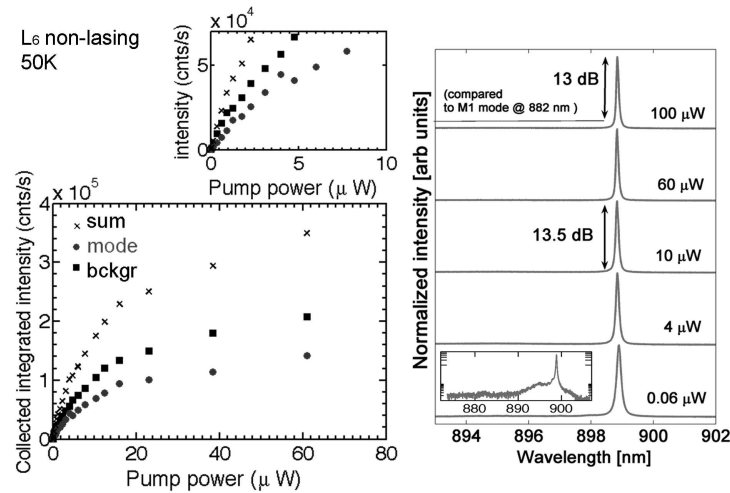


**Figure 7.10:** (a) Output power (in units of CCD counts per second) dependency for *non-lasing* QWR-PhC devices ( $L_6$  structure here). The LL curve of the cavity mode is qualitatively similar to that of a background emission.

vice (i.e. single mode, high peak-to-background ratio). However the LL curve evaluated for the cavity mode and the LL curves for the QWR background are qualitatively identical (also resembling those of the background emission of the Fig. 7.9). This suggests

that such a light output is basically due to the QWR spontaneous emission efficiently filtered by the cavity mode. In essence, the device is an *LED* although having *laser-like properties* (i.e. a narrow linewidth and good side-mode discrimination). A comparison on the basis of the differential efficiency (Fig. 7.11) with a lasing  $L_6$ -cavity device clearly indicates that, before the general emission saturation (at  $\sim 20\mu W$ ), whereas for the laser the differential efficiency  $dL_{out}/dL_{in}$  increases with pump power, for the LED it declines. This illustrates clearly the difference between the two device types.

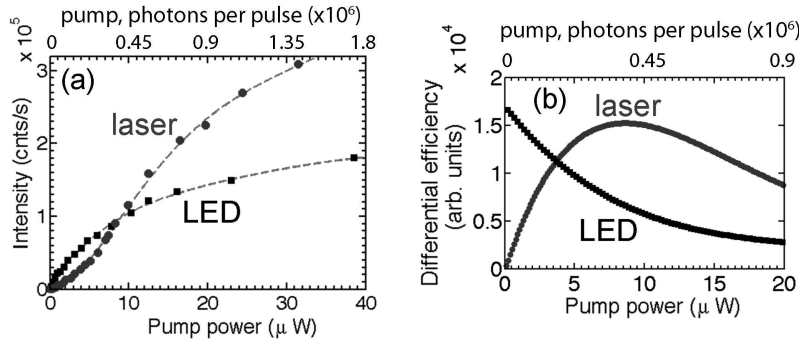


**Figure 7.11:** Comparison of the non-lasing  $L_6$  cavity to the lasing  $L_6$  one. (a) LL curves (dashed lines are guides to the eye). (b) Inferred from (a), differential efficiency illustrating, at low powers (below  $10\mu W$ ), the difference between a lasing and a LED devices.

### 7.3.3.2 $\beta$ -factor

Although in the short-pulse excitation mode evaluation of the  $\beta$ -factor can be difficult [286], we shall roughly estimate it for the QWR-PhC lasing structures. In order to do so we apply the rate-equations model (section 2.2.1), namely, Eq. 2.24 to fit the measured LL-curves. Here  $V_a = 3 \times (5 \times 5 \times 1000)(nm^3)$  (i.e. 3 QWRs),  $\tau_{nr} \simeq 1.1ns$  (see section 4.4.2.6), and all the other parameters are the same as those used in section 2.2.2<sup>18</sup>. The fitting results are shown in Fig. 7.12. For the  $L_{3m}$  and the  $L_6$  cavity  $\beta \sim 0.3 \pm 0.1$  is derived as a conservative estimation. The value of  $\beta$  can serve only as a coarse approximation, although much smaller or larger values do not fit (also shown in Fig. 7.12). There is a certain discrepancy at very low pump powers [see Fig. 7.12 (b)], although in a linear scale the fit is rather reasonable [inset in Fig. 7.12 (b)]. More importantly, at high excitation powers a complete divergence is observed. This is clearly due to gain saturation effects when the excitation is done using very short pulse durations (e.g.  $\sim 1ps$ ), which may influence the accuracy of the  $\beta$  determination [286]. The saturation in our case does take place at about  $20\mu W$  (checked for several measured devices), which is well above threshold, i.e. there are about two decades available for the proper fit before the saturation. So the conclusions on the  $\beta$ -factor are then not unreasonable [279]. However we still regard the estimation as indicative. The *threshold* average pump power deduced from the fitting is around  $1\mu W$ . Considering the saturation and the LL-curve smoothness at low powers, this estimation has some ambiguity. We will eliminate this ambiguity by analyzing the linewidth narrowing trends in the following subsection.

<sup>18</sup>Note also that non-scaling shift is needed to properly account for the collected output power. This however does not affect the model LL curve.

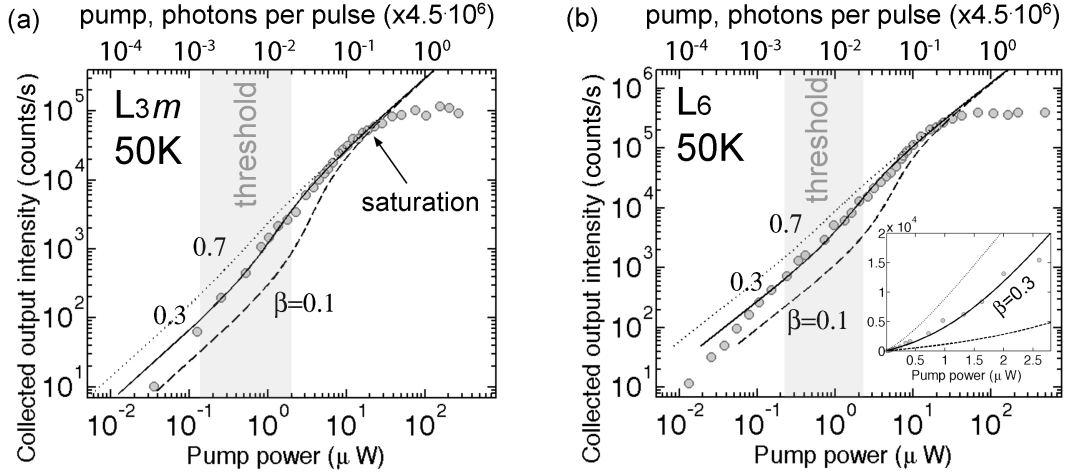


**Figure 7.12:** Estimation of the  $\beta$ -factor using LL-curves from fits to the rate-equation model (a) for the  $L_{3m}$  and (b) for the  $L_6$  cavity. According to a conservative estimate,  $\beta \sim 0.3$  in both cases.

### 7.3.3.3 Linewidth and the threshold

An uncertainty of the threshold estimation in the LL-curves can be resolved with the help of the power dependence of the linewidth. Secondly, a difference between a lasing and a non-lasing structures can be established with greater confidence. This is demonstrated in Fig. 7.13. As can be clearly seen, for the LED  $L_6$  cavity the measured inverse linewidth increases in a "linear" fashion on the logarithmic scale. On the contrary, the linewidth power dependencies for the *lasing* devices ( $L_{3m}$  and  $L_6$ ) are quite peculiar. Importantly, the major linewidth decrease here has a much steeper slope compared to the LED case, which is due to the steady built-up of *coherence* provided by the stimulated emission. Note that the results shown in the Fig. 7.6 (c) and Fig. 7.7 are also consistent with this particular regime.

As discussed in section 7.1.2, for a semiconductor laser with a non-zero  $\alpha$ -factor linewidth broadening should occur, which helps indicating the threshold [114, 262, 269]. This is apparently observed in our QWR-PhC lasing structures. This feature – consistent with arguments in ref. [214] and the fact that the  $\alpha$ -factor is expected to be small in low-dimensional semiconductor nanostructures [9] – is relatively smooth, and in some devices it resulted in a relatively constant plateau prior to the onset of the steady linewidth decrease<sup>19</sup>. From these particular linewidth trends (Fig. 7.13), the inferred lasing threshold is only  $\sim 0.3\mu W$  for both  $L_{3m}$  and  $L_6$  devices introduced in Fig. 7.9. Several other similar structures (measured at 10-50K) exhibited a threshold  $\sim 0.8 \div 1\mu W$ . Similar PhC cavities reported in the literature, implemented with high-density self-assembled QDs exhibited lasing thresholds at around  $1 \div 2\mu W$  in pulsed [116] and CW regimes [269, 278]. Some  $\sim 100$  QDs [269] can contribute to the cavity mode in these cases. Here in our triple-QWR PhC structures  $\sim 100 \div 200$  excitons

<sup>19</sup>Possibly,  $\alpha$ -dependent.

may be contributing. This is assuming, on one hand, that along a  $\sim 1\mu\text{m}$ -long wire excitons localize (at low pump power) within  $\sim 15 \div 20\text{nm}$  segments ([82, 287], and section 4.4.1.2); and on the other hand, that at high excitation power the localization can be smeared off (sec. 4.1) enabling more extended QWR states to contribute.

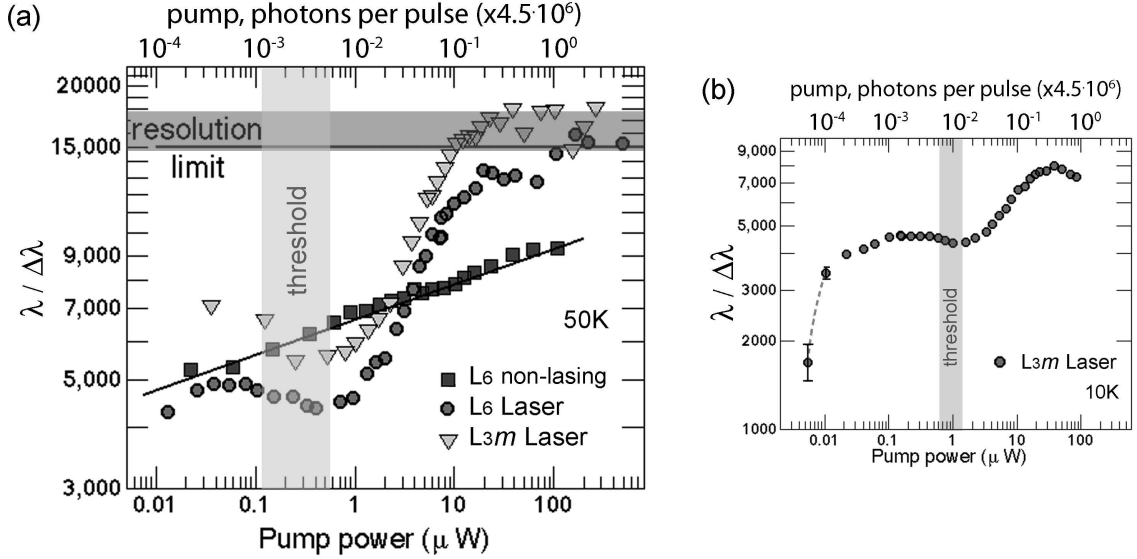


**Figure 7.13:** Power dependence of the linewidth. (a)  $L_{3m}$  and  $L_6$  laser linewidths are compared to that of a non-lasing  $L_6$ . For the lasers the threshold region is indicated (see section 7.1.2). For the LED the continuous line is a guide to the eye. (b)  $L_{3m}$  laser from a different sample, also indicating the measured linewidth at very low powers suggesting the power region where absorption saturation takes place.

So far the reported pump powers are those measured before the objective lens of the optical set-up. If we take into account the *absorbed power* within the GaAs membrane<sup>20</sup> and the effective area ratio between the pump spot and the cavity<sup>21</sup>, the threshold values are scaled by  $F = f_{abs}f_{spot} \simeq 0.215 \times 0.25$ . However, since there can be an additional inflow of carriers towards the cavity due to spatial hole burning [211], the  $f_{spot}$  factor can still be ill-defined. Dropping it altogether gives a conservative estimate of the threshold average powers in the range of  $L_{th} \sim 60 \div 215\text{nW}$ .

### 7.3.3.4 Discussion: carrier density and saturation

A useful means for experimentally estimating the carrier density in the active medium of a laser is tracking the cavity mode *shift* with excitation power [255, 256]. Injected free

<sup>20</sup>This part is  $(1-R)(1-e^{-\alpha L})$ , plus the part from the first internal reflection  $(1-R)e^{-\alpha L}R(1-e^{-\alpha L})$  and one reflection from the substrate  $(1-R)^3e^{-\alpha L}R(1-e^{-\alpha L})$ , which with  $R \simeq 0.3$ ,  $L = 260\text{nm}$ ,  $\alpha_{GaAs} = 10^4\text{cm}^{-1}$  gives  $0.16 + 0.037 + 0.018 = 0.215$  of the incident power absorbed within the membrane.

<sup>21</sup>Gaussian spot with FWHM  $\sim 1.4\mu\text{m}$  overlapping with the effective cavity conservatively assumed to be a  $\sim 450\text{nm}$  wide stripe.

carriers reduce the refractive index [288] lowering therefore the mode effective index, which shifts the mode to a higher frequency<sup>22</sup> (i.e., *blue-shift* takes place). Note that compared to long-wavelength *InP*-based structures [255, 256], such a shift in *GaAs*-based material is reduced by more than an order of magnitude [289].

In our experiments we observed the cavity-mode blueshift (Fig. 7.14), however only well *above* threshold. Moreover, there is a difference between lasing and non-lasing structures. For the lasing samples we observe [Fig. 7.14 (a)] a red-shift at very low powers (below threshold), and a blueshift at somewhat high powers ( $\gtrsim 4\mu W$ ), and most importantly, a smooth transition *without* an appreciable mode shift between these two regions. The overall blueshift is  $\delta\lambda \approx -0.04nm$  on average (from several structures). Interestingly, for the LED devices the blueshift sets in immediately at very low powers and its overall magnitude tends to be larger ( $\delta\lambda \approx -0.07nm$ ). This difference indicates that the carrier density grows more slowly in the lasing structures above threshold, possibly due to a faster conversion governed by the stimulated emission, whereas in the LED structures that are based on a slower spontaneous emission the carrier density is larger. At higher pump powers (e.g.  $\gtrsim 4 \div 7\mu W$ ) the blueshift occurs also for the lasers

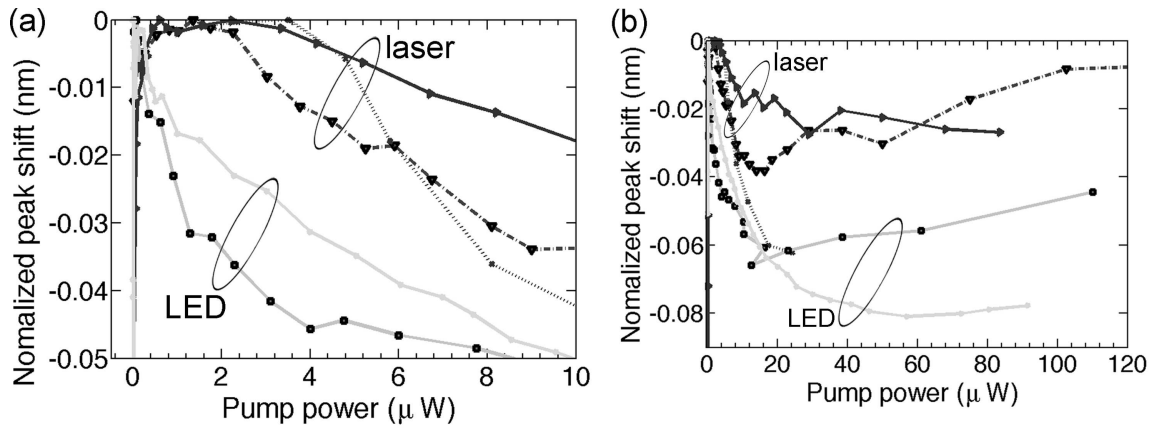


**Figure 7.14:** Mode peak shift measured for single-mode QWR-PhC structures. (a) Interestingly, for the lasing devices there is a pump-power range where the peak does not shift. (b) At relatively high pump powers red-shift occurs.

meaning that the carrier density is increased. This can be due to both the increased number of carriers photogenerated within the GaAs matrix, the QWs and the carriers in the QWRs, which should then be a consequence of the QWR band-filling effect. According to 3D FDTD simulations performed on a test  $L_3$  cavity<sup>23</sup>, the effective-index change corresponding to  $\delta\lambda = -0.04 \div -0.07nm$  is  $\delta n_{fc} \simeq -1.6 \times 10^{-4} \div -2.8 \times 10^{-4}$ . These values are expected to correspond to the carrier density at the QWR emission saturation level (sec. 4.4.2.4, Fig. 4.14), i.e. above  $N \sim 10^{18}cm^{-3}$ . Given a bulk-GaAs

<sup>22</sup>This is easy to see e.g. from a standard  $\omega - \beta_p$  (dispersion) diagram of a waveguide, where  $\beta_p$  is the propagation constant [119].

<sup>23</sup>Tracking the wavelength of the fundamental  $M_0$  cavity mode, an index change of  $-0.0148$  induces a blueshift of  $-3.66nm$  at  $\lambda \sim 880nm$ .

carrier-induced refractive-index change rate of  $\delta n_{fc} \simeq 1.5 \times 10^{-21} N$  [289], the obtained carrier density change is  $\lesssim 10^{17} \text{cm}^{-3}$ . However, taking into account the QWR optical confinement factor of  $\sim 0.005^{24}$  gives roughly  $N \sim 10^{19} \text{cm}^{-3}$ . Therefore the blueshift is mainly due to the increased carrier density in the QWRs. The band-filling effect is also present, which is evidenced by the appearance of the first higher-order mode of the  $L_6$  cavity at high pump-power levels<sup>25</sup> (see e.g. Fig. 7.7).

Secondly, according to the observed photon dynamics (sec. 7.3.2), the pump-response *delay time starts increasing* at about  $\sim 5 \div 10 \mu\text{W}$  reflecting a slow-down in the laser response, which at higher powers ( $\sim 20 \mu\text{W}$ ) is followed by *emission saturation*. Additionally, as at high pump rate the carrier temperature can significantly grow [215], subsequent cooling (i.e. energy transfer to the lattice) can induce local thermal effects within the active medium, severely deteriorating the laser output. The thermal effect would then result in a mode *red-shift* [255], which is observed here at pump powers  $\gtrsim 20 \div 40 \mu\text{W}$  [Fig. 7.14].

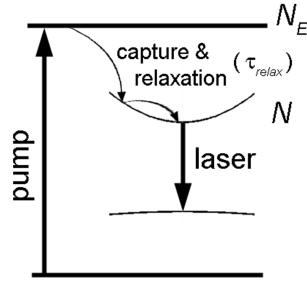


**Figure 7.15:**  
Schematics of a level diagram.

The saturation is likely to be connected to the slow-down in the carrier relaxation at high pump powers (which was observed both for bare QWRs and for non-lasing QWR-PhC structures). Here we would like to briefly discuss the influence of slow carrier relaxation on the photon dynamics using rate equations. To this end, we add to Eq. 2.20 and Eq. 2.21 a third rate equation which implements the pumping into the  $GaAs$  matrix and relaxation rate given by the time constant  $\tau_{relax}$ . Assuming for simplicity that carrier dissipation from the pump level (see Fig. 7.15) happens mainly via relaxation (to the QWRs), we have the following system:

$$\frac{dN_E}{dt} = \frac{L_{in}}{\hbar\omega_{in}V_a} - \frac{N_E}{\tau_{relax}} \quad (7.2)$$

$$\frac{dN}{dt} = \frac{N_E}{\tau_{relax}} - \frac{N}{\tau_{sp}} - \frac{N}{\tau_{nr}} - \frac{gp}{V_a} \quad (7.3)$$

$$\frac{dp}{dt} = -\frac{\omega_{cav}}{Q}p + gp + \frac{\beta NV_a}{\tau_{sp}} \quad (7.4)$$

for the carrier number at pump level ( $N_E$ ), the carrier number at emission level ( $N$ ) and the photon number ( $p$ ), respectively. Fig. 7.16 displays example calculations for  $\tau_{relax} = 25 \text{ps}$  and  $\tau_{relax} = 100 \text{ps}$ . This can be compared<sup>26</sup> to Fig. 7.1 (where  $P_{th} =$

<sup>24</sup>Estimated from the overlap between 3 QWRs and the 3D electric-field distribution.

<sup>25</sup>Which is also consistent with observations of the higher-order modes from the  $L_{35}$  cavity (sec. 7.2.2.1).

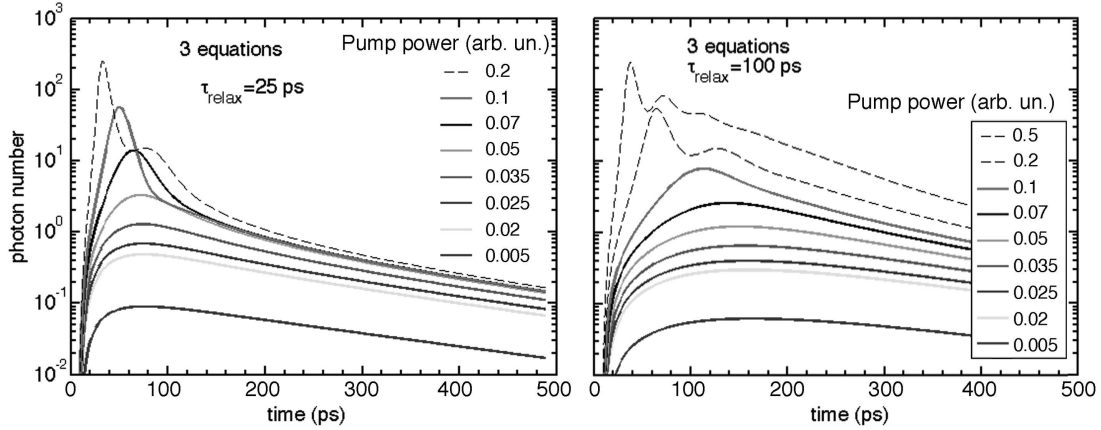


**Figure 7.16:** Photon dynamics (photon number vs time) calculated from a system of three rate equations containing slow relaxation rate from the pump to the emission level. (a)  $\tau_{relax} = 25ps$ , (b)  $\tau_{relax} = 100ps$ .

0.025 in arbitrary units). In the response now the output pulse broadens and at high power levels the laser relaxation oscillations are present. If we consider that at a given power level  $\tau_{relax}$  increases, we may observe the following saturation trend. As a simple example, depicted in Fig. 7.17 (a), we assumed  $\tau_{relax} = 25ps$  at  $P = 0.1$  and  $\tau_{relax} = 150ps$  at  $P = 0.15$  (i.e. at  $4 \times P_{th}$  and  $6 \times P_{th}$ , respectively, where  $P_{th} = 0.025$  at  $\tau_{relax} = 1ps$ ). We see that the delay time increases quite significantly and the fast decay component is smeared out. Note that in such a situation, despite the peak pulse power also goes down, the time-integrated intensity (within the mode) may still be higher (e.g. as compared here to  $P = 0.1$ ). In the experiment we observed somewhat similar

<sup>26</sup>Parameters and the gain model for the rate equations are kept the same as in section 7.1.3.1.

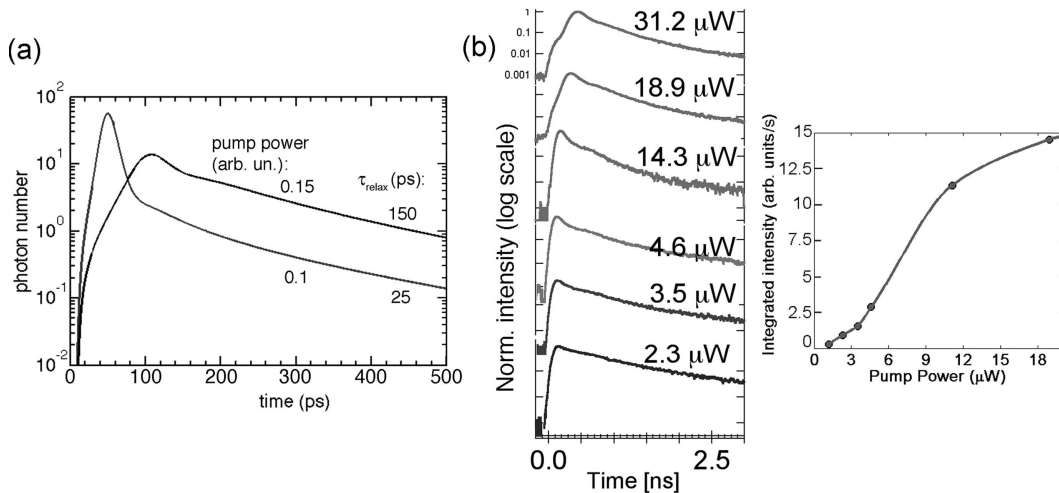


**Figure 7.17:** (a) Effect of increasing carrier relaxation time with pump power on the delay time. (b) Experimentally observed saturation trend for a  $L_3m$  cavity at 20K (in log scale each transient spans 3 decades). LL curve is also shown, for reference.

trend of saturation, regarding the delay time. An example is shown in Fig. 7.17 (b) showing measurements at 20K for a  $L_3m$  cavity. We did not however see clearly laser relaxation oscillations (as might be expected from Fig. 7.16), which might be due to insufficient set-up resolution ( $\sim 60ps$ ) and also because these signal details might get hidden in the convolved response (e.g. see Fig. 7.4 ( $L_{35}$  laser) for which the bumps at around  $0.5 \div 0.6ns$  are most likely due to the convolution with the instrumental-response function).

## 7.4 Chapter summary

In summary, we demonstrated, for the first time, photonic-crystal microcavity lasers that employ site-controlled quantum wires as an active medium. Both single-mode ( $L_3m$  and  $L_6$ ) and multi-mode ( $L_{35}$ ) devices were considered. The lasing action in the pulsed mode was established through the observation and analysis of the emission in the spectral and time domains, in comparison to non-lasing devices. In particular, the build-up of coherence due to stimulated emission was evidenced by measuring the emission decay transients, pump-response delay times and the linewidth narrowing. At the same time, non-linearity in input/output curves was registered. Based on these characteristics, threshold average pump powers of  $\sim 1\mu W$  ( $\sim 250nW$  in absorbed power) were thus achieved with an estimated spontaneous-emission coupling factor  $\sim 0.3$ .

In parallel, HBT interferometry experiments for determining the threshold from photon statistics were tried. However, observations were challenging due to unknown threshold power, therefore from a few points measured it was not possible to draw firm conclusions. On the other hand, details of the laser characteristics (differential efficiency, linewidth, dynamics) were elaborated and comparisons to the LED regime of operation were made. The dynamics was found to be faster in the QWR-PhC lasers operating at higher temperature (70K compared to 20K), however the output power is then compromised by non-radiative recombination. Further studies at higher temperatures (all the way up to room temperature) and quasi-CW pumping regime would be of interest. This might require implementing surface passivation methods. Emission saturation effects were observed at pump-power levels of  $\sim 10 \div 20\mu W$  for all QWR-PhC structures, evident from LL curves, linewidth trends and time-resolved photon dynamics. It is believed that the saturation is due to high carrier density effects acting to slow down the carrier relaxation to the QWRs (hence slowing down the population of the emission level). However, a full microscopic model would be required to quantitatively explain such effects.

# Chapter 8

## Conclusions and outlook

In this thesis work we have developed and studied experimentally semiconductor 2D photonic-crystal microcavities integrated with quantum-wire nanostructures. Based on existing general knowledge in PhC micro-fabrication and QWR MOVPE growth, we established a technology that allows for integration of *site-controlled* nanostructures such as QWRs (and also QDs [133]) into 2D membrane PhC cavities, suited for cavity-QED experiments and promising for realization of novel light sources. Within the framework of the thesis we fabricated QWR-PhC structures achieving routinely a relevant site-control *accuracy* of  $\sim 40nm$ , implemented with conventional patterning techniques, and single-mode cavity *Q*-factors  $\sim 5000 \div 6000$ .

With this particular system in hand, our major interest was twofold, which developed into the following main results:

- ★ exploiting the embedded QWRs as an efficient *local* internal light source, we probed the characteristics of a general class of 1D-like  $L_N$  PhC microcavities, and examined directly-coupled single-mode PhC cavities;
- ★ we conducted studies on light-matter coupling in the PhC-QWR system, observing spontaneous emission, and furthermore achieving stimulated emission and lasing action based on the microcavity and spontaneous-emission-control concepts.

Looking into the properties of  $L_N$  PhC cavities of increasing length we were able to evidence a *transition* from fully confined photonic cavities to 1D PhC waveguides. These studies were carried out using extensive micro-photoluminescence measurements, numerical finite-difference modeling and theoretical basis assuming that cavity modes can be written as a linear combination of the Bloch modes of the corresponding waveguide. We found that, effectively, 1D photonic states in such PhC system start forming when the cavity length is  $N \simeq 30 \div 40$  (missing holes in a row), which, at this point, signifies the *onset of a 1D-band* formation. We further observed and analyzed effects of distributed *disorder* that induces arbitrary partial *mode localization* reducing an effective cavity length. This is extremely important for structure design in applications to on-chip single-photon sources and photon transfer lines. We also concluded that coupling and photon transfer (e.g., of an isolated cavity) to modes of a realistic finite-size

waveguide is not affected by the PhC disorder if, within the waveguide dispersion band, *index-guided modes* are used.

Considering further directly-coupled PhC cavities, we implemented a scheme by which – using two independent QWR local light sources each positioned within a single cavity – it was possible to evidence the *degree of mode localization* in the PL spectra, which gives information about the *formation of the coupled states* in the system. Secondly, we noticed that in the coupled system *splitting of losses* may arise. The experimental observations were confirmed by numerical analysis using 3D FDTD and theoretical background of simple coupled harmonic oscillators. In particular, it was concluded that the splitting of loss is given by the non-vanishing imaginary part of the coupling-strength term, which, in essence, in the 2D PhC system arises due to difference in *diffractive* losses of the symmetric and the anti-symmetric supermodes. The loss splitting may affect the *energy transfer* between the cavities during the system's time evolution. Furthermore, we showed that – owing to the diffractive loss origin – there is large room for coupling design via coupling-barrier engineering and dynamical control using, for example, a scanning-probe tip.

Following mode spectroscopy experiments performed on single-cavity QWR-PhC structures ( $L_3, L_6$ ) which suggested that QWR - cavity-mode coupling can be efficient in terms of light output into the mode, we looked into the dynamics of spontaneous emission in the QWR-PhC system. Transient spectroscopy (at low temperature, 20K) revealed that indeed the QWR spontaneous-emission rate into the cavity mode can be *enhanced* by a factor of  $\sim 2 \div 2.5$ . At the same time, we evidenced that the non-coupled emission is *inhibited* by a factor  $\sim 3$  owing to the PhC bandgap effects. Although it suggested that the measured emission properties are subject to averaging due to exciton localization effects, we see that the spontaneous emission into the cavity mode can be enhanced by a factor  $\sim 6$  with respect to all other available modes. This is significant, as for example, in the *microcavity laser* concept such an enhancement is one of the basic principles for obtaining superior output characteristics due to high spontaneous-emission coupling.

Finally, we explored power-dependent light output from multi- and single-mode PhC-cavity samples employing vertically stacked triple-QWRs. *Lasing action* in such QWR-PhC system was achieved *for the first time*. As characteristic input-output curves were rather smooth – hence not indicative of a threshold –, firm conclusions on observation of stimulated emission and lasing required a complex analysis. We performed measurements of the input-output dependence taking into account background spontaneous emission, linewidth, peak shift, and time-resolved photon dynamics. Results were compared to non-lasing (LED) structures. In particular, it was found that for QWR-PhC lasers the *linewidth* not only narrows significantly with increasing pump power – pointing therefore to *build-up of coherence* due to stimulated emission – but also follows a trend consistent with that of a semiconductor laser with a non-zero linewidth enhancement factor. Secondly, in contrast to LED structures, an appearance of a fast component in the transient photoluminescence signal was registered. With this, a decrease of the pump-signal *delay time* was also noticed. From these data *extremely low threshold* pump powers  $\sim 0.5 \div 2\mu W$  of incident average power (which is only

$\sim 125 \div 500nW$  in absorbed power) were inferred. The measured photon-dynamics trends were further compared to and verified qualitatively by a *rate-equation model*, where we also considered the emission saturation – observed in the experiment at relatively high pump power – by power-dependent increase of the carrier relaxation time. From fitting the experimental data by theoretical input-output curve, we deduced a relatively *large spontaneous-emission coupling* factor  $\beta \simeq 0.3$ .

Due to exciton localization, the *gain* in our QWR-PhC structures might be possibly QD-like. On the other hand, lasing was observed predominantly on the high-energy side of the QWR emission spectrum where excitonic states should be more extended. Taking into account the observed carrier-density-dependent blueshift of the QWR emission – reflecting a carrier population at higher energies – we consider that the gain in our QWR-PhC structures is likely due to Coulomb-correlated electron-hole plasma [89]. At elevated temperatures (70K, compared to 20K) the saturation – seen as a strong delay-time increase – is less pronounced pointing thus to the importance of the exciton localization effects at lower temperatures. A full microscopic model would be needed to explain the carrier relaxation effects quantitatively in such a complex system. On the other hand, we found that QWR-PhC lasers tend to have a faster response at elevated temperatures, which is interesting for applications.

However, at high temperature ( $\sim 70K$ ) the QWR-cavity photon dynamics was observed to be appreciably affected by the non-radiative recombination due to *GaAs-air* interfaces. **In perspective**, high-temperature device operation is not only mandatory for many practical applications but also favorable for achieving higher modulation speeds. Therefore, *surface passivation* methods [282, 290] have large potential of application. Such solutions, however, should result in a prolonged effect, thus stabilization of the passivated PhC areas has to be developed. A second challenge in the practical implementation of light-emitting PhC microdevices is *electrical pumping*. One of the solutions, although quite challenging, for the membrane-based microcavities could be carrier injection through a post [291], which would also produce efficient heat dissipation [292], the latter being necessary for CW laser operation. To this end, wafer-fusion technology along with tunnel-junction injection [293] might be employed.



# Appendix A

## Samples and recipes description

### A.1 Figure / sample correspondence

Figure	Samples
Fig. 2.6	#2295 on 0.27- $\mu\text{m}$ -pitch grating #G027siKA-GRTST04 (depth 180nm) on (100)ex <i>GaAs</i> . Growth: buffer <i>GaAs</i> 25 nm, QWR <i>In</i> <sub>0.15</sub> <i>Ga</i> <sub>0.85</sub> <i>As</i> 5 nm, cap <i>GaAs</i> 300 nm
Fig. 2.19	#2930-J on 1 $\mu\text{m}$ -pitch grating #G1siKA-PhC13 (depth 195 nm) on membrane sample #2753. Growth: buffer <i>GaAs</i> 20 nm, (QWR <i>In</i> <sub>0.15</sub> <i>Ga</i> <sub>0.85</sub> <i>As</i> 2.7 nm) $\times$ 3, spacer ( <i>GaAs</i> 11 nm) $\times$ 2, cap <i>GaAs</i> 14.9 nm
Fig. 3.1 (f)	#2461-XX1, 2930-J
Fig. 3.6	#2300-B. Grating #G1siKA-GST02 (depth 250 nm). Growth: buffer <i>GaAs</i> 5nm, (marker <i>Al</i> <sub>0.5</sub> <i>Ga</i> <sub>0.5</sub> <i>As</i> 3 nm) $\times$ 10, (spacer <i>GaAs</i> 15nm) $\times$ 10, cap <i>GaAs</i> 400nm
Fig. 3.7	#2870. Grating #G1siKA-GST07 (depth 190 nm). Growth: buffer <i>GaAs</i> 16 nm, (QWR <i>In</i> <sub>0.15</sub> <i>Ga</i> <sub>0.85</sub> <i>As</i> 3 nm) $\times$ 3, spacer ( <i>GaAs</i> 12 nm) $\times$ 2, cap <i>GaAs</i> 16 nm
Fig. 3.8 (a)	#2868. Grating #G1siKA-GST06 (depth 190 nm). Growth: buffer <i>GaAs</i> 16 nm, QWR <i>In</i> <sub>0.15</sub> <i>Ga</i> <sub>0.85</sub> <i>As</i> 3 nm, cap <i>GaAs</i> 46 nm
Fig. 3.8 (b)	#2928, grating #G1siKA-PhC12 (depth 195 nm) on membrane sample #2753; growth: buffer <i>GaAs</i> 20 nm, (QWR <i>In</i> <sub>0.15</sub> <i>Ga</i> <sub>0.85</sub> <i>As</i> 2.5 nm) $\times$ 3, spacer ( <i>GaAs</i> 11 nm) $\times$ 2, cap <i>GaAs</i> 15.5 nm. #2930 (see Fig. 2.19)

**Table A.1:** Table indicating sample references.

Fig. 3.13 (b)	Membrane sample #HM1451 (MBE). (111)B $GaAs$ , $1\mu m$ $Al_{0.75}Ga_{0.25}As$ , 450 nm $GaAs$
Fig. 3.13 (c)	#2928-C (see Fig. 3.8 (b))
Fig. 3.15-3.18	#TestICP80nm, #TestICP80nmMembr series
Fig. 4.1 (a),(b)	#2930-D (see Fig. 2.19), #2295 (see Fig. 2.6)
Fig. 4.4	#2690-F. Grating #G1siKA-PhC08 (depth 155 nm) on membrane sample #2630. Growth: buffer $GaAs$ 29 nm, QWR $In_{0.15}Ga_{0.85}As$ 5 nm, cap $GaAs$ 31 nm
Fig. 4.5 (a), Fig. 4.6	#2375-E. Grating #G1siKA-PhC01 (depth 190 nm) on membrane sample #2312. Growth: buffer $GaAs$ 30 nm, QWR $In_{0.15}Ga_{0.85}As$ 5 nm, cap $GaAs$ 35 nm
Fig. 4.7, 4.8, 4.10, 4.12-4.16	#2930-D (see Fig. 2.19)
Fig. 4.11	#2690-F (see Fig. 4.4)
Fig. 5.2, Fig. 5.8	#2930-D (see Fig. 2.19)
Fig. 6.3, Fig. 6.4	#2690-F (see Fig. 4.4)
Fig. 7.3, 7.4, 7.6, 7.7, 7.9, 7.10	#2930-D (see Fig. 2.19)
Fig. 7.13 (a), (b)	#2930-D, #2930-E (see Fig. 2.19)
Fig. 7.17	#2930-D (see Fig. 2.19)

**Table A.2:** Table indicating sample references (continued).

## A.2 Some recipes

Consult also Chapter 3.

**V-groove pattern.** On exactly oriented (100) $GaAs$ . Bake at  $160^{\circ}C$  20'; spin PMMA 950k A4, 6000 rpm, 30"; bake 1h30' (can also be 15'). e-beam writing. Wet etch  $Br : HBr(62\%) : H_2O$  (1:10:107 ml) etch  $1 \div 2''$  (grating depths  $\simeq 150 \div 200nm$ ). Cleaning: acetone rinse, acetone rinse in US bath (power 85%)  $\sim 3'$ , isopropanol rinse,  $H_2O$  rinse,  $N_2$  dry.  $O_2$ -plasma (Plasmaline) clean 0.35Torr/50W/1'. Deoxidation before growth:  $HCl$  rinse until  $GaAs$  surface is hydrophobic<sup>1</sup>.

**PhC pattern.** On MOVPE-grown sample. Standard  $SiO_2$  (80 nm, e.g. for ICP) PECVD (Oxford). Bake 20'; spin PMMA 950k A4, 2000 rpm, 30"; bake 15  $\div$  20'. e-beam writing. Pattern transfer  $O_2 + CHF_3/Ar$  RIE (Oxford). Cleaning: acetone rinse  $\sim 3'$  (no US bath), isopropanol rinse,  $H_2O$  rinse,  $N_2$  dry;  $O_2$ -plasma (Plasmaline) clean 0.35Torr/50W/5'. *Pattern correction* (optional): wet etch  $BHF : H_2O$  (1:3) (isotropic etch rate 2 nm/s). ICP etching (see Sec. 3.1.5.5). *Membrane release*: preheat (at  $\sim 40 \div 50^{\circ}C$ ) teflon beaker  $\sim 5'$ , put then (only a large droplet on bottom)  $HF(40\%) : H_2O$  (1:10), warm it up  $\sim 2'$ , put sample, etch 24  $\div$  27'' (undercut  $\sim 3 \div 4\mu m$ ), add water and continue wash ( $\sim 1 \div 2'$ ).

<sup>1</sup>On epi-ready wafers  $\sim 1h$ , on grown  $GaAs$  (membrane samples)  $\sim 5'$ .

# Bibliography

- [1] M. C. Roco, R. S. Williams, and P. Alivisatos. *Nanotechnology Research Directions*. Kluwer Academic Publishers, Dordrecht, 2000.
- [2] C. Weisbuch and B. Vinter. *Quantum Semiconductor Structures*. Academic Press, New York, 1991.
- [3] N. W. Ashcroft and N. D. Mermin. *Solid State Physics*. Thomson Brooks/Cole, USA, 1976.
- [4] J. M. Luttinger and W. Kohn. Motion of electrons and holes in perturbed periodic fields. *Phys. Rev.*, 97(4):869–883, 1955.
- [5] J. M. Luttinger. Quantum theory of cyclotron resonance in semiconductors: General theory. *Phys. Rev.*, 102(4):1030–1041, 1956.
- [6] P. Y. Yu and M. Cardona. *Fundamentals of Semiconductors*. Springer-Verlag, Berlin, Heidelberg, 1996.
- [7] G. Bastard. *Wave mechanics applied to semiconductor heterostructures*. John Wiley and Sons, Les Ulis, France, 1990.
- [8] E. Rosencher and B. Vinter. Ch. 5. semiconductor band structure. In *Optoelectronics*, page 199. Cambridge University Press, Cambridge, UK, 2002.
- [9] Eli Kapon. Quantum wire lasers. *Proceedings IEEE*, 80(3):398–410, 1992.
- [10] W. Lei and Ch. Jagadish. Lasers and photodetectors for mid-infrared 2–3  $\mu\text{m}$  applications. *J. Appl. Phys.*, 104(9):091101–11, 2008.
- [11] L. Van Hove. The occurrence of singularities in the elastic frequency distribution of a crystal. *Phys. Rev.*, 89(6):1189, 1953.
- [12] M. Asada, Y. Miyamoto, and Y. Suematsu. Gain and the threshold of 3-dimensional quantum-box lasers. *IEEE J. Quantum Electron.*, 22(9):1915–1921, 1986.
- [13] Y. Arakawa and H. Sakaki. Multidimensional quantum well laser and temperature dependence of its threshold current. *Appl. Phys. Lett.*, 40(11):939–941, 1982.

- 
- [14] R. P. Feynman, R. B. Leighton, and M. Sands. *The Feynman Lectures in Physics*, Ch. 23. Addison-Wesley, Mass, 1964.
- [15] O. Svelto. *Principles of Lasers*. Plenum Press, New York, 3rd edition, 1989.
- [16] E. Rosencher and B. Vinter. Ch. 3. quantum mechanics of electron-photon interaction. In *Optoelectronics*, page 91. Cambridge University Press, Cambridge, UK, 2002.
- [17] S. Haroche and D. Kleppner. Cavity quantum electrodynamics. *Physics Today*, 42(1):24–30, 1989.
- [18] P. R. Berman. *Cavity Quantum Electrodynamics*. Academic Press, Boston, 1994.
- [19] E. M. Purcell. Spontaneous emission probabilities at radio frequencies. *Phys. Rev.*, 69:681, 1946.
- [20] J. M. Gérard and B. Gayral. Strong purcell effect for inas quantum boxes in three-dimensional solid-state microcavities. *J. Lightwave Technol.*, 17(11):2089–2095, 1999.
- [21] K. J. Vahala. Optical microcavities. *Nature*, 424(6950):839–846, 2003.
- [22] H. Kogelnik and C. V. Shank. Coupled-wave theory of distributed feedback lasers. *J. Appl. Phys.*, 43(5):2327–2335, 1972.
- [23] A. Hardy and W. Streifer. Coupled mode theory of parallel waveguides. *J. Lightwave Technol.*, LT-3(5):1135–1146, 1985.
- [24] M. Born and E. Wolff. *Principles of Optics*. Pergamon, New York, 1959.
- [25] Zh I. Alferov, V. M. Andreev, R. F. Kazarinov, E. L. Portnoi, and R. A. Suris. Semiconductor optical quantum generator. *Inventor's Certificate No. 392875 [in Russian]*, 1971.
- [26] G. Tayeb, B. Gralak, and S. Enoch. Structural colors in nature and butterfly-wing modeling. *Opt. Photon. News*, 14(2):38–43+49, 2003.
- [27] S. Kinoshita and S. Yoshioka. Structural colors in nature: The role of regularity and irregularity in the structure. *ChemPhysChem*, 6(8):1443–1459, 2005.
- [28] M. Plihal and A. A. Maradudin. Photonic band structure of two-dimensional systems: The triangular lattice. *Phys. Rev. B*, 44(16):8565–8571, 1991.
- [29] V. P. Bykov. Spontaneous emission in a periodic structure. *Sov. Phys. JETP*, 35:269–273, 1972.
- [30] V. P. Bykov. Spontaneous emission from a medium with a band spectrum. *Sov. J. Quantum. Electron.*, 4(7):861–871, 1975.

- [31] E. Yablonovitch. Inhibited spontaneous emission in solid-state physics and electronics. *Phys. Rev. Lett.*, 58(20):2059–2062, 1987.
- [32] S. John. Strong localization of photons in certain disordered dielectric superlattices. *Phys. Rev. Lett.*, 58(23):2486–2489, 1987.
- [33] H. Yokoyama, K. Ujihara, and eds. *Spontaneous Emission and Laser Oscillation in Microcavities*. CRC Press, Boca Raton, 1995.
- [34] G. Khitrova, H. M. Gibbs, M. Kira, S. W. Koch, and A. Scherer. Vacuum rabi splitting in semiconductors. *Nature Physics*, 2(2):81–90, 2006.
- [35] G. Khitrova, H. M. Gibbs, F. Jahnke, M. Kira, and S. W. Koch. Nonlinear optics of normal-mode-coupling semiconductor microcavities. *Rev. Mod. Phys.*, 71(5):1591–1639, 1999.
- [36] J. M. Raimond and S. Haroche. Atoms in cavities. In E. Burstein and C. Weisbuch, editors, *Confined Electrons and Photons: New Physics and Applications*. Plenum Press, New York, 1995.
- [37] F. Jahnke, M. Kira, S. W. Koch, G. Khitrova, E. K. Lindmark, T. R. Nelson Jr, D. V. Wick, J. D. Berger, O. Lyngnes, H. M. Gibbs, and K. Tai. Excitonic nonlinearities of semiconductor microcavities in the nonperturbative regime. *Phys. Rev. Lett.*, 77(26):5257–5260, 1996.
- [38] A. Kavokin, G. Malpuech, and F. P. Laussy. Polariton laser and polariton superfluidity in microcavities. *Phys. Lett. A*, 306(4):187–199, 2003.
- [39] C. Santori, D. Fattal, J. Vučković, G. S. Solomon, and Y. Yamamoto. Indistinguishable photons from a single-photon device. *Nature*, 419(6907):594, 2002.
- [40] E. Knill, R. Laflamme, and G. J. Milburn. A scheme for efficient quantum computation with linear optics. *Nature*, 409(6816):46–52, 2001.
- [41] M. A. Nielsen and I. L. Chuang. *Quantum computation and quantum information*. Cambridge University Press, 2000.
- [42] N. Gisin, G. Ribordy, W. Tittel, and H. Zbinden. Quantum cryptography. *Rev. Mod. Phys.*, 74(1):145–195, 2002.
- [43] H. Mabuchi and A. C. Doherty. Cavity quantum electrodynamics: Coherence in context. *Science*, 298(5597):1372, 2002.
- [44] F. Illuminati. Quantum optics: Light does matter. *Nature Physics*, 2(12):803–804, 2006.
- [45] P. J. Blythe and B. T. H. Varcoe. A cavity-qed scheme for cluster-state quantum computing using crossed atomic beams. *New Journal of Physics*, 8, 2006.

- [46] G. Björk, Y. Yamamoto, and H. Heitman. Spontaneous emission control in semiconductor microcavities. In E. Burstein and C. Weisbuch, editors, *Confined Electrons and Photons*, page 467. Plenum Press, New York, 1995.
- [47] F. De Martini and G. R. Jacobovitz. Anomalous spontaneous stimulated-decay phase transition and zero-threshold laser action in a microscopic cavity. *Phys. Rev. Lett.*, 60(17):1711–1714, 1988.
- [48] H. Yokoyama. Physics and device applications of optical microcavities. *Science*, 256(5053):66–74, 1992.
- [49] S. Noda. Seeking the ultimate nanolaser. *Science*, 314(5797):260–261, 2006.
- [50] H. Altug, D. Englund, and J. Vučković. Ultrafast photonic crystal nanocavity laser. *Nature Physics*, 2(7):484–488, 2006.
- [51] E. Yablonovitch. Photonic band-gap structures. *J. Opt. Soc. Am.*, 10(2):283–295, 1993.
- [52] K. F. Karlsson. *Spectroscopic studies of InGaAs/GaAs/AlGaAs quantum dots and wires*. PhD thesis, Linköping University, 2004.
- [53] J. Frenkel. On the transformation of light into heat in solids. i. *Phys. Rev.*, 37(1):17–44, 1931.
- [54] G. H. Wannier. The structure of electronic excitation levels in insulating crystals. *Phys. Rev.*, 52(3):191–197, 1937.
- [55] F. Bassani. *Electronic States and Optical Transitions in Solids*. Pergamon Press, London, 1975.
- [56] E. Rosencher and B. Vinter. Ch. 8. quantum heterostructures and quantum wells. In *Optoelectronics*, page 380. Cambridge University Press, Cambridge, UK, 2002.
- [57] A. Baldereschi and N. C. Lipari. Energy levels of direct excitons in semiconductors with degenerate bands. *Phys. Rev. B*, 3(2):439, 1971.
- [58] F. Rossi, G. Goldoni, and E. Molinari. Shape-independent scaling of excitonic confinement in realistic quantum wires. *Phys. Rev. Lett.*, 78(18):3527–3530, 1997.
- [59] Y. C. Chang, L. L. Chang, and L. Esaki. A new one-dimensional quantum well structure. *Appl. Phys. Lett.*, 47(12):1324–1326, 1985.
- [60] H. Akiyama. One-dimensional excitons in GaAs quantum wires. *J. Phys. Condensed Matter*, 10(14):3095–3139, 1998.
- [61] F. Rossi and E. Molinari. Coulomb-induced suppression of band-edge singularities in the optical spectra of realistic quantum-wire structures. *Phys. Rev. Lett.*, 76(19):3642–3645, 1996.

- [62] M. A. Dupertuis, D. Y. Oberli, and E. Kapon. Computing excitons in v-shaped quantum wires including band-structure and dielectric effects : Binding energies and polarization anisotropy of the bright a<sub>1</sub>, b<sub>1</sub>, a<sub>2</sub> excitons. In *2002 International Conference on Computational Nanoscience and Nanotechnology - ICCN 2002*, pages 227–230, 2002.
- [63] K. F. Karlsson, M. A. Dupertuis, H. Weman, and E. Kapon. Fractional-dimensional excitonic absorption theory applied to v-groove quantum wires. *Phys. Rev. B*, 70(15), 2004.
- [64] S. Palmgren, H. Weman, A. Schoenberg, K. F. Karlsson, M. A. Dupertuis, K. Leifer, A. Rudra, and E. Kapon. Polarization-resolved optical absorption in single v-groove quantum wires. *Appl. Phys. Lett.*, 89(19):191111–3, 2006.
- [65] T. Ogawa and T. Takagahara. Optical absorption and sommerfeld factors of one-dimensional semiconductors: An exact treatment of excitonic effects. *Phys. Rev. B*, 44(15):8138–8156, 1991.
- [66] S. Schmittrink, D. S. Chemla, and D. A. B. Miller. Linear and nonlinear optical-properties of semiconductor quantum wells. *Advances in Physics*, 38(2):89–188, 1989.
- [67] M. Shinada and S. Sugano. Interband optical transitions in extremely anisotropic semiconductors .i. bound and unbound exciton absorption. *J. Phys. Soc. Jpn.*, 21(10):1936, 1966.
- [68] S. Hughes and D. S. Citrin. High-field franz-keldysh effect and exciton ionization in semiconductor quantum wires. *Phys. Rev. Lett.*, 84(18):4228–4231, 2000.
- [69] J. Singh and K. K. Bajaj. Role of interface roughness and alloy disorder in photoluminescence in quantum-well structures. *J. Appl. Phys.*, 57(12):5433–5437, 1985.
- [70] E. C. Ferreira, J. A. K. Freire, V. N. Freire, J. A. P. Da Costa, E. L. Albuquerque, P. W. Mauriz, and G. A. Farias. Interfacial fluctuations effects on confined excitons in single gaas/alxga1-xas quantum wells. *Surf. Sci.*, 532-535:774–779, 2003.
- [71] H. Castella and J. W. Wilkins. Splitting of the excitonic peak in quantum wells with interfacial roughness. *Phys. Rev. B*, 58(24):16186–16193, 1998.
- [72] F. Intonti, V. Emiliani, C. Lienau, T. Elasaesser, V. Savona, E. Runge, R. Zimmermann, R. Nötzel, and K. H. Ploog. Quantum mechanical repulsion of exciton levels in a disordered quantum well evidenced by near-field spectroscopy. *Physica E*, 13(2-4):178–181, 2002.
- [73] D. Gammon, E. S. Snow, B. V. Shanabrook, D. S. Katzer, and D. Park. Fine structure splitting in the optical spectra of single gaas quantum dots. *Phys. Rev. Lett.*, 76(16):3005, 1996.

- [74] R. Zimmermann, F. Grofle, and E. Runge. Excitons in semiconductor nanostructures with disorder. *Pure Appl. Chem.*, 69(6):1179–1186, 1997.
- [75] N. Moret. *Exciton Localization and Diffusion in Low-Dimensional Nanostructures Formed on Non-Planar Substrates*. PhD thesis, EPFL, Lausanne, Switzerland, 2008.
- [76] D. S. Citrin. Radiative lifetimes of excitons in quantum wells: Localization and phase-coherence effects. *Phys. Rev. B*, 47(7):3832–3841, 1993.
- [77] I. V. Ponomarev, L. I. Deych, and A. A. Lisyansky. Effect of interwall surface roughness correlations on optical spectra of quantum well excitons. *Phys. Rev. B*, 71(15):1–10, 2005.
- [78] V. Savona and W. Langbein. Realistic heterointerface model for excitonic states in growth-interrupted gaas quantum wells. *Phys. Rev. B*, 74(7), 2006.
- [79] V. Savona, S. Haacke, and B. Deveaud. Optical signatures of energy-level statistics in a disordered quantum system. *Phys. Rev. Lett.*, 84(1):183, 2000.
- [80] E. Runge and R. Zimmermann. Level repulsion in excitonic spectra of disordered systems and local relaxation kinetics. *Annalen der Physik (Leipzig)*, 7(5-6):417–426, 1998.
- [81] M. Yoshita, H. Akiyama, T. Someya, and H. Sakaki. Microphotoluminescence characterization of cleaved edge overgrowth t-shaped inxga1-xas quantum wires. *J. Appl. Phys.*, 83(7):3777–3783, 1998.
- [82] T. Guillet, R. Grousseau, V. Voliotis, X. L. Wan, and M. Ogura. Local disorder and optical properties in v-shaped quantum wires: Toward one-dimensional exciton systems. *Phys. Rev. B*, 68(4):453191–453198, 2003.
- [83] F. Vouilloz, S. Wiesendanger, D. Y. Oberli, B. Dwir, F. Reinhardt, and E. Kapon. Direct observation of localized excitons in quantum wires by spatially resolved photoluminescence. *Physica E*, 2(1-4):862–866, 1998.
- [84] F. Intonti, V. Emiliani, C. Lienau, T. Elsaesser, Richard Nötzel, and K. H. Ploog. Near-field optical spectroscopy of localized and delocalized excitons in a single gaas quantum wire. *Phys. Rev. B*, 63(7):075313, 2001.
- [85] A. Feltrin, R. Idrissi Kaitouni, A. Crottini, M. A. Dupertuis, J. L. Staehli, B. Deveaud, V. Savona, X. L. Wang, and M. Ogura. Exciton relaxation and level repulsion in gaas/alxga1-xas quantum wires. *Phys. Rev. B*, 69(20):205321, 2004.
- [86] R. Zimmermann, E. Runge, and V. Savona. Level repulsion of exciton states in disordered semiconductor nanostructures. *Phys. Stat. Sol. B*, 238(3):478–485, 2003.

- [87] J. Hasen, L. N. Pfeiffer, A. Pinczuk, S. He, K. W. West, and B. S. Dennis. Metamorphosis of a quantum wire into quantum dots. *Nature*, 390(6655):54–57, 1997.
- [88] H. Haug and S. Schmitt-Rink. Electron theory of the optical properties of laser-excited semiconductors. *Progr. Quantum Electron.*, 9(1):3–100, 1984.
- [89] H. Akiyama, L. N. Pfeiffer, M. Yoshita, A. Pinczuk, P. B. Littlewood, K. W. West, M. J. Matthews, and J. Wynn. Coulomb-correlated electron-hole plasma and gain in a quantum-wire laser of high uniformity. *Phys. Rev. B*, 67(4):041302, 2003.
- [90] H. Akiyama, L. N. Pfeiffer, A. Pinczuk, K. W. West, and M. Yoshita. Observation of large many-body coulomb interaction effects in a doped quantum wire. *Sol. State Comm.*, 122(3-4):169–173, 2002.
- [91] S. Schmitt-Rink, D. S. Chemla, and D. A. B. Miller. Theory of transient excitonic optical nonlinearities in semiconductor quantum-well structures. *Phys. Rev. B*, 32(10):6601–6609, 1985.
- [92] J. Fernández-Rossier, C. Tejedor, L. Muñoz, and L. Viña. Polarized interacting exciton gas in quantum wells and bulk semiconductors. *Phys. Rev. B*, 54(16):11582, 1996.
- [93] F. Vouilloz, D. Y. Oberli, S. Wiesendanger, B. Dwir, F. Reinhardt, and E. Kapon. Density dependence of localized excitonic recombination in quantum wires. *Phys. Stat. Sol. A*, 164(1):259–263, 1997.
- [94] S. V. Nair and T. Takagahara. Weakly correlated exciton pair states in large quantum dots. *Phys. Rev. B*, 53(16):R10516, 1996.
- [95] U. Bockelmann and G. Bastard. Interband optical transitions in semiconductor quantum wires: Selection rules and absorption spectra. *Europhys. Lett.*, 15(2):215–220, 1991.
- [96] F. Vouilloz, D. Y. Oberli, M. A. Dupertuis, A. Gustafsson, F. Reinhardt, and E. Kapon. Polarization anisotropy and valence band mixing in semiconductor quantum wires. *Phys. Rev. Lett.*, 78(8):1580–1583, 1997.
- [97] M. G. A. Bernard and G. Duraffourg. Laser conditions in semiconductors. *Phys. Stat. Sol.*, 1:699, 1961.
- [98] F. Tassone and C. Piermarocchi. Electron-hole correlation effects in the emission of light from quantum wires. *Phys. Rev. Lett.*, 82(4):843–846, 1999.
- [99] E. Burstein and C. Weisbuch, editors. *Confined Electrons and Photons: New Physics and Applications*, volume 340 of *NATO ASI Series B: Physics*. Plenum Press, New York, 1995.

- [100] K. Ujihara. Effects of atomic broadening on spontaneous emission in an optical microcavity. In H. Yokoyama and K. Ujihara, editors, *Spontaneous Emission and Laser Oscillation in Microcavities*. CRC Press, Boca Raton, 1995.
- [101] T. Kobayashi, T. Segawa, A. Morimoto, and T. Sueta. Novel-type lasers, emitting devices, and functional optical devices by controlling spontaneous emission. In *46th Fall Meeting of the Japanese Applied Physics Society*, pages paper 29a-B-6, Tokyo, Japan, 1982. (in Japanese).
- [102] G. Bjork and Y. Yamamoto. Analysis of semiconductor microcavity lasers using rate equations. *IEEE J. Quantum Electron.*, 27(11):2386–2396, 1991.
- [103] H. Yokoyama and S. D. Brorson. Rate equation analysis of microcavity lasers. *J. Appl. Phys.*, 66(10):4801–4805, 1989.
- [104] M. Grundmann and D. Bimberg. Theory of random population for quantum dots. *Phys. Rev. B*, 55(15):9740–9745, 1997.
- [105] L. Sirigu, D. Y. Oberli, L. Degiorgi, A. Rudra, and E. Kapon. Excitonic lasing in semiconductor quantum wires. *Phys. Rev. B*, 61(16), 2000.
- [106] S. Noda, M. Fujita, and T. Asano. Spontaneous-emission control by photonic crystals and nanocavities. *Nature Photonics*, 1(8):449–458, 2007.
- [107] S. Noda, K. Tomoda, N. Yamamoto, and A. Chutinan. Full three-dimensional photonic bandgap crystals at near-infrared wavelengths. *Science*, 289(5479):604–606, 2000.
- [108] J. D. Joannopoulos. Self-assembly lights up. *Nature*, 414(6861):257–258, 2001.
- [109] T. F. Krauss and R. M. De La Rue. Photonic crystals in the optical regime - past, present and future. *Progress Quantum Electron.*, 23(2):51–96, 1999.
- [110] T. Yoshie, A. Scherer, J. Hendrickson, G. Khitrova, H. M. Gibbs, G. Rupper, C. Ell, O. B. Shchekin, and D. G. Deppe. Vacuum rabi splitting with a single quantum dot in a photonic crystal nanocavity. *Nature*, 432(7014):200–203, 2004.
- [111] A. Badolato, K. Hennessy, M. Atatüre, J. Dreiser, E. Hu, P. M. Petroff, and A. Imamoglu. Deterministic coupling of single quantum dots to single nanocavity modes. *Science*, 308(5725):1158–1161, 2005.
- [112] K. Hennessy, A. Badolato, M. Winger, D. Gerace, M. Atatüre, S. Gulde, S. Fält, E. L. Hu, and A. Imamoglu. Quantum nature of a strongly coupled single quantum dot-cavity system. *Nature*, 445(7130):896–899, 2007.
- [113] D. Englund, A. Faraon, I. Fushman, N. Stoltz, P. Petroff, and J. Vučković. Controlling cavity reflectivity with a single quantum dot. *Nature*, 450(7171):857–861, 2007.

- [114] S. Strauf, K. Hennessy, M. T. Rakher, Y. S. Choi, A. Badolato, L. C. Andreani, E. L. Hu, P. M. Petroff, and D. Bouwmeester. Self-tuned quantum dot gain in photonic crystal lasers. *Phys. Rev. Lett.*, 96(12):1–4, 2006.
- [115] M. Nomura, S. Iwamoto, K. Watanabe, N. Kumagai, Y. Nakata, S. Ishida, and Y. Arakawa. Room temperature continuous-wave lasing in photonic crystal nanocavity. *Opt. Express*, 14(13):497–504, 2006.
- [116] D. Englund, H. Altug, B. Ellis, and J. Vučković. Ultrafast photonic crystal lasers. *Laser Photon. Rev.*, 2(4):264–274, 2008.
- [117] K. Sakoda. *Optical properties of photonic crystals*. Springer, Berlin, 2001.
- [118] J.-M. Lourtioz. *Photonic crystals: towards nanoscale photonic devices*. Springer, Berlin, 2nd edition, 2008.
- [119] H. Kogelnik. Theory of optical waveguides. In T. Tamir, editor, *Guided-Wave Optoelectronics*. Springer-Verlag, Berlin, Heidelberg, 2nd edition, 1990.
- [120] D. T. F. Marple. Refractive index of gaas. *J. Appl. Phys.*, 35(4):1241–1242, 1964.
- [121] M. Qiu. Band gap effects in asymmetric photonic crystal slabs. *Phys. Rev. B*, 66(3):331031–331034, 2002.
- [122] E. V. Arzhanov, A. P. Bogatov, V. P. Konyaev, O. M. Nikitina, and V. I. Shveikin. Waveguiding properties of heterolasers based on ingaas/gaas strained quantum-well structures and characteristics of their gain spectra. *Quantum Electron.*, 24(7):581–587, 1994.
- [123] D. Bhattacharyya, E. A. Avrutin, A. C. Bryce, J. H. Marsh, D. Bimberg, F. Heinrichsdorff, V. M. Ustinov, S. V. Zaitsev, N. N. Ledentsov, P. S. Kop’ev, Zh. I. Alferov, A. I. Onischenko, and E. P. O’Reilly. Spectral and dynamic properties of inas-gaas self-organized quantum-dot lasers. *IEEE J. Sel. Top. Quantum Electron.*, 5(3):648–657, 1999.
- [124] W. W. Bewley, C. L. Canedy, C. S. Kim, I. Vurgaftman, M. Kim, and J. R. Meyer. Antimonide type-ii ”w” lasers: Growth studies and guided-mode leakage into substrate. *Physica E*, 20(3-4):466–470, 2004.
- [125] A. Taflove and S. C. Hagness. *Computational Electrodynamics: The Finite-Difference Time-Domain Method*. Artech House Publishers, 3 edition, 2005.
- [126] W. H. Guo, W. J. Li, and Y. Z. Huang. Computation of resonant frequencies and quality factors of cavities by fdtd technique and padé approximation. *IEEE Microwave and Wireless Components Letters*, 11(5):223–225, 2001.
- [127] M. Qiu. Micro-cavities in silicon-on-insulator photonic crystal slabs: Determining resonant frequencies and quality factors accurately. *Microwave and Optical Technology Letters*, 45(5):381–385, 2005.

- [128] J. S. Blakemore. Semiconducting and other major properties of gallium arsenide. *J. Appl. Phys.*, 53(10):R123–R181, 1982.
- [129] K. Srinivasan and O. Painter. Momentum space design of high-q photonic crystal optical cavities. *Opt. Express*, 10(15):670–684, 2002.
- [130] Y. Akahane, T. Asano, B. S. Song, and S. Noda. High-q photonic nanocavity in a two-dimensional photonic crystal. *Nature*, 425(6961):944–947, 2003.
- [131] B. S. Song, S. Noda, T. Asano, and Y. Akahane. Ultra-high-q photonic double-heterostructure nanocavity. *Nature Materials*, 4(3):207–210, 2005.
- [132] D. Englund, I. Fushman, and J. Vučković. General recipe for designing photonic crystal cavities. *Opt. Express*, 13(16):5961–5975, 2005.
- [133] P. Gallo, M. Felici, B. Dwir, K. A. Atlasov, K. F. Karlsson, A. Rudra, A. Mohan, G. Biasiol, L. Sorba, and E. Kapon. Integration of site-controlled pyramidal quantum dots and photonic crystal membrane cavities. *Appl. Phys. Lett.*, 92(26):263101, 2008.
- [134] G. Biasiol, F. Reinhardt, A. Gustafsson, and E. Kapon. Self-limiting omcvd growth of gaas on v-grooved substrates with application to ingaas/gaas quantum wires. *J. Electro. Mater.*, 26(10):1194–1198, 1997.
- [135] K. Hennessy, A. Badolato, A. Tamboli, P. M. Petroff, E. Hu, M. Atatüre, J. Dreiser, and A. Imamoğlu. Tuning photonic crystal nanocavity modes by wet chemical digital etching. *Appl. Phys. Lett.*, 87(2):1–3, 2005.
- [136] L. F. Thompson, C. G. Willson, and M. J. Bowden. *Introduction to microlithography*. ACS professional reference book. American Chemical Society, Washington, DC, 2nd edition, 1994.
- [137] S. Yasin, D. G. Hasko, and H. Ahmed. Fabrication of 5 nm width lines in poly(methylmethacrylate) resist using a water:isopropyl alcohol developer and ultrasonically-assisted development. *Appl. Phys. Lett.*, 78(18):2760–2762, 2001.
- [138] R. Bhat, E. Kapon, D. M. Hwang, M. A. Koza, and C. P. Yun. Patterned quantum well heterostructures grown by omcvd on non-planar substrates: Applications to extremely narrow sqw lasers. *J. Cryst. Growth*, 93(1-4):850–856, 1988.
- [139] G. B. Stringfellow. *Organometallic vapor phase epitaxy: theory and practice*. Academic Press, San Diego, 2nd edition, 1999.
- [140] P. D. Dapkus, H. M. Manasevit, K. L. Hess, T. S. Low, and G. E. Stillman. High purity gaas prepared from trimethylgallium and arsine. *J. Cryst. Growth*, 55(1):10–23, 1981.
- [141] K. Fujii, K. Kawamura, and H. Gotoh. Impurity incorporation of unintentionally doped alxga1-xas during movpe. *J. Cryst. Growth*, 221(1-4):41–46, 2000.

- [142] S. H. Jones, L. S. Salinas, J. R. Jones, and K. Mayer. Crystallographic orientation dependence of the growth rate for gas low pressure organometallic vapor phase epitaxy. *J. Electron. Mater.*, 24(1):5–14, 1995.
- [143] G. Biasiol and E. Kapon. Mechanism of self-limiting epitaxial growth on nonplanar substrates. *J. Cryst. Growth*, 201:62–66, 1999.
- [144] G. Biasiol and E. Kapon. Mechanisms of self-ordering of quantum nanostructures grown on nonplanar surfaces. *Phys. Rev. Lett.*, 81(14):2962–2965, 1998.
- [145] C. Constantin, E. Martinet, D. Y. Oberli, E. Kapon, B. Gayral, and J. M. Gérard. Quantum wires in multidimensional microcavities: Effects of photon dimensionality on emission properties. *Phys. Rev. B*, 66(16):1653061–16530613, 2002.
- [146] F. Reinhardt, B. Dwir, and E. Kapon. Oxidation of gas/algas heterostructures studied by atomic force microscopy in air. *Appl. Phys. Lett.*, 68(22):3168–3170, 1996.
- [147] F. Lelarge, C. Constantin, K. Leifer, A. Condo, V. Iakovlev, E. Martinet, A. Rudra, and E. Kapon. Effect of indium segregation on optical properties of v-groove ingas/gas strained quantum wires. *Appl. Phys. Lett.*, 75(21):3300–3302, 1999.
- [148] C. Constantin, E. Martinet, F. Lelarge, K. Leifer, A. Rudra, and E. Kapon. Influence of strain and quantum confinement on the optical properties of ingas/gas v-groove quantum wires. *J. Appl. Phys.*, 88(1):141–147, 2000.
- [149] K. A. Atlasov, K. F. Karlsson, E. Deichsel, A. Rudra, B. Dwir, and E. Kapon. Site-controlled single quantum wire integrated into a photonic-crystal membrane microcavity. *Appl. Phys. Lett.*, 90(15):153107, 2007.
- [150] L. Ren and B. Chen. Proximity effect in electron beam lithography. In *International Conference on Solid-State and Integrated Circuits Technology Proceedings, ICSICT*, volume 1, pages 579–582, 2004.
- [151] K. Hennessy, C. Reese, A. Badolato, C. F. Wang, A. Imamoglu, P. M. Petroff, and E. Hu. Fabrication of high q square-lattice photonic crystal microcavities. *J. Vac. Sci. Technol.*, 21(6):2918–2921, 2003.
- [152] M. A. Lieberman and A. J. Lichtenberg. *Principles of Plasma Discharges and Materials Processing*. Wiley, Hoboken, 2 edition, 2005.
- [153] J. Moosburger, M. Kamp, A. Forchel, R. Ferrini, D. Leuenberger, R. Houdre, S. Anand, and J. Berggren. Nanofabrication of high quality photonic crystals for integrated optics circuits. *Nanotechnology*, 13(3):341, 2002.
- [154] A. R. Clawson. Guide to references on iii-v semiconductor chemical etching. *Mater. Sci. Eng. R: Reports*, 31(1-6):1–438, 2001.

- [155] K. Asakawa, T. Yoshikawa, S. Kohmoto, Y. Nambu, and Y. Sugimoto. Chlorine-based dry etching of iii/v compound semiconductors for optoelectronic application. *Jpn. J. Appl. Phys.*, 37(2):373–387, 1998.
- [156] D. C. Hays, K. P. Lee, B. P. Gila, F. Ren, C. R. Abernathy, and S. J. Pearton. Dry etch selectivity of gd<sub>2</sub>o<sub>3</sub> to gan and aln. *J. Electron. Mater.*, 29(3):285, 2000.
- [157] Oxford instruments gmbh, [www.oxford-instruments.co.uk](http://www.oxford-instruments.co.uk).
- [158] T. Maeda, J. W. Lee, R. J. Shul, J. Han, J. Hong, E. S. Lambers, S. J. Pearton, C. R. Abernathy, and W. S. Hobson. Inductively coupled plasma etching of iii-v semiconductors in bcl<sub>3</sub>-based chemistries. i. gaas, gan, gap, gasb and algaas. *Appl. Surf. Sci.*, 143(1):174, 1999.
- [159] P. Strasser, R. Wüest, F. Robin, D. Erni, and H. Jäckel. Detailed analysis of the influence of an inductively coupled plasma reactive-ion etching process on the hole depth and shape of photonic crystals in inp/ingaasp. *J. Vac. Sci. Technol.*, 25(2):387, 2007.
- [160] R. J. Shul, G. B. McClellan, R. D. Briggs, D. J. Rieger, S. J. Pearton, C. R. Abernathy, J. W. Lee, C. Constantine, and C. Barratt. High-density plasma etching of compound semiconductors. *J. Vac. Sci. Technol.*, 15(3):633, 1997.
- [161] J. W. Lee, M. W. Devre, B. H. Reelfs, D. Johnson, J. N. Sasserath, F. Clayton, D. Hays, and S. J. Pearton. Advanced selective dry etching of gaas/algaas in high density inductively coupled plasmas. *J. Vac. Sci. Technol.*, 18(4 I):1220, 2000.
- [162] S. Gourrier, L. Smit, P. Friedel, and P. K. Larsen. Photoemission studies of molecular beam epitaxially grown gaas (001) surfaces exposed to a nitrogen plasma. *J. Appl. Phys.*, 54(7):3993, 1983.
- [163] G. Binnig, C. F. Quate, and Ch Gerber. Atomic force microscope. *Phys. Rev. Lett.*, 56(9):930, 1986.
- [164] Y. Martin, C. C. Williams, and H. K. Wickramasinghe. Atomic force microscope-force mapping and profiling on a sub 100-Å scale. *J. Appl. Phys.*, 61(10):4723–4729, 1987.
- [165] H. H. Rose. Optics of high-performance electron microscopes. *Sci. Technol. Adv. Mater.*, 9(1):014107, 2008.
- [166] Energy table for eds analysis, jeol usa, [www.jeolusa.com](http://www.jeolusa.com).
- [167] D. B. Williams and C. B. Carter. *Transmission electron microscopy: a text book for material science*. Plenum Press, New York, 1996.
- [168] K. W. Böer. *Survey of Semiconductor Physics*. Van Norstrand Reinhold, New York, 1990.

- [169] H. W. Yoon, D. R. Wake, and J. P. Wolfe. Effect of exciton-carrier thermodynamics on the gas quantum well photoluminescence. *Phys. Rev. B*, 54(4):2763–2774, 1996.
- [170] A. Gustafsson, M.-E. Pistol, L. Montelius, and L. Samuelson. Local probe techniques for luminescence studies of low-dimensional semiconductor structures. *J. Appl. Phys.*, 84(4):1715–1775, 1998.
- [171] R. E. Slusher, A. F. J. Levi, U. Mohideen, S. L. McCall, S. J. Pearton, and R. A. Logan. Threshold characteristics of semiconductor microdisk lasers. *Appl. Phys. Lett.*, 63(10):1310–1312, 1993.
- [172] R. S. Meltzer and R. M. Wood. Nanosecond time-resolved spectroscopy with a pulsed tunable dye laser and single photon time correlation. *Appl. Opt.*, 16(5):1432–1434, 1977.
- [173] A. J. Shields. Semiconductor quantum light sources. *Nature Photonics*, 1(4):215, 2007.
- [174] H. Akiyama, T. Someya, and H. Sakaki. Optical anisotropy in 5-nm-scale t-shaped quantum wires fabricated by the cleaved-edge overgrowth method. *Phys. Rev. B*, 53(8):R4229–R4232, 1996.
- [175] J. Johansson, L. S. Karlsson, C. P. T. Svensson, T. Mårtensson, B. A. Wacaser, K. Deppert, L. Samuelson, and W. Seifert. Structural properties of (111)b - oriented iii-v nanowires. *Nature Materials*, 5(7):574–580, 2006.
- [176] M. A. Kaliteevski, S. Brand, R. A. Abram, V. V. Nikolaev, M. V. Maximov, N. N. Ledentsov, C. M. Sotomayor Torres, and A. V. Kavokin. Exciton polaritons in a cylindrical microcavity with an embedded quantum wire. *Phys. Rev. B*, 61(20):13791–13797, 2000.
- [177] H. Yagi, T. Sano, K. Ohira, D. Plumwongrot, T. Maruyama, A. Haque, S. Tamura, and S. Arai. Gainasp/inp partially strain-compensated multiple-quantum-wire lasers fabricated by dry etching and regrowth processes. *Jap. J. Appl. Phys.*, 43(6 A):3401–3409, 2004.
- [178] A. Chavez-Pirson, H. Ando, H. Saito, and H. Kanbe. Quantum wire microcavity laser made from gas fractional layer superlattices. *Applied Physics Letters*, 64(14):1759–1761, 1994.
- [179] K. Ohira, N. Nunoya, and S. Arai. Stable single-mode operation of distributed feedback lasers with wirelike active regions. *IEEE J. Sel. Top. Quantum Electron.*, 9(5):1166–1171, 2003.
- [180] Y. Yamamoto, S. MacHida, and G. Björk. Microcavity semiconductor laser with enhanced spontaneous emission. *Phys. Rev. A*, 44(1):657–668, 1991.

- [181] T. Arakawa, M. Nishioka, Y. Nagamune, and Y. Arakawa. Fabrication of vertical-microcavity quantum wire lasers. *Appl. Phys. Lett.*, 64(17):2200–2202, 1994.
- [182] S. H. Kim, G. H. Kim, S. K. Kim, H. G. Park, Y. H. Lee, and S. B. Kim. Characteristics of a stick waveguide resonator in a two-dimensional photonic crystal slab. *J. Appl. Phys.*, 95(2):411–416, 2004.
- [183] T. Baba, N. Fukaya, and A. Motegi. Clear correspondence between theoretical and experimental light propagation characteristics in photonic crystal waveguides. *Electron. Lett.*, 37(12):761–762, 2001.
- [184] F. Vouilloz, D. Y. Oberli, M. A. Dupertuis, A. Gustafsson, F. Reinhardt, and E. Kapon. Effect of lateral confinement on valence-band mixing and polarization anisotropy in quantum wires. *Phys. Rev. B*, 57(19):12378–12387, 1998.
- [185] K. F. Karlsson, K. A. Atlasov, and E. Kapon. Design of high-q membrane photonic crystal defect cavity for integration with semiconductor quantum wires. In *9th International Conference on Near-field Optics (NFO-9)*, page 282, Lausanne, Switzerland, September 10-15 2006. EPFL.
- [186] K. A. Atlasov, K. F. Karlsson, E. Deichsel, B. Dwir, A. Rudra, and E. Kapon. Membrane photonic crystal defect cavities for quantum wire lasers and 1d polariton. In *14th Int. Symp. Nanostructures: Physics and Technology*, pages 289–290, St Petersburg, Russia, 2006. Ioffe Institute.
- [187] S. Mosor, J. Hendrickson, B. C. Richards, J. Sweet, G. Khitrova, H. M. Gibbs, T. Yoshie, A. Scherer, O. B. Shchekin, and D. G. Deppe. Scanning a photonic crystal slab nanocavity by condensation of xenon. *Appl. Phys. Lett.*, 87(14):1–3, 2005.
- [188] S. Mujumdar, A. F. Koenderink, T. Süner, B. C. Buchler, M. Kamp, A. Forchel, and V. Sandoghdar. Near-field imaging and frequency tuning of a high-q photonic crystal membrane microcavity. *Opt. Express*, 15(25):17214–17220, 2007.
- [189] I. Märki, M. Salt, and H. P. Herzig. Tuning the resonance of a photonic crystal microcavity with an afm probe. *Opt. Express*, 14(7):2969–2978, 2006.
- [190] H. J. Kimble. Strong interactions of single atoms and photons in cavity qed. *Physica Scripta T*, 76:127–137, 1998.
- [191] J. McKeever, A. Boca, A. D. Boozer, J. R. Buck, and H. J. Kimble. Experimental realization of a one-atom laser in the regime of strong coupling. *Nature*, 425(6955):268–271, 2003.
- [192] J. McKeever, A. Boca, A. D. Boozer, R. Miller, J. R. Buck, A. Kuzmich, and H. J. Kimble. Deterministic generation of single photons from one atom trapped in a cavity. *Science*, 303(5666):1992–1994, 2004.

- [193] D. Englund, A. Faraon, B. Zhang, Y. Yamamoto, and J. Vučković. Generation and transfer of single photons on a photonic crystal chip. *Opt. Express*, 15:5550–5558, 2007.
- [194] D. Y. Oberli, M. A. Dupertuis, F. Reinhardt, and E. Kapon. Effect of disorder on the temperature dependence of radiative lifetimes in v-groove quantum wires. *Phys. Rev. B*, 59(4):2910–2914, 1999.
- [195] C. Constantin, D. Y. Oberli, E. Martinet, A. Rudra, and E. Kapon. Use of an optical microcavity to probe exciton relaxation in strained v-groove quantum wires. *Phys. Stat. Sol. (A)*, 178(1):161–165, 2000.
- [196] J. F. Ryan, A. C. Maciel, C. Kiener, L. Rota, K. Turner, J. M. Freyland, U. Marti, D. Martin, F. Morier-Gemoud, and F. K. Reinhart. Dynamics of electron capture into quantum wires. *Phys. Rev. B*, 53(8):R4225–R4228, 1996.
- [197] R. Ambigapathy, I. Bar-Joseph, D. Y. Oberli, S. Haacke, M. J. Brasil, F. Reinhardt, E. Kapon, and B. Deveaud. Coulomb correlation and band gap renormalization at high carrier densities in quantum wires. *Phys. Rev. Lett.*, 78(18):3579–3582, 1997.
- [198] R. Zimmermann and E. Runge. Exciton lineshape in semiconductor quantum structures with interface roughness. *J. Lumin.*, 60-61(C):320–323, 1994.
- [199] T. Guillet, R. Grousson, V. Voliotis, M. Menant, X. L. Wang, and M. Ogura. Mott transition from a diluted exciton gas to a dense electron-hole plasma in a single v-shaped quantum wire. *Phys. Rev. B*, 67(23):2353241–2353246, 2003.
- [200] A. K. Saxena. The conduction band structure and deep levels in Ga<sub>1-x</sub>Al<sub>x</sub> alloys from a high-pressure experiment. *J. Phys. C*, 13(23):4323–4334, 1980.
- [201] L. Rota, F. Rossi, P. Lugli, and E. Molinari. Ultrafast relaxation of photoexcited carriers in semiconductor quantum wires: A monte carlo approach. *Phys. Rev. B*, 52(7):5183–5201, 1995.
- [202] L. C. Andreani, G. Panzarini, and J. M. Gérard. Strong-coupling regime for quantum boxes in pillar microcavities: Theory. *Phys. Rev. B*, 60(19):13276–13279, 1999.
- [203] L. C. Andreani. Optical transitions, excitons, and polaritons in bulk and low-dimensional semiconductor structures. In E. Burstein and C. Weisbuch, editors, *Confined Electrons and Photons*, page 57. Plenum Press, New York, 1995.
- [204] J. Feldmann, G. Peter, E. O. Göbel, P. Dawson, K. Moore, C. Foxon, and R. J. Elliott. Linewidth dependence of radiative exciton lifetimes in quantum wells. *Phys. Rev. Lett.*, 59(20):2337–2340, 1987.

- [205] J. Bellessa, V. Voliotis, R. Grousson, X. L. Wang, M. Ogura, and H. Matsuhata. Quantum-size effects on radiative lifetimes and relaxation of excitons in semiconductor nanostructures. *Phys. Rev. B*, 58(15):9933, 1998.
- [206] D. S. Citrin. Long intrinsic radiative lifetimes of excitons in quantum wires. *Phys. Rev. Lett.*, 69(23):3393–3396, 1992.
- [207] N. Moret, D. Y. Oberli, B. Dwir, A. Rudra, and E. Kapon. Diffusion of electron-hole pairs in disordered quantum wires. *Appl. Phys. Lett.*, 93(19):192101, 2008.
- [208] A. V. Gopal, R. Kumar, A. S. Vengurlekar, T. Melin, F. Laruelle, and B. Etienne. Exciton-phonon scattering in gaas/aias quantum wires. *Appl. Phys. Lett.*, 74(17):2474–2476, 1999.
- [209] H. Akiyama, S. Koshiha, T. Someya, K. Wada, H. Noge, Y. Nakamura, T. Inoshita, A. Shimizu, and H. Sakaki. Thermalization effect on radiative decay of excitons in quantum wires. *Phys. Rev. Lett.*, 72(6):924–927, 1994.
- [210] K. J. Luo, J. Y. Xu, H. Cao, Y. Ma, S. H. Chang, S. T. Ho, and G. S. Solomon. Dynamics of gaas/algaas microdisk lasers. *Appl. Phys. Lett.*, 77(15):2304–2306, 2000.
- [211] T. Baba, D. Sano, K. Nozaki, K. Inoshita, Y. Kuroki, and F. Koyama. Observation of fast spontaneous emission decay in gainasp photonic crystal point defect nanocavity at room temperature. *Appl. Phys. Lett.*, 85(18):3989–3991, 2004.
- [212] T. Tawara, H. Kamada, Y. H. Zhang, T. Tanabe, N. I. Cade, D. Ding, S. R. Johnson, H. Gotoh, E. Kuramochi, M. Notomi, and T. Sogawa. Quality factor control and lasing characteristics of inas/ingaas quantum dots embedded in photonic-crystal nanocavities. *Opt. Express*, 16(8):5199–5205, 2008.
- [213] S. Park, V. Zapasskii, D. V. Wick, T. R. Nelson Jr, C. Ell, H. M. Gibbs, G. Khitrova, A. Schulzgen, M. Kira, F. Jahnke, and S. W. Koch. Spontaneous emission lifetime of carriers in a semiconductor microcavity measured by photoluminescence without distortion by reabsorption. *Opt. Express*, 4(13):512–524, 1999.
- [214] G. Bjork, A. Karlsson, and Y. Yamamoto. On the linewidth of microcavity lasers. *Appl. Phys. Lett.*, 60(3):304–306, 1992.
- [215] S. W. Koch, F. Jahnke, and W. W. Chow. Physics of semiconductor microcavity lasers. *Semicond. Sci. Technol.*, 10(6):739–751, 1995.
- [216] W. H. Chang, W. Y. Chen, H. S. Chang, T. P. Hsieh, J. I. Chyi, and T. M. Hsu. Efficient single-photon sources based on low-density quantum dots in photonic-crystal nanocavities. *Phys. Rev. Lett.*, 96(11):117401, 2006.

- [217] V. S. C. Manga Rao and S. Hughes. Single quantum dot spontaneous emission in a finite-size photonic crystal waveguide: Proposal for an efficient "on chip" single photon gun. *Phys. Rev. Lett.*, 99(19):193901–4, 2007.
- [218] M. Notomi, K. Yamada, A. Shinya, J. Takahashi, C. Takahashi, and I. Yokohama. Extremely large group-velocity dispersion of line-defect waveguides in photonic crystal slabs. *Phys. Rev. Lett.*, 87(25):253902, 2001.
- [219] J. D. Joannopoulos, R. D. Meade, and J. N. Winn. *Photonic Crystals: Molding the Flow of Light*. Princeton University Press, Princeton, NJ, 1995.
- [220] Q. Zhu, K. F. Karlsson, E. Pelucchi, and E. Kapon. Transition from two-dimensional to three-dimensional quantum confinement in semiconductor quantum wires/quantum dots. *Nano Lett.*, 7(8):2227, 2007.
- [221] D. Labilloy, H. Benisty, C. Weisbuch, T. F. Krauss, R. M. De La Rue, V. Bardinal, R. Houdre, U. Oesterle, D. Cassagne, and C. Jouanin. Quantitative measurement of transmission, reflection, and diffraction of two-dimensional photonic band gap structures at near-infrared wavelengths. *Phys. Rev. Lett.*, 79(21):4147, 1997.
- [222] M. Felici, K. Atlasov, and E. Kapon. to be published, 2009.
- [223] E. Rosencher and B. Vinter. Ch. 13i. mode competition: cross gain modulators. In *Optoelectronics*, page 708. Cambridge University Press, Cambridge, UK, 2002.
- [224] T. Süner, C. Schneider, M. Strauß, A. Huggenberger, D. Wiener, S. Höfling, M. Kamp, and A. Forchel. Scalable fabrication of optical resonators with embedded site-controlled quantum dots. *Optics Lett.*, 33(15):1759–1761, 2008.
- [225] D. O'Brien, M. D. Settle, T. Karle, A. Michaeli, M. Salib, and T. F. Krauss. Coupled photonic crystal heterostructure nanocavities. *Opt. Express*, 15(3):1228–1233, 2007.
- [226] E. Ozbay, M. Bayindir, I. Bulu, and E. Cubukcu. Investigation of localized coupled-cavity modes in two-dimensional photonic bandgap structures. *IEEE J. Quantum Electron.*, 38(7):837–843, 2002.
- [227] S. Mookherjea and A. Yariv. Coupled resonator optical waveguides. *IEEE J. Sel. Top. Quantum Electron.*, 8(3):448–456, 2002.
- [228] S. V. Zhukovsky, D. N. Chigrin, A. V. Lavrinenko, and J. Kroha. Switchable lasing in multimode microcavities. *Phys. Rev. Lett.*, 99(7):073902, 2007.
- [229] S. Ishii, A. Nakagawa, and T. Baba. Modal characteristics and bistability in twin microdisk photonic molecule lasers. *IEEE J. Sel. Top. Quantum Electron.*, 12(1):71–77, 2006.

- [230] M. T. Hill, H. J. S. Dorren, T. De Vries, X. J. M. Leijtens, J. H. Den Besten, B. Smalbrugge, Y. S. Oel, H. Binsma, G. D. Khoe, and M. K. Smit. A fast low-power optical memory based on coupled micro-ring lasers. *Nature*, 432(7014):206–209, 2004.
- [231] A. Imamoglu, D. D. Awschalom, G. Burkard, D. P. DiVincenzo, D. Loss, M. Sherwin, and A. Small. Quantum information processing using quantum dot spins and cavity qed. *Phys. Rev. Lett.*, 83(20):4204–4207, 1999.
- [232] M. J. Hartmann, F. G. S. L. Brando, and M. B. Plenio. Strongly interacting polaritons in coupled arrays of cavities. *Nature Physics*, 2(12):849–855, 2006.
- [233] A. D. Greentree, C. Tahan, J. H. Cole, and L. C. L. Hollenberg. Quantum phase transitions of light. *Nature Physics*, 2(12):856–861, 2006.
- [234] S. V. Boriskina. Coupling of whispering-gallery modes in size-mismatched microdisk photonic molecules. *Opt. Lett.*, 32(11):1557–1559, 2007.
- [235] M. Bayer, T. Gutbrod, J. P. Reithmaier, A. Forchel, T. L. Reinecke, P. A. Knipp, A. A. Dremin, and V. D. Kulakovskii. Optical modes in photonic molecules. *Phys. Rev. Lett.*, 81(12):2582–2585, 1998.
- [236] M. Ghulinyan, C. J. Oton, G. Bonetti, Z. Gaburro, and L. Pavesi. Free-standing porous silicon single and multiple optical cavities. *J. Appl. Phys.*, 93(12):9724–9729, 2003.
- [237] T. Mukaiyama, K. Takeda, H. Miyazaki, Y. Jimba, and M. Kuwata-Gonokami. Tight-binding photonic molecule modes of resonant bispheres. *Phys. Rev. Lett.*, 82(23):4623–4626, 1999.
- [238] B. E. Little, S. T. Chu, H. A. Haus, J. Foresi, and J. P. Laine. Microring resonator channel dropping filters. *J. Lightwave Technol.*, 15(6):998–1005, 1997.
- [239] T. D. Happ, M. Kamp, A. Forchel, A. V. Bazhenov, I. I. Tartakovskii, A. Gorbunov, and V. D. Kulakovskii. Coupling of point-defect microcavities in two-dimensional photonic-crystal slabs. *J. Opt. Soc. Am. B*, 20(2):373–378, 2003.
- [240] S. Ishii, K. Nozaki, and T. Baba. Photonic molecules in photonic crystals. *Jap. J. Appl. Phys.*, 45(8 A):6108–6111, 2006.
- [241] D. P. Fussell and M. M. Dignam. Engineering the quality factors of coupled-cavity modes in photonic crystal slabs. *Appl. Phys. Lett.*, 90(18):183121, 2007.
- [242] E. Centeno and D. Felbacq. Rabi oscillations in bidimensional photonic crystals. *Phys. Rev. B*, 62(15):10101–10108, 2000.

- [243] S. Lam, A. R. A. Chalcraft, D. Szymanski, R. Oulton, B. D. Jones, D. Sanvitto, D. M. Whittaker, A. M. Fox, M. S. Skolnick, D. O'Brien, T. F. Krauss, H.-Y. Liu, P. W. Fry, and M. Hopkinson. Coupled resonant modes of dual l3-defect planar photonic crystal cavities. In *Conference on Lasers and Electro-Optics/Quantum Electronics and Laser Science, CLEO/QELS*, page paper QFG6. Optical Society of America, 2008.
- [244] D. Sarchi, I. Carusotto, M. Wouters, and V. Savona. Coherent dynamics and parametric instabilities of microcavity polaritons in double-well systems. *Phys. Rev. B*, 77(12):125324, 2008.
- [245] C. Cohen-Tannoudji, B. Diu, and F. Laloë. *Quantum Mechanics*. Wiley, New York, 1977.
- [246] K. A. Atlasov, K. F. Karlsson, A. Rudra, B. Dwir, and E. Kapon. Wavelength and loss splitting in directly coupled photonic-crystal defect microcavities. *Opt. Express*, 16(20):16255–16264, 2008.
- [247] L. Goldberg, H. F. Taylor, J. F. Weller, and D. R. Scifres. Injection locking of coupled-stripe diode laser arrays. *Appl. Phys. Lett.*, 46(3):236–238, 1985.
- [248] E. G. Lariontsev, I. Zolotoverkh, P. Besnard, and G. M. Stephan. Injection locking properties of a microchip laser. *Eur. Phys. J. D*, 5(1):107–117, 1999.
- [249] F. Intonti, S. Vignolini, F. Riboli, A. Vinattieri, D. S. Wiersma, M. Colocci, L. Balet, C. Monat, C. Zinoni, L. H. Li, R. Houdre, M. Francardi, A. Gerardino, A. Fiore, and M. Gurioli. Spectral tuning and near-field imaging of photonic crystal microcavities. *Phys. Rev. B*, 78(4):041401, 2008.
- [250] W. C. L. Hopman, A. J. F. Hollink, R. M. De Ridder, K. O. Van Der Werf, V. Subramaniam, and W. Bogaerts. Nano-mechanical tuning and imaging of a photonic crystal micro-cavity resonance. *Opt. Express*, 14(19):8745–8752, 2006.
- [251] <http://probe.olympus-global.com>.
- [252] M. T. Hill, Y. S. Oei, B. Smalbrugge, Y. Zhu, T. De Vries, P. J. Van Veldhoven, F. W. M. Van Otten, T. J. Eijkemans, J. P. Turkiewicz, H. De Waardt, E. J. Geluk, S. H. Kwon, Y. H. Lee, R. Nötzel, and M. K. Smit. Lasing in metallic-coated nanocavities. *Nature Photonics*, 1(10):589–594, 2007.
- [253] S. M. K. Thiyagarajan and A. F. J. Levi. The effect of scaling microlasers on modal noise. *Appl. Phys. Lett.*, 69(23):3459–3461, 1996.
- [254] S. Chakravarty, P. Bhattacharya, S. Chakrabarti, and Z. Mi. Multiwavelength ultralow-threshold lasing in quantum dot photonic crystal microcavities. *Optics Letters*, 32(10):1296–1298, 2007.

- [255] M. Fujita, R. Ushigome, and T. Baba. Large spontaneous emission factor of 0.1 in a microdisk injection laser. *IEEE Photonics Technol. Lett.*, 13(5):403–405, 2001.
- [256] H. Y. Ryu, M. Notomi, E. Kuramoto, and T. Segawa. Large spontaneous emission factor (0.1) in the photonic crystal monopole-mode laser. *Appl. Phys. Lett.*, 84(7):1067–1069, 2004.
- [257] Y. Yamamoto and G. Bjork. Lasers without inversion in microcavities. *Jpn. J. Appl. Phys.*, 30(12A):L2039–L2041, 1991.
- [258] A. Yariv. *Quantum Electronics*. John Wiley & Sons, New York, 3rd edition, 1989.
- [259] E. Rosencher and B. Vinter. Ch. 13g. laser diode noise and linewidth. In *Optoelectronics*, page 696. Cambridge University Press, Cambridge, UK, 2002.
- [260] Y. Yamamoto and N. Imoto. Internal and external field fluctuations of a laser oscillator: Part i—quantum mechanical langevin treatment. *IEEE J. Quantum Electron.*, 22(10):2032–2042, 1986.
- [261] G. P. Agrawal and G. R. Gray. Intensity and phase noise in microcavity surface-emitting semiconductor lasers. *Appl. Phys. Lett.*, 59(4):399–401, 1991.
- [262] Z. Toffano. Investigation of threshold transition in semiconductor lasers. *IEEE J. Sel. Top. Quantum Electron.*, 3(2):485–490, 1997.
- [263] C. H. Henry. Theory of the linewidth of semiconductor lasers. *IEEE J. Quantum Electron.*, QE-18(2):259–264, 1982.
- [264] C. H. Henry, R. A. Logan, and K. A. Bertness. Spectral dependence of the change in refractive index due to carrier injection in gas lasers. *J. Appl. Phys.*, 52(7):4457–4461, 1981.
- [265] G. Hunziker, W. Knop, P. Unger, and C. Harder. Gain, refractive index, linewidth enhancement factor from spontaneous emission of strained gainp quantum-well lasers. *IEEE J. Quantum Electron.*, 31(4):643–646, 1995.
- [266] G. Bjork. Personal communication, 2008.
- [267] R. Hui, N. Caponio, S. Benedetto, and I. Montrosset. Linewidth of a semiconductor laser operating near threshold. *IEEE Phot. Technol. Lett.*, 4(8):841–843, 1992.
- [268] J. Hendrickson, B. C. Richards, J. Sweet, S. Mosor, C. Christenson, D. Lam, G. Khitrova, H. M. Gibbs, T. Yoshie, A. Scherer, O. B. Shchekin, and D. G. Deppe. Quantum dot photonic-crystal-slab nanocavities: Quality factors and lasing. *Phys. Rev. B*, 72(19):1–4, 2005.

- [269] M. Nomura, S. Iwamoto, N. Kumagai, and Y. Arakawa. Temporal coherence of a photonic crystal nanocavity laser with high spontaneous emission coupling factor. *Phys. Rev. B*, 75(19), 2007.
- [270] U. Mohideen, R. E. Slusher, F. Jahnke, and S. W. Koch. Semiconductor microlaser linewidths. *Phys. Rev. Lett.*, 73(13):1785–1788, 1994.
- [271] Y. Hanamaki, H. Akiyama, and Y. Shiraki. Spontaneous emission alteration in ingaas/gaas vertical cavity surface emitting laser (vcsel) structures. *Semicond. Sci. Technol.*, 14(9):797–803, 1999.
- [272] K. Nozaki, S. Kita, and T. Baba. Room temperature continuous wave operation and controlled spontaneous emission in ultrasmall photonic crystal nanolaser. *Opt. Express*, 15(12):7506–7514, 2007.
- [273] E. Rosencher and B. Vinter. Ch. 4.6. cavity rate equations and the dynamic behaviour of lasers. In *Optoelectronics*, page 156. Cambridge University Press, Cambridge, UK, 2002.
- [274] C. Ellmers, F. Höhnsdorf, J. Koch, C. Agert, S. Leu, D. Karaiskaj, M. Hofmann, W. Stolz, and W. W. Rühle. Ultrafast (gain)(nas)/gaas vertical-cavity surface-emitting laser for the 1.3  $\mu\text{m}$  wavelength regime. *Appl. Phys. Lett.*, 74(16):2271–2273, 1999.
- [275] M. Hilpert, H. Klann, M. Hofmann, C. Ellmers, M. Oestreich, H. C. Schneider, F. Jahnke, S. W. Koch, W. W. Rühle, H. D. Wolf, D. Bernklau, and H. Riechert. Influence of carrier relaxation on the dynamics of stimulated emission in microcavity lasers. *Appl. Phys. Lett.*, 71(26):3761–3763, 1997.
- [276] M. Fox. *Quantum optics: an introduction*. Oxford University Press, New York, 2006.
- [277] R. Jin, D. Boggavarapu, M. Sargent Iii, P. Meystre, H. M. Gibbs, and G. Khitrova. Photon-number correlations near the threshold of microcavity lasers in the weak-coupling regime. *Phys. Rev. A.*, 49(5):4038–4042, 1994.
- [278] Y. S. Choi, M. T. Rakher, K. Hennessy, S. Strauf, A. Badolato, P. M. Petroff, D. Bouwmeester, and E. L. Hu. Evolution of the onset of coherence in a family of photonic crystal nanolasers. *Appl. Phys. Lett.*, 91(3):031108, 2007.
- [279] S. M. Ulrich, C. Gies, S. Ates, J. Wiersig, S. Reitzenstein, C. Hofmann, A. Löffler, A. Forchel, F. Jahnke, and P. Michler. Photon statistics of semiconductor microcavity lasers. *Phys. Rev. Lett.*, 98(4):043906, 2007.
- [280] D. Weidmann, F. K. Tittel, T. Aellen, M. Beck, D. Hofstetter, J. Faist, and S. Blaser. Mid-infrared trace-gas sensing with a quasi-continuous-wave peltier-cooled distributed feedback quantum cascade laser. *Appl. Phys. B*, 79(7):907–913, 2004.

- [281] D. Englund, H. Altug, I. Fushman, and J. Vučković. Efficient terahertz room-temperature photonic crystal nanocavity laser. *Appl. Phys. Lett.*, 91(7):071126, 2007.
- [282] D. Englund, H. Altug, and J. Vučković. Low-threshold surface-passivated photonic crystal nanocavity laser. *Appl. Phys. Lett.*, 91(7):071124, 2007.
- [283] G. Beister, J. Maegerle, D. Gutsche, G. Erbert, J. Sebastian, K. Vogel, M. Weyers, J. Würfl, and O. P. Daga. Simple method for examining sulphur passivation of facets in ingaas-algaas ( $\lambda = 0.98\mu\text{m}$ ) laser diodes. *Appl. Phys. Lett.*, 68(18):2467–2468, 1996.
- [284] H. Altug and J. Vučković. Two-dimensional coupled photonic crystal resonator arrays. *Appl. Phys. Lett.*, 84(2):161–163, 2004.
- [285] L. F. Lester and B. K. Ridley. Hot carriers and the frequency response of quantum well lasers. *J. Appl. Phys.*, 72(7):2579–2588, 1992.
- [286] C. Gies, J. Wiersig, and F. Jahnke. Output characteristics of pulsed and continuous-wave-excited quantum-dot microcavity lasers. *Phys. Rev. Lett.*, 101(6):067401–4, 2008.
- [287] T. Otterburg, D. Y. Oberli, M. A. Dupertuis, N. Moret, E. Pelucchi, B. Dwir, K. Leifer, and E. Kapon. Enhancement of the binding energy of charged excitons in disordered quantum wires. *Phys. Rev. B*, 71(3):1–4, 2005.
- [288] B. R. Bennett, R. A. Soref, and J. A. Del Alamo. Carrier-induced change in refractive index of inp, gaas, and ingaasp. *IEEE J. Quantum Electron.*, 26(1):113–122, 1990.
- [289] H. C. Casey and M. B. Panish. *Heterostructure Lasers. Part A: Fundamental Principles*. Quantum Electronics - Principles and Applications. Academic Press, Orlando, USA, 1978.
- [290] C. González, I. Benito, J. Ortega, L. Jurczyszyn, J. M. Blanco, R. Pérez, F. Flores, T. U. Kampen, D. R. T. Zahn, and W. Braun. Selenium passivation of gaas(001): A combined experimental and theoretical study. *J. Phys. Cond. Mat.*, 16(13):2187–2206, 2004.
- [291] H. G. Park, S. H. Kim, S. H. Kwon, Y. G. Ju, J. K. Yang, J. H. Baek, S. B. Kim, and Y. H. Lee. Electrically driven single-cell photonic crystal laser. *Science*, 305(5689):1444–1447, 2004.
- [292] T.-W. Lu, P.-T. Lee, C.-C. T., and Y.-Y. Tsai. Modal properties and thermal behaviors of highquality factor quasi-photonic crystal microcavity. *Opt. Express*, 16(17):12591–12598, 2008.

- 
- [293] V. Iakovlev, G. Suruceanu, A. Caliman, A. Mereuta, A. Mircea, C. A. Berseth, A. Syrbu, A. Rudra, and E. Kapon. High-performance single-mode vcsels in the 1310-nm waveband. *IEEE Photon. Technol. Lett.*, 17(5):947–949, 2005.



# Publications

## Relevant papers

*1D Photonic Band Formation in Finite-Size Photonic-Crystal Waveguides*, K. A. Atlasov, M. Felici, K. F. Karlsson, P. Gallo, A. Rudra, B. Dwir and E. Kapon, to be submitted (2009).

*Observation of Stimulated Emission and Lasing in Quantum-Wire Photonic-Crystal Nanocavities*, K. A. Atlasov, K. F. Karlsson, P. Gallo, A. Rudra, B. Dwir and E. Kapon, in Proc. IEEE/LEOS Winter Topical Meeting Series, 2009, 4-5, paper MA 1.3 (2009).

*Wavelength and loss splitting in directly coupled photonic-crystal defect microcavities*, K. A. Atlasov, K. F. Karlsson, A. Rudra, B. Dwir and E. Kapon, Opt. Express **16** (20), 16255-16264, (2008).

*Integration of Site-Controlled Pyramidal Quantum Dots and Photonic Crystal Membrane Cavities*, P. Gallo, M. Felici, B. Dwir, K. A. Atlasov, K. F. Karlsson, A. Rudra, A. Mohan, G. Biasiol, L. Sorba, and E. Kapon, Appl. Phys. Lett. **92**, 263101, (2008).

*Site-controlled single quantum wire integrated into a photonic-crystal membrane microcavity*, K. A. Atlasov, K. F. Karlsson, E. Deichsel, A. Rudra, B. Dwir, E. Kapon, Appl. Phys. Lett. **90** (15), 153107, (2007).

*Membrane Photonic Crystal Defect Cavities for Quantum Wire Lasers and 1D Polariton*, K. A. Atlasov, K. F. Karlsson, E. Deichsel, A. Rudra, B. Dwir, E. Kapon, Extended Abstracts of the 14<sup>th</sup> International Symposium "Nanostructures: Physics and Technology", Ioffe Institute, St. Petersburg, Russia, 289-290, (2006).

## Presentations at International Conferences

*Short ( $\sim 1\mu\text{m}$ ) Quantum-Wire Single-Mode Photonic-Crystal Microcavity Laser*, K. A. Atlasov, M. Calic, K. F. Karlsson, P. Gallo, A. Rudra, B. Dwir, and E. Kapon, Conference on Lasers and Electro-Optics (CLEO) 2009, Baltimore, MD, USA, May 31 - June 5, (2009). **Oral** presentation (accepted).

*Observation of Stimulated Emission and Lasing in Quantum-Wire Photonic-Crystal Nanocavities*, K. A. Atlasov, K. F. Karlsson, P. Gallo, A. Rudra, B. Dwir, and E. Kapon, IEEE/LEOS Winter Topicals: Nano and Nonlinear Photonics, Innsbruck, Austria, January 12-14, (2009). **Oral** presentation.

*Mode coupling and switching in photonic-crystal microcavities*, K. A. Atlasov, K. F. Karlsson, A. Rudra, B. Dwir, and E. Kapon, COST MP0702 (Towards Functional Sub-Wavelength Photonic Structures) Workshop, Bratislava, Slovak Republic, October 27-28, (2008). **Oral** presentation.

*Quantum-Wire Lasers Based on Photonic-Crystal Nanocavities*, K. A. Atlasov, K. F. Karlsson, P. Gallo, A. Rudra, B. Dwir, and E. Kapon, 17<sup>th</sup> International Laser Physics Workshop (LPHYS'08), Trondheim, Norway, June 30 - July 4, (2008). **Oral** presentation, **invited**.

*Observation of Wavelength- and Loss-Splitting of Supermodes in Coupled Photonic-Crystal Microcavities*, K. A. Atlasov, K. F. Karlsson, A. Rudra, B. Dwir, and E. Kapon, Conference on Lasers and Electro-Optics / Quantum Electronics and Laser Science Conference (CLEO/QELS) 2008, San Jose, CA, USA, May 4-9, (2008). **Oral** presentation.

*Towards Single-Photon Emission Control and Routing Using Photonic-Crystal Structures*, E. Kapon, K. A. Atlasov, K. F. Karlsson, P. Gallo, M. Felici, V. Troncale, B. Dwir, A. Rudra, COST MP0702 (Towards Functional Sub-Wavelength Photonic Structures) Kick-off Workshop, Warsaw, Poland, April 28-29, (2008). **Oral** presentation.

*1D Exciton-Photon Confinements in V-groove Quantum Wires Embedded into Photonic-Crystal Membrane Microcavities*, K. A. Atlasov, K. F. Karlsson, A. Rudra, B. Dwir, and E. Kapon, The 2<sup>nd</sup> International Conference on One-dimensional Nanomaterials (ICON 2007), Malmö, Sweden, September 26-29, (2007). **Poster** presentation.

*Site-controlled single quantum wire integrated into photonic-crystal membrane microcavity*, K. A. Atlasov, K. F. Karlsson, E. Deichsel, B. Dwir, A. Rudra, and E. Kapon, COST P11 (Advances in Physics and Technology of Photonic Crystals) Workshop, Czech Technical University, Prague, Czech Republic, April 19-20, (2007). **Oral** presentation.

*Integration of a Single V-groove Quantum Wire into 2D Photonic Crystal Membrane*

*Microcavity*, K. A. Atlasov, K. F. Karlsson, E. Deichsel, A. Rudra, B. Dwir and E. Kapon, 6<sup>th</sup> International Conference on Physics of Light-Matter Coupling in Nanostructures (PLMCN6), Magdeburg, Germany, September 25-29, (2006). **Poster** presentation.

*Design of High-Q Membrane Photonic Crystal Defect Cavity for Integration with Semiconductor Quantum Wires*, K. A. Atlasov, K. F. Karlsson, and E. Kapon, 9<sup>th</sup> International Conference on Near-field Optics, Nanophotonics and Related Techniques (NFO<sup>-9</sup>), Lausanne, Switzerland, September 10-15, (2006). **Poster** presentation.

*Membrane Photonic Crystal Defect Cavities for Quantum Wire Lasers and 1D Polariton*, K. A. Atlasov, K. F. Karlsson, E. Deichsel, B. Dwir, A. Rudra, and E. Kapon, 14<sup>th</sup> International Symposium "Nanostructures: Physics and Technology", St. Petersburg, Russia, June 26-30, (2006). **Oral** presentation.

*Modeling of Membrane Photonic Crystal Defect Cavities for Semiconductor Quantum Wire Laser Applications*, K. F. Karlsson, K. A. Atlasov, and E. Kapon, XV International Workshop on Optical Waveguide Theory and Numerical Modeling (OWTNM 2006), Varese, Italy, April 20-21, (2006). **Oral** presentation.



# Acknowledgements

Although research necessarily implies quite some individual effort, good results are only possible when many other people participate offering collaboration, encouragement and support.

First of all, I am indebted to Eli Kapon for giving me an opportunity to join his group in 2004 and get involved in nanotechnology and photonics experimental research, and for offering me an almost complete freedom and independency in work.

Secondly, I would like to thank Sanna Palmgren, Hakon Reichardt, Helge Weman, Valentina Troncale and Milan Calic as my office colleagues at different times and also as good friends of mine, I'm sure, on a timeless scale. I wish to thank also Martin Baier and Tim Otterburg with whom I shared an office during the very first couple of months.

I profited a lot from a scientific collaboration with Eckard Deichsel, Fredrik Karlsson, Pascal Gallo and Marco Felici – postdocs in the group who helped greatly expanding my experience in micro-processing, numerical computations and optical measurements. I'm very grateful to Benny Dwir, Nicolas Leiser, Damien and Yoan Trolliet, Marcin Byszewski for their continuous technical support in different labs. I also thank clean-room experts Alexei Sirbu and Andrei Caliman. A special acknowledgement is for Alok Rudra who took care of the MOVPE crystal growth, as well as for Zhanbing He who took TEM pictures. I wish to acknowledge also Vlad Iakovlev for his sharing a thousand of ideas when meeting in a corridor as well as jokes and who continuously asked "so, is it lasing?", which stimulated further effort in actually making lasers (see Chapter 7).

I would like to thank Daniel Oberli for critically reading Chapter 4 of this thesis and a very useful discussion and detailed comments. Throughout the thesis time I appreciated a lot numerous fruitful scientific and non-scientific discussions with Fredrik, Davide Sarchi, Dmitri Boiko, Dmitri Klinov, Nicolas Moret, Qing Zhu, Vasily Zabelin, Pascal, and Marco who, in particular, is always willing to dedicate, if needed, an infinite amount of his time to discuss various matters.

I'm very grateful to Profs. Dennis Deppe, Yong-Hee Lee and Vincenzo Savona for having accepted to be Referees of my thesis and for bringing up important questions to discussion during the defense time.

Going to scientific meetings I would like to mention, in particular, a highly collaborative atmosphere and interesting people that I met at COST (P11 and MP0702) workshops.

During all the time, I enjoyed a very friendly atmosphere in the group, at EPFL, and well beyond the campus. I wish to thank secretaries Denise Paroz, Gabriella Fuchs, Anita Berdoz, Beatrice Bliesener and Pierrette Paulou for their kind help of sorting out paper-work problems and for their extremely welcoming attitude. For numerous great parties, skiing/hiking/beach-volley and travel adventures I would like to acknowledge all the friends of mine Sanna, Eckard, Hakon, Tim, Anton Malko, Dmitri Klinov, Antonis Papazoglou, Andrea Dunbar, Pierre Lugan, Lars Lundeberg, Nicolas Moret, Sascha Dalessi, Benjamin Chalupar, Qing, Valentina, Davide, Alessandro Surrente, Romain Carron, Milan, Arun Mohan, Marcin, Lukas Mutter, Pascal, Philipp Ridha, Oleg Yazyev, Ivan Orlov, Julia Shakurova, Ira Pshenichnaya, Dmytro Dudenko, Audrius Alkauskas, Gleb Skobeltsyn, really many people from St. Petersburg and many others unintentionally missing in this list. I sincerely appreciate a continuous personal support and encouragement by Pascal, Sanna, Valentina, Davide, Nicolas, Qing, Oleg and Julia, Audrius and my parents Vera and Alexander.

# ATLASOV Kirill

Born 5<sup>th</sup> January, 1980  
in St. Petersburg, Russian Federation

E-mail: [kirill.atlasov@epfl.ch](mailto:kirill.atlasov@epfl.ch)  
[kirill.atlasov@gmail.com](mailto:kirill.atlasov@gmail.com)



---

**EDUCATION**

**PhD IN PHYSICS (2009)** *Jun 2004 – Apr 2009*  
Swiss Federal Institute of Technology, Lausanne (EPFL)  
Major: nanotechnology, photonics, light-matter interaction at nanoscale.  
Thesis: “Light control and microcavity lasers based on quantum wires integrated in photonic-crystal cavities”.

**MASTER IN PHYSICS (2003)** *Sep 1997 – Jul 2003*  
Institute of Fine Mechanics and Optics (IFMO, Technical University), St. Petersburg  
Major: physical engineering, optics, applied laser technology.  
Thesis: “Laser technology of forming probes for near-field scanning optical microscopy”.

**PARTICIPANT (WITH HONORS)** *Apr 2001, Apr 2000*  
SOKRATES International Intensive Program “Applications of Laser Technology”  
Institute für Lasertechnik Ostfriesland (ILO), Emden, Germany.

---

**PROFESSIONAL**

**SWISS FEDERAL INSTITUTE OF TECHNOLOGY** *Jun 2004 – Present*  
(Lausanne, Switzerland)  
Research assistant at the Institute of Photonics and Quantum Electronics. Design and fabrication of semiconductor nanostructures integrated with photonic-crystal resonators by micro-processing (e-beam nanolithography, ICP RIE) and epitaxy (MOVPE). Characterization by optical spectroscopy and microscopy (SEM, AFM). Data analysis and modelling. Writing scientific papers and project reports. Presentations at international conferences. Teaching assistant for undergraduate courses (Math Analysis; and Laboratory Training in Physics). Supervisor for a bachelor thesis of an undergraduate student.

**INSTITUTE OF FINE MECHANICS AND OPTICS** *Jan 2000 – Jan 2004*  
(St. Petersburg, Russia)  
Research assistant at the Department of Applied Laser Technology. Laser processing of optical telecom fibres. Fabrication of tapered-fibre probes for near-field optical microscopy. Design and implementation of a non-standard optical scheme. Writing scientific papers. Presentations at international conferences.

**SRC “LENINETZ PLANT” Inc.** (St. Petersburg, Russia) *Mar 2003 – May 2003*  
Operator at the Micro-electronics Department. Laser-assisted fine tuning of thin-film resistors for RF integrated circuits.

---

**PERSONAL**

**LANGUAGES**  
Russian: mother tongue  
English: fluent  
French: good knowledge

**COMPUTER**  
PC and Mac standard and office applications; notions in Matlab, Maple, Mathcad, COMSOL, Igor Pro; HTML basics; LaTeX, Photoshop, Premiere

**HOBBIES**  
Alpine skiing, hiking, travel, surfing

---

